UNIVERSITY OF MESSINA

Department of Chemical, Biological, Pharmaceutical and Environmental Sciences

Doctorate School in Chemical Sciences (XXXVII cycle)
SSD CHEM/07-A

_____

Design, Synthesis, and Biological Evaluation of Peptide-based Inhibitors of SARS-CoV-2 Proteases

PhD Thesis of:
Elsa CALCATERRA

Supervisor:
Prof. Maria Zappalà

Co-Supervisor:
Dr. Santo Previti

PhD Coordinator:
Prof. Concetta De Stefano

2023/2024 ACCADEMIC YEAR

Table of Contents

1. Aim of Research

SARS-CoV-2 is the virus responsible of COVID-19 (COronaVIrus Disease 19), an endemic disease that has caused the death of millions of people in the last four years and which still represents a global health problem. On 5th May 2023, the World Health Organization (WHO) declared the end of the SARS-CoV-2 pandemic following an evaluation of declining trends in deaths and hospitalizations and increasing levels of population immunity.[1] Despite that, the long-term efficacy of antibodies and the onset of new variants of the virus are unknown aspects for the coming years. In light of this, the development of effective antiviral agents still remains a priority in the fight of COVID-19.

SARS-CoV-2 is a positive-sense single-stranded RNA virus belonging to the Coronaviridae family together with MERS-CoV and SARS-CoV. Its genome is translated in two large polyproteins, pp1a and pp1ab, which are then cleaved into mature non-structural proteins. This cleavage occurs by two proteases, the main protease (M^{pro} or $3CL^{pro}$) and the papain-like protease (PL^{pro}), essential in the process of viral replication and in the control of the host's immune response. Due to their key role and the low tendency to undergo mutations, the inhibition of these enzymes represents a valid strategy for the development of antiviral agents.[2]

SARS-CoV-2 M^{pro} consists of three domains with the catalytic dyad Cys145-His41. The catalytic site is located in the intersection between domains I and II, and has five enzymatic pockets: S1', S1, S2, S3 and S4, respectively occupied by the P1', P1, P2 and P3/P4 portions of the viral polyproteins.[3] The cleavage of the protein substrate by $3CL^{pro}$ occurs between the glutamine residue at the P1 position and a small amino acid at P1′, such as a serine, glycine, or alanine residue.

SARS-CoV-2 PL^{pro} is instead made up of four domains: the thumb, the palm, the zinc-finger, and N-terminal ubiquitin-like domains. The catalytic triad, which consists of Cys111, His272, and Asp286 is located where the thumb and palm domains converge. The limited binding pockets at the P1 and P2 binding sites (Gly-Gly recognition) are the major factor contributing to the lack of effective PL^{pro} inhibitors.[4] This makes it difficult to find drugs quickly and represents a big challenge for inhibitor design.

In addition to viral proteins, human proteins are also well suited to the development of antiviral agents. As is known, human cathepsin L (hCatL) mediates the cleavage of the SARS-CoV-2 spike protein, necessary for the endosomal entry route of the virus into host cells. Therefore,

the double inhibition of the SARS-CoV-2 M^{pro} and hCatL could provide a synergistic antiviral effect *in vivo*.[5]

Starting from the hit-compounds **1** and **2**,[6] which modestly inhibit SARS-CoV-2 M^{pro} (IC$_{50}$: 157 µM and 47.2 µM respectively), two different series of molecules were developed (Figure 1).
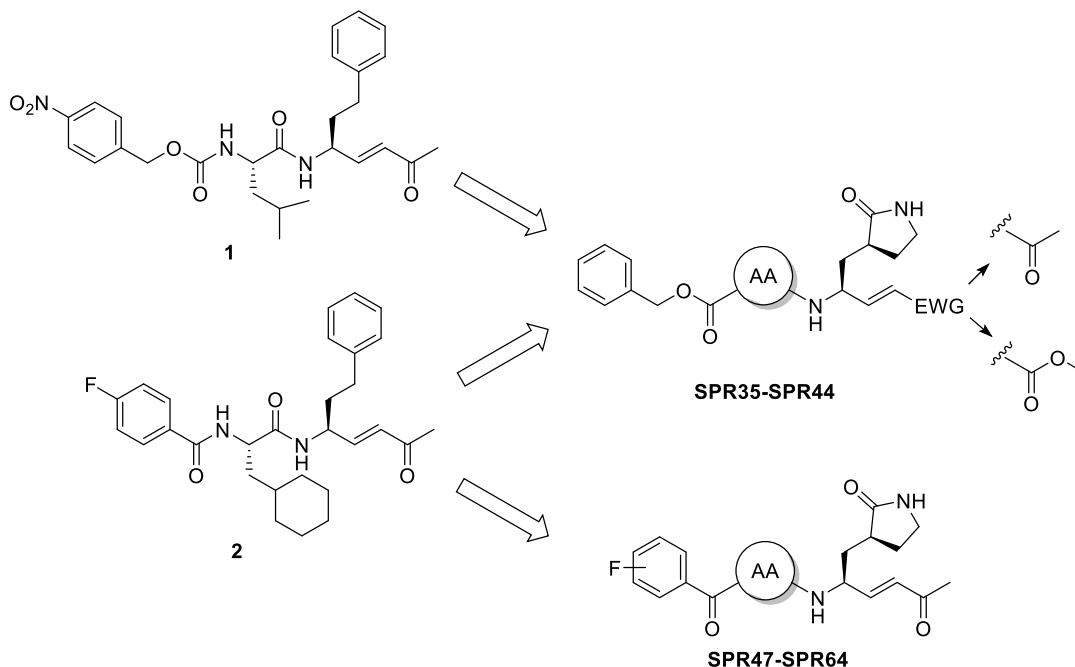
Figure 1. Hit-compounds **1** and **2** with the general structures of the two novel series of molecules **SPR35-SPR44** and **SPR47-SPR64**.

With regard to **SPR35-SPR44**, the hPhe of the hit-compounds **1** and **2** was replaced with a Gln pentatomic surrogate at the P1 site, since it is common in the most potent SARS-CoV-2 M^{pro} inhibitors. A panel of seven aliphatic amino acids was introduced at the P2 position, to explore the effect of different aliphatic side chains on the binding affinity. The carbobenzyloxy (Cbz) group was inserted as *N*-capping at P3 since it is present in a variety of SARS-CoV-2 M^{pro} inhibitors, including **GC376** and **UAWJ9-36-3** (Figure 2).[78]
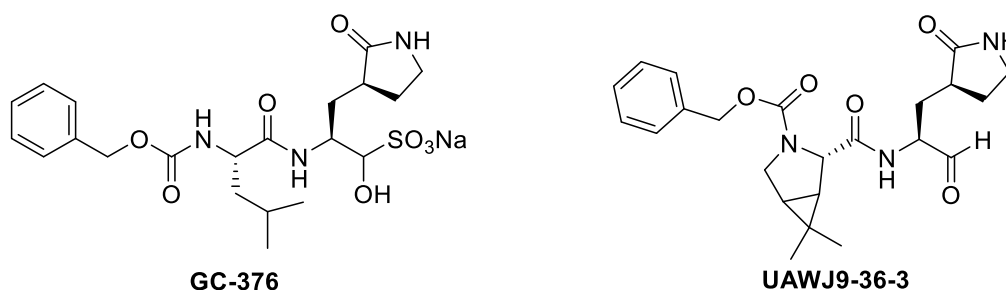
Figure 2. Chemical structure of SARS-CoV-2 inhibitors **GC376** and **UAWJ9-36-3**.

Lastly, the methyl vinyl ketone warhead of **1** and **2** was maintained and also the methyl vinyl ester warhead was evaluated.

The synthesized compounds were tested against SARS-CoV-2 M^{pro} and hCatL through fluorogenic assays to evaluate their inhibitory activity. In order to study the selectivity of these compounds, enzymatic assays were also performed through human cathepsin B (hCatB).

Finally, dialysis assays were performed to clarify the mechanism of action of these inhibitors and docking studies of the most active inhibitors were carried out to clarify the binding mode of the new class of inhibitors.

The results of these investigations will present in the section "Results and Discussion" of this thesis.

Concerning to **SPR47-SPR64**, the structure of the hit-compound **2** was modified.[9] The warhead methyl vinyl ketone was retained because it is well suited for the inhibition of both proteases. As regards the P1 position, cGln is in place, while in the P2 site, in addition to the cyclohexylalanine (Cha) of the hit, the best aliphatic amino acids of the previous series were inserted. The aromatic ring at P3 was maintained, and the role of the fluorine atom was evaluated by its introduction in the *ortho*, *meta* or *para* positions. The insertion of fluorine atoms, an highly used approach in medical chemistry, could improve enzyme-inhibitor binding interactions, as well as ensuring better pharmacokinetic and chemical-physical properties, metabolic stability and better penetration of cell membranes. Furthermore, numerous peptide inhibitors of both SARS-CoV-2 M^{pro} and hCatL have fluorine atoms at this position.[10,11]

All the new synthesized inhibitors were evaluated against the SARS-CoV-2 M^{pro} at 1 μM. The molecules were then tested against hCatL, but, since the aim of the research was to identify possible dual inhibitors, the K_i values were calculated only for the active compounds against M^{pro}. The most active dual inhibitors were also evaluated in cellular assays, first analyzing their cytotoxicity, an essential parameter in the drug discovery process. Considering the CC$_{50}$ values shown, no cytotoxic compounds were analyzed to determine the antiviral effect through Huh-7-ACE2 cells infected by SARS-CoV-2. Finally docking studies have been carried out for the most active inhibitors.

Another series of potential dual inhibitors was developed starting from Calpain Inhibitor XII (SARS-CoV-2 M^{pro}, IC$_{50}$: 453 nM; hCatL, IC$_{50}$: 1.62 nM).[12] The α-keto-amide warhead of the lead compound was replaced with a panel of differently substituted vinyl amide warheads. At P1 site Nva or Nle were inserted and at P2-P3 positions Cbz-Leu or Cbz-Phe were introduced (Figure 3). Biological evaluation of the new potential inhibitors **EC1-EC8** is ongoing. Part of

this project was caried out during my period abroad at the Juame I University in Castellon de la Plana, Spain.
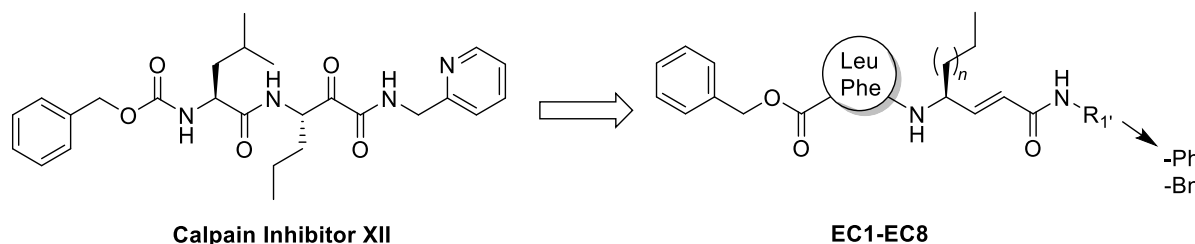
Figure 3. Calpain Inhibitors XII and the novel potential SARS-CoV-2 M^{pro}/hCatL dual inhibitors **EC1-EC8**.

Lastly, a series of potential inhibitors of SARS-CoV-2 PL^{pro} was developed. The design of the novel molecules started from the structure of a powerful inhibitor existing in literature, **VIR251** (SARS-CoV-2 PL^{pro}, IC_{50}: 50 µM) (Figure 4).[13]
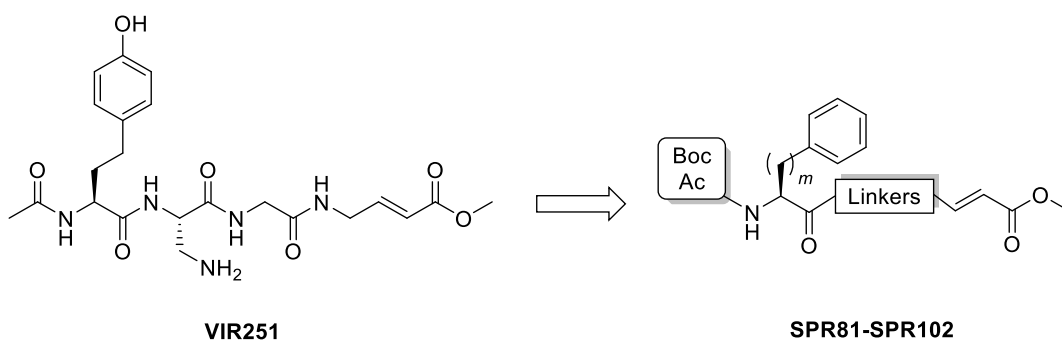
Figure 4. VIR251 with the new series of PLpro inhibitors **SPR81-SPR102**.

With a process of molecular simplification, the methyl vinyl ester warhead of the lead compound was maintained, and various aliphatic linkers between the aromatic ring at P4 and the warhead were introduced. Therefore, in the P1-P2 or P1-P3 portions, Glycine (Gly) and its homologues β-Alanine (βAla) and Gamma-Aminobutyric Acid (GABA) were alternatively inserted. The introduction of these residues without a side chain should allow the warhead to reach the catalytic Cysteine (Cys), and the rest of the molecule could interact *via* hydrogen bonds with the various residues at the S1, S2, and S3 pockets. Homotyrosine (hTyr) was replaced by hPhe or Phe, whereas the *N*-capping acetyl group was maintained.

The novel molecules **SPR81-SPR91**, which are the *N*-Boc-containing intermediates, and the Ac-analogues **SPR92-SPR102** are currently under evaluation towards SARS-CoV-2 PL^{pro}.

In conclusion, several SARS-CoV-2 proteases inhibitors as potential antiviral agents were produced. Novel dual inhibitors of SARS-CoV-2 M^{pro} and hCatL were synthetized and tested

against both proteases and in cell-based assays. Another series of potential dual inhibitors is under evaluation against both enzymes. Finally, a new series of molecules is being tested towards SARS-CoV-2 PL^{pro}.

2. Coronavirus Disease-19

2.1. Emergence and Spread

On December 31, 2019, the World Health Organization (WHO) was alerted of a disease outbreak associated with pneumonia-like symptoms of unknown etiology detected in Hubei province, Wuhan city, China (Figure 5).[14]

Patients displayed symptoms of viral pneumonia, such as fever, coughing, and chest pain. In more severe cases, they also displayed bilateral lung infiltration and dyspnea.[15] These symptoms were similar to those of patients with *Severe Acute Respiratory Syndrome* (SARS) and *Middle East Respiratory Syndrome* (MERS). The majority of the first 27 hospitalized patients to be recorded had an epidemiological connection to Huanan Seafood Wholesale Market, a wet market in Wuhan's downtown that sells live animals, including poultry and wildlife, in addition to seafood.[16]A retrospective study indicates that the first recorded case began on December 8, 2019. Wuhan Municipal Health Commission alerted the public to a pneumonia outbreak with an unknown cause on December 31.

On January 1, 2020, the Huanan Seafood Wholesale market was completely closed for disinfection and sanitization purposes since viral pneumonia was associated with the market.[17]

The Incident Management System of the WHO was activated on January 2, 2020. Then the Central Committee of the Communist Party of China, together with the State Council, launched a national emergency program, and between December 31, 2019, and January 3, 2020, 44 people were infected with the new virus in Wuhan, China.[18] The first imported case of the new coronavirus outside Wuhan was confirmed on January 13, 2020, in Thailand, followed by the second wave of the imported case confirmed in Japan on January 15, 2020.

The virus rapidly spreads to all 34 of China's provinces in just one month. There was a sharp rise in the number of confirmed cases, with thousands of new cases being diagnosed every day in late January.[19] The novel coronavirus outbreak was deemed a public health emergency of international concern on January 30. On February 11, the WHO designated the illness as "*COronaVIrus Disease 19* (COVID-19)" and the International Committee on Taxonomy of Viruses named the new coronavirus "*Severe Acute Respiratory Syndrome Coronavirus 2* (SARS-CoV-2)".[20]

Severely affected countries include India, the United States, Italy, China, Spain, Russia, Brazil, and the United Kingdom.

The rapid global spread of COVID-19 was made possible by the high transmission efficiency of SARS-CoV-2 and the prevalence of international travel.

The WHO formally classified the global COVID-19 outbreak as a pandemic on March 11, 2020. While COVID-19 has been effectively contained in China since March, the number of cases in the USA, Europe, and other regions has sharply increased. Over 20 million COVID-19 cases had been reported from 216 countries and regions across all six continents as of August 11, 2020, and over 733,000 patients had died, according to the COVID-19 dashboard maintained by the Center for System Science and Engineering at Johns Hopkins University. High mortality was more common when there were insufficient resources for healthcare. The nation with the greatest number of cases to date is the USA.

Almost 3 years later, thanks to the development of protocols, vaccines and functional therapies, the WHO announced that the spread of SARS-CoV-2 is no longer considered a global health emergency during a press conference on May 5, 2023. The decision was made by the WHO emergency committee following examination of the declining trend in COVID-19 deaths, the reduction in related hospital admissions and the high levels of SARS-CoV-2 population immunity. They came to the conclusion that COVID-19 should now be regarded as a recognized and continuing health issue that does not qualify as a global public health emergency. [1]

However, it was deemed necessary to implement close surveillance of the trend of registered cases, deaths, and the onset of new variants.
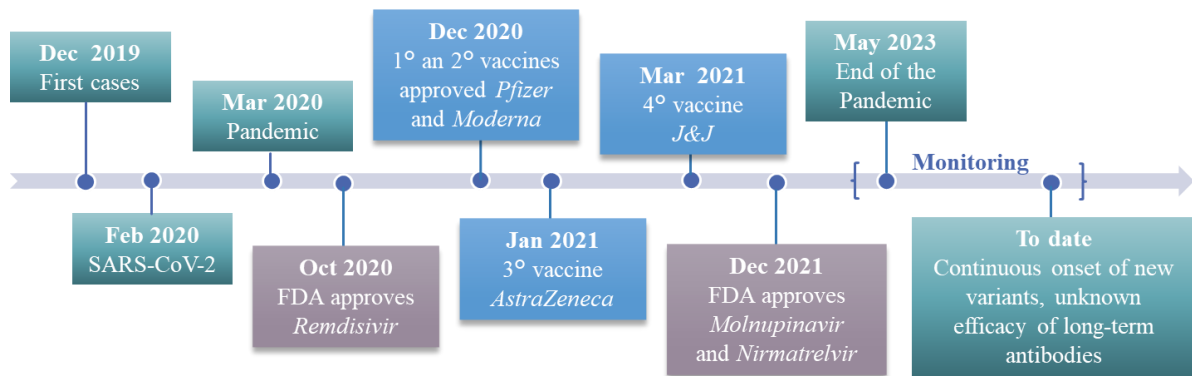
Figure 5. COVID-19 timeline.

To date, the WHO reports 777,007,137 confirmed cases worldwide since the start of the pandemic and 7,059,612 deaths with 13.64 bn of vaccine doses administered (data as of September, 11, 2024) and despite the end of the pandemic, various issues raise concerns about a new wave of cases.[21] One of the possible causes of a new increase in both the number of cases and deaths is the constant appearance of new variants of SARS-CoV-2, which makes the spread and pathogenicity of the virus unpredictable. In addition to this, the effectiveness and the long-term duration of vaccinations are unknown, as well as the natural antibodies produced by the

immune system following infection. In addition to vaccines, the great effort of the scientific community has led to the approval of a limited number of antiviral agents, introduced into therapy as a further weapon to contain the symptoms of COVID-19.[22]

2.2. Clinical Manifestations of COVID-19

All age groups seem to be at risk of contracting SARS-CoV-2, with the median infection age being approximately 50 years old.[23] Indeed, the clinical signs change with age. Generally, hospitalization for severe respiratory illness is more common in older men (over 60) with co-morbidities. In contrast, the majority of children and young adults are either asymptomatic or have only mild illnesses (such as non-pneumonia or mild pneumonia).[24]

Notably, pregnant women did not have a higher risk of illness. Nonetheless, evidence of SARS-CoV-2 transplacental transmission from an infected mother to a newborn was documented.[25]

COVID-19 is categorized into three levels based on the severity of the disease: mild, severe, and critical. Most patients experience mild symptoms and eventually recover; there have also been reports of asymptomatic cases. The mayor symptoms include fever, dry cough, and tiredness. Less common symptoms include sputum production, headache, hemoptysis, diarrhea, anorexia, chest pain, nausea, and vomiting (Figure 6). Patients in Italy also reported taste and smell disorders.[26] The majority of patients developed symptoms after an incubation period of 1-14 days, usually 5 days, and pneumonia and dyspnea appeared 8 days after the illness started on average.
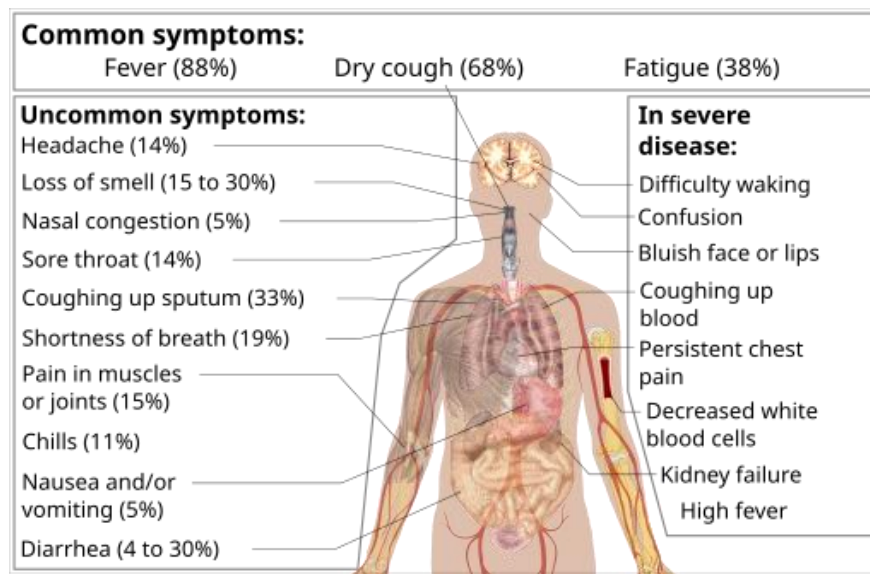
Figure 6. Clinical manifestation of COVID-19.

Initially, the disease usually has a gradual onset, but later, can become fatal, particularly in the elderly and in people with significant comorbidities such as diabetes, strokes, severe asthma, and chronic obstructive lung diseases.

2.3. Prevention

Since SARS-CoV-2 transmission is considered a public health concern, the first step in managing this viral infection is to ensure adequate isolation to prevent transmission to another individual. Cleaning and disinfecting surfaces are the best way to reduce the spread of COVID-19 and other viral respiratory infections in homes and public places. In order to stop virus spread and isolate those who have been exposed, it is crucial to use personal protective equipment (PPE), such as masks and general body hygiene, in both homes and healthcare facilities. Most countries around the world have adopted various precautionary measures, such as lockdown policies to reduce the transmission rate by reducing social activities and contacts. This has had a significant negative impact on the economics of different societies worldwide, so there was an urgency to develop safe and effective vaccines to mitigate the current viral disease. In order to combat the pandemic, clinical researchers from all over the world conducted extensive research in this area, and major advancements were made in the creation of effective vaccines against SARS-CoV-2.

There are currently a number of SARS-CoV-2 vaccinations in use, and more are being developed. Everything depends on the technology platforms being used to produce vaccines, each of which has advantages of its own. The well-established manufacturing method known as the "inactivated platform" is used to create purified whole SARS-CoV-2 components. For instance, Chinese scientists have been using this technology to create BBIBP-CorV and CoronaVac (PicoVacc). Vaccines based on viral vectors and nucleic acids are the other two most recent platforms. Nucleic acid platforms are typically quick and inexpensive to produce. They can be either self-amplifying mRNA type, which was used to produce LNP-nCoVsaRNA vaccine by Imperial College London, or lipid-encapsulated mRNA, like in the mRNA1273 vaccine produced by the United States based company Moderna and BNT162b1 from BioNTech/Fosun Pharma/Pfizer.[27]

Contrarily, the viral vector involves strong humoral and cellular vaccine immunity. This technology was employed in the manufacturing of the human adenovirus types 5 and 26 (Ad5-nCoV and Ad26.COV2-S) by Japanese pharmaceutical companies, as well as in the manufacturing of the chimpanzee adenovirus (ChAdOx1 nCoV19) by AstraZeneca, University

of Oxford.[28] Other researchers are working on the designs of vaccine candidates. Samad et al. used the SARS-CoV-2 spike glycoprotein to identify the immunodominant T- and B-cell epitopes. From these three epitopes—the helper T-lymphocyte, the cytotoxic T-lymphocyte, and the linear B-lymphocyte—they were able to design a vaccine construct that was immunogenic, antigenic, and non-allergenic with improved solubility and appropriate physicochemical characteristics.[29]

Madhi et al. looked into the vaccines' effectiveness against newly emerging SARS-CoV-2 variants of concern, such as the B.1.351 (501Y.V2) variant that was first discovered in South Africa. Two doses of the ChAdOx1 nCoV-19 vaccine did not protect against mild-to-moderate COVID-19 symptoms caused by the B.1.351 variant in the group of 25 participants who were tested using pseudovirus and live-virus neutralization assays against the original D614G virus and the variant by obtaining the participants' serum after the second dose.[30] This suggests that the vaccine is less effective against the variant B.1.351 than against other variants.

After receiving the ChAdOx1 nCoV-19 vaccine (Oxford/AstraZeneca), side effects including cerebral venous sinus thrombosis with thrombocytopenia—a dangerous disorder involving blood clotting—were documented in certain regions of Europe. The human adenoviral vector-based Ad26.COV2. S COVID-19 vaccine (Janssen/Johnson & Johnson) was approved for use in the US on February 27, 2021, and by April 2021, six cases of cerebral venous sinus thrombosis had been reported.[31]

2.4. Treatment

Since the onset of the COVID-19 pandemic in March 2020, SARS-CoV-2 has caused the death of millions of people around the world.[32] During this time, research into therapies for COVID-19 has progressed at an astonishing pace. Therapeutic agents studied during the pandemic include pharmaceutical specialties with various mechanisms of action, such as antiviral therapies that directly inhibit viral replication, recombinant monoclonal antibodies that block viral entry into host cells, adjuvant therapies that target the immune response of the host (for example, anti-inflammatory and antithrombotic therapies), and therapies targeting the renin-angiotensin-aldosterone system (RAAS) (Figure 7). Numerous randomized clinical trials (RTCs) have evaluated the safety and efficacy of these drugs, which include new or already marketed drugs. Numerous therapies have obtained emergency use authorization, while some pharmaceutical specialties have obtained marketing approval from the Food and Drug Administration (FDA) and European Medicines Agency (EMA).[33]
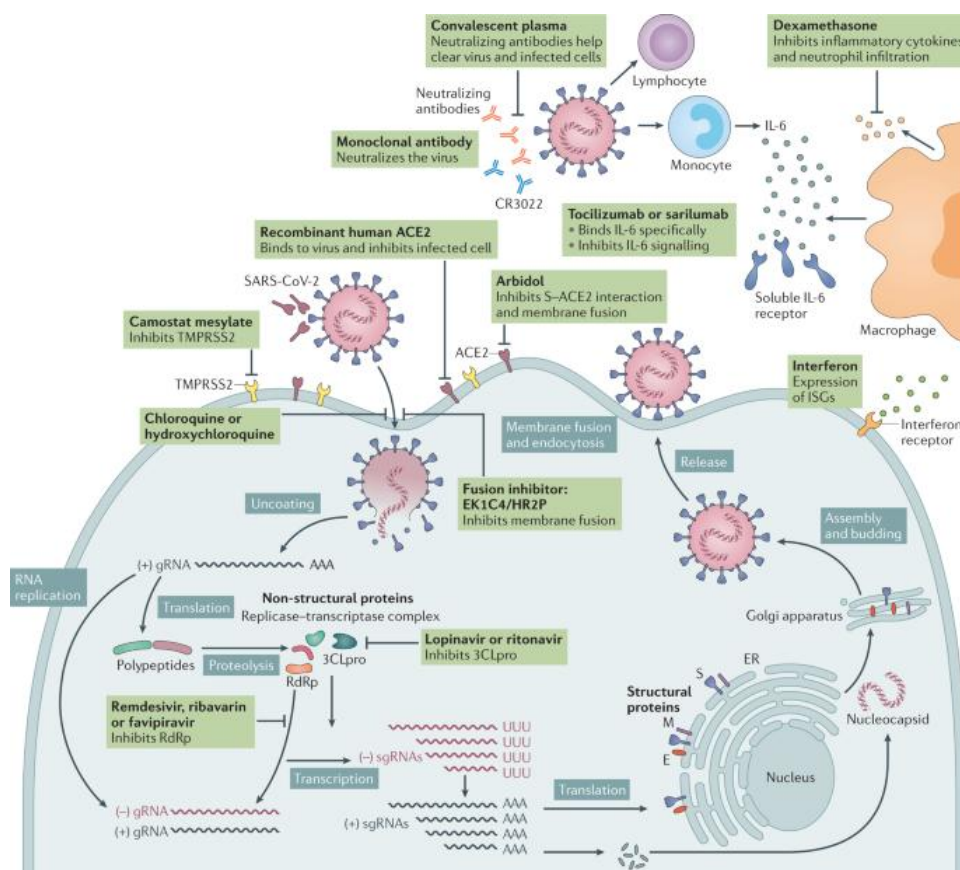
Figure 7. Therapeutic agents with various mechanisms of action. [33]

Remdesivir (GS-5734), a broad-spectrum nucleoside analogue antiviral prodrug, has been shown in a study by Cao et al. to have some effects on pathogenic animal and human coronaviruses, such as SARS-CoV-2 (Figure 8). *In vitro* studies have also shown that it can inhibit the replication of SARS-CoV and MERS-CoV. Nevertheless, the drug combined with baricitinib, it reduced the amount of time that COVID-19 patients needed to recover.[34]
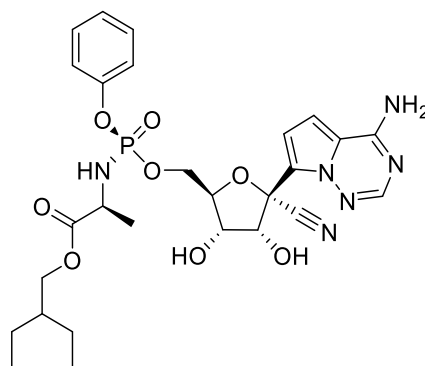
Remdesivir

Figure 8. Chemical structure of Remdesivir.

There were numerous disagreements among scientists regarding the effectiveness of hydrochloroquine (HCQ). This was approved in France, China, and Korea, among other countries. It was suggested that it be used in combination with lopinavir, ritonavir, umifenovir and α-interferon (and frequently with azithromycin, AZ). It was discovered that HCQ effectively cleared the viral nasopharyngeal carriage of SARS-CoV-2 in COVID-19 patients in as little as three to six days (for the majority of patients). Earliest on the third day after inclusion, a noteworthy distinction was noted between the patients receiving hydroxychloroquine and the control group.

Reports suggest that other anti-inflammatory medications can decrease the requirement for invasive ventilation. In a clinical trial comprising 21,550 patients, 4116 were included in the RECOVERY trial program, where they were receiving oxygen and exhibited signs of systemic inflammation; 2022 patients received tocilizumab treatment, a medication intended to support the immune system; and 729 (35%) of the 2094 patients who were maintained under standard care passed away in less than 28 days. The trial demonstrated that tocilizumab administration was linked to a higher likelihood of hospital discharge within 28 days (57% vs. 50%), indicating that the medication has reduced the need for invasive ventilation.[35]

An additional oral medication called Molnupiravir EIDD-2801, a broad-spectrum oral antiviral agent, was employed since an animal model showed a notable decrease in the amount of SARS-CoV-2 in the lungs (Figure 9). It is regarded as having potential for the prevention and treatment of COVID-19 since it is presently in the late stages of clinical trials and has been shown to inhibit SARS-CoV-2 replication *in vivo*.[36]
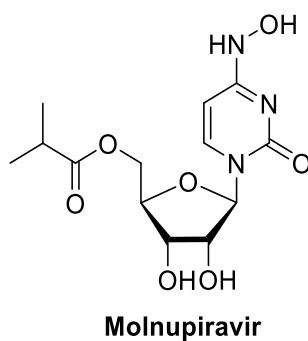
Molnupiravir

Figure 9. Chemical structure of Molnupivar.

Researchers are using computational drug repurposing as a result of recent technological advancements to find possible inhibitors of the spike angiotensin-converting enzyme 2 (ACE-2), which is the primary protease of SARS-CoV-2. A few of the substances that are currently undergoing clinical trials are being tested for their ability to combat viruses. In the

computational workflow, a set of inhibitors from the DrugBank database are analyzed to determine which ligands are needed. Next, the protein-ligand interaction is optimized by examining the geometries and binding free energy estimations, assessing the complementarity of the protein-ligand through visual inspection, analyzing the activity annotations and therapeutic indications of the possible candidate compounds, and finally selecting the best candidate.[37]

Other medications should be investigated as possible COVID-19 treatments because stopping ACE-2, which helps SARS-CoV-2 enter cells, is crucial to the disease's recovery. In their work on drug repurposing, Lazniewski et al. (2021) used simeprevir, a protease inhibitor used to treat hepatitis C, and zafirlukast, a medication used to treat asthma by blocking a leukotriene receptor. Both drugs have the potential to be investigated *in vitro* and *in vivo* against SARS-CoV-2 due to their average binding affinity of −22 kcal/mol for spike proteins originating from different lineages.[38]

As of 2022, the United States FDA had granted three therapeutic antibodies through the Emergency Use Authorization (EUA). One is a combination of etesevimab and bamlanivimab; data indicate that this combination may cause patients' viral levels to decrease. In the second, imdevimab and casirivimab are used as a cocktail pair. The final one is a sotrovimab single antibody, whose clinical trial demonstrated an 85% decrease in hospitalization or death. At the moment, the US FDA has only authorized Paxlovid (nirmatrelvir and ritonavir tablets) for use in emergency situations (Figure 10). These tablets are loaded to prevent the virus from replicating.[39]
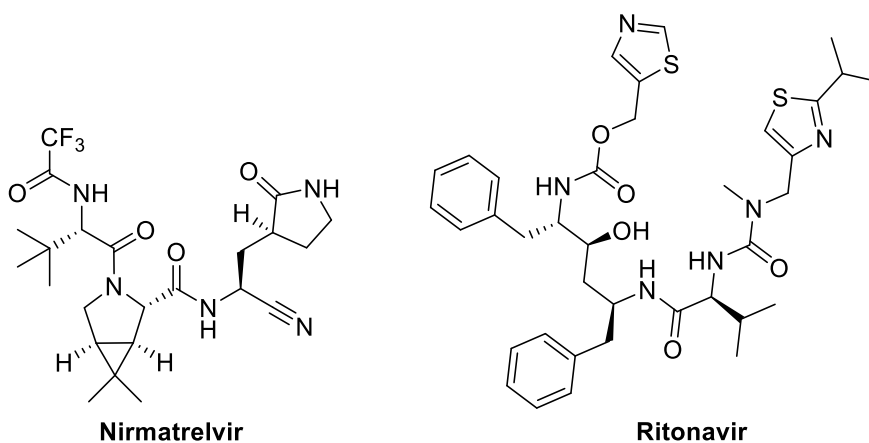
Figure 10. Chemical structure of Nirmatrelvir and Ritonavir.

3. SARS-CoV-2

Coronaviruses belong to the Coronaviridae family, which in turn belongs to the Nidovirales order. The Coronaviruses name is due to the crown-like spikes that protrude from the virus surface. These viruses can infect both animals and humans, resulting in diseases with different clinical manifestations. Human coronaviruses were first identified in the mid-1960s, and they are known to cause a variety of diseases including pneumonia, enteritis, hepatitis, polyserositis, encephalomyelitis, pyelonephritis, bronchitis, reproductive diseases, and other cellular/physiological disorders.[40] Genetically, coronaviruses are enveloped viruses with a positive-sense single-stranded RNA (+ssRNA) genome. With respect to the RNA viruses, the genome size of coronaviruses in unusually longer, ranging from approximately 26 to 32 kilobases (kb) in length. This substantial size gives coronaviruses the largest RNA genomes known among viruses.

Coronaviruses are classified into four major subgroups: alpha, beta, gamma, and delta. Among these, only alpha and beta coronaviruses are known to infect humans. These human coronaviruses (HCoVs) are responsible for a range of respiratory illnesses, from mild colds to severe diseases like SARS, MERS, and COVID-19. The seven strains of human coronaviruses include two alpha coronaviruses, HCoV-229E and HCoV-NL63, and five beta coronaviruses, HCoV-OC43, HCoV-HKU1, SARS-CoV, MERS-CoV, SARS-CoV-2.[41]

Structurally, coronaviruses consist of complex virions that exhibit several defining structural features. The virions are pleomorphic (variable shape) spherical, measuring between 80 and 220 nanometers (nm) in diameter. The coronavirus virion contains four major structural proteins, namely the spike glycoprotein (S), the nucleocapsid (N), the membrane glycoprotein (M), and the envelope glycoprotein (E).

The S glycoprotein is essential for attachment and entry into the host cell. More in detail, it consists of two subunits: S1 subunit, which is responsible for the binding to the host cell receptor, and S2 subunit that mediates the fusion of the viral and cellular membranes. Some betacoronaviruses possess an additional structural protein, the hemagglutinin-esterase (HE), which forms shorter spikes. The HE protein is involved in binding to sialic acid on host cells and may aid in the spread of the virus within the host.

The nucleocapsid protein (N) is a structural protein of coronaviruses responsible for encapsulating the viral RNA genome. It plays a key role in the packaging and protection of the viral RNA, as well as in the replication and transcription of the viral genome.

The membrane glycoprotein (M) is the most abundant structural protein in the coronavirus envelope. It spans the viral membrane and is essential for virus assembly, shaping the virion, and ensuring the proper curvature of the membrane.

The envelope glycoprotein (E) is a small structural protein found in the envelope of coronaviruses. Despite its small size, it plays a crucial role in virus assembly, release, and pathogenesis. The E protein has a transmembrane domain that anchors it to the viral membrane and a small luminal domain. It is involved in the formation of the viral envelope and interacts with the M protein to drive the budding process of new virions. Additionally, the E protein has ion channel activity that is important for the virus's life cycle and can influence the host cell's environment to favor viral replication.

The RNA genome of Coronaviruses is highly infectious and includes a 5' cap and a 3' polyadenylated tail, similar to eukaryotic mRNA, which facilitates translation and stability of the viral RNA. Coronavirus assembly occurs in the endoplasmic reticulum (ER) and Golgi apparatus. The viral proteins and RNA genome are assembled into new virions by budding into the lumen of the ER-Golgi intermediate compartment (ERGIC). The newly formed enveloped virions are transported to the cell surface in vesicles and released from the host cell through the process of exocytosis.[42]

Novel coronavirus disease 2019 (COVID-19) is the well-known upper respiratory disease caused by SARS-CoV-2.[43] The new virus was first identified in Wuhan, China, in late 2019. The disease quickly spread globally, leading to widespread illness, economic disruption, and the implementation of public health measures to control the spread of the virus.

SARS-CoV-2 has a diameter of roughly 60 to 140 nm and a round, elliptic, and frequently pleomorphic form. It is heat- and UV-sensitive, similarly to other CoVs, as well as, 90% of SARS-CoV-2 is rendered inactive on a stainless-steel surface maintained at an air temperature of 54.5°C (130°F) for about 36 minutes.[44] On the contrary, SARS-COV-2 can withstand temperatures as low as 0°C. Organic solvents, such as ether (75%), ethanol, chloroform, peroxyacetic acid, chlorine-containing disinfectants (apart from chlorhexidine), can effectively inactivate the virus.

According to genomic analyses, SARS-CoV-2 most likely originated from a bat strain. High homology (96%) was found between the human SARS-CoV-2 sequence and the betaCoV RaTG13 of bats (*Rhinolophus affinis*), according to a genomic comparison of the human SARS-CoV-2 sequence and known animal coronaviruses. It has been suggested that SARS-CoV-2 spreads from bats to intermediate hosts like pangolins and minks, and then to humans. This

transmission pathway is similar to that of other coronaviruses like MERS-CoV and SARS-CoV.[45]

3.1. SARS-CoV-2 Life Cycle

The replication of SARS-CoV-2 involves a complex series of steps, ensuring the virus can effectively reproduce within the host cell (Figure 11). SARS-CoV-2 can enter host cells through two distinct pathways, both involving cleavage of the spike (S) protein at specific sites of the subunits S1 and S2.[46] The first cleavage occurs at the boundary between the S1 and S2 subunits. This site is often referred to as the S1/S2 cleavage site. This cleavage is typically mediated by host cell proteases such as furin, a proprotein convertase that recognizes a specific cleavage motif (often a polybasic sequence) present at the S1/S2 site. Cleavage at this site separates the S1 subunit, which contains the receptor-binding domain (RBD), from the S2 subunit, which contains the machinery necessary for membrane fusion.

The second critical cleavage occurs at a site within the S2 subunit, referred to as the S2' site. The specific protease that cleaves the S2′ site depends on the entry route. If the target cell has low levels of transmembrane protease serine 2 (TMPRSS2) or if the virus–ACE2 complex does not encounter TMPRSS2, the virus–ACE2 complex is internalized via clathrin-mediated endocytosis into the endolysosomes. In this acidic environment, cathepsins cleave the S2′ site. In contrast, if TMPRSS2 is present, the S2′ cleavage occurs directly at the cell surface. In both pathways, cleavage at the S2′ site is essential for exposing the fusion peptide (FP). This process, combined with the dissociation of S1 from S2, causes dramatic conformational changes in the S2 subunit, especially in heptad repeat 1 (HR1). These changes propel the FP into the target membrane, initiating membrane fusion, both in the endosomal pathway and in the TMPRSS2 pathway.

The fusion between the viral and cellular membranes creates a fusion pore, allowing the viral RNA to enter the host cell cytoplasm for uncoating and replication. The released positive-sense RNA (+ssRNA) serves directly as mRNA for the synthesis of viral proteins. The RNA-dependent RNA polymerase (RdRp), encoded by non-structural protein 12 (nsp12), synthesizes a complementary negative-sense RNA (mRNA-cn-) from the +ssRNA template.[47] This mRNA-cn- will then serve as a template for producing new positive-sense RNA (mRNA-cn+), which acts as mRNA for viral protein synthesis and as genomic RNA for new virions.[48] The mRNA directs the synthesis of both structural proteins: nucleocapsid (N), envelope (E), membrane (M), and spike (S) proteins, and two large polyproteins, pp1a and pp1ab, that will be then cleaved

by viral proteases into 16 non-structural proteins (nsps).[49] Among these, nsp1, nsp3, nsp5, nsp12 actively participate in the replication and transcription of the viral genome, which occur within membranous complexes derived from the endoplasmic reticulum (ER) and the Golgi apparatus.
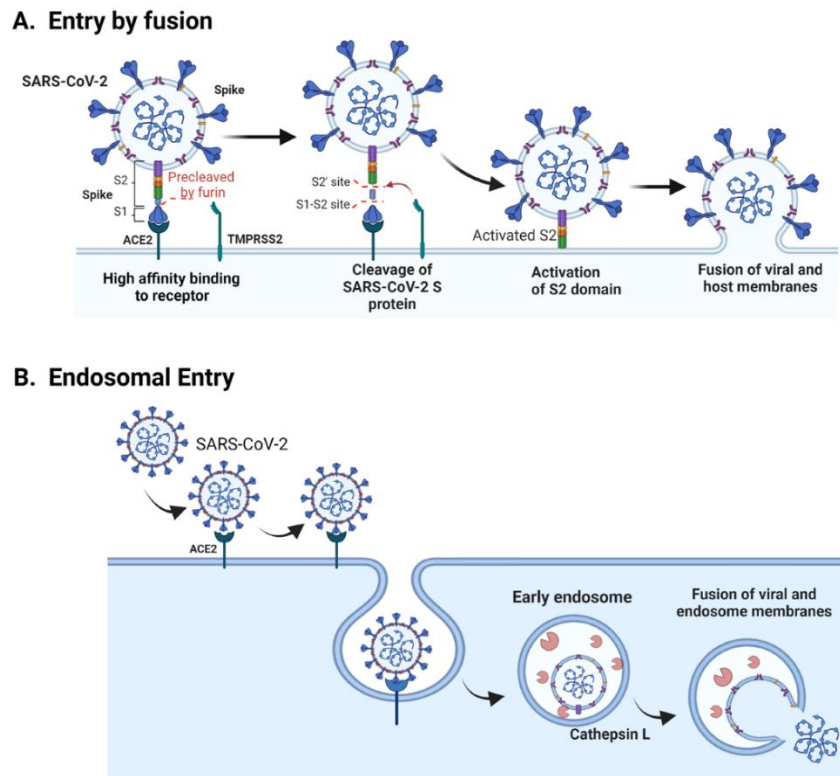
Figure 11. The two pathways for the entry of the virus into host cells.[50]

Nsp1 mediates RNA processing and replication, while nsp2 modulates host cell survival signaling pathway. Nsp3 encodes papain-like protease (PL^{pro}), responsible of the cleavage of part of polyproteins into mature proteins. Nsp3 is also responsible for the separation of translated proteins by ribosomes. Nsp4 alters ER membrane functionality with its transmembrane domain 2 (TM2). Nsp5 encodes the main protease (M^{pro}), which, together with PL^{pro}, is responsible for the cleavage of pp1a and pp1ab into mature proteins. It should be underlined that both PL^{pro} and M^{pro} are capable of self-cleavage from polyproteins, and do not require any viral or human components for their activation. It has been hypothesized that nsp6 is a transmembrane domain of ribosomes, while nsp7 and nsp8 significantly increase the binding between the mRNA, which acts as a template, and nsp12, which contains the RNA-dependent RNA polymerase (RdRp), crucial component of coronavirus replication and transcription. Nsp9 functions as a (+)ssRNA strand-binding protein, while nsp10 is critical for

methylation of the cap of viral mRNAs. Nsp13 participates in replication and transcription, binds ATP and zinc-binding domain (Zn domain). Nsp14 encodes exoribonuclease, whose action limits the number of errors in the translation process and guarantees structurally complete and mature proteins, like nsp15, which functions as an Mn^{2+}-dependent endoribonuclease. Lastly, nsp16 is a ribose 2'-O-methyltransferase.[51]

Viral components are assembled in membranous complexes derived from the ER and the Golgi apparatus and the new virions bud into the lumen of the ER-Golgi intermediate compartment (ERGIC) and are transported to the cell surface in vesicles. They are released from the host cell through exocytosis.

It is well clear that the replication cycle of SARS-CoV-2 involves a series of well-coordinated steps, and that key non-structural proteins (nsps) play various roles in ensuring efficient viral RNA synthesis, protein processing, and genome replication (Figure 12). Understanding these steps and the functions of nsps is crucial for developing antiviral strategies and treatments.
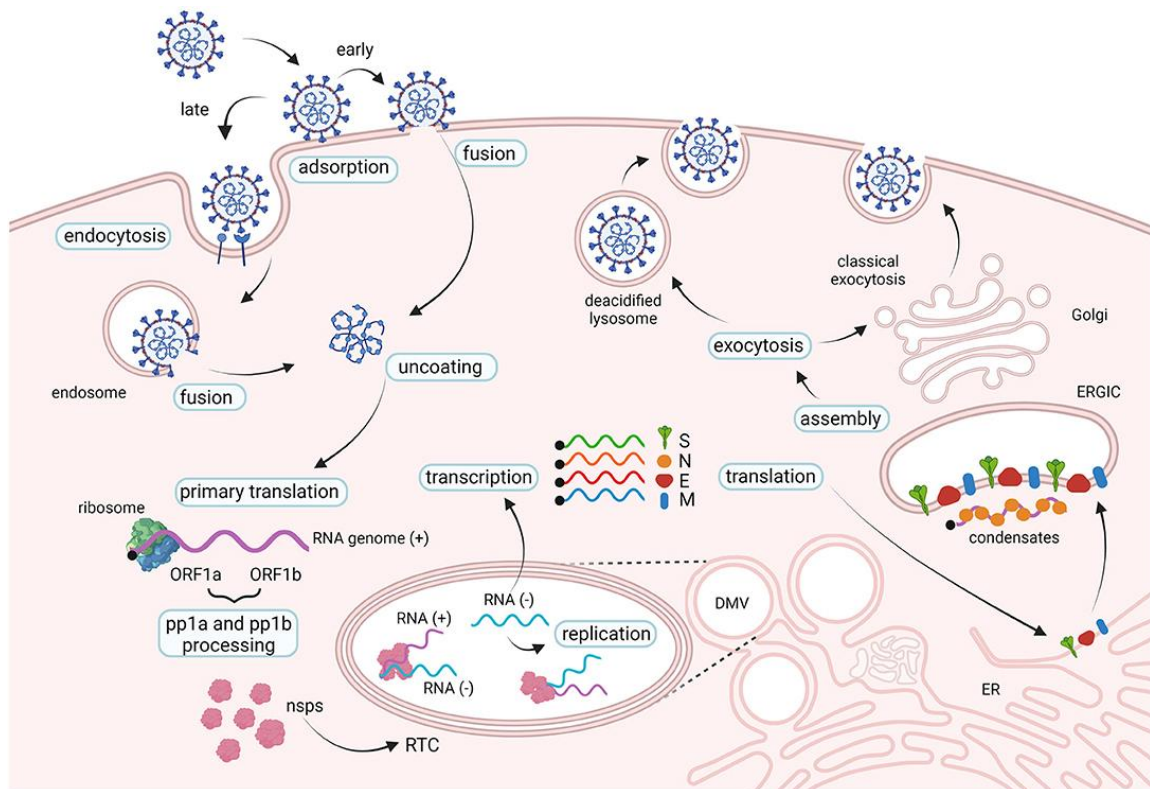
Figure 12. SARS-CoV-2 life cycle.[52]

3.2. Genetic Variability and Emergence of Variants

Like other RNA viruses, SARS-CoV-2 is inherently unstable and prone to genetic changes. These changes can occur through two main mechanisms:

- Mutations: small changes in the viral RNA sequence that can occur during viral replication.
- Viral Recombination: exchange of genetic material between different viral strains when co-infecting a host.

These genetic changes can lead to the development of new variants with different characteristics compared to the original strain. Throughout the COVID-19 pandemic, numerous SARS-CoV-2 variants have emerged globally.

To manage and respond to these variants effectively, classification systems have been independently developed by World Health Organization (WHO) and United States Centers for Disease Control and Prevention (CDC). These systems classify variants into two main categories:

- Variants of Interest (VOIs): these are variants with genetic changes that are predicted or known to affect virus characteristics such as transmissibility, disease severity, immune escape, diagnostic or therapeutic escape, and have been identified to cause significant community transmission or multiple COVID-19 clusters.

- Variants of Concern (VOCs): these variants have evidence of increased transmissibility, more severe disease (*e.g.*, increased hospitalizations or deaths), significant reduction in neutralization by antibodies generated during previous infection or vaccination, reduced effectiveness of treatments or vaccines, or diagnostic detection failures. Several variants have been classified as VOCs due to their impact on public health. Some of the notable VOCs include:

  - Alpha (the lineage B.1.1.7): In last December 2020, whole-genome sequencing of samples from patients who tested positive for SARS-CoV-2 led to the UK's announcement of the Alpha variant, also known as GRY (previously GR/501Y.V1).[53] A commercial test that detected the variant by looking for the absence of the S gene (S-gene target failure, SGTF) in PCR samples was also used to identify it. There are 17 mutations in the viral genome of the B.1.1.7 variant. Of these, the spike (S) protein contains eight mutations. The spike protein of N501Y exhibits a higher affinity for ACE 2 receptors, which facilitates the attachment of the virus and its subsequent entry into host cells.[54] According to a study, compared to other SARS-CoV-2 variants, the B 1.1.7 variant was linked to a higher death rate (HR=1.61, 95% CI 1.42-1.82). In fact, people with confirmed B.1.1.7 infection had a higher risk of dying (adjusted hazard ratio 1.67, 95% CI 1.34-2.09) than people with non-B.1.1.7 SARS-CoV-2.[55]

- Beta (B.1.351 lineage): The second wave of COVID-19 infections was caused by the Beta variant, or GH501Y.V2 with multiple spike mutations, which was initially identified in October 2020 in South Africa.[56] The spike protein of the B.1.351 variant has nine mutations, three of which are in the receptor binding domain (RBD) and enhance the protein's affinity for ACE receptors. At the end of January 2021, reports of SARS-CoV-2 501Y.V2 (B.1.351 lineage) were made in the United States. This variation was less likely to be neutralized by post-vaccination sera, convalescent sera, or monoclonal antibody therapy, and it posed a higher risk of transmission.[57]

- Gamma (P.1 lineage): The Gamma variant, also known as GR/501Y.V3, was discovered in Brazil in December 2020 and was initially discovered in the United States in January 2021. Ten mutations have been found in the spike protein of this B.1.1.28 variant. Like the B.1.351 variant, three mutations (L18F, K417N, and E484K) are found in the RBD.[58]

- Delta (B.1.617.2 lineage): The deadly second wave of COVID-19 infections in India in April 2021 was caused by the Delta variant, which was first discovered in December 2020 there. This variant was discovered for the first time in the US in March 2021.[59] Ten mutations in the spike protein are present in the B.1.617.2 variant.

- Omicron (B.1.1.529 lineage): The Omicron variant was first identified in South Africa on 23 November 2021 after an uptick in the number of cases of COVID-19.[60] Omicron was quickly recognized as a VOC due to more than 30 changes to the spike protein of the virus and the sharp rise in the number of cases observed. The reported mutations are located in the envelope, in the nucleocapsid protein, in the matrix, in the N-terminal domain of the spike, in the receptor-binding domain of the spike, in the fusion peptide of the spike, in the heptad repeat 1 of the spike as well as in the non-structural proteins and spike protein.[61] Many subvariants of Omicron, such as BA.1, BA.2, BA.3, BA.4, and BA.5, have been identified.

Continuous monitoring and research are essential to understand the impact of these variants on public health, vaccine efficacy, and treatment options. Efforts include:

- Genomic Surveillance: Tracking changes in the virus's genetic code.
- Epidemiological Studies: Assessing the spread and impact of different variants.
- Laboratory Research: Studying how mutations affect virus behaviour and response to treatments and vaccines.

4. SARS-CoV-2 Proteases

4.1. Main Protease

Main protease (M[pro] or 3CL[pro]) and Papain-like protease (PL[pro]) are two cysteine proteases of SARS-CoV-2 that play a critical role in the virus's replication and survival. These proteases are responsible for cleaving the viral polyproteins pp1a and pp1ab into mature non-structural proteins, which are necessary for the viral lifecycle. Numerous crystal structures of SARS-CoV-2 M[pro] have been deposited at the Protein Data Bank (PDB), with a resolution between 1.2 and 2.98 Å after crystallization at temperatures between 277 and 300 K. The average molecular weight of the monomeric M[pro] is approximately 34.21 kDa. M[pro] reaches its dimeric form upon maturation, which is crucial for its highest hydrolytic activity. The monomeric form, in contrast, exhibits reduced enzymatic activity and is typically a transient state. Each monomer contains three domains: domain I, domain II, and domain III.[62] Domain I (residues 8-101) contains 6 β-strands and an α-helical portion. Domain II (residues 102-184) and domain III (residues 201-303) contain 6 β-strands and 5 α-helical portions, respectively. All domains are interconnected via long loops (Figure 13). Domain III has an extra helix domain that plays a crucial role in M[pro] dimerization.[63] A strong binding between the N-finger (at the N-terminus) and the C-terminus is essential for dimer formation. Particularly important is the salt bridge connecting Arg4 and Arg298.[64]

The M[pro] catalytic site, crucial for the proteolytic processing of viral polyproteins, is located at the interface of domains I and II. This site contains the key residues and structural features required for its proteolytic activity. The catalytic site includes five primary enzymatic pockets: S1', S1, S2, S3, and S4. These pockets accommodate specific portions of the viral polyproteins, which are designated as P1', P1, P2, and P3/P4.[65] P1, P2, and P1' positions primarily control M[pro] substrate specificity, whereas P3 and P4 positions enhance substrate recognition and stabilize binding, ensuring efficient proteolysis.

The S1 pocket is crucial for recognizing a glutamine (Gln) residue at the P1 position of the substrate. It consists mainly of the side chains of Phe140, His163, His164, Glu166, and His172. The Oβ atom of glutamate can interact with the oxyanion hole formed by residues 143–145 (Gly143, Ser144, and Cys145). This interaction allows the thiol group of Cys145 to act as a nucleophile, attacking the carbonyl of the glutamine residue.[66] The S2 pocket is composed of hydrophobic amino acids, including Met49, Tyr54, Met165, Pro168, and Val186. This hydrophobic nature accommodates hydrophobic residues in the P2 position of the substrate.

The S3/S4 pockets are more solvent-exposed and are made up of Gln189, Ala191, Gln192, and Gly25 residues.
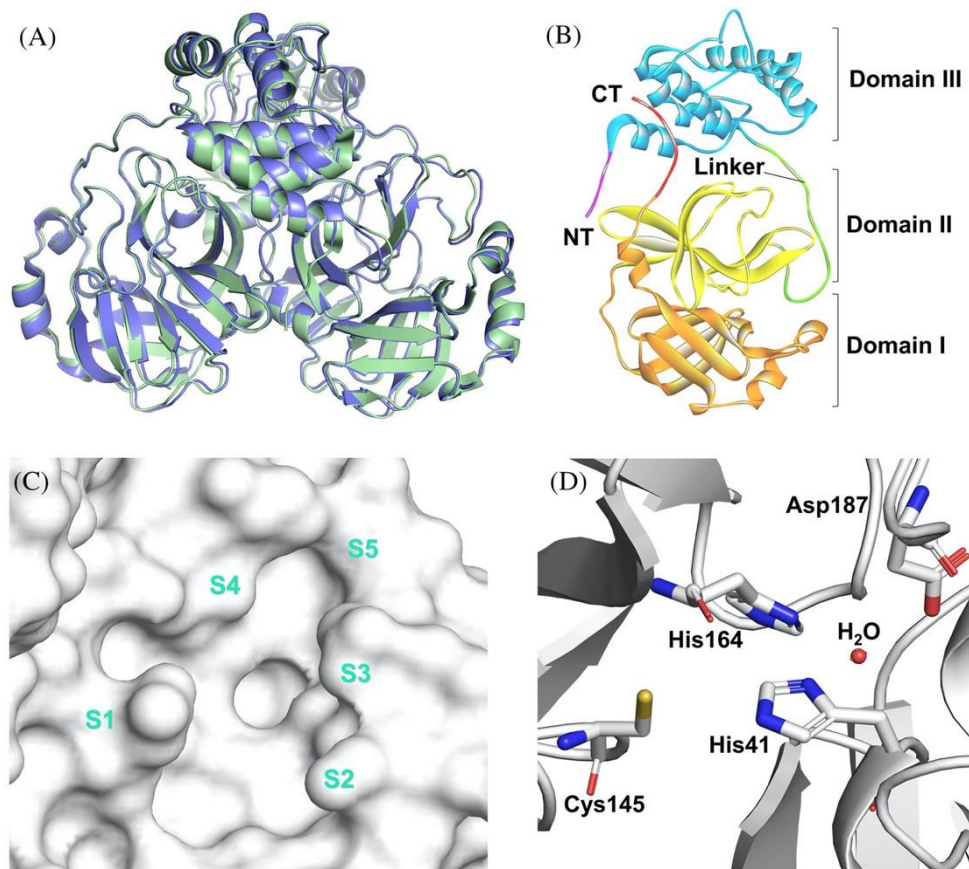
Figure 13. (A) 3D structure of SARS-CoV-2 M^{pro} (green PDB: 6XHU) and SARS-CoV (light blue, PDB: 1UJ1). (B) The three structural domains of M^{pro} monomer. (C) The surface of the catalytic site of the enzyme. (D) The catalytic residues of the active site.[67]

Unlike the catalytic triad seen in other chymotrypsin-like proteases, M^{pro} features a catalytic dyad composed of two critical residues: Cys145 that acts as a nucleophile and His41 that functions as a base to deprotonate the cysteine thiol group.[68] M^{pro} cleaves the amide bonds in the viral polyproteins pp1a and pp1ab. The cleavage occurs specifically between a glutamine (Gln) residue at the P1 position and a small amino acid (Ser, Gly, or Ala) at the P1′ position. The His41 residue, through its basic nitrogen, abstracts a proton from the thiol group of Cys145 (Figure 14). This deprotonation results in the formation of a highly reactive thiolate anion on Cys145. The thiolate anion of Cys145 performs a nucleophilic attack on the electrophilic carbonyl carbon of the amide bond in the substrate. This attack results in the formation of a tetrahedral intermediate, which is stabilized by the oxyanion hole (formed by residues Gly143, Ser144, and Cys145). The tetrahedral intermediate collapses, leading to the cleavage of the amide bond. The histidine residue (His41) stabilizes the transition state and then returns to its

deprotonated form, ready to participate in another catalytic cycle. The cleavage results in the formation of a thioester intermediate between the Cys145 and the substrate. A water molecule, activated by the restored His41, performs a nucleophilic attack on the thioester bond. This attack leads to the hydrolysis of the thioester intermediate, releasing the C-terminal product of the substrate. The hydrolysis restores the free thiol group on Cys145 and the basic form of His41. The catalytic dyad is thus ready for another cycle of substrate cleavage.[69]
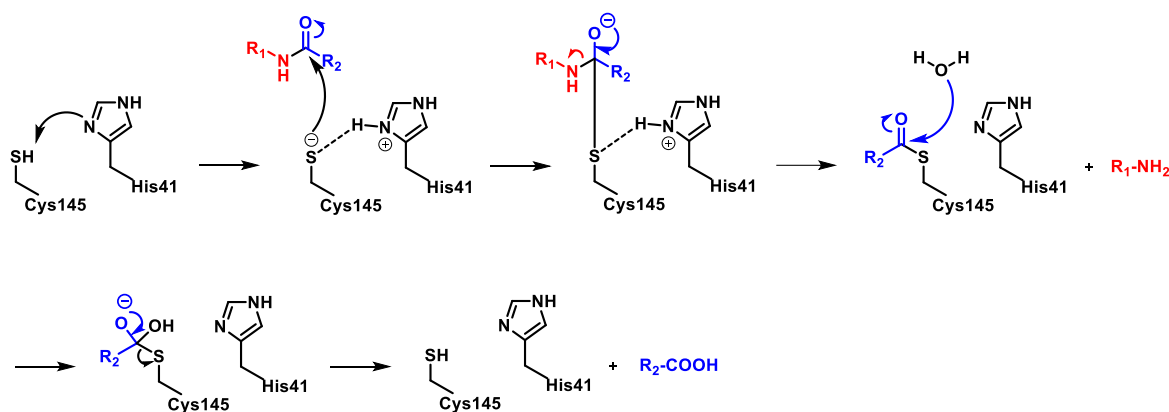
Figure 14. Mechanism of hydrolysis mediated by SARS-CoV-2 M^{pro}.

Given its crucial role in the replication process of SARS-CoV-2, M^{pro} has been widely validated as a prime target for the development of anti-COVID-19 agents.[70]

No homologous protease exists in humans, which means that drugs targeting M^{pro} can be designed to be highly specific for the viral enzyme, reducing the likelihood of off-target effects and minimizing potential side effects. Because of its unique structure and function, selective inhibitors can be developed to specifically target M^{pro} without significantly affecting human proteases. This specificity is crucial for the safety and efficacy of antiviral agents. Unlike the spike protein, which undergoes frequent mutations, M^{pro} is less prone to genetic changes. This stability means that inhibitors designed for one variant of M^{pro} are likely to remain effective against other variants, providing a consistent therapeutic option. Given these characteristics, M^{pro} is a highly suitable target for antiviral drug development. Potent inhibitors can be engineered to bind and inactivate the protease, effectively halting viral replication.

In summary, the crucial role of M^{pro} in SARS-CoV-2 replication, combined with its absence of human homologues and low mutation rate, makes it an excellent target for developing selective and potent antiviral inhibitors. These inhibitors can provide a robust therapeutic option with minimal side effects, potentially effective across various SARS-CoV-2 variants.

4.2. Papain-Like Protease

Similar to M^{pro}, PL^{pro} (Papain-like protease) processes viral polyproteins to release non-structural proteins essential for viral replication. PL^{pro} also plays a crucial role in subverting the host's immune response. It achieves this by removing post-translational modifications from host proteins, particularly ubiquitin (Ub) and ubiquitin-like proteins (UbL), including interferon-stimulated gene product 15 (ISG15).

Ubiquitination is a process where ubiquitin molecules are attached to host proteins, often marking them for degradation or modulating their activity. By removing ubiquitin from proteins, PL^{pro} can prevent their degradation by the proteasome, which can disrupt normal cellular processes and contribute to the pathogenesis of the virus.

Interferons are key signaling proteins in the immune response to viral infections. ISG15 is an interferon-stimulated gene product that is conjugated to proteins (a process known as ISGylation). This modification is part of the antiviral response.[71] By deubiquitinating and de-ISGylating host proteins involved in the interferon pathway, PL^{pro} helps the virus evade the immune system, promoting viral replication and persistence.

Ub and UbL can modify host proteins, influencing their cellular localization, stability, and involvement in specific cellular processes, including antiviral immunity. These modifications act as regulatory signals that can activate or deactivate protein functions, direct proteins to specific cellular compartments, or target proteins for degradation.

PL^{pro} acts as a deubiquitinase (DUB), cleaving the C-terminal RLRGG sequence of Ub and UbL from modified host proteins. This cleavage disrupts the regulatory signals imposed by ubiquitination and ISGylation, undermining the host's ability to mount an effective immune response. PL^{pro} DUB activity can dysregulate the initial inflammatory response, leading to an inappropriate or excessive activation of inflammation. By removing ISG15 from proteins, PL^{pro} inhibits the interferon-stimulated gene response, weakening the antiviral state of the host cells and facilitating viral replication. The dysregulation of inflammatory and interferon responses by PL^{pro} activity is linked to the development of cytokine storms, a major cause of severe disease and mortality in COVID-19 patients. Cytokine storms are characterized by excessive and uncontrolled release of pro-inflammatory cytokines, leading to widespread tissue damage and organ failure.[72] PL^{pro}-mediated deubiquitination and de-ISGylation interfere with normal signaling pathways that control inflammation and immune responses. This interference can prevent the timely resolution of inflammation and allow for unchecked viral replication, contributing to severe disease outcomes.

Inhibitors of PL^pro could restore normal ubiquitination and ISGylation processes, helping to regulate the immune response and reduce the risk of cytokine storms. By preventing PL^pro from cleaving ubiquitin and ISG15, these inhibitors could enhance the host's antiviral defenses and improve clinical outcomes.

Drugs targeting PL^pro might not only inhibit viral replication but also mitigate the dysregulated immune responses that lead to severe disease. This dual benefit makes PL^pro an attractive target for comprehensive therapeutic strategies against COVID-19.

SARS-CoV-2 PL^pro is structured into four distinct domains: thumb, palm, zinc-finger, and N-terminal ubiquitin-like domains (Figure 15). The catalytic triad, crucial for the protease activity, is located at the interface of the thumb and palm domains. This triad is conserved between SARS-CoV-1 and SARS-CoV-2, highlighting its essential role in the protease's function. The zinc-finger motif consists of four cysteine residues coordinating a zinc ion. This motif is critical for both the structural stability and the enzymatic activity of PL^pro.
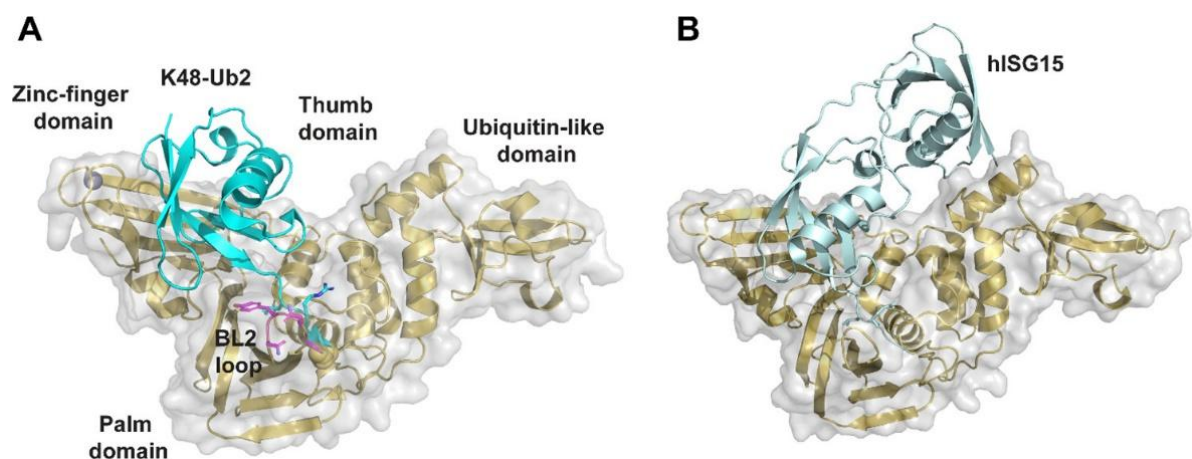
Figure 15. SARS-CoV-2 PL^pro's X-ray crystal structures. (A) Lys48-linked Ub2 in the SARS-CoV-2 PL^pro Cys111Ser mutant's X-ray crystal structure (PDB: 7RBR). The color of the BL2 loop is magenta. (B) The SARS-CoV-2 PL^pro Cys111Ser mutant's X-ray crystal structure with human ISG15 (PDB: 7RBS).[73]

The C-terminal residues (73–76) of ubiquitin (Ub) are bound within the narrow active site channel of PL^pro. These residues are designated as P4 (Leu73), P3 (Arg74), P2 (Gly75), and P1 (Gly76) sites. The substrate binding channel is particularly narrow at the P1 and P2 sites, reflecting high specificity for glycine residues at these positions. The amino acid residues around the P4–P1 sites are conserved between SARS-CoV-1 and SARS-CoV-2.[74] The P1 and P2 sites engage in polar interactions with the substrate. Gly271 and Gly163 form hydrogen bonds with the substrate, whereas Leu163 and Tyr164 interact via van der Waals contacts, stabilizing the substrate position. The binding channel becomes solvent-exposed at the P3 site,

allowing for greater flexibility in accommodating different substrates. The channel widens at the P4 site to fit larger side chains, such as those of leucine and arginine, facilitating the interaction with a broader range of substrates.

Notably, the β11–12 loop, also known as the BL loop, forms a boundary around the P3–P4 sites. In the absence of a substrate (apo structures), the BL loop exhibits high conformational flexibility. This dynamic behavior includes significant movements in both the backbone and side chains, suggesting that the BL loop can adapt to various substrates by changing its conformation.[75]

The mechanism of hydrolysis catalyzed by PL[pro] involves several key steps assisted by the catalytic triad comprising Cys111, His272, and Asp286 (Figure 16).[76] Asp286 forms a hydrogen bond with the side chain of His272, stabilizing its orientation. This alignment ensures that His272's side chain faces Cys111. His272 deprotonates Cys111, increasing its nucleophilicity. The deprotonated Cys111 attacks the carbonyl carbon of the amide bond in the substrate, forming a tetrahedral intermediate. The negative charge on the oxygen of the carbonyl group in the intermediate is stabilized by the oxyanion hole, which includes the amino acid residue Trp106. The tetrahedral intermediate collapses, leading to the cleavage of the amide bond. The carboxyl-terminus (C-terminus) of the substrate forms a thioester intermediate with Cys111, and the amine group is released. His272 donates a proton to the amine group of the substrate, ensuring the release of the amine fragment. The thioester bond is subsequently hydrolyzed, releasing the carboxylic acid substrate fragment and restoring the enzyme.
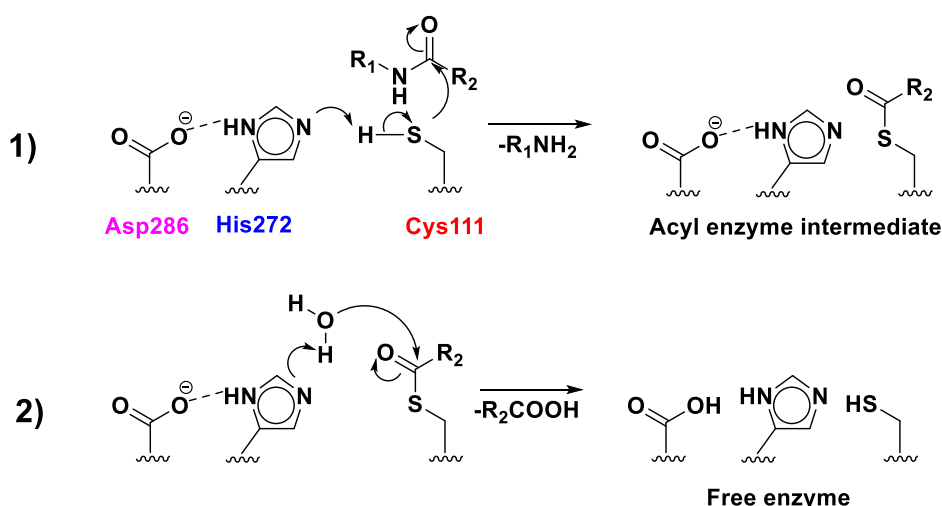
Figure 16. Mechanism of hydrolysis catalyzed by SARS-CoV-2 PL[pro].

This detailed mechanism underscores the intricate coordination between the catalytic triad and other active site residues, facilitating the precise and efficient cleavage of the substrate by SARS-CoV-2 PL^{pro}.

Given its dual role in viral replication and immune evasion, PL^{pro} is an attractive target for antiviral drug development. Inhibitors that block PL^{pro}'s activity could potentially halt viral replication and restore the host's immune response. Developing inhibitors that specifically target PL^{pro} without affecting human deubiquitinases is challenging. Structure-based drug design and high-throughput screening are strategies that can be employed to identify potent and selective PL^{pro} inhibitors.

5. Host-Directed Therapy

In the past decade, a novel approach to treating viral infections has gained prominence: host-directed therapy (HDT). Unlike traditional antiviral therapies that directly target the pathogens, HDTs focus on modifying host cellular processes to enhance the body's defense mechanisms against infections.

By strengthening the immune response against pathogens and modifying virulence factors and inflammation associated with disease, HDTs improve host defense mechanisms. All of this may lead to improved clinical outcomes, including reductions in organ and tissue damage, mortality, and morbidity. HDTs are less prone to drug resistance than traditional antiviral therapies targeted at pathogens because their host targets—which are essential to the survival of viruses—are stable from an evolutionary perspective and their expression is regulated by a variety of genes. As a result, it would take numerous, consecutive mutations before drug resistance could develop.[77]

Since all viruses are obligatory intracellular parasites, they cannot survive outside of their host cells and rely on the host's cellular machinery and energy sources for replication. Upon infection, viruses must engage with and often subvert the host's intrinsic defense mechanisms to evade immune responses. This dependence on host components at every stage of their life cycle presents opportunities for the development of antiviral treatments. Identifying critical host-virus interactions at each stage of the viral life cycle (*i.e.*, entry, replication, assembly, and release) provides potential targets for HDT.

Host-directed therapy represents a promising shift in the treatment of viral infections. By targeting the host's biological pathways and enhancing natural defense mechanisms, HDTs offer a robust alternative to traditional antiviral therapies. Their potential to reduce drug resistance, coupled with improved clinical outcomes, underscores their growing importance in the fight against viral diseases.

5.1. Host Proteases Involved in SARS-CoV-2 Infection

The Spike (S) protein of SARS-CoV-2 is a trimeric glycoprotein consisting of an ectodomain, a single transmembrane anchor, and an intracellular tail. Each monomer of the S protein comprises two subunits: S1 subunit that contains the N-terminal domain (NTD) and the C-terminal domain (CTD) responsible for recognizing and binding to the human ACE2 receptor, and S2 subunit, involved in membrane fusion, which contains the fusion peptide and the HR1 and HR2 heptad repeats.

The S1 subunit binds to the ACE2 receptor on the host cell membrane, initiating viral entry. For the S protein to mediate fusion, it must undergo cleavage by host proteases. This cleavage is essential for the activation of the fusion potential of the S protein. The host proteases involved in the entry and activation of SARS-CoV-2 are: proprotein convertases (furin), extracellular proteases (elastase), cell surface proteases (TMPRSS2), and lysosomal proteases (hCatL and hCatB).

Furin is a member of the proprotein convertase family that processes precursor proteins into their mature forms by cleaving at specific sites. Furin cleaves the Spike protein of SARS-CoV-2 at the S1/S2 junction, which is a crucial step for the activation of the fusion peptide. This cleavage prepares the S protein for subsequent processing by other proteases, facilitating viral entry.

Elastase is an extracellular protease that degrades elastin and other extracellular matrix proteins. Elastase can cleave the S protein at specific sites, enhancing viral infectivity and facilitating the spread of the virus within tissues.

Transmembrane protease serine 2 (TMPRSS2) is a cell surface protease that cleaves and activates various proteins. TMPRSS2 cleaves the S protein of SARS-CoV-2 at the S2' site, directly activating the fusion peptide and enabling the fusion of the viral and host cell membranes. This cleavage is essential for the virus to enter the host cell cytoplasm.

Cathepsins are lysosomal proteases that degrade proteins within the acidic environment of lysosomes. Cathepsin L (hCatL) cleaves the S protein within endosomes after the virus has been internalized by endocytosis. This cleavage facilitates the release of the viral genome into the host cell cytoplasm. Cathepsin B (hCatB), similar to hCatL, can also cleave the S protein in endosomes, aiding in the viral entry process.

5.2. Human Cathepsin L

Cathepsins, derived from the Greek word "katahepsein," meaning "to digest," are a family of proteases responsible for recycling cellular proteins within lysosomes.[78] They are categorized into serine, aspartate, and cysteine cathepsins based on the nucleophilic agent involved in their catalytic activity. These enzymes can also be classified based on their specific activity into endopeptidases and exopeptidases, depending on the location of the hydrolytic bond they cleave.

Cathepsins are initially synthesized in an inactive form known as zymogens. They undergo translocation from the ER to the Golgi apparatus. During their transport to lysosomal and

endosomal compartments, cathepsins undergo proteolytic cleavage, which removes segments known as the dominance and prodomain portions. This cleavage activates the enzymes from their zymogen state.

Cathepsins exhibit optimal hydrolytic activity at the acidic pH of lysosomes, typically between 4.5 and 5.0.

Cathepsins are essential for many physiological processes in humans. They play a key role in breaking down components of the extracellular matrix, which is essential for tissue remodeling and repair. Cathepsins degrade proteins into peptides that can be presented by major histocompatibility complex (MHC) class II molecules, facilitating the immune response. Certain cathepsins are involved in the execution phase of apoptosis, contributing to the controlled dismantling of cellular components. They are critical in the processing and presentation of antigens to T cells, thus playing a pivotal role in the immune system. They are critical in the processing and presentation of antigens to T cells, thus playing a pivotal role in the immune system. Cathepsins with a cysteine residue in the active site are particularly important in the degradation of misfolded or damaged proteins within lysosomes, ensuring cellular homeostasis.

Cathepsin L (hCatL) is a cysteine protease expressed in all cellular tissues and plays a crucial role in proteolytic activities, including the degradation of protein antigens internalized via endocytosis.[79] Structurally, hCatL consists of two domains (left and right) with a catalytic triad composed of Cys25, His163, and Asp187 situated in a cleft between these domains.[80] While hCatL is primarily recognized as a lysosomal protease, it can also be secreted outside lysosomal environments. This extracellular secretion is implicated in various pathological conditions, many of which are associated with inflammatory processes.[81]

hCatL degrades protein antigens, aiding in antigen presentation and subsequent immune responses. Excessive secretion of hCatL can contribute to several pathological conditions, particularly those involving inflammation. There is a correlation between hCatL activity and inflammatory markers, such as elevated neutrophil counts in the blood, indicating an ongoing inflammatory response.

Toll-Like Receptor (TLR) can enhance the proteolytic activity of hCatL without altering mRNA expression, increasing its intracellular activity. hCatL activates heparanase, an enzyme that, in turn, activates macrophages and amplifies the inflammatory cascade.[82]

Heparanase plays a significant role in viral infection processes, including facilitating entry and spread within host tissues.[83] Cathepsins, particularly hCatL, have emerged as valuable therapeutic targets for developing novel drugs, especially antivirals, due to their crucial roles in

various pathologies.[84,85] hCatL is critically involved in the ability of the SARS-CoV-2 virus to enter host cells by mediating the proteolysis of the viral S protein following its binding to the ACE2 receptor.

hCatL plays a critical role in the proteolytic processing of the S protein within endosomes (Figure 17).[85] The S protein undergoes two cleavage steps: S1/S2 cleavage and S2' cleavage. The initial cleavage separates the S1 and S2 subunits. A second cleavage within the S2 subunit activates the fusion peptide, enabling viral membrane fusion with the host cell membrane.
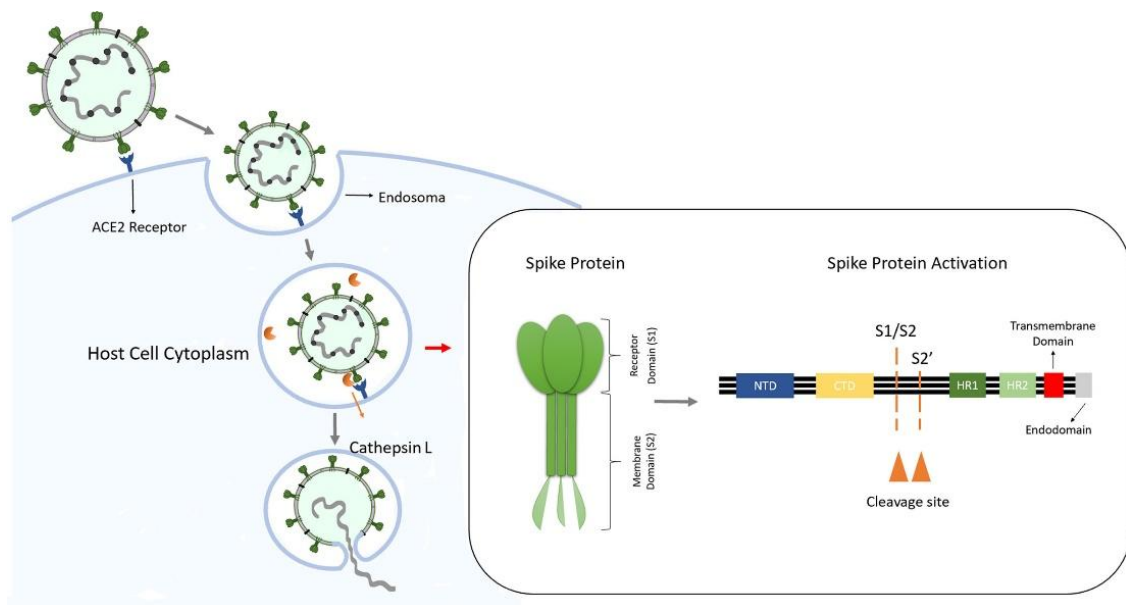
Figure 17. Entry of SARS-CoV-2 into the target cell via endosomes. hCatL activates the spike protein through cleavage of the S1/S2 boundary and the S2' site.[85]

Cathepsin L (hCatL) is a critical protease involved in the entry of SARS-CoV-2 into host cells by mediating the cleavage of the Spike (S) protein following its binding to the ACE2 receptor. Understanding the role of hCatL in viral entry mechanisms provides valuable insights for developing targeted antiviral therapies. Inhibitors of hCatL have the potential to prevent viral entry and replication, offering a promising strategy for treating COVID-19 and other viral infections that utilize similar entry pathways.

6. SARS-CoV-2 M^{pro}/hCatL Dual Inhibitors

Since the onset of the COVID-19 pandemic, the scientific community has made significant advances in developing both vaccines and therapeutic drugs. Various strategies have been employed to quickly identify antiviral agents with promising efficacy, minimal toxicity, and favorable pharmacokinetic properties.

Initially, the "drug repurposing" approach was adopted, evaluating existing drugs with established Absorption, Distribution, Metabolism, Excretion, and Toxicity (ADMET) properties for anti-SARS-CoV-2 activity. Remdesivir, originally developed for Ebola, and hydroxychloroquine, used for malaria and autoimmune diseases, were among the first drugs repurposed.[86]

Artificial Intelligence (AI) has accelerated the identification of potential antiviral agents by analyzing large datasets, predicting molecular interactions, and optimizing drug design. AI has been used for both drug repurposing and the discovery of novel compounds with antiviral activity.[87]

Furthermore, the de novo development of new anti-COVID-19 agents has been based on previous results from Structure-Activity Relationship (SAR) studies conducted on viral targets of SARS-CoV, MERS, Ebola, and HIV.[88,89]

Several studies have been conducted to develop inhibitors targeting SARS-CoV-2 M^{pro} and hCatL, given their crucial roles in the viral life cycle. The identification and development of dual inhibitors targeting both M^{pro} and hCatL hold great promise for comprehensive antiviral therapy against COVID-19. Consequently, significant efforts have been directed towards identifying and developing dual inhibitors that can target both proteins. Continued research and optimization of these dual inhibitors are essential to bring effective treatments to clinical use. The current state of research and development in this field is summarized in the next paragraph.

6.1. MG-132

MG-132, a peptide aldehyde, is a potent inhibitor of the proteasome's chymotrypsin-like activity, widely utilized in drug discovery, particularly for anticancer agents. Structurally, it comprises three leucine residues, with an N-terminal benzyloxycarbonyl (Cbz) group and a C-terminal aldehyde, the latter serving as the electrophilic warhead that undergoes nucleophilic attack by catalytic cysteine residues (Figure 18).[89]

In 2020, **MG-132** gained attention for its potential as an antiviral agent against SARS-CoV-2.[90] It demonstrated significant inhibitory effects on the replication of SARS-CoV-2, similar to its

action on SARS-CoV, by targeting a key host protease, calpain-m. This contrasts with its primary action on the proteasome, indicating a versatile mechanism of inhibition.[91] **MG-132** has shown inhibitory effects against several other viruses, such as Herpes Simplex Virus 1, Hepatitis E Virus, and Human Cytomegalovirus. These antiviral activities are primarily through interference with the ubiquitin-proteasome system, crucial for viral entry and replication in host cells.[92] In *in vitro* assays against SARS-CoV-2 M^{pro}, **MG-132** exhibited an IC$_{50}$ value of 3.91 µM.[93]
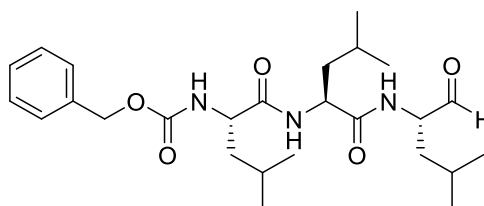
MG132
M^{pro} SARS-CoV-2, IC$_{50}$ = 3.91 µM
hCatL, IC$_{50}$ = 2,5-2.7 nM
Vero E6 infected cells, EC$_{50}$ = 0.1 µM

Figure 18. Structure of **MG-132** and his biological characterization.

The inhibition mechanism involves the catalytic Cys145 of M^{pro} attacking the aldehyde group of **MG-132**, leading to the formation of a covalent hemithioacetal bond. This reaction is stereoselective, forming a new chiral center with the S absolute configuration, characteristic of aldehyde-based cysteine protease inhibitors. The inhibitory effect of **MG-132** was consistent regardless of the presence of the reducing agent dithiothreitol (DTT), indicating that a reducing environment does not significantly affect its activity. IC$_{50}$ values increased with longer preincubation times with M^{pro}, suggesting reversible inhibition, similar to the inhibition profile of **GC376**, a known covalent but reversible inhibitor of M^{pro}.[94]

MG-132 demonstrated an EC$_{50}$ value of 0.1 µM against SARS-CoV-2 in Vero E6 cells, indicating potent antiviral activity.[92]

Detailed structural analysis revealed **MG-132** binding to the S1–S4 subsites of each M^{pro} protomer, forming interactions through hydrogen bonds and hydrophobic contacts (Figure 19). The hemithioacetal group of **MG-132** occupies the "oxyanion hole" formed by the peptide backbone amides of Gly143, Ser144, and Cys145. The leucine residues of **MG-132** occupy the S1, S2, and S3 subsites, while the benzyloxycarbonyl (Cbz) group fits into the S4 subsite. **MG-132** forms hydrophobic interactions with His41, Glu166, Pro168, and Gln189, and hydrogen bonds with the amide group of Glu166, the carbonyl groups of His164 and Glu166, and the amide side chain of Gln189.[92]
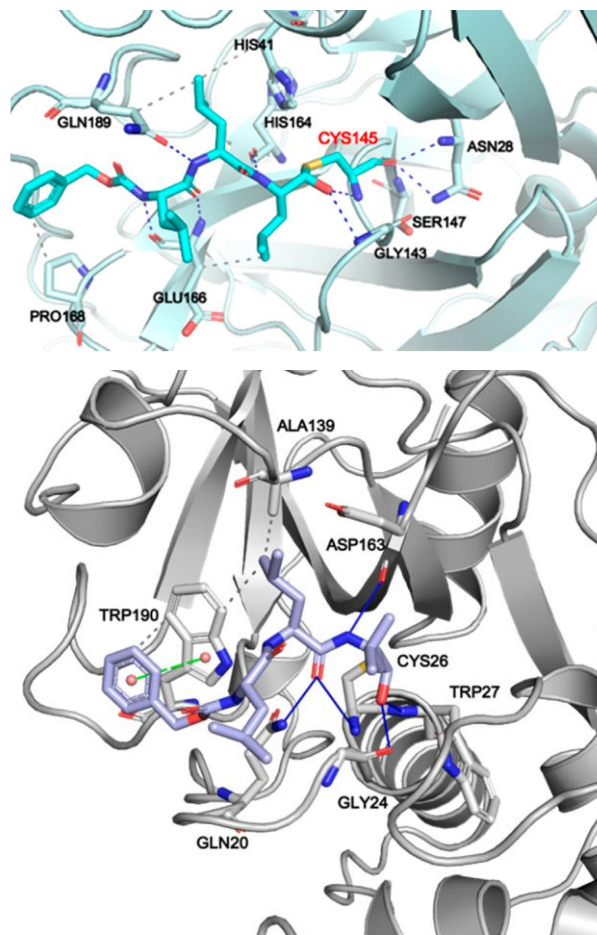
Figure 19. Key Interactions of **MG-132** with SARS-CoV-2 M^{pro} (Top) and hCatL (Bottom).[92]

MG-132 also inhibits hCatL, with IC$_{50}$ values of 2.7 nM and 2.5 nM in different studies.[95] Covalent docking experiments revealed two main orientations of **MG-132** within the hCatL binding pocket (PDB ID: 3OF9): Orientation A involving hydrophobic interactions of Cbz group with Leu70, Met71, Ala136, and Ala215, and Orientation B involving interactions of the aromatic portion with Trp190, Glu193, and Trp193.[96]

These findings highlight **MG-132**'s potential as a potent SARS-CoV-2 M^{pro}/hCatL dual inhibitor, with implications for antiviral drug development.

6.2. SM141 e SM142

In 2022, a series of novel inhibitors targeting the SARS-CoV-2 M^{pro} and hCatL was developed. [97] This study focused on the SAR of 10 Michael acceptors with a vinyl methyl ester warhead. Key structural features of these inhibitors included a cyclic glutamine (*c*Gln) surrogate at the P1 site, which is essential for mimicking the natural substrate and ensuring binding affinity and specificity, phenylalanine (Phe) or 4-fluorophenylalanine (4F-Phe), contributing to the
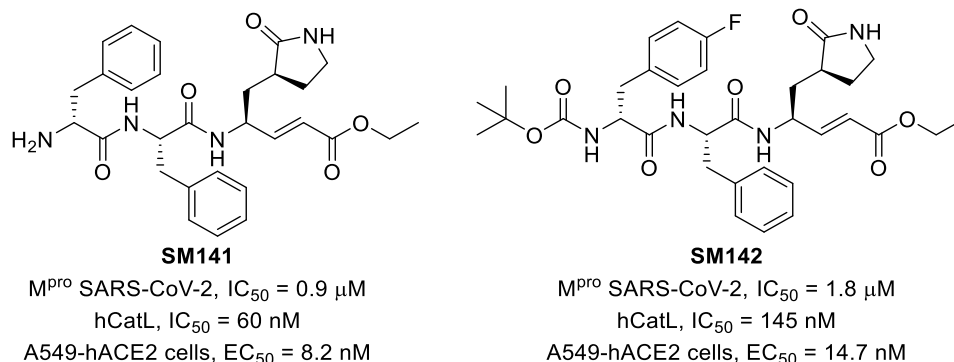
hydrophobic interactions and enhancing binding stability at P2, and the same Phe and 4F-Phe with an R absolute configuration at the P3 position. Variations in the N-terminal portion were explored to optimize the inhibitors' pharmacokinetic properties and protease binding. The amine group was left free or protected with a tert-butoxycarbonyl (Boc) group or a terminal alkyne-containing ether chain (Figure 20).

In the biological evaluation, **SM141** and **SM142** exhibited significant inhibitory capabilities against SARS-CoV-2 M^{pro}, with IC_{50} values in the micromolar and sub-micromolar range.

When tested against hCatL, **SM141** and **SM142** demonstrated IC_{50} values that were 1 to 2 orders of magnitude lower than those for M^{pro} inhibition.

Both **SM141** and **SM142** showed excellent selectivity towards M^{pro} and hCatL, with IC_{50} values greater than 40 µM for other proteases like SARS-CoV-2 PL^{pro} and human cathepsin B (hCatB). This indicates a lack of significant inhibitory activity against these off-target proteases, highlighting the specificity of these inhibitors.

The development of **SM141** and **SM142** underscores the importance of designing inhibitors that target multiple viral and host enzymes with high specificity. Such specificity is crucial for creating effective antiviral therapies with minimal off-target effects, reducing the potential for side effects and enhancing therapeutic efficacy.

SM141
M^{pro} SARS-CoV-2, IC_{50} = 0.9 µM
hCatL, IC_{50} = 60 nM
A549-hACE2 cells, EC_{50} = 8.2 nM

SM142
M^{pro} SARS-CoV-2, IC_{50} = 1.8 µM
hCatL, IC_{50} = 145 nM
A549-hACE2 cells, EC_{50} = 14.7 nM

Figure 20. Chemical structure of the potent dual inhibitors **SM141** e **SM142**.

Both compounds showed excellent antiviral efficacy against SARS-CoV-2 in A549-hACE2 cells, with EC_{50} values of 8.2 nM for **SM141** and 14.7 nM for **SM142**. Moreover, intranasal and intraperitoneal administration of **SM141** and **SM142** significantly reduced viral replication and viral load in the lungs and increased survival probability in K18-hACE2 mice infected with SARS-CoV-2.

Crystallographic studies on **SM141** (PDB ID: 7MB0) confirmed the formation of a covalent bond between the inhibitor's β-carbon and the catalytic Cys of M^{pro} (Figure 21). The warhead carbonyl group forms two hydrogen bonds with the NH groups of Cys145 and Gly143 (Figure

21). The pentatomic ring at the P1 site establishes strong hydrogen bonds with the γ-COOH group of Glu166, the C=O of Phe140, and an NH of the side chain of His163. The aromatic rings at P2 and P3 exhibit "T-shaped" interactions with aromatic residues in their respective pockets, enhancing enzyme-inhibitor binding stability. The peptide backbone participates in hydrogen bonding interactions (NH-P1/CO His164, CO-P3/NH Glu166, and NH2-P3/CO Glu166).
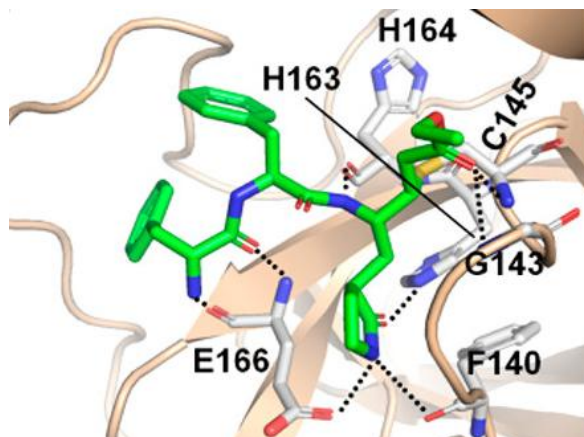
Figure 21. SM141 binding with SARS-CoV-2 M^{pro}. [98]
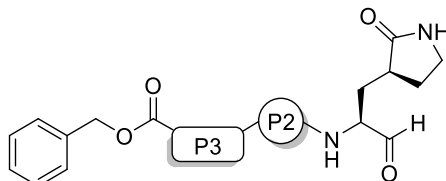
6.3. MPIs

Another SAR study aimed to identify new SARS-CoV-2 M^{pro} and hCatL dual inhibitors led to the development of nine molecules featuring an aldehydic warhead and various structural modifications aimed at optimizing their inhibitory activity.[99] The developed inhibitors feature a classic cyclic glutamine (*c*Gln) surrogate at the P1 position, and various aliphatic or aromatic residues at the P2 site (Phe, Leu, and Cha). In two of these molecules, the NH of Phe at P2 was protected either with a Cbz group (**MPI1**) or with 2-F,4-Cl-cinnamic acid (**MPI2**). In the remaining molecules, Val and Thr(tBu) were introduced at the P3 site, and the NH at P3 was again protected with either Cbz or 2-F,4-Cl-cinnamic acid (Figure 22).
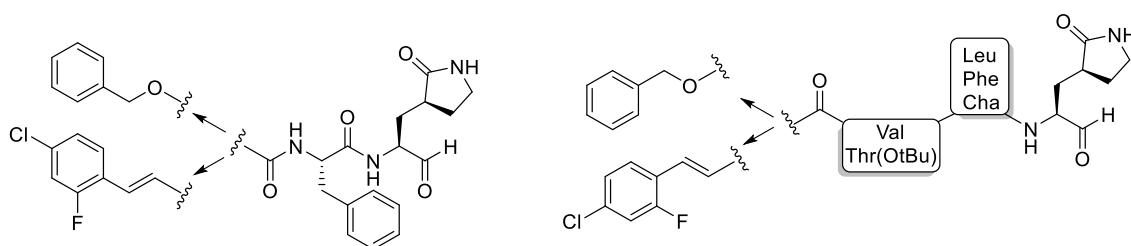
**Figure 22.** Structures of aldehyde derivatives MPIs.

In the biological evaluation against SARS-CoV-2 M^{pro}, all inhibitors exhibited IC_{50} values in the nanomolar range, ranging from 105 nM to 8.5 nM (Table 1). The most potent inhibitor was found to be **MPI3** (Cbz-Val-Leu-cGln-H), which was co-crystallized with the viral target (PDB ID: 7JQ0).[100]

Table 1. Biological Characterization of the Most Promising MPI Analogues.

Cmpd	P2	P3	IC$_{50}$ (nM)			
			SARS-CoV-2 M^{pro}	hCatL	hCatB	hCatK
MPI3	Leu	Val	8.5 ± 1.5	0.30 ± 0.07	112 ± 10	1.18 ± 0.18
MPI5	Cha	Val	33 ± 2	2.3 ± 1.9	80 ± 6	134 ± 18
MPI7	Phe	Thr(tBu)	47 ± 3	0.61 ± 0.15	64 ± 7	51 ± 6
MPI8	Cha	Thr(tBu)	105 ± 22	1.2 ± 1.0	230 ± 20	180 ± 50

It has been observed that **MPI3** occupies the S1, S2, and S4 pockets, leaving the S3 pocket vacant (Figure 23). Besides the covalent bond between the C=O of the warhead, an extensive network of hydrogen bonds and van der Waals interactions contribute to stabilizing the enzyme-inhibitor complex. The cGln fits well into the S1 pocket of the viral cysteine protease, which is primarily composed of Phe140, Asn142, His163, Glu166, and His172. The lactam group is thus able to form three hydrogen bonds with the γ-COOH of Glu166, the imidazole NH of His163, and the C=O of Phe140. Regarding the S2 pocket, Met49 folds upon itself allowing the Leu at the P2 site of **MPI3** to fit well in this pocket. It has been noted that Leu is the best residue for fitting into the S2 pocket, where its binding is strongly stabilized by van der Waals interactions. The Val at P3 does not occupy the S3 pocket. However, its side chain is involved in van der Waals interactions with Glu166 and Pro168. Lastly, the Cbz group fits well into the S4 pocket and into a channel formed by the amino acids between Pro168 and Gln192. Overall, the peptidyl backbone of MPI3 is involved in six hydrogen bonds with the SARS-CoV-2 M^{pro}. Specifically, two bonds are formed between the Val at P3 and the NH and α-CO groups of Glu166. A water molecule mediates a hydrogen bond between the amino group of Leu at P2 and the side chain of Gln189. The amino group of cGln at P1 forms a hydrogen bond with the carbonyl of His164, while the carbonyl oxygen of the aldehyde warhead forms two hydrogen bonds with the amine

groups of Gly143 and Cys145. These two hydrogen bonds could justify the higher potency of reversible covalent inhibitors compared to Michael acceptors, where the amide bond of the substrate is replaced by an alkene.
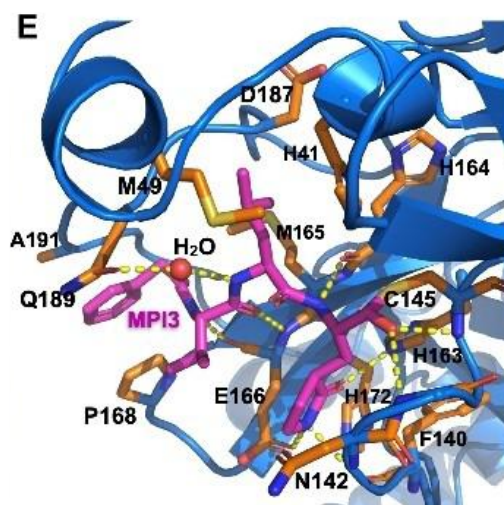
Figure 23. X-Ray crystal structure of **MPI3** bound to the SARS-CoV-2 M^pro.[100]

The authors evaluated the ability of new inhibitors to prevent the cytopathic effect (CPE) caused by SARS-CoV-2 in Vero E6 cells, with concentrations ranging from 80 nM to 10 µM. Three inhibitors, **MPI5**, **MPI7**, and **MPI8**, showed better CPE reduction than the positive control, **GC376**. **MPI3**, however, did not fully prevent the CPE. The EC_{50} values for these inhibitors were significantly lower than the concentrations needed for complete CPE abolition.

In further tests using human alveolar epithelial A549/ACE2 cells, **MPI5** and **MPI8** fully abolished the CPE at concentrations between 160 nM and 310 nM, performing better than in Vero E6 cells. Their EC_{50} values were also lower than the concentrations required for complete CPE abolition, indicating strong antiviral activity.
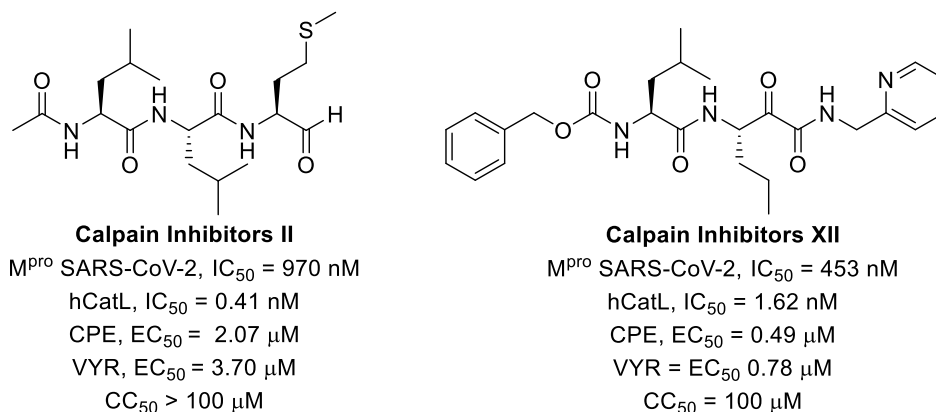
Additional studies on these inhibitors showed no inhibition of the serine proteases furin and TMPRSS2 but demonstrated nanomolar and sub-nanomolar IC_{50} values against hCatL. The inhibitors also showed some activity against hCatB and hCatK, but with higher IC_{50} values compared to hCatL. This suggests that the MPI analogs exert their antiviral effects through a multitarget inhibition mechanism involving both SARS-CoV-2 M^pro and hCatL.

6.4. Calpain Inhibitors II and XII

During the first year of the COVID-19 pandemic, potent inhibitors of the SARS-CoV-2 M^pro were identified, including **Calpain Inhibitors II** and **Calpain InhibitorXII**, which differ significantly from traditional viral cysteine protease inhibitors like **GC-376** (Figure 24). Both

inhibitors feature hydrophobic residues at the P1 site: methionine (Met) for **Inhibitor II** and norvaline (Nva) for **Inhibitor XII**.[101,102]

In biological evaluations against the SARS-CoV-2 M^{pro}, both inhibitors showed promising IC_{50} values in the sub-nanomolar range. Evaluated for the abolition of the CPE and reduction of viral load (VYR) in cellular tests, both inhibitors demonstrated promising EC_{50} values and no cytotoxicity up to 100 μM. Both **Calpain Inhibitors II** and **XII** inhibit hCatL with IC_{50} values 0.41 nM and 1.62 nM respectively.

Calpain Inhibitors II
M^{pro} SARS-CoV-2, IC_{50} = 970 nM
hCatL, IC_{50} = 0.41 nM
CPE, EC_{50} = 2.07 μM
VYR, EC_{50} = 3.70 μM
CC_{50} > 100 μM

Calpain Inhibitors XII
M^{pro} SARS-CoV-2, IC_{50} = 453 nM
hCatL, IC_{50} = 1.62 nM
CPE, EC_{50} = 0.49 μM
VYR = EC_{50} 0.78 μM
CC_{50} = 100 μM

Figure 24. Chemical structure and biological evaluation of **Calpain Inhibitors II** and **XII**.
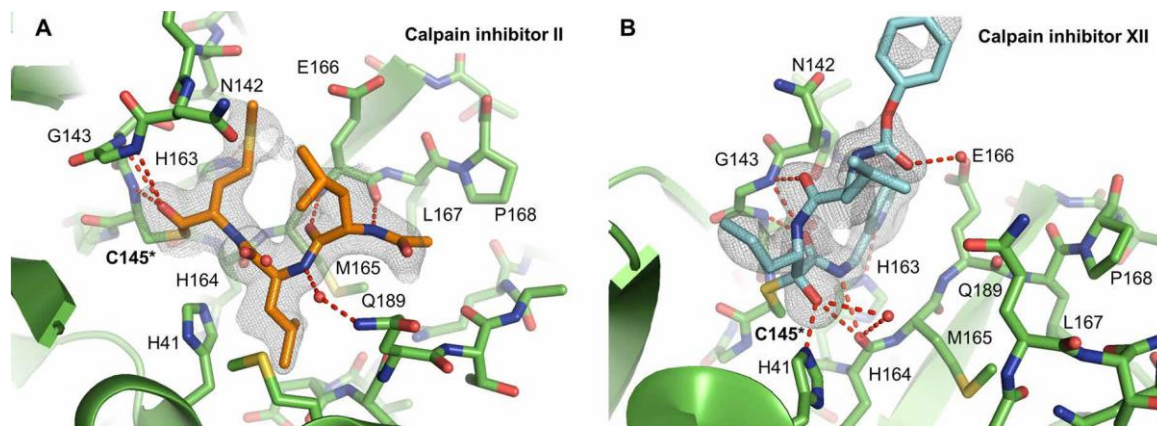
The crystal structures of the SARS-CoV-2 M^{pro} in complex with **Calpain Inhibitors II** and **XII** (PDB 6XA4 and 6XFN) reveal how the inhibitors bind to the enzyme and provide insights into their mechanisms of action (Figure 25).[102]

Calpain Inhibitor II forms a thiohemiketal adduct with M^{pro}, occupying the "oxyanion hole" formed by Gly143, Ser144, and Cys145. Methionine at P1 fits into the S1 pocket, forming a weak hydrogen bond with His163. Leucine at P2 interacts hydrophobically with its pocket, while Leucine at P3 is exposed to the solvent. The complex is further stabilized by hydrogen bonds involving His164, Met165, and Glu166.

In contrast, **Calpain Inhibitor XII** exhibits an atypical binding mode compared to other inhibitors with an α-ketoamide warhead.[102]

Pyridine group at P1' occupies the S1 pocket, while norvaline at P1 fits into the S1' pocket. Leucine at P2 fits into the S2 pocket, and the Cbz group at P3 folds back towards the S1 pocket. This binding induces a specific interaction between Asn142 and Glu166 mediated by a water molecule, resulting in an R absolute configuration of the thiohemiketal adduct. This is in contrast to other SARS-CoV-2 M^{pro} inhibitors with α-ketoamide warheads where the thiohemiketal adduct typically assumes an S configuration.

Calpain Inhibitors II and **XII** are effective multitarget inhibitors with potent activity against SARS-CoV-2 M^{pro} and hCatL. Their unique binding modes and high potency, combined with low cytotoxicity, make them promising candidates for further antiviral therapy development.

Figure 25. X-Ray crystal structures of **Calpain Inhibitors II** (A) and **XII** (B) with the SARS-CoV-2 M^{pro}.[12]

6.5. Analogs of CV11

In 2023, a series of potential inhibitors targeting the SARS-CoV-2 M^{pro} and hCatL have been developed starting from **CV11**, a dual inhibitor with potent activity against both enzymes (Figure 26).
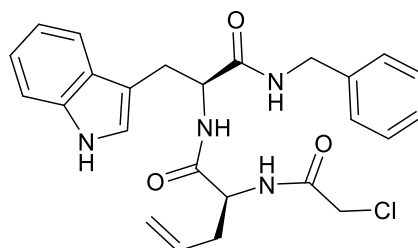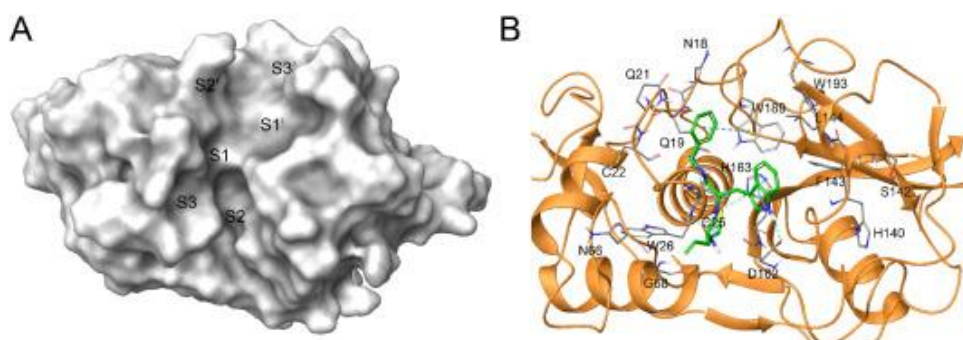

CV11
SARS-CoV-2 M^{pro}, IC$_{50}$ =1720.44 nM
hCatL, IC$_{50}$ =19.80 nM

Figure 26. Chemical structure and biological characterization of **CV11**.

Molecular docking experiments have revealed that **CV11** forms a variety of interactions (polar, hydrophobic, and π-π interactions) with hCatL, particularly involving residues in the S1, S1', and partially S3/S2' subsites (Figure 27).

Important interactions include π-π contacts with His163 and Trp189, and hydrogen bonds with Ala138, Gly18, and His163. The indole moiety's interactions with Ala138, His163, and Trp189

were identified as crucial for binding. The butenyl moiety partially occupying the S3 subsite warranted further investigation.[103]


Figure 27. A) Binding subsites of hCatL enzyme and their orientation on the protein structure (PDB code: 2XU3). B) **CV11** (colored by atom type: C green, O red, N blue, polar H light grey) in docking with hCatL (secondary structure in ribbons and colored in orange; key residues are reported as sticks and colored by atom type: C grey, O red, N blue, S yellow, polar H light grey). H-bonds and π-π interactions are reported in green and cyan dotted lines, respectively.[104]

The computational hypothesis was validated by an enzymatic assay, in which **CV11** demonstrated significant inhibitory potency with an IC_{50} of 19.8 nM.[105]

A SAR study was then developed in order to optimize the structure of **CV11** (Figure 28). Removal of the butenyl group (**CV17**) resulted in a slight decrease in inhibitory activity, validating the importance of the S3 subsite interactions. Substituting the butenyl group with an isobutyl moiety significantly enhanced inhibitory activity against hCatL (**CV13**: IC_{50} = 2.82 nM). Inversion of chirality at the carbon bearing the isobutyl moiety altered the binding mode, leading to a significant reduction in inhibitory activity (**CV15**: IC_{50} 35 times higher than **CV11**). Replacing the isobutyl group with a benzyl moiety maintained potent inhibitory activity (**CV16**: IC_{50} = 3.17 nM). Inclusion of both isobutyl and benzyl moieties but positioned differently resulted in decreased, but still potent, activity (**CV31**: IC_{50} = 10.30 nM).

Considering the promising enzymatic inhibitory data, further investigations were conducted using cell-based assays to evaluate the antiviral efficacy of the synthesized derivatives against five different variants of SARS-CoV-2. These variants included Wuhan, African, UK, Delta, and Omicron strains. The compounds' ability to decrease the production of cytopathic effects (CPE) in infected Vero cells was assessed. Additionally, the cytotoxic effects of these compounds were evaluated by examining cell morphology (MCC) and cell growth (CC_{50}).
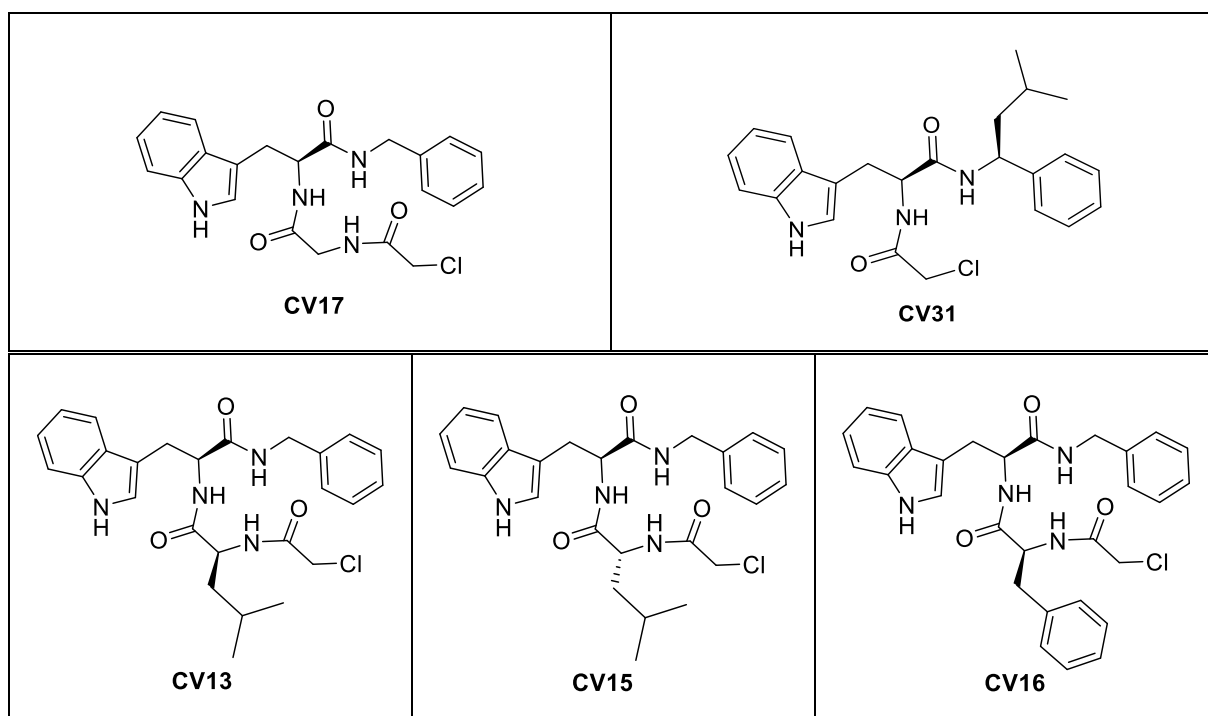
Figure 28. Chemical structure and biological characterization of **CV11** analogs. **CV13**, **CV16**, and **CV31** exhibited IC$_{50}$ values in the high nanomolar to low micromolar range against SARS-CoV-2 M^{pro}.

Many derivatives exhibited significant activity in inhibiting virus growth. Remarkable antiviral activity was observed against the Omicron variant, which is currently considered the most resistant strain. Additionally, most of the tested compounds did not show any cytotoxic effects across a wide panel of cell lines.

Several derivatives showed activity against human coronaviruses HCoV-229E and HCoV-OC43, which require cathepsin L for host cell entry, supporting the proposed mechanism of action. However, the derivatives were ineffective against other viruses tested, including Influenza, RSV, Herpes simplex, Yellow fever, Sindbis, and Semliki Forest viruses.[106]

The promising results from these cell-based assays suggest that the derivatives not only possess strong inhibitory activity against multiple SARS-CoV-2 variants but also exhibit a favourable safety profile. These findings provide a strong basis for further preclinical and clinical investigations, potentially leading to the development of new antiviral drugs that are effective against current and emerging variants of SARS-CoV-2.

7. PLᴾʳᵒ Inhibitors

Similar to the Mᴾʳᵒ, the SARS-CoV-2 PLᴾʳᵒ shares 100% active-site homology with its SARS-CoV counterpart. However, targeting PLᴾʳᵒ with repurposed drugs is challenging because there are very few potent inhibitors of PLᴾʳᵒ with experimentally validated efficacy.[107] A primary reason for this deficiency is the restricted binding pockets at the P1 and P2 substrate binding sites, which recognize Gly-Gly sequences. This limitation complicates quick drug discovery and poses significant challenges for designing effective inhibitors.[108]

7.1. GRL0617

In 2008, a screening of a structurally diverse library comprising 50,080 compounds for inhibitors of the SARS-CoV PLᴾʳᵒ was conducted. To prevent non-specific binding of electrophiles to the catalytic cysteine, the assay included 5 mM dithiothreitol (DTT).[109] This screening identified a hit compound **7724772**, which inhibited PLᴾʳᵒ with an IC_{50} value of 20.1 μM. Subsequent hit-to-lead process led to the development of **GRL0617** by adding a naphthyl group and an amino group to the *ortho*-methyl benzene ring. **GRL0617** exhibited a significantly improved IC_{50} of 0.6 μM toward SARS-CoV-1 PLᴾʳᵒ, inhibited SARS-CoV viral replication in Vero E6 cells with an EC_{50} of 14.5 μM, and showed no associated cytotoxicity (Figure 29).

GRL0617 was tested against SARS-CoV-2 PLᴾʳᵒ, showing an IC_{50} value of 2.4 μM and on VeroE6 cells infected by SARS-CoV-2 revealing an EC_{50} of 21 μM. This result was expected since the catalytic site, including the P1–P4 positions, is strictly conserved between SARS-CoV-1 and SARS-CoV-2 PLᴾʳᵒ.[110]
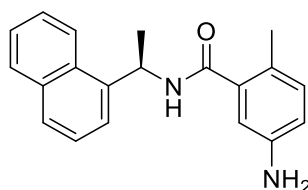
GRL0617
SARS-CoV-2 PLᴾʳᵒ,IC_{50} = 2.4 μM
Vero E6 infected cells, EC_{50} = 21 μM

Figure 29. Structure of **GR0617** and its biological activity towards SARS-CoV-2 PLᴾʳᵒ.

GRL0617 also inhibited the deISGylation activity of PLᴾʳᵒ in a cell-based assay.

The structure of SARS-CoV-2 PLᴾʳᵒ complexed with **GRL0617** (PDB: 7JRN) reveals significant conformational changes compared to the apo-structure of PLᴾʳᵒ Cys111Ser (PDB:

6WRH) (Figure 30). **GRL0617** occupies the P3–P4 positions near the active site substrate cleft. Upon binding, the BL loop, which connects α3 and α4, closes towards the inhibitor. The side chains of Tyr268 and Gln269 move closer to **GRL0617**, exposing a hydrophobic region and forming polar and hydrophobic interactions. Specifically, Tyr268 interacts with the substituted benzene group and the 1-naphthyl group, while the aliphatic portion of Gln269 forms van der Waals contacts with the benzene ring.

The 1-naphthyl group engages in hydrophobic interactions with the aromatic rings of Tyr264 and Tyr268. Residues Pro247 and Pro248 are crucial in defining the substrate binding pocket boundaries. The (R)-methyl group of **GRL0617** points towards Tyr264 and Thr301. Additionally, the carbonyl oxygen of **GRL0617** forms a hydrogen bond with the backbone nitrogen of Gln269.
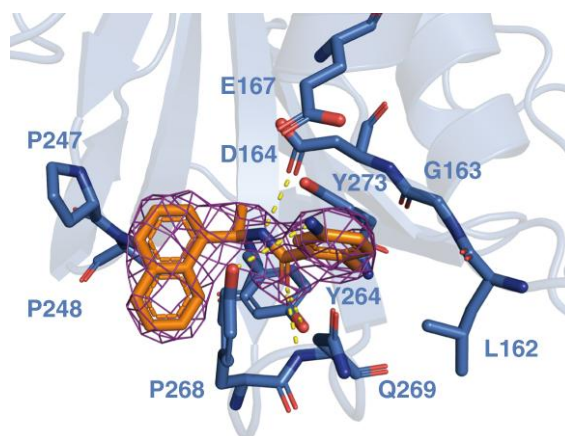
**Figure 30.** SARS-CoV-2 PL^pro with **GRL0617** (PDB: 7JRN).

The disubstituted benzene ring of **GRL0617** occupies the putative P3 position and interacts with the aliphatic portions of residues Gly163, Asp164, and Gln269. The *ortho*-methyl group is surrounded by the side chains of Tyr264, Tyr273, and Leu162. Additionally, the amino group of the aniline moiety interacts with the side chain oxygens of Gln269 and Glu167, as well as the hydroxyl group of Tyr268. These interactions potentially form hydrogen bonds with the side chains of Tyr268 and Glu167, further stabilizing the inhibitor within the active site of PL^pro.[111] These structural insights highlight the importance of the BL loop and specific residue interactions in inhibitor binding, making **GRL0617** a promising candidate for antiviral drug discovery against SARS-CoV-2 PL^pro.

7.2. VIR250 and VIR251

The Hybrid Combinatorial Substrate Library (HyCoSuL) is a combinatorial library of tetrapeptides that integrates both natural and unnatural amino acids at the P4–P2 positions, with a fixed amino acid at the P1 position, and an ACC (7-amino-4-carbamoylmethylcoumarin) fluorescent tag at the P1' position.[112] When a protease cleaves the peptide, the ACC tag is released, generating a measurable fluorescence signal.[113]

A series of tetrapeptide-ACC substrates, including both natural and unnatural amino acid residues, was designed and synthesized to determine the optimal amino acid composition for targeting SARS-CoV-2 PL[pro]. The preferred substrates, Ac-Abu(Bth)-Dap-Gly-Gly-ACC and Ac-hTyr-Dap-Gly-Gly-ACC, were converted into inhibitors **VIR250** and **VIR251** by replacing the fluorescent tag with a vinylmethyl ester (VME) group (Figure 31).[114]
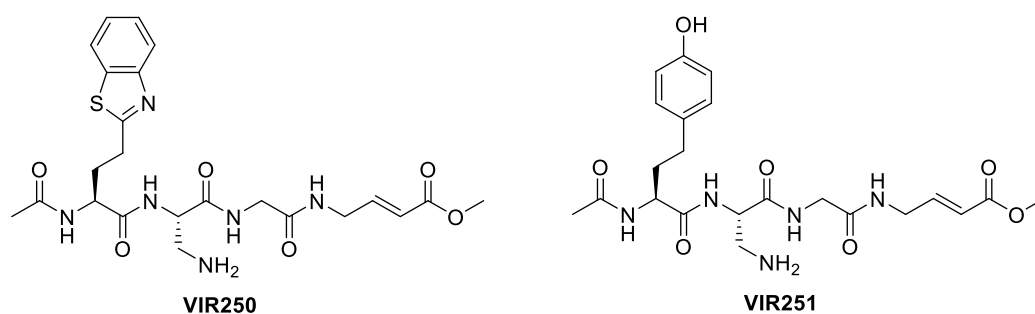
Figure 31. Chemical structure of **VIR250** and **VIR251**.

Both **VIR250** and **VIR251** demonstrated high selectivity and strong inhibition towards both SARS-CoV-1 and SARS-CoV-2 PL[pro], without inhibiting the human DUB UCH-L3, which is crucial for drug discovery.

The crystal structures of these inhibitors complexed with SARS-CoV-2 PL[pro] allowed to understand their binding modes and facilitate the refinement of these inhibitors (Figure 32).[114] As anticipated, the catalytic Cys111 residue of PL[pro] covalently links to the β carbon of the VME warheads of the inhibitors through thioether linkages.

Both inhibitors occupy the P1–P4 pockets of SARS-CoV-2 PL[pro]. The P1 and P2 sites of the inhibitors contain Gly residues, which are similar to those found in ubiquitin and ISG15. At the P3 position, the inhibitors feature Dap, an unnatural amino acid residue, in contrast to Arg in Ub and Pro in ISG15. In **VIR250**, Dap forms a backbone-backbone hydrogen bond with Gly271 and Tyr268, while in **VIR251**, Dap forms a hydrogen bond with Tyr268 (Figure 31).

Importantly, while the P1–P3 residues engage in similar interactions with PL[pro] from both viruses, the P4 residues show significant conformational diversity. For instance, when

crystallized with SARS-CoV-2, the P4 Abu (Bth) of **VIR250** projects towards the Finger domain, engaging in van der Waals interactions with Met208, Pro247, P248, and Thr301. This differs from its conformation when crystallized with SARS-CoV-1, where the side chain flips about 90°, pointing towards the palm domain. Conversely, in SARS-CoV-2, the P4 hTyr of **VIR251** projects towards the palm domain, similar to the conformation of the P4 side chain in SARS-CoV-1 **VIR250**, but opposite to the P4 conformation of SARS-CoV-2 VIR251. Interestingly, the P4 side chain of SARS-CoV-2 **VIR250** points in a similar direction to the P4 side chain of SARS-CoV-2 **VIR251**.

The significant freedom of the P4 site aligns with the observation that the P1–P2 sites are narrow and less accessible, the P3 site is half-exposed, and the P4 site is broad and well solvent-exposed. The P3–P4 sites are targeted by both small-molecule inhibitors and peptide inhibitors. The various conformations of the P4 side chain of inhibitors are accompanied by slight shifts in the BL loop and different rotamers of key residues, including Tyr268 and Gln269. Interestingly, when compared with the **GRL0617**-bound PL^{pro} structure, the side chains at the P4 positions of inhibitors partially overlap with the naphthalene group of **GRL0617**. Given the previous success in replacing naphthalene with longer biaryls, it may be possible to elongate the side chain at the P4 position of peptide inhibitors in future refinement efforts.

This comprehensive structural insight enables the design and refinement of potent PL^{pro} inhibitors, offering a promising strategy for developing antiviral therapies against SARS-CoV-2.
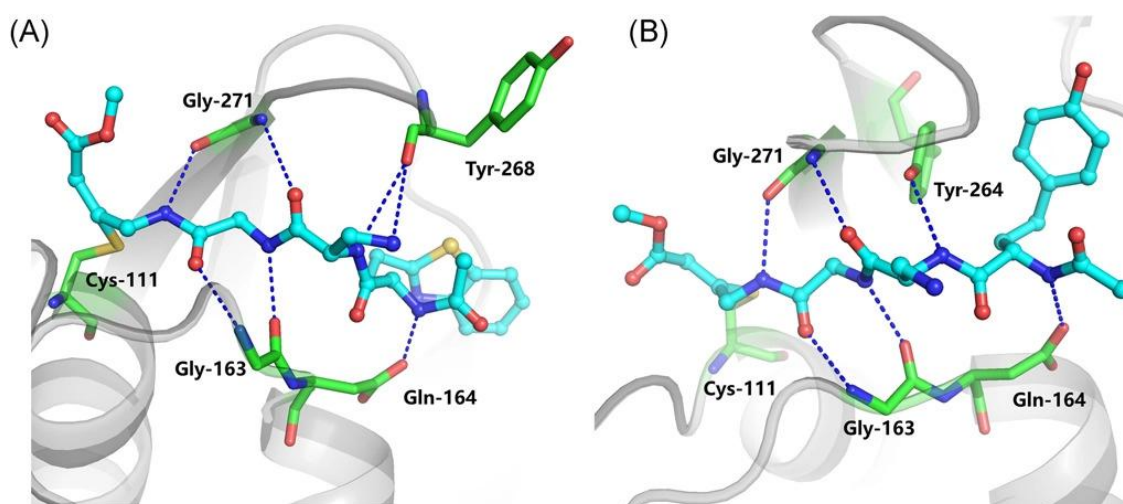

Figure 32. SARS-CoV-2 PL^{pro} with (A) **VIR250** (PDB: 6WUU) and (B) **VIR251** (PDB: 6WXA) respectively.

8. Results and Discussion

8.1. Design of SPR35-SPR44 and SPR47-SPR64

In a recent study, the research group of Prof. Zappalà reported the results of a virtual screening campaign against SARS-CoV-2 M^{pro} employing an in-house database of peptide and non-peptide ligands characterized by different types of warheads able to interact as Michael acceptors with the target.[115] These ligands were originally designed as inhibitors of rhodesain, a cysteine protease from *Trypanosoma brucei rhodesiense*.[116–122]

Using the **N3**/SARS-CoV-2 M^{pro} complex structure (PDB: 7BQY),[123] the small library (~100 compounds) was docked into the catalytic site of SARS-CoV-2 M^{pro}. Based on the predicted binding free energy values, fifteen compounds were tested *in vitro* towards SARS-CoV-2 M^{pro} using fluorimetric enzyme inhibition assays. Notably, two dipeptidyl inhibitors, identified as compounds **1** and **2**, exhibited IC$_{50}$ values in the micromolar range against the viral cysteine protease (Figure 33).

1
SARS-CoV-2 M^{pro}, IC$_{50}$ = 157 μM

2
SARS-CoV-2 M^{pro}, IC$_{50}$ = 47.2 μM
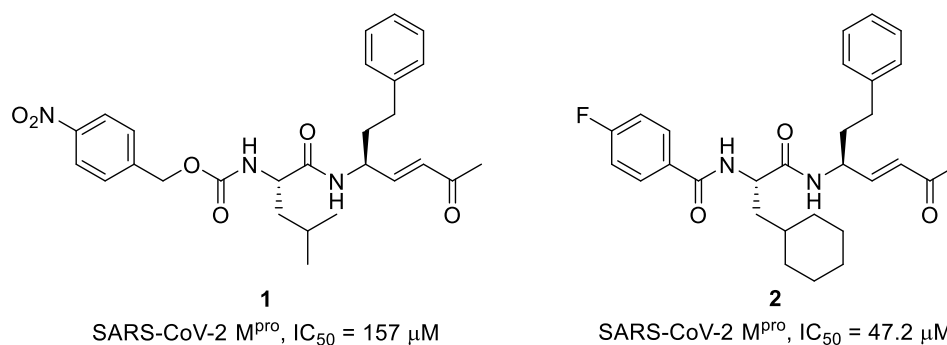
Figure 33. Structure of the two identified hit-compounds with IC$_{50}$ values against SARS-CoV-2 M^{pro}.

These two inhibitors are characterized by the presence of a methyl vinyl ketone warhead, a homophenylalanine (hPhe) residue at the P1 position, an aliphatic amino acid (specifically cyclohexylalanine and leucine) at the P2 site, and a phenyl ring with an electron-withdrawing group at the *para* position of the P3 site. Covalent docking studies revealed that the methyl vinyl ketone warhead in both inhibitors is able to form a covalent bond with the catalytic Cys145 residue of the viral protease (Figure 34).[6] Additionally, the carbonyl group of the inhibitors forms an hydrogen bond with the NH group of Gly143 of SARS-CoV-2 M^{pro}. The backbone of these peptide inhibitors engages in multiple hydrogen bonds and van der Waals interactions with the enzyme.
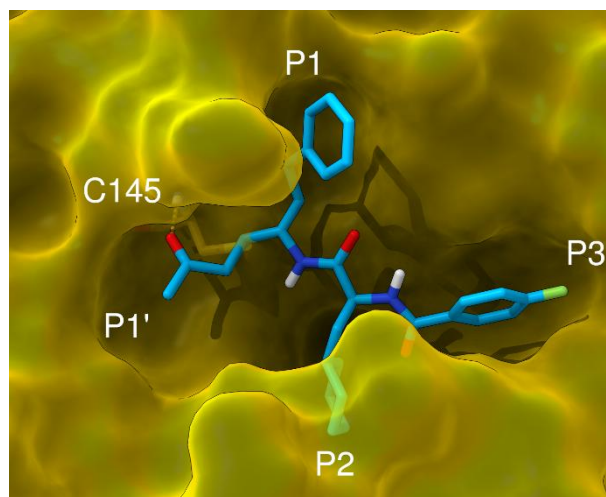
Figure 34. Predicted binding mode of compound **2**. The protein is represented as a yellow surface while the ligands as blue sticks.[6]
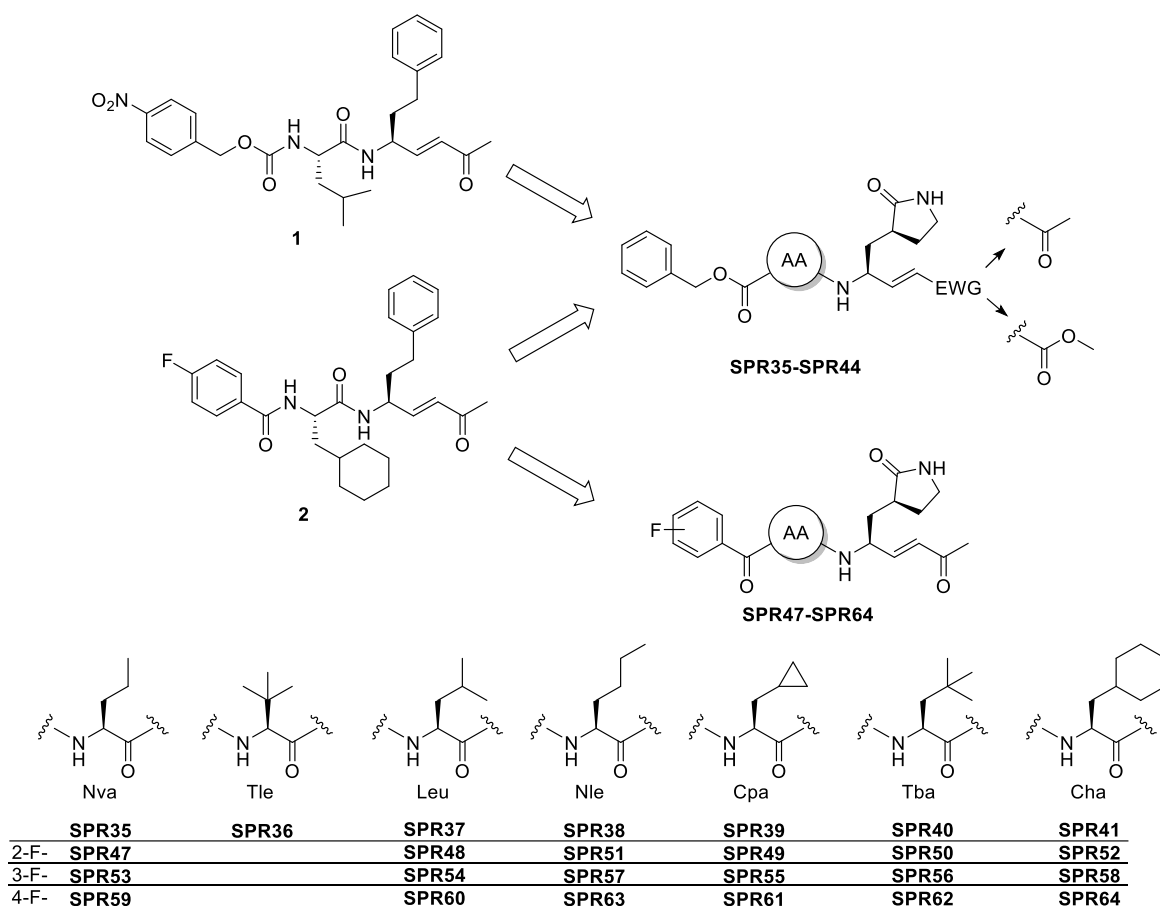
The docking results emphasize the role of hydrophobic residues at the P2 site, while the aromatic ring at the P3 site fits well into the S3 pocket. However, molecular dynamics (MD) simulations suggest that the hPhe residue at the P1 position does not form strong interactions with its corresponding pocket.

Compounds **1** and **2** mainly differed from the potent SARS-CoV-2 M^pro inhibitors due to the presence of an aromatic residue at the P1 site, instead of the Gln pentatomic surrogate (*c*Gln), which was found to be crucial for a strong binding affinity.[124] Thus, two series of peptide-based Michael acceptors (**SPR35-SPR44** and **SPR47-SPR64**) incorporating the *c*Gln at the P1 site were designed. To assess the impact of various aliphatic side chains on binding affinity, a panel of seven aliphatic amino acids at the P2 position were introduced. Linear, branched, and cyclic amino acids were selected due to their promising data reported in the literature.[125] Among these, Leu was selected, since it is present in the structure of potent SARS-CoV-2 inhibitors, as well as, in the hit-compound **1**. The bulkier and more rigid analogues of Leu, namely *tert*-butyl alanine (Tba) and *tert*-leucine (Tle) were also inserted. To explore the influence of Leu's branched side chain, its linear isomers *nor*-leucine (Nle) and *nor*-valine (Nva) were included. The cyclic analogs of Leu, *i.e.*, cyclopropylalanine (Cpa), along with its bulkier derivative cyclohexylalanine (Cha), were examined, since potent SARS-CoV-2 inhibitors have these residues at the P2 site.[126]

Considered the presence of carbobenzyloxy (Cbz) group in potent SARS-CoV-2 M^pro inhibitors like **GC376** and **UAWJ9-36-3**,[127,128] this moiety was incorporated as the *N*-capping in the new compounds **SPR35-SPR44**. Differently, in the second series (**SPR47-SPR64**), an *ortho*/*meta*/*para* fluoro-benzoyl group was inserted at the P3. As well known, the incorporation

of a fluorine atom could increase binding interactions, metabolic stability, and membrane penetration, as well as different pharmacokinetic and physicochemical properties. Aromatic rings and fluorine atoms are well-tolerated in potent inhibitors of both SARS-CoV-2 M^{pro} and hCatL.[10]

The methyl vinyl ketone warhead of the hit-compounds **1** and **2** was maintained. One of the main goal of the first series (**SPR35**-**SPR41**) was the validation of this electrophilic moiety as a warhead for SARS-CoV-2 M^{pro} inhibition. Considering the promising predicted binding free energy values of some compounds carry the methyl vinyl ester warhead, this Michael acceptor was also evaluated in derivatives with bulkier residues at the P2 position, such as Nle, Tba, and Cha (*i.e.*, **SPR42**-**SPR44**) (Figure 35).

	Nva	Tle	Leu	Nle	Cpa	Tba	Cha
	SPR35	SPR36	SPR37	SPR38	SPR39	SPR40	SPR41
2-F-	SPR47		SPR48	SPR51	SPR49	SPR50	SPR52
3-F-	SPR53		SPR54	SPR57	SPR55	SPR56	SPR58
4-F-	SPR59		SPR60	SPR63	SPR61	SPR62	SPR64

Figure 35. Design of the new peptide-based Michael acceptors **SPR35**-**SPR44** and **SPR47**-**SPR64**. Nva, nor-valine; Tle, *tert*-leucine; Leu, leucine; Nle, nor-leucine; Cpa, cyclopropylalanine; Tba, *tert*-butyl alanine; Cha, cyclohexylalanine.

The second series was designed taking into consideration the results obtained from the first series. Indeed, only the vinyl methyl ketone warhead was incorporated in **SPR47**-**SPR64**. With respect to the P2 site, the rigid residue Tle was not introduced.

8.2. Synthesis of SPR35-SPR44 and SPR47-SPR64

The novel compounds were synthesized in solution using Boc-chemistry techniques. This method involved constructing the peptide backbone from the C-terminus to the N-terminus, with the warheads being added in the final step (Scheme 1). Specifically, the Weinreb amide at the C-terminal portion was reduced to the corresponding aldehyde, which was then used in a Wittig reaction to produce the desired final compounds, following a protocol recently established.[129]

The synthesis of **SPR35-SPR44** began with the commercially available ester **3**, which was hydrolyzed under alkaline conditions to yield acid **4**. This acid was then coupled with N,O-dimethylhydroxylamine hydrochloride using O-(Benzotriazol-1-yl)-*N,N,N',N'*-tetramethyluronium tetrafluoroborate (TBTU) as the coupling reagent and (*N*-Methylmorpholine) NMM as the base to give intermediate **5**. It's worth noting that other common bases like *N,N*-Diisopropylethylamine (DIPEA) and Triethylamine (TEA) resulted in lower yields during this step.
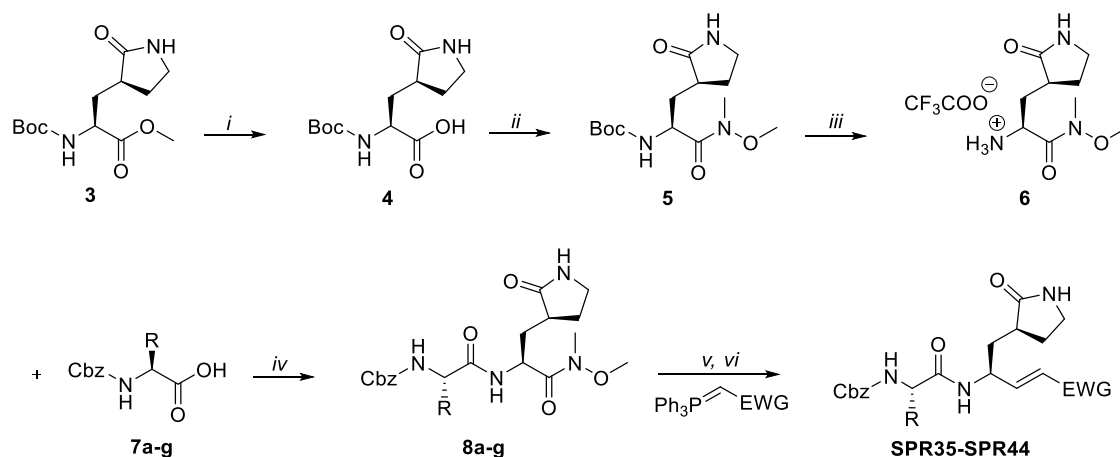
Cmpd	R	EWG	Cmpd	R	EWG
a, SPR35	-CH$_2$-CH$_3$ (Nva)		SPR42	-(CH$_2$)$_2$-CH$_3$ (Nle)	
b, SPR36	-(CH$_3$)$_3$ (Tle)		SPR43	-C-(CH$_3$)$_3$ (Tba)	
c, SPR37	-CH-(CH$_3$)$_2$ (Leu)		SPR44	-c-C$_6$H$_{11}$ (Cha)	
d, SPR38	-(CH$_2$)$_2$-CH$_3$ (Nle)				
e, SPR39	-c-C$_3$H$_5$ (Cpa)				
f, SPR40	-C-(CH$_3$)$_3$ (Tba)				
g, SPR41	-c-C$_6$H$_{11}$ (Cha)				

Scheme 1. Reagents and conditions: *i*) NaOH, MeOH, H$_2$O, -5 °C – 0 °C, 1 h; *ii*) TBTU, NMM, 0 °C, 30 min, then *N,O*-dimethylhydroxylamine hydrochloride, rt, 12h; *iii*) 30% TFA in DCM, 0 °C–rt, 4h; *iv*) **7a-g**, TBTU, NMM, 0 °C, 30 min, then **6**, rt, 12h; *v*) LiAlH$_4$, dry THF, -10 °C, 4h; *vi*) DCM, appropriate Wittig reagent, rt, 2 h.

Following the removal of the Boc protecting group with TFA, the resulting trifluoroacetate **6** was coupled with N-Cbz amino acids **7a-g**. The resulting N-Cbz-dipeptides **8a-g** were then

reduced with LiAlH$_4$ to form aldehydes. Finally, a Wittig reaction between these aldehydes and the appropriate Wittig reagent (*i.e.* 1-(triphenylphosphoranylidene)-2-propanone for ketone warhead or methyl (triphenylphosphoranylidene)acetate for ester warhead) produced the final compounds **SPR35-SPR44**. The optimized synthetic strategy allowed to obtain the desired products with only two purifications by column chromatography, with limited use of solvents. Indeed, high yields were obtained in several steps, so much that some intermediates were used for the next step without purification. The effective synthetic strategy lends itself well both to small and medium scales to obtain a few mg and moderate amount (> 1 g), respectively.

For the synthesis of **SPR47-SPR64,** the process started from intermediate **6** above described, which was coupled with the appropriate Boc-protected amino acids **9a-f** to yield the dipeptides **10a-f** (Scheme 2). After purification, these dipeptides were treated with TFA to remove the Boc protecting group, resulting in intermediates **11a-f**, which were then coupled with various fluorine-substituted benzoic acids **12-14** to afford compounds **15a-f/17a-f.** The methyl vinyl warhead was introduced as above reported providing the final desired products **SPR47-SPR64**.

R		F		R	2F	3F	4F
a = -CH$_2$-CH$_3$		12, 15 = 2-F		-CH$_2$-CH$_3$ (Nva)	SPR47	SPR53	SPR59
b = -CH-(CH$_3$)$_2$		13, 16 = 3-F		-CH-(CH$_3$)$_2$ (Leu)	SPR48	SPR54	SPR60
c = -c-C$_3$H$_5$		14, 17 = 4-F		-c-C$_3$H$_5$ (Cpa)	SPR49	SPR55	SPR61
d = -C-(CH$_3$)$_3$				-C-(CH$_3$)$_3$ (Tba)	SPR50	SPR56	SPR62
e = -(CH$_2$)$_2$-CH$_3$				-(CH$_2$)$_2$-CH$_3$ (Nle)	SPR51	SPR57	SPR63
f = -c-C$_6$H$_{11}$				-c-C$_6$H$_{11}$ (Cha)	SPR52	SPR58	SPR64
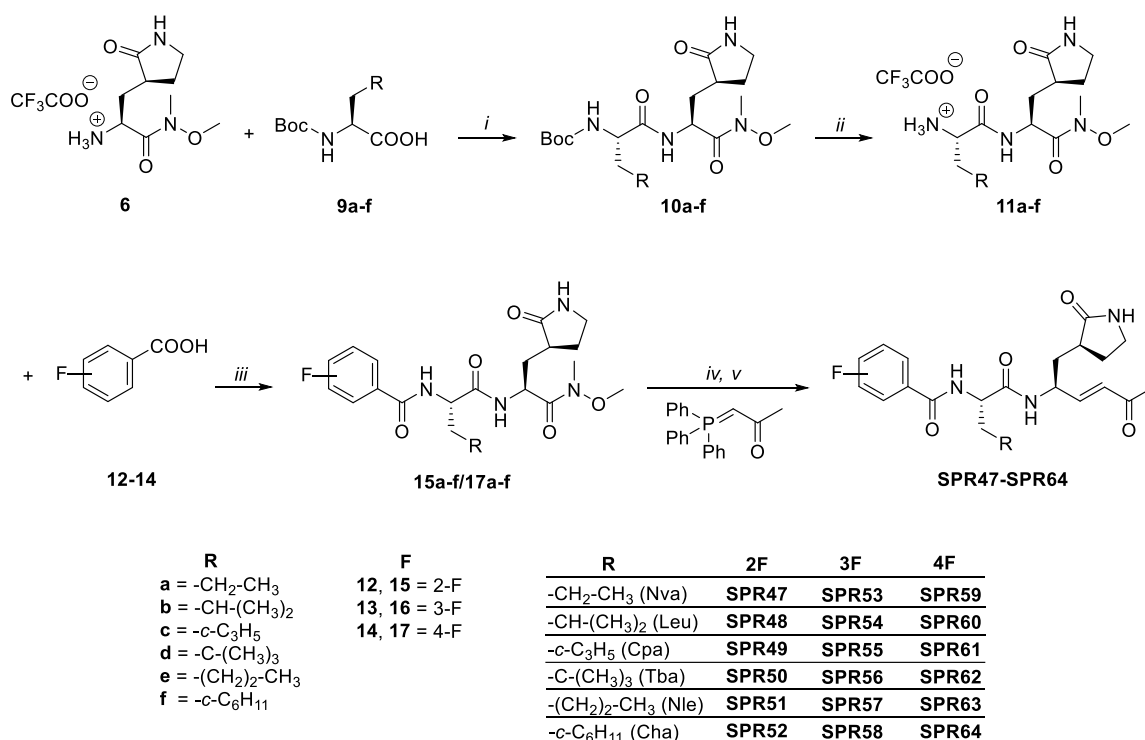
Scheme 2. Reagents and conditions: *i*) TBTU, NMM, DCM, 0°C, 10 min, then **6**, rt, 12h; *ii*) 30% TFA in DCM, 0 °C to rt, 4h; *iii*) TBTU, NMM, DCM/DMF, 0°C, 30 min, then **11a-f**, rt, 12h; *iv*) LiAlH$_4$, dry THF, -10 °C, 4h; *v*) DCM, 1-(triphenylphosphoranylidene)-2-propanone, rt, 2 h.

8.3. Biological Evaluation of SPR35-SPR44

Compounds **SPR35-SPR44** were initially screened for inhibitory activity against SARS-CoV-2 M^{pro} at a concentration of 20 µM; the K_i values were determined only for compounds that exhibited more than 90% inhibition (Table 2). Nirmatrelvir served as positive control, while DMSO was used as a negative (solvent) control. The K_i value obtained for Nirmatrelvir (3.15 ± 0.42 nM) weas consistent with that reported in the literature,[130] validating the accuracy of our biological assays.

Except for **SPR35** and **SPR36**, the vinyl ketone derivatives **SPR37**-**SPR41** demonstrated K_i values in the sub-micromolar range against SARS-CoV-2 M^{pro}, ranging from 0.184 µM to 0.416 µM. Notably, the Cha-analog **SPR41** exhibited the most favorable K_i value, while **SPR38** and **SPR39**, which include Nle and Cpa respectively, showed comparable binding affinity. However, the presence of Leu (**SPR37**) and Tba (**SPR40**) resulted in a slight reduction in affinity. The comparable activities observed for **SPR38** and **SPR41**, despite their significantly different side chains (linear and cyclic, respectively) at the P2 site, indicate a limited specificity of the S2 pocket towards bulky aliphatic amino acids. This suggests that the S2 pocket can accommodate both linear and cyclic bulky aliphatic side chains without a substantial impact on the activity of these compounds.
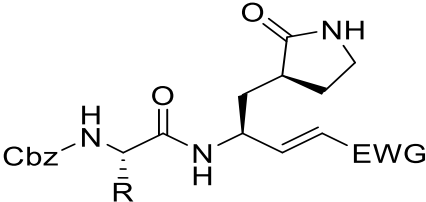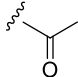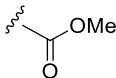
Conversely, the Nva-containing analog **SPR35** displayed a higher K_i value in the low micromolar range and the Tle derivative **SPR36** showed only minimal inhibition at the screening concentration. This suggests that reducing the side chain size negatively influences the inhibitory properties towards SARS-CoV-2 M^{pro}. Specifically, the Nva derivative **SPR35** exhibited a binding affinity almost 7-fold lower compared to the Nle analog **SPR38**, which differs only in the length of the side chain (*n*-propyl vs. *n*-butyl, respectively). Additionally, a significant loss of affinity was observed with the rigid *tert*-butyl side chain of **SPR36**. Overall, incorporating aliphatic amino acids with bulky and hindering side chains at the P2 site, whether linear, cyclic, or branched, resulted in inhibitors with sub-micromolar binding affinities towards SARS-CoV-2 M^{pro}. In contrast, the presence of Nva and Tle at P2 site, as seen in **SPR35** and **SPR36**, led to a loss of activity, suggesting that smaller or more rigid side chains do not fit well into the S2 pocket.

Unexpectedly, the vinyl methyl ester derivatives **SPR42** through **SPR44** did not show significant inhibition at the screening concentration, suggesting that the vinyl ester warhead of our compounds does not effectively react with the catalytic cysteine. Despite sharing the

binding site recognition with potent inhibitors like **SPR38**, **SPR39**, and **SPR41**, the lack of activity in **SPR42**, **SPR43**, and **SPR44** is attributed to their different warheads.

The most promising vinyl methyl ketone derivatives were selected for further biological evaluation against a panel of cysteine proteases. **SPR38**, **SPR39**, and **SPR41** showed no inhibition at 100 µM against SARS-CoV-2 PL[pro], which is crucial for processing viral polyproteins.[131] This outcome was anticipated, as the most potent PL[pro] inhibitors feature different peptide-based recognition moieties. Similarly, no inhibitory activity was observed against the dengue virus NS2B/NS3 serine protease at 100 µM.

Table 2. Biological evaluation of novel SPRs towards SARS-CoV-2 M[pro] and selectivity assessment.

SPR35-SPR44

Cmpd	EWG	AA	K_i (µM) or % of inhibition at 20 µM		
			SARS-CoV-2 M[pro]	hCatL	hCatB
SPR35		Nva	1.77 ± 0.16	-	-
SPR36		Tle	$33 \pm 2\%$	-	-
SPR37		Leu	0.386 ± 0.055	-	-
SPR38		Nle	0.260 ± 0.066	1.92 ± 0.10	11.1 ± 1.2
SPR39		Cpa	0.252 ± 0.028	3.38 ± 0.20	7.88 ± 0.65
SPR40		Tba	0.416 ± 0.058	-	-
SPR41		Cha	0.184 ± 0.025	0.252 ± 0.018	14.4 ± 1.2
SPR42		Nle	$29 \pm 4\%$	-	-
SPR43		Tba	$50 \pm 5\%$	-	-
SPR44		Cha	$47 \pm 2\%$	-	-
Nirmatrelvir	-	-	0.003 ± 0.0004	-	-

When tested against human cathepsins (hCats), specifically hCatL and hCatB, both enzymes were sensitive to SPRs inhibition within the micromolar range, with **SPR41** showing sub-micromolar inhibition of hCatL. It is well known that hCatL mediates the cleavage of the SARS-CoV spike protein, facilitating the virus entry into host cells via the endosomal route. hCatL

plays a similar role in SARS-CoV-2 infection, aiding viral entry, and its plasma levels are elevated in patients with severe COVID-19 compared to those with milder forms. High circulating levels of hCatL are directly correlated with the progression and severity of the disease.[132,133]

The antiviral effects of hCatL inhibitors are well-documented, and dual inhibition of SARS-CoV-2 M^{pro} and hCatL could offer a synergistic antiviral effect *in vivo*. Targeting two distinct pathways involved in viral and cellular processes offers significant advantages over antiviral agents that act on a single target, as extensively reported in various drug discovery and medicinal chemistry research areas.[134–137] In lights of these findings, the inhibitory properties of **SPR38**, **SPR39**, and **SPR41** against hCatL suggest potential positive effects on antiviral activity *in vivo*, as reported for the potent dual inhibitor **MPI8**.[138] Additionally, these three Michael acceptors demonstrated moderate inhibition against hCatB. Specifically, **SPR38** and **SPR39** showed K_i values that were nearly 2- and 6-fold higher, respectively, compared to their inhibition of hCatL. **SPR41**, on the other hand, displayed a mild selectivity towards hCatL with a selectivity index (SI = K_i hCatB/ K_i hCatL) of 57.

To further understand the nature of inhibition of M^{pro} and hCatL, we conducted dilution assays as previously described.[139,140] These assays involved preparing inhibitor solutions at 5 times their IC_{50} concentration to ensure effective inhibition, followed by dilution to 0.1 x IC_{50} concentration after incubation (Figure 36).
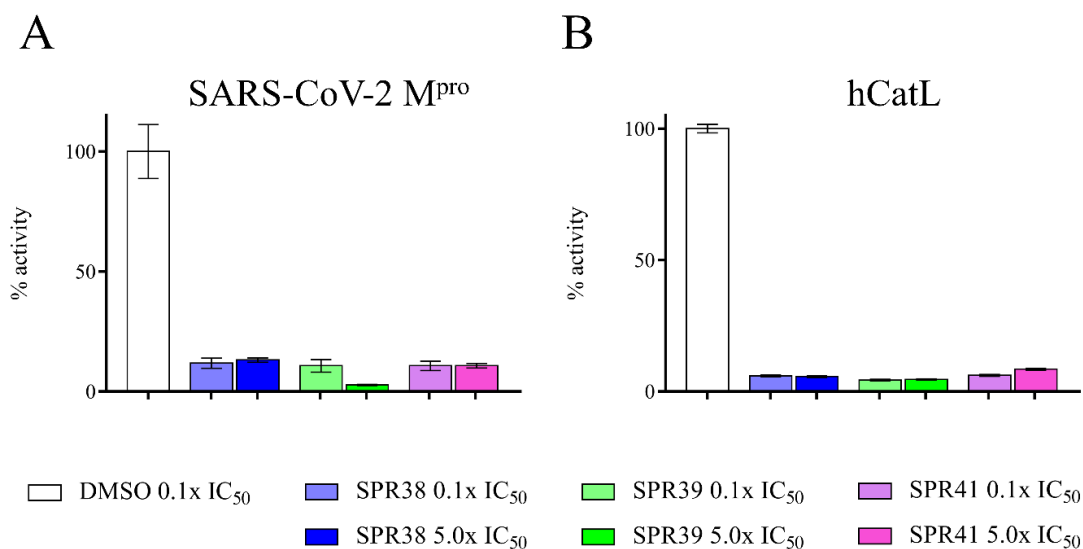
Figure 36. A) Dilution assay results for **SPR38** (blue), **SPR39** (green), **SPR41** (purple), and a DMSO-treated reference (white) against SARS-CoV-2 M^{pro} are shown. The bar chart illustrates the relative enzyme activities, indicating that there is no significant recovery of activity after dilution. B) Dilution assay results against hCatL are presented. The bar chart depicts the relative enzyme activities, showing that there is no substantial recovery of activity following dilution.

Given these observations, we aimed to determine the kinetic parameters for this inhibition mechanism. Although the results pointed to a covalent irreversible binding mode, time-dependent measurements did not exhibit a significant curvature that could be used to derive the kinetic parameters K_i, K_{inact}, and K_{2nd}. Therefore, a bi-phasic inhibition mechanism was hypothesized: high inhibitor concentrations lead to irreversible inhibition, while lower concentrations result in reversible binding. For the first time, a biphasic inhibition mechanism of the SARS-CoV-2 M^{pro} has been observed. Enzyme activities were measured before and after dilution. In the case of non-covalent or reversible-covalent binding, enzyme activity is expected to recover post-dilution. However, for both M^{pro} and hCatL, none of the tested compounds showed recovery in enzyme activity, suggesting a covalent irreversible binding mode.

The dilution assay setup was not suitable for Nirmatrelvir, a reversible control substance, due to its low IC$_{50}$ value, which would result in inhibitor concentrations significantly lower than the enzyme concentration (Figure 37). Therefore, to further validate the covalent irreversible binding of SPR compounds, we performed a dialysis assay, as previously described.[139,140]

In this assay, M^{pro} was incubated with inhibitor concentrations at 10 times the IC$_{50}$ value for the most potent inhibitors, **SPR39**, **SPR41**, and Nirmatrelvir (as a reversible control), followed by 25 hours of dialysis. Enzyme activities were recorded at various time points. Due to its high affinity and covalent reversible binding mode, Nirmatrelvir dialyzed slowly, with only 50% of enzymatic activity recovered after 25 hours of dialysis. In contrast, no recovery of enzymatic activity was observed for **SPR39** and **SPR41**, further confirming the covalent irreversible binding mode.
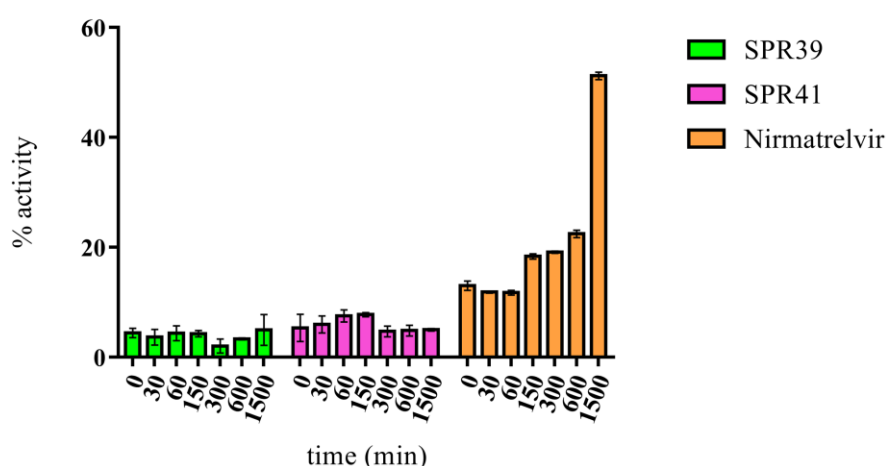
Figure 37. Dialysis assay results for **SPR39**, **SPR41**, and Nirmatrelvir (used as a covalent reversible control). The bar chart illustrates the mean relative enzyme activities after dialysis, with error bars representing the variability between technical duplicates.

Finally, the antiviral activity of these selected M^{pro} inhibitors was evaluated in SARS-CoV-2 infected Huh-7-ACE2 cells, which are considered one of the most appropriate cell lines to determine the anti-SARS-CoV-2 effects. Given the importance of cytotoxicity in drug discovery, **SPR39** and **SPR41** were evaluated on uninfected Huh-7-ACE2 cells to determine their CC$_{50}$ values.[141]

SPR39 and **SPR41** showed promising single-digit micromolar EC$_{50}$ values in line with their M^{pro} inhibition properties (Table 3), while **SPR38** showed only modest antiviral properties. Derivative **SPR39** with Cpa at the P2 site showed a CC$_{50}$ value of 100 µM and a SI of 66.6 demonstrating absence of toxicity, whereas **SPR41**, containing Cha, has proven to be cytotoxic.
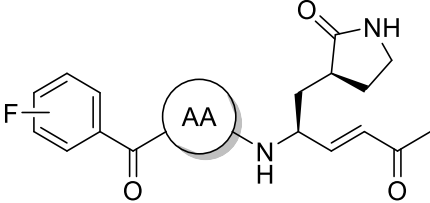
Table 3. Antiviral and cytotoxicity evaluation of the most promising SARS-CoV-2 M^{pro} inhibitors.

Cmpd	Huh-7-ACE2 cells infected EC$_{50}$ (µM)	Huh-7-ACE2 cells CC$_{50}$ (µM)	SI
SPR38	18.5 ± 6.5	60.9 ± 11.5	3
SPR39	1.5 ± 0.3	100	66.6
SPR41	1.8 ± 0.1	14.5 ± 3.4	8
Nirmatrelvir	<0.01	>100	>10.000

8.4. Biological Evaluation of SPR47-SPR64

The biological investigation of compounds **SPR47-SPR64** started from an initial screening against SARS-CoV-2 M^{pro} at 1 µM (Table 4). For compounds showing enzyme activity by more than 30% K_i values were determined. Consistent with previous observations, time-dependent measurements did not reveal significant curvature changes. The compounds with a Cha residue at P2 **SPR52**, **SPR58**, and **SPR64** (with fluorine in *ortho*, *meta*, and *para* positions, respectively) showed the strongest binding affinities to SARS-CoV-2 M^{pro}, with K_i values ranging from 1.61 ± 0.21 µM to 3.66 ± 0.23 µM. The positioning of the fluorine atom on the phenyl ring did not significantly affect protease inhibition for these compounds.

However, the side chains at the P2 site and the position of the fluorine atom on the aromatic ring did impact the activity of other inhibitors. Regarding the *ortho* substitution, only **SPR49** with Cpa at P2 exhibited a promising K_i value of 2.95 ± 0.29 µM against the viral protease. The introduction of a fluorine atom in the *meta* position generally led to inactive compounds (**SPR53-SPR57**). Conversely, the *para*-fluorine position was more favorable, with Leu, Tba, and Nle-containing analogs (**SPR60**, **SPR62** and **SPR63**) demonstrating K_i values between

5.54 ± 0.31 µM and 10.72 ± 0.84 µM. All the Nva-containing analogs (**SPR47**, **SPR53** and **SPR59**) were inactive against the viral protease, confirming that shorter hydrophobic side chains at the P2 site diminish binding affinity.

Table 4. Biological evaluation of the new series against the enzyme targets.

SPR47-SPR64

Cmpd	F	AA	SARS-CoV-2 M^{pro}		hCatL	
			residual activity (%) at 1 µM	K_i (µM)	residual activity (%) at 1 µM	K_i (µM)
SPR47	2-F	Nva	101.1 ± 15.6	-	12.0 ± 0.5	-
SPR48		Leu	88.7 ± 14.6	-	5.3 ± 0.3	-
SPR49		Cpa	57.9 ± 6.8	2.95 ± 0.29	23.2 ± 1.6	0.294 ± 0.042
SPR50		Tba	89.4 ± 6.9	-	33.5 ± 3.3	-
SPR51		Nle	98.7 ± 19.1	-	8.66 ± 0.4	-
SPR52		Cha	56.3 ± 5.7	1.61 ± 0.21	3.4 ± 0.9	0.012 ± 0.001
SPR53	3-F	Nva	100.9 ± 12.0	-	8.61 ± 0.4	-
SPR54		Leu	99.5 ± 4.6	-	10.9 ± 1.2	-
SPR55		Cpa	92.7 ± 3.4	-	9.76 ± 0.3	-
SPR56		Tba	77.0 ± 7.9	-	34.7 ± 2.7	-
SPR57		Nle	86.0 ± 3.1	-	6.81 ± 0.5	-
SPR58		Cha	64.2 ± 4.3	3.66 ± 0.23	3.6 ± 0.4	0.004 ± 0.001
SPR59	4-F	Nva	96.5 ± 6.8	-	19.1 ± 0.4	-
SPR60		Leu	64.9 ± 5.4	5.58 ± 0.32	5.8 ± 0.2	0.020 ± 0.002
SPR61		Cpa	83.7 ± 5.6	-	26.8 ± 0.7	-
SPR62		Tba	68.8 ± 6.0	5.54 ± 0.31	45.1 ± 3.0	0.701 ± 0.066
SPR63		Nle	58.8 ± 10.6	10.72 ± 0.84	15.2 ± 1.0	0.141 ± 0.011
SPR64		Cha	68.2 ± 9.2	3.14 ± 0.33	5.0 ± 1.2	0.017 ± 0.001
Nirmatrelvir[6]			-	0.003	-	-
SM142 [97,98]			-	1.8	-	0.145

The new compounds were also tested against hCatL, following previously reported methods. Unlike the evaluation against SARS-CoV-2 M^{pro}, all analogs exhibited potent inhibitory properties, with residual enzyme activity ranging from 45.1% to 3.4% at 1 μM. For dual inhibition assessment, only the seven compounds that inhibited SARS-CoV-2 M^{pro} were further characterized for their hCatL inhibitory properties.

In this series, derivatives containing cyclohexylalanine (Cha) at the P2 site (compounds **SPR52**, **SPR58** and **SPR64**) exhibited the strongest inhibitory effects against human cathepsin L (hCatL), with K_i values in the nanomolar to low nanomolar range (Table 4). Among these, compound **SPR60**, which has leucine at the P2 site and a *para*-fluorinated phenyl ring at the P3 position, showed comparable inhibition to the Cha-containing analogs. Compounds **SPR49**, **SPR62** and **SPR63** also demonstrated sub-micromolar K_i values, indicating significant potency. In total, seven novel dual inhibitors for SARS-CoV-2 M^{pro} and hCatL were identified. Notably, the presence of aliphatic amino acids at the P2 site combined with a fluorine atom on the phenyl ring at the P3 position did not guarantee potent inhibition of SARS-CoV-2 M^{pro}. This suggests a complex interplay between the nature of the P2 side chains, which fit into the S2 pocket of SARS-CoV-2 M^{pro}, and the positioning of the fluorine atom on the P3 phenyl ring. This interdependence appears to be less critical for hCatL inhibition compared to SARS-CoV-2 M^{pro}. Interestingly, the K_i values for the hCatL inhibitors were consistently better than those for SARS-CoV-2 M^{pro}, often by one to three orders of magnitude.

Although the new compounds demonstrated lower inhibitory activity against SARS-CoV-2 M^{pro} compared to Nirmatrelvir, their K_i values were similar to those reported for **SM142**,[97] a promising Michael acceptor dual inhibitor of SARS-CoV-2 M^{pro} and hCatL. The Cha-containing analogs (**SPR52**, **SPR58** and **SPR64**) and **SPR60** showed slightly better binding affinity for hCatL compared to **SM142**, with K_i values of 12 nM, 4 nM, 17 nM, and 20 nM respectively, versus 145 nM for **SM142**.

Next, the seven dual inhibitors were first tested on uninfected Huh-7-ACE2 cells to determine their CC_{50} values (Table 5). Cha analogs **SPR52**, **SPR58** and **SPR64** exhibited moderate toxicity with CC_{50} values ranging from 12.6 ± 7.7 μM to 46.9 ± 11.2 μM. The remaining derivatives showed no significant toxicity, with CC_{50} values greater than 100 μM. The moderate cytotoxicity observed in Cha-containing analogs could be attributed to their potent hCatL inhibitory activities in the nanomolar range. Interestingly, compounds **SPR49**, **SPR60**, **SPR62** and **SPR63** showed no cytotoxicity. Considering their CC_{50} values, three dual inhibitors (**SPR49**, **SPR60** and **SPR62**) were tested for antiviral efficacy against SARS-CoV-2-infected Huh-7-ACE2 cells.[142] These compounds exhibited promising EC_{50} values in the low

micromolar range, in agreement with their inhibitory effects on SARS-CoV-2 M^{pro}. Compared to **SPR39**, our previously identified top dual inhibitor, the new compounds had slightly higher K_i values against SARS-CoV-2 M^{pro} but demonstrated comparable antiviral effects, likely due to their superior hCatL inhibition.

Table 5. Biological evaluation of the dual inhibitors towards uninfected and infected Huh-7-ACE2 cells.

Cmpd	Huh-7-ACE2 uninfected cells, CC_{50} (μM)	Huh-7-ACE2 infected cells, EC_{50} (μM)
SPR49	> 100	10.3 ± 3.9
SPR52	12.6 ± 7.7	n.d.
SPR58	22.6 ± 2.3	n.d.
SPR60	> 100	7.63 ± 2.2
SPR62	> 100	3.50 ± 1.1
SPR63	> 100	n.d.
SPR64	46.9 ± 11.2	n.d.
SPR39	100	1.5
n.d.: not determined		

Further biological characterization of the antiviral agents **SPR49**, **SPR60** and **SPR62** included testing their inhibitory activities against human cathepsins B (hCatB) and S (hCatS) (Table 6). For hCatB, these Michael acceptors displayed K_i values in the micromolar range, specifically > 15 μM, 10.9 ± 0.5 μM, and 7.70 ± 0.32 μM for **SPR49**, **SPR60** and **SPR62**, respectively. In contrast, hCatS was more sensitive to these compounds, with K_i values in the nanomolar and sub-nanomolar range (95.4 ± 0.6 nM, 6.23 ± 0.25 nM, and 0.7 ± 0.1 nM for **SPR49**, **SPR60** and **SPR62**, respectively). While the hCatB inhibitory properties were comparable to our previous findings, a moderate preference for hCatS was observed in this study. The significant inhibition of hCatS by these peptide-based compounds is novel and warrants further investigation.

Table 6. Biological characterization of **SPR49**, **SPR60** and **SPR62** against hCatB and hCatS.

Cmpd	hCatB, K_i (μM)	hCatS, K_i (nM)
SPR49	> 15	95.4 ± 0.6
SPR60	10.9 ± 0.5	6.23 ± 0.25
SPR62	7.70 ± 0.32	0.7 ± 0.1

8.5. Molecular Modeling Studies

Molecular modeling studies provide molecular-level insights into the binding mode of the most promising compounds (*i.e.*, **SPR39** and **SPR62**) and rationalize the structure-activity relationship (SAR) data. The AutoDock4 (AD4) docking software's covalent docking protocol, known as the "flexible side-chain method",[143] was employed to predict the binding pose of **SPR39** in the M^{pro} X-ray structure (PDB code 7BQY).[144] This compound was chosen due to its promising biological activity *in vitro* and in cell-based experiments.

The calculated binding pose showed a covalent adduct with the catalytic Cys145 residue and an additional hydrogen bond with the backbone NH of Gly143 (Figure 38). The γ-lactam glutamine derivative at the P1 site occupied the S1 pocket, forming double hydrogen bonds with His163 and Glu166, analogously to the N3 peptide co-crystallized in the 7BQY structure. The P2 Cpa residue fit well into the S2 pocket, establishing favorable hydrophobic interactions with side chains of several amino acids. Different chemically related substituents were explored at this position, resulting in comparable potencies, except for Tle, which proved to be detrimental for enzyme inhibition probably because of its intrinsic rigidity that negatively influenced ligand-enzyme recognition or covalent adduct formation.

The P3 side chain was situated in a cleft comprised of several residues, where the terminal phenyl ring potentially formed hydrophobic contacts and π-stacking interactions.
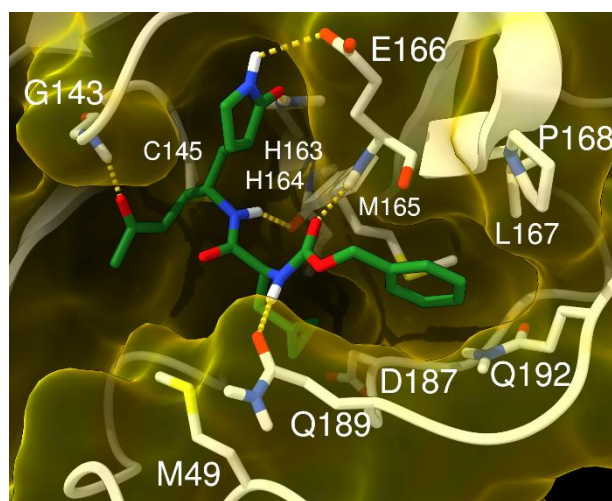
Figure 38. Predicted binding mode of **SPR39** into the X-ray SARS-CoV-2 M^{pro} structure. The protein is represented as yellow surface and white sticks, and the ligand as green sticks. H-bond interactions are represented as dashed yellow lines.

To assess the stability of these interactions, molecular dynamics (MD) simulations were conducted for the AD4-predicted **SPR39**-SARS-CoV-2 M^{pro} complex. This process involved conducting a 100 ns molecular dynamics (MD) simulation, followed by an analysis of the

ligand's root mean square deviations (L-rmsd) and fluctuations (L-rmsf) to monitor changes in the positions of the ligand atoms.

The results, (as depicted in Figure 39 A), indicate that the AD4 predicted binding mode remains highly stable throughout the entire simulation period. Analyzing the main ligand fluctuations broken down by atom reveals that the P3 site exhibits the highest flexibility, while the remainder of the molecule, including the P2 site, maintains a stable conformation (Figure 39 B).

This stable binding conformation is likely attributable to the robust ligand-enzyme interactions, as evidenced by plotting the interaction fraction of the protein-ligand contacts throughout the simulation (Figure 39 C and D).
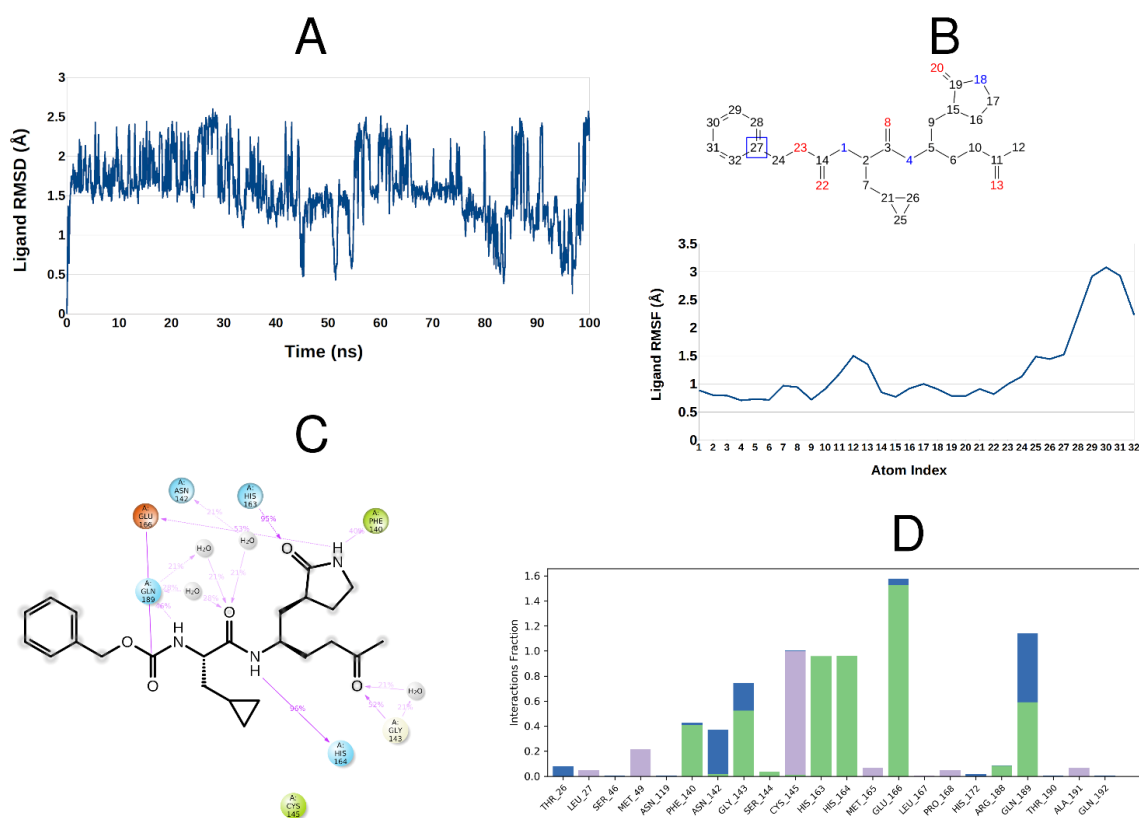
Figure 39. (A) rmsd (Å) plot of **SPR39** over time (ns). (B) L-rmsf plot broken down by atom corresponding to the reported two-dimensional structure of **SPR39**. (C and D) Protein interactions of **SPR39** throughout the simulation categorized into H-bonds, hydrophobic, ionic, and water bridges.

The same protocol of molecular modeling was applied to **SPR62**, which bears a Tba residue at the P2 and a 4-fluorobenzoyl group at the P3, selected on the basis of its potent *in vitro* inhibition against the target enzymes and its antiviral efficacy in infected cells.

The predicted binding mode of **SPR62** closely resembled that of the co-crystal N3 inhibitor in M^{pro}, with significant overlap in various structural regions. Specifically, the covalent adduct formed with the enzyme's Cys145 residue facilitated the formation of a hydrogen bond between

the oxygen of the vinyl ketone warhead and the backbone NH of Gly143 and the side chain of Asn142 (Figure 40A).

At the P1 site, the γ-lactam glutamine derivative occupied the S1 pocket and formed a double hydrogen bond interaction with the side chains of His163 and Glu166. Conversely, the P2 residue Tba was situated within the S2 pocket, establishing favorable hydrophobic interactions with the side chains of His41, Met49, Met165, and Asp187. Additionally, its backbone formed hydrogen bonds with Asn189 and the backbone NH of Glu166. These interactions suggest that the bulky Tba side chain enhances interactions with the enzyme, resulting in promising K_i values. Similar results were observed for comparably bulky substituents (such as Cha and Nle) at the P2 position.

Interestingly, among all the P2 residues investigated, Cha appeared to yield the best M^{pro} inhibition potencies regardless of the P3 substitution (as seen in compounds **SPR52**, **SPR58** and **SPR64** in Table 5). The strong interactions established by the Cha group with the enzyme likely offset any adverse effects of the P3 site on enzyme modulation. In compound **SPR62**, this P3 residue was accommodated within a pocket formed by Met165, Leu167, Pro168, Gln189, and Gln192. In this context, the terminal phenyl ring established hydrophobic connections with these residues and participated in π-stacking interactions with adjacent backbone amides.

These interactions were likely reinforced by the presence of the 4-F substitution, which appeared to be easily accommodated in the S3 cleft. Conversely, the steric hindrance of this enzyme pocket likely prevented the easy accommodation of the fluorine atom in positions 2 and 3 of the pendant phenyl ring, explaining the generally low potencies observed for compounds **SPR47**, **SPR48**, **SPR50**, **SPR51** and **SPR53**-**SPR57**.

Compound **SPR62** was also covalently docked into the hCatL 3D structure (PDB code: 3OF9),[145] in complex with covalent inhibitor Z-FY(tBu)-DMK. Double hydrogen bond interactions were observed between the P1' warhead carbonyl group and the side chains of Trp190 and Gln20 (Figure 40B). Additionally, the P1 backbone NH formed a hydrogen bond interaction with the backbone CO of Asp163, while the γ-lactam glutamine side chain fit well into the S1 pocket. Furthermore, the P2 backbone CO engaged in hydrogen bond interactions with the backbone NH of Gly69. Interestingly, the P2 backbone NH also formed hydrogen bond interactions with the backbone CO of Gly69, while its side chain nestled comfortably in the hydrophobic pocket of hCatL's S2, making contacts with Leu70, Met71, Ala136, Met162, and Gly165. The P3 residue of **SPR62** was well inserted into the S3 cleft (Glu64, Asn67, Gly68,

Leu70, and Tyr73), where the 4-F-phenyl aromatic residue could engage in favorable interactions with Leu70 and Tyr73.
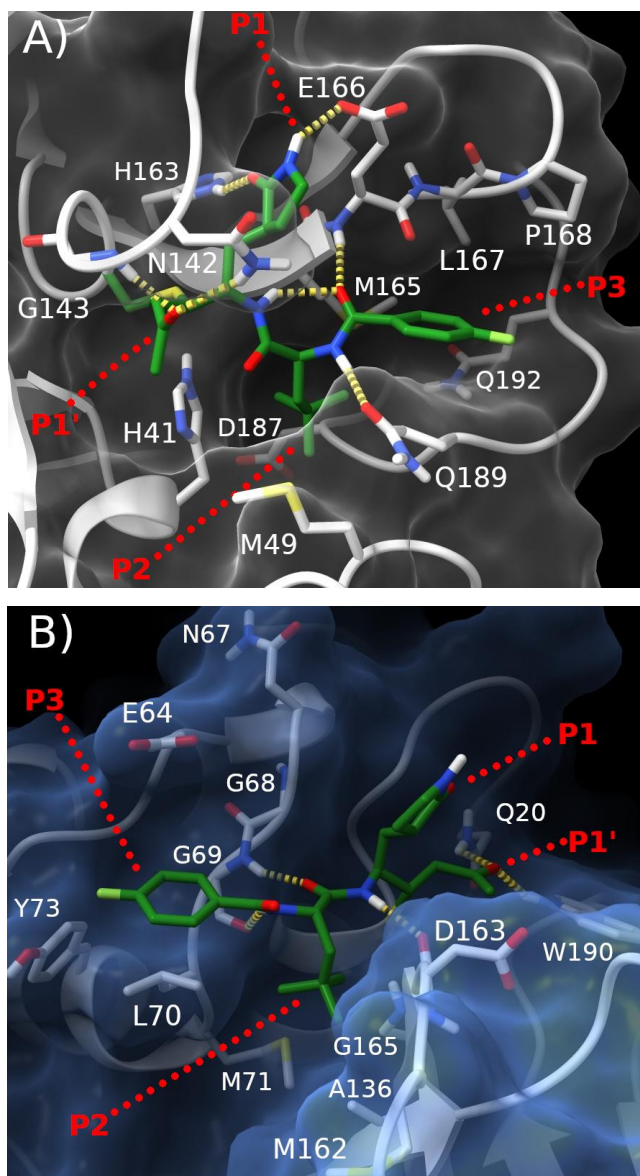
Figure 40. Predicted binding mode of **SPR62** into the X-ray SARS-CoV-2 Mᵖʳᵒ (A) and hCatL (B) structures. The proteins are represented as white sticks and grey and blue surfaces, respectively. H-bond interactions are represented as dashed yellow lines while the ligand is represented as green sticks.

8.6. Solubility Determination

In the drug discovery process, the solubility of a drug candidate in pure solvents (such as water and ethanol) or in multi-component systems (like blood plasma, urine, and saliva) is a crucial factor influencing pharmacokinetics and pharmacodynamics. Notably, Nirmatrelvir exhibited very low solubility in pure water.

The molecular structure of the drug candidate **SPR62** lacks ionizable groups, meaning its solubility corresponds solely to the concentration of its neutral species.[146] The solubility of **SPR62**, expressed as mM concentration, was measured in water at 37.0°C using UV–Vis spectrophotometry after sonication. To determine the solubility of **SPR62**, the calibration straight line obtained by measuring the absorbance signal at a fixed wavelength λ = 226 nm of five standard solutions prepared in the range of concentration 0.013−0.064 mM , was used. The choice of wavelength is based on UV-Vis scans conducted at 37.0°C and λ = 200-800 nm on both standard and saturated solutions, revealing 226 nm as the wavelength of maximum absorption.[147,148]

Based on these observations and experimental data, the solubilities of eight different **SPR62** 1:100 diluted saturated solutions were determined. Subsequently, considering the applied dilutions, the solubilities of the compound in saturated solutions were calculated. Taking into account all determined data, the average solubility value in water at 37.0°C was computed to be 5.5±0.8 mM. This concentration could serve as a reference point for future structural modifications aimed at enhancing the water solubility of **SPR62** analogues.

8.7. Design of EC1-EC8

Another series of potential dual SARS-CoV-2 Mpro/hCatL inhibitors was developed starting from **Calpain Inhibitor XII**, shown in Figure 41.[149] It exhibited potent inhibitory properties towards both cysteine protease, with relevant antiviral effect (SARS-CoV-2 Mpro, IC_{50} = 453 nM; hCatL, IC_{50} = 1.62 nM, EC_{50} = 0.49 μM). Several potent antiviral agents carry the α-keto-amide warhead, indicating as this portion well reacts with the catalytic site of viral proteases.[150] Differently from the most potent SARS-CoV-2 Mpro inhibitors reported in the literature, the **Calpain Inhibitor XII** bears Nva at the P1 site. Docking studies demonstrated that the aliphatic chain of Nva fits-well into the S1' pocket, whereas the 2-methyl pyridine at the P1' accommodates into the S1 pocket. This finding was an important novelty, since the incorporation of Gln residue at the P1 was considered essential for a strong binding affinity.

On these bases, a small series of **Calpain Inhibitor XII** analogues was developed. The α-keto-amide warhead of the lead compound was replaced with a panel of differently substituted vinyl amide warheads. The incorporation of this rigid electrophilic moiety could mimic the α-keto-amide region, although the number of H-bond acceptors is reduced. The pyridine of **Calpain Inhibitor XII** was replaced with phenyl and benzyl rings, since potent SARS-CoV-2 Mpro inhibitors have both residues at the P1' site. At the P1 position, Nva of the lead compound was

maintained, and the impact of its higher homologue Nle was also assessed. At the P2 site, Leu and Phe were inserted, since various inhibitors characterized by apolar amino acids showed potent binding affinities towards both SARS-CoV-2 M^{pro} and hCatL. Lastly, Cbz was maintained as the *N*-capping, given its presence in the lead compound and in the first series of dual inhibitors (*i.e.*, **SPR35-SPR44**) above described. Part of this project was caried out at the Juame I University in Castellon de la Plana, Spain, where I spent a four-month period under the supervision of Prof. Florenci Vicent González Adelantado.

Calpain Inhibitor XII
SARS-CoV-2 M^{pro}, IC$_{50}$ = 453 nM
hCatL, IC$_{50}$ = 1.62 nM
EC$_{50}$ = 0.49 μM

	n	P2	R$_{1'}$		*n*	P2	R$_{1'}$
EC1 =	1	Leu	Ph	**EC5** =	1	Leu	Bn
EC2 =	1	Phe	Ph	**EC6** =	1	Phe	Bn
EC3 =	2	Leu	Ph	**EC7** =	2	Leu	Bn
EC4 =	2	Phe	Ph	**EC8** =	2	Phe	Bn
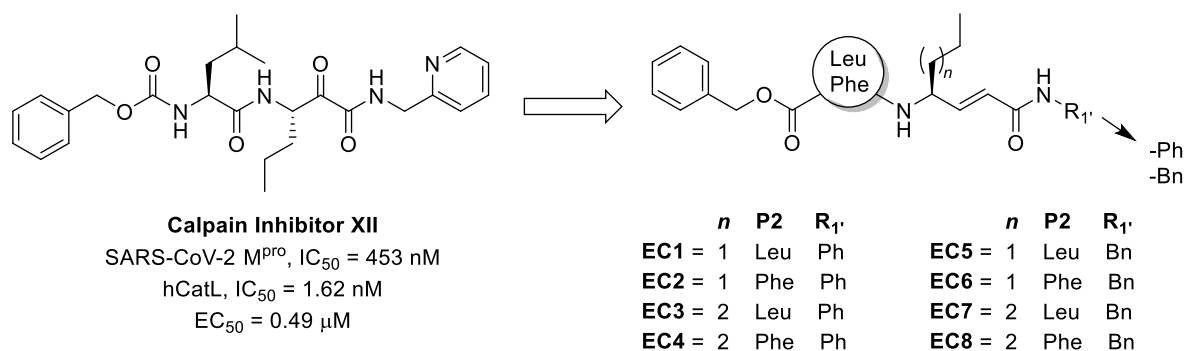
Figure 41. Calpain Inhibitors XII and the new potential dual SARS-CoV-2 M^{pro}/hCatL inhibitors.

8.8. Synthesis of EC1-EC8

The synthesis started from the commercially available *N*-Boc-amino acids **18-19**, which were coupled with *N,O*-dimethylhydroxylamine hydrochloride using TBTU as the coupling reagent and DIPEA as the base in order to obtain the desired Weinreb amides (Scheme 3). Following the removal of the Boc protecting group with TFA, the resulting trifluoroacetates **22-23** were coupled with *N*-Cbz amino acids **24-25**. The resulting *N*-Cbz-dipeptides **26-29** were then reduced with LiAlH$_4$ to obtain aldehydes. Sequentially, a Wittig reaction between these aldehydes and the appropriate Wittig reagent -methyl (triphenylphosphoranylidene)acetate-produced the compounds **30-33.**

At this point, hydrolysis was performed using LiOH in a mixture of solvents (MeOH, THF, H$_2$O, 5:1:1), to obtain the corresponding carboxylic acids **34-37**. The final coupling with different aromatic amines gave the final products **EC1-EC8.**
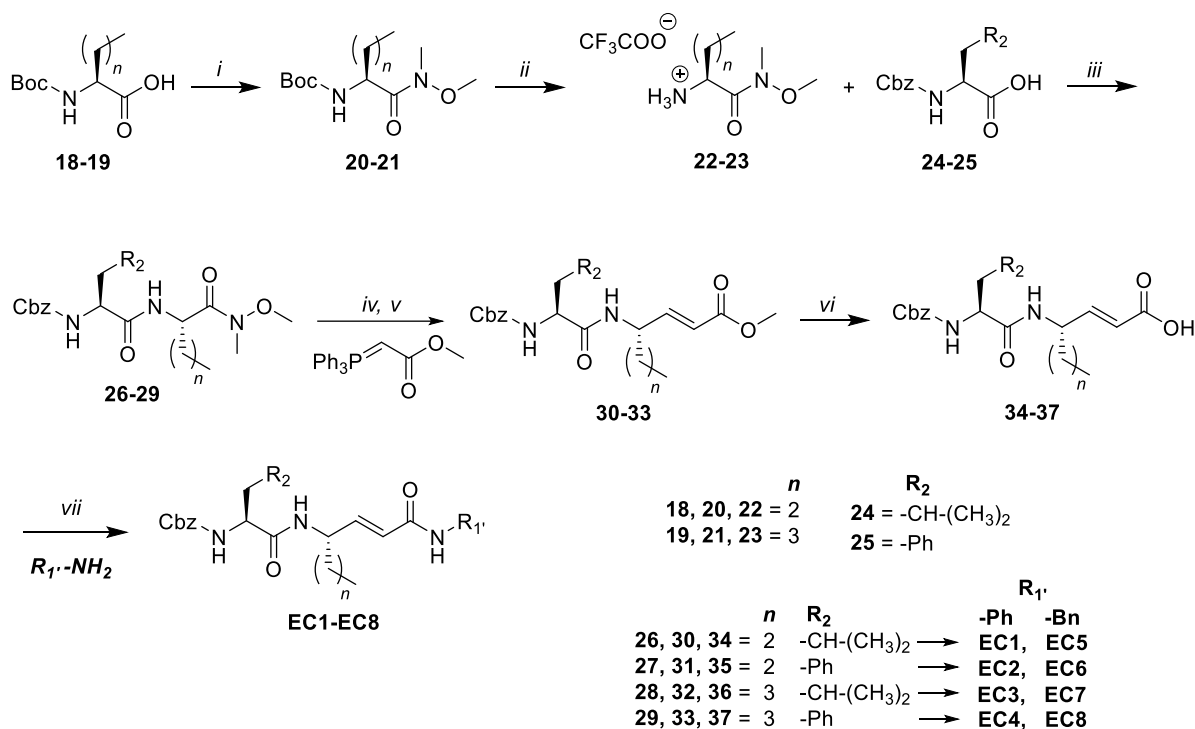
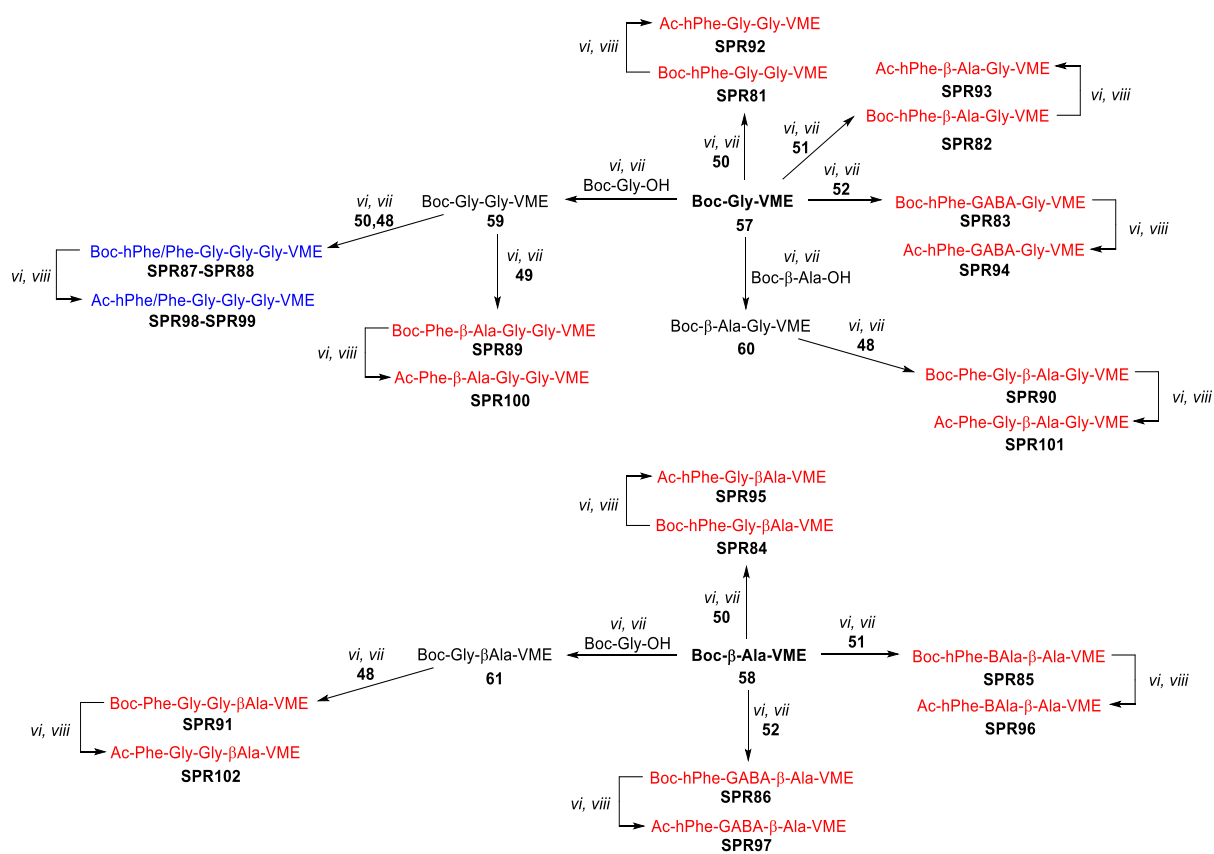**Scheme 3.** Reagents and conditions: *i*) TBTU, DIPEA, DCM, 0 °C, 30 min, then *N,O*-dimethylhydroxylamine hydrochloride, rt, 12h; *ii*) 30% TFA in DCM, 0 °C–rt, 4h; *iii*) **24-25**, TBTU, DIPEA, DCM, 0 °C, 30 min, then **22-23**, rt, 12h; *iv*) LiAlH₄, dry THF, -10 °C, 4h*v*) DCM, methyl (triphenylphosphoranylidene)acetate, rt, 2 h; *vi*) MeOH, THF, H₂O (5:1:1), rt, 12h; *vii*) TBTU, DIPEA, DCM, 0 °C, 30 min, then **R₁'-NH₂**, rt, 12h.

EC1-EC8 are under biological evaluation towards SARS-CoV-2 M^pro and hCatL. Since intermediates **30-37** are Michael acceptors, their biological characterization towards both targets will be assessed.

8.9. Design of SPR81-SPR102

Lastly, a series of potential inhibitors of SARS-CoV-2 PL^pro was developed. The design of the novel molecules started from the structure of an interesting peptide-based inhibitor reported in the literature (*i.e.*,**VIR251**), shown at the Figure 42 (SARS-CoV-2 PL^pro, IC$_{50}$ = 50 µM).[151] This inhibitor features a vinyl methyl ester warhead, two glycine residues at positions P1-P2, the diaminopropionic acid (Dap) at the P3. Finally, homotyrosine (hTyr) at the P4, and the acetyl group as the *N*-capping.
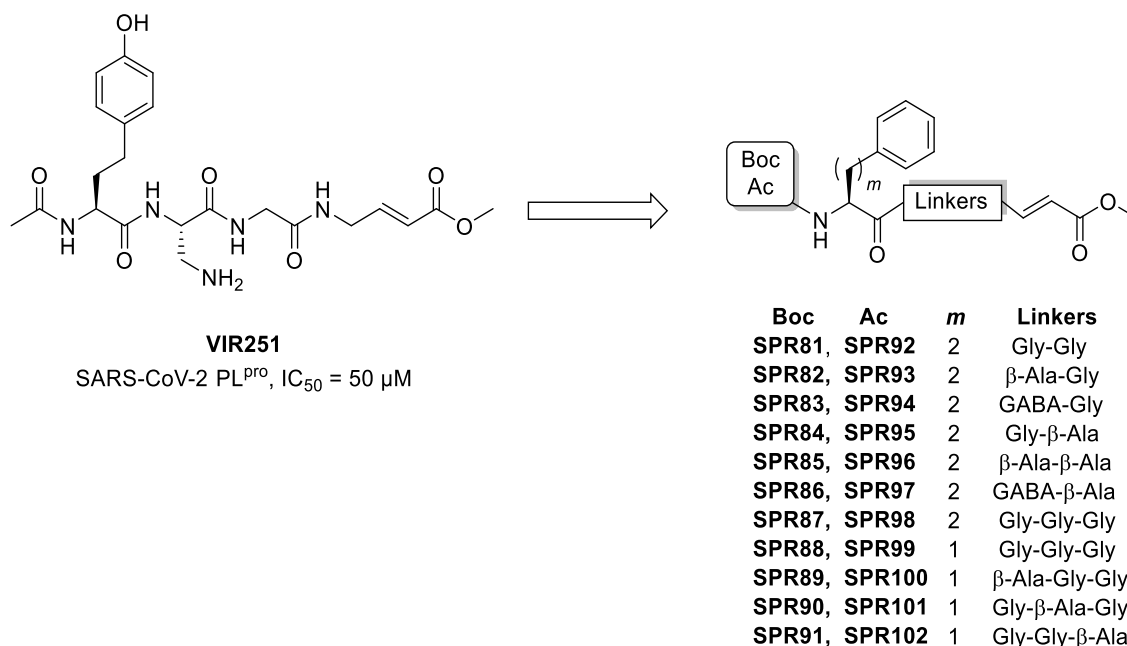
Figure 42. VIR251 with the new potential PL^pro inhibitors **SPR81-SPR102**.

With the aim of simplifying the chemical structure of **VIR251**, several modifications were performed. Dap at the P3 was removed, whereas hTyr was replaced by hPhe and Phe. Various linkers, which differ for length, number of amino acids, and number of H-bond donor/acceptor were incorporated between the phenyl ring of hPhe/Phe and the methyl vinyl ester warhead. Since the cavities of S1 and S2 pockets are narrow and devoid of space, Gly, β-Ala and GABA were introduced as the linkers at the P1-P2 or P1-P2-P3 regions. The introduction of these residues without side chains should allow the warhead to reach the catalytic Cys of PL^pro, and all the peptide backbone could interact via H-bonds with various residues in the S1, S2, and S3 pockets. Finally, both Boc and acetyl (Ac) groups were introduced as the *N*-capping.

Two sets of molecules were developed: **SPR81-SPR91**, which feature Boc as *N*-Cap and **SPR92-SPR102** which have the Ac group at that position.

8.10. Synthesis of SPR81-SPR102

The synthesis was carried-out through coupling reactions between the P1-warhead or P2-P1-warhead fragments and the Boc-Phe-P3 or Boc-hPhe/Phe-P2 building blocks.

The synthesis of the Boc-Phe-P3 or Boc-hPhe/Phe-P2 portion started from the N-Boc amino acids **38-39**, which reacted with amines **40-42** in order to obtain the corresponding esters **43-47** (Scheme 4). At this point, hydrolysis was performed producing the corresponding carboxylic acids **48-52**.
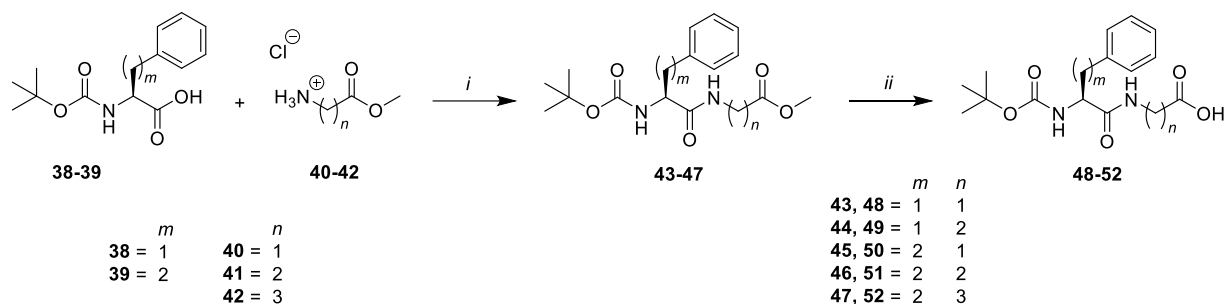
Scheme 4. Reagents and condition: *i*) DCM, TBTU, DIPEA, 0 °C to rt, 12h; *ii)* Dioxane, MeOH, H_2O, LiOH, 0 °C to rt, 12h.

For the P1-warhead fragment (Scheme 5), the synthesis began with the *N*-Boc amino acids **53-54**, which were converted into the corresponding Weinreb amides through a coupling reaction with *N,O*-dimethylhydroxylamine hydrochloride using TBTU as the coupling reagent and DIPEA as the base. The α,β-unsaturated portion was then obtained by treating with $LiAlH_4$, followed by a Wittig reaction, as previously described, to produce the vinyl methyl esters **57-58**.
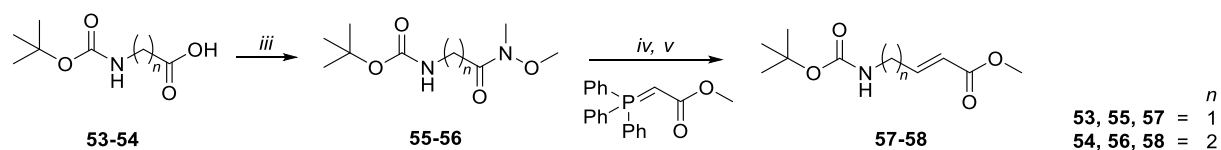
Scheme 5. Reagents and condition: *iii)* DCM, TBTU, DIPEA, 0 °C, 30 min, then *N,O*-dimethylhydroxylamine hydrochloride, rt, 12h; *iv)* $LiAlH_4$, dry THF, -10 °C, 4h; *v)* DCM, methyl (triphenylphosphoranylidene)acetate, rt, 2 h.

At this point, the amine group of these vinyl methyl esters was deprotected using TFA, and a coupling with the Boc-hPhe-P2 **50-52** yielded the compounds **SPR81-SPR86** (Scheme 6).

While for the rest of compounds is necessary another TFA deprotection and another coupling before the inserting of the Boc-Phe-P3 **48-49** (or Boc-hPhe-P3 **50**) fragment in order to obtain the desired tetrapeptide **SPR87-SPR91**.

The final step consists in the removal of the Boc-protecting group and a following coupling with the acetic anhydride in order to obtain the desired compounds **SPR92-SPR102**.

Scheme 6. Reagents and condition: *vi)* 30% TFA in DCM, 0 °C to rt, 4h; *vii)* DCM, TBTU, DIPEA, 0 °C to rt, 12h; *viii)* DCM, DIPEA, Acetic anhydride, 0 °C to rt, 12h.

The Michael acceptors obtained are currently being screened against the SARS-CoV-2 PL[pro] to evaluate their biological activity and provide further insights for continuing research in this area.

9. Experimental Section

9.1. Chemistry

Reagents and solvents were purchased from several commercial suppliers. TBTU, *N,O*-dimethylhydroxylamine hydrochloride, TFA, the Cbz-amino acids and and all the Boc-amino acids were obtained from Fluorochem. *N*-Methyl morpholine were purchased from VWR. TFA, LiAlH$_4$, methyl (triphenylphosphoranylidene) acetate, and methyl (triphenylphosphoranylidene)-2-propanone were obtained from Merck, as well as silica gel 60 F254 plates and silica gel (200–400 mesh) employed for TLC and column chromatography, respectively. All the TLC were treated with an ethanol solution of phosphomolybdic acid hydrate (15%), which was obtained by Fluorochem, meanwhile, TLC in which aldehydes were evaluated, were treated with 2,4-dinitrophenylhydrazine TLC stain. All the ^{1}H and ^{13}C spectra were performed on a Varian 500 MHz, operating at 499.74 and 125.73 MHz for ^{1}H and ^{13}C, respectively. Deuterated solvents, namely CDCl$_3$ and MeOD, were obtained from Merck and the signal of the solvents was used as the internal standard. Splitting patterns are described as singlet (s), doublet (d), doublet of doublet (dd), triplet (t), quartet (q), multiplet (m), and broad singlet (bs). Chemical shifts are expressed in ppm and coupling constants (*J*) in Hz. Elemental analyses were performed on a C. Erba model 1106 (elemental analyzer for C, H, and N) apparatus, and ±0.4% of the theoretical values were found.

9.1.1. Synthesis of Compounds SPR35- SPR44

(S)-2-((tert-Butoxycarbonyl)amino)-3-((S)-2-oxopyrrolidin-3-yl)propanoic acid (4)
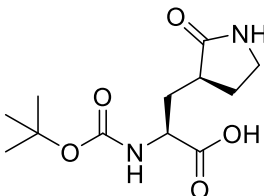
In a round bottom flask (A), the commercially available Boc-*c*Gln-OMe **3** (1 eq.) was dissolve in MeOH (0.7 mL/mmol) and cooled down up to -5 °C with ice/salt bath. Meanwhile, an aqueous solution of NaOH (4 eq., same volume of MeOH) was prepared, cooled down and added dropwise to the flask A over 10 min, keeping the temperature below 0 °C. The reaction was maintained in stirring and the temperature was constantly monitored (not more than 2–3 °C). After 1 h, TLC monitoring (EtOAc/light petroleum, 7:3. *R*$_f$ starting material: 0.30 in this mixture) showed the disappearance of the starting material, the pH was neutralized up to 7 with 1 M HCl and methanol was removed *in vacuo*. Subsequently, 1 M HCl was added up to pH 1, and the organic phase was extracted with EtOAc (x 3), washed with brine (x 3), dried over

Na$_2$SO$_4$ and concentrated *in vacuo*. The resulting residue was used for the next step without further purification. Consistency = white foamy powder. R_f = 0.0 in EtOAc/light petroleum (7:3). Yield: 74%. ^{1}H NMR (500 MHz) in CDCl$_3$, δ = 1.44 (s, 9H), 1.83-1.97 (m, 2H,), 2.13-2.24 (m, 1H), 2.38-2.49 (m, 1H), 2.57-2.66 (m, 1H), 3.34-3.46 (m, 2H), 4.33-4.41 (m, 1H), 5.69 (d, J = 7.6 Hz, 1H), 6.98 (s, 1H). ^{13}C NMR (125 MHz) in CDCl$_3$, δ = 27.74, 28.31, 33.79, 37.98, 41.00, 52.05, 80.05, 155.79, 174.82, 181.17. NMR data are in agreement with those already reported in the literature.[152]

tert-butyl   ((S)-1-(Methoxy(methyl)amino)-1-oxo-3-((S)-2-oxopyrrolidin-3-yl)propan-2-yl)carbamate (5)
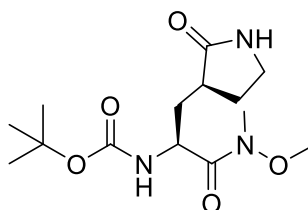
In a round-bottom flask, the acid **4** (1 eq.) was dissolved in DCM (10 mL/mmol) and stirred at 0 °C. TBTU (1.2 eq.) and NMM (2 eq.) were added and the reaction was maintained in stirring for 30 min at 0 °C. After this time, *N,O*-dimethylhydroxylamine hydrochloride (1.1 eq.) was added portion-wise, and the pH was checked (>8). The reaction was vigorously stirred at rt on. After this time, DCM vas removed *in vacuo*, and the resulting residue was dissolved in EtOAc washed with 1 M HCl (x 2), NaHCO$_3$ saturated solution (x 2), and brine (x 2), dried over Na$_2$SO$_4$, and concentrated. The crude was purified using EtOAc/MeOH 9:1 as the eluent mixture. Consistency = pale yellow poder. Yield = 86%. R_f = 0.62 in EtOAc/MeOH 9:1. ^{1}H NMR (500 MHz) in CDCl$_3$, δ = 1.43 (s, 9H), 1.63-1.71 (m, 1H), 1.78-1.88 (m, 1H), 2.10 (t, J = 11.1 Hz, 2H), 2.44-2.55 (m, 2H), 3.21 (s, 3H), 3.31-3.36 (m, 2H), 3.79 (s, 3H), 4.67 (t, J = 8.3 Hz, 1H), 5.48 (d, J = 8.8 Hz, 1H), 6.44 (s, 1H). ^{13}C NMR (125 MHz) in CDCl$_3$, δ = 28.07, 28.48, 32.37, 34.45, 38.13, 40.42, 49.44, 61.74, 79.75, 155.91, 172.69, 179.95. NMR data are in agreement with those already reported in the literature.[152]

(S)-1-(Methoxy(methyl)amino)-1-oxo-3-((S)-2-oxopyrrolidin-3-yl)propan-2-aminium 2,2,2-trifluoroacetate (6)
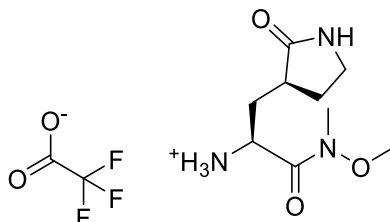
In a round-bottom flask, intermediate **5** was dissolved in DCM (5 mL/mmol) at 0 °C and an equivalent volume of TFA was added drop-wise and the resulting solution was vigorously stirred. The reaction was monitored through TLC (eluent mixture EtOAc/MeOH 9:1) and maintained in stirring until the disappearance of the starting material (around 1 h). After that,

DCM was easily removed *in vacuo*, and the resulting suspension was further evaporated with toluene, chloroform, and diethyl ether. The obtained white powder was used for the next step without purification. Consistency = white powder. Yield = 93%. R_f = 0.0 in EtOAc/MeOH 9:1. ^{1}H NMR (500 MHz) in MeOD, δ = 1.79-1.89 (m, 1H), 1.89-1.98 (m, 1H), 2.04 (ddd, J = 15.0, 5.0, 2.8 Hz, 1H), 2.43-2.36 (m, 1H), 2.74-2.83 (m, 1H), 3.26 (s, 3H), 3.36-3.41 (m, 2H), 3.82 (s, 3H), 4.40 (dd, J = 9.5, 2.8 Hz, 1H). ^{13}C NMR (125 MHz) in MeOD, δ = 29.58, 32.59, 33.24, 41.92, 42.06, 52.45, 62.38, 161.26, 181.62.

General Procedure for the Synthesis of Intermediates 8a-g

In a round bottom flask (A), the commercially available Cbz-amino acids **7a-g** (1.5 eq.) were dissolved in DCM (10 mL/mmol) and cooled down up to 0 °C with an ice bath. TBTU (1.5 eq.) and NMM (2 eq.) were added and the reaction was kept in vigorously stirring for 30 min. Meanwhile, the trifluoroacetate salt **6** (1 eq.) was suspended in DCM (10 mL/mmol) and NMM (2eq.) was added at 0 °C. The pH was checked (>8) and the resulting solution was added dropwise to the flask A. After that, the reaction was left in stirring at rt on. Subsequently, DCM vas removed *in vacuo*, and the residue was dissolved in EtOAc and washed with 1 M HCl (x 2), NaHCO$_3$ saturated solution (x 2), and brine (x 2), dried over Na$_2$SO$_4$, and concentrated *in vacuo*. The obtained crude was purified using the appropriate eluent mixture below described.

Benzyl ((S)-1-(((S)-1-(methoxy(methyl)amino)-1-oxo-3-((S)-2-oxopyrrolidin-3-yl)propan-2-yl)amino)-1-oxopentan-2-yl)carbamate (8a)
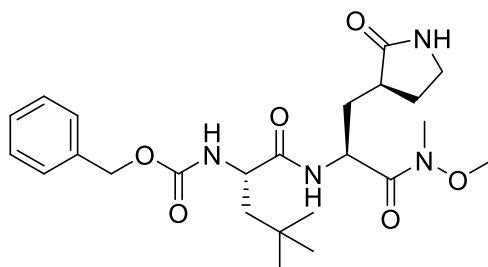

In this reaction Cbz-Nva-OH **7a** was used as the acid. Eluent mixture: EtOAc/MeOH, 19:1. Consistency = pale yellow solid; Yield = 71%. R_f = 0.24 in EtOAc/MeOH 19:1. ^{1}H NMR (500 MHz) in CDCl$_3$, δ = 0.80-0.93 (m, 3H), 1.26-1.43 (m, 2H), 1.49-1.84 (m, 4H), 2.05-2.20 (m, 1H), 2.26-2.48 (m, 2H), 31.7 (s, 3H), 3.18-3.28 (m, 2H), 3.78 (s, 3H), 4.21-4.32 (m, 1H), 4.79-4.91 (m, 1H), 5.05 (d, J = 12.1 Hz, 1H), 5.08 (d, J = 12.0 Hz, 1H), 5.74 (d, J = 8.5 Hz, 1H), 6.77 (d, J = 11.2 Hz, 1H), 7.18-7.36 (m, 5H), 7.72 (d, J = 7.5 Hz, 1H). ^{13}C NMR (125 MHz) in CDCl$_3$, δ = 13.85, 18.74, 28.18, 33.23, 35.50, 38.40, 40.48, 48.59, 53.54, 54.76, 61.62, 66.84, 128.06, 128.10, 128.53, 136.47, 156.09, 171.83, 172.46, 180.02.

Benzyl ((S)-1-(((S)-1-(methoxy(methyl)amino)-1-oxo-3-((S)-2-oxopyrrolidin-3-yl)propan-2-yl)amino)-3,3-dimethyl-1-oxobutan-2-yl)carbamate (8b)
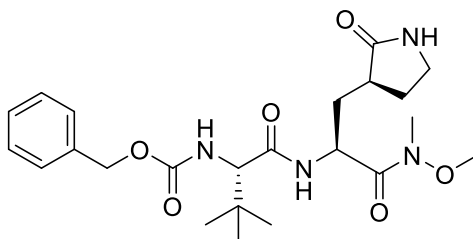
In this reaction Cbz-Tle-OH **7b** was used as the acid. Eluent mixture: EtOAc/MeOH, 19:1. Consistency = pale yellow solid; Yield = 60%. R_f = 0.33 in EtOAc/MeOH 19:1. ^{1}H NMR (500 MHz) in CDCl$_3$, δ = 1.01 (s, 9H), 2.10-2.21 (m, 1H), 2.30-2.48 (m, 2H), 3.19 (s, 3H), 3.21-3.33 (m, 2H), 3.80 (s, 3H), 4.12 (d, J = 9.5 Hz, 1H), 4.74-4.84 (m, 1H), 5.06 (d, J = 12.4 Hz, 1H), 5.09 (d, J = 12.3 Hz, 1H), 5.67 (d, J = 9.5 Hz, 1H), 6.68 (s, 1H), 7.27-7.36 (m, 5H), 7.87 (d, J = 6.3 Hz, 1H). ^{13}C NMR (125 MHz) in CDCl$_3$, δ = 26.66, 28.46, 32.43, 32.79, 35.10, 38.71, 40.57, 49.36, 61.67, 62.63, 66.89, 128.08, 128.15, 128.57, 136.56, 156.38, 171.02, 171.81, 180.01.

Benzyl ((S)-1-(((S)-1-(methoxy(methyl)amino)-1-oxo-3-((S)-2-oxopyrrolidin-3-yl)propan-2-yl)amino)-4-methyl-1-oxopentan-2-yl)carbamate (8c)
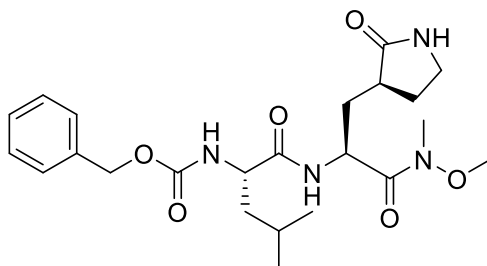
In this reaction Cbz-Leu-OH **7c** was used as the acid. Eluent mixture: EtOAc/MeOH, 19:1. Consistency = pale yellow solid; Yield = 76%. R_f = 0.45 in EtOAc/MeOH 19:1. ^{1}H NMR (500 MHz) in CDCl$_3$, δ = 0.86 (t, J = 6.0 Hz, 6H), 1.40-1.51 (m, 1H), 1.52-1.75 (m, 4H), 2.03-2.14 (m, 1H), 2.22-2.43 (m, 2H), 3.12 (s, 3H), 3.14-3.23 (m, 2H), 3.72 (s, 3H), 4.22-4.30 (m, 1H), 4.78-4.86 (m, 1H), 4.99 (d, J = 12.6 Hz, 1H), 5.03 (d, J = 11.9 Hz, 1H), 5.66 (d, J = 8.6 Hz, 1H), 6.86 (s, 1H), 7.16-7.30 (m, 5H), 7.66 (d, J = 7.6 Hz, 1H). ^{13}C NMR (125 MHz) in CDCl$_3$, δ = 21.88, 23.09, 24.68, 28.11, 32.25, 33.26, 38.36, 40.49, 42.28, 48.48, 53.51, 61.58, 66.81, 127.99, 128.05, 128.48, 136.47, 156.11, 171.83, 172.92, 180.11.

Benzyl ((S)-1-(((S)-1-(methoxy(methyl)amino)-1-oxo-3-((S)-2-oxopyrrolidin-3-yl)propan-2-yl)amino)-1-oxohexan-2-yl)carbamate (8d)
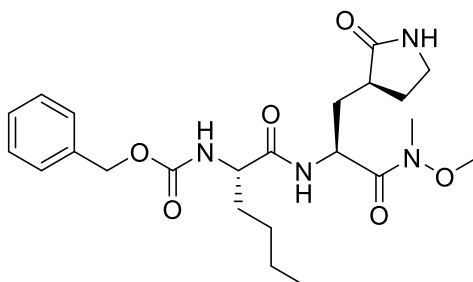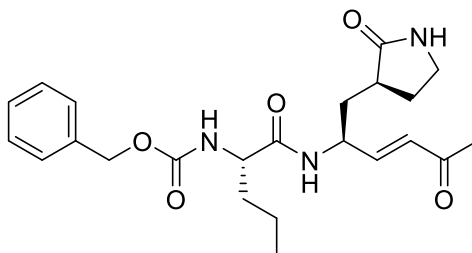
In this reaction Cbz-Nle-OH **7d** was used as the acid. Eluent mixture: EtOAc/MeOH, 19:1. Consistency = pale yellow solid; Yield = 79%. R_f = 0.36 in EtOAc/MeOH 19:1. ^{1}H NMR (500 MHz) in CDCl₃, δ = 0.80 (t, J = 6.6 Hz, 3H), 1.20-1.30 (m, 4H), 1.50-1.59 (m, 1H), 1.60-1.68 (m, 1H), 1.68-1.80 (m, 2H), 2.05-2.14 (m, 1H), 2.26-2.42 (m, 2H), 3.12 (s, 3H), 3.73 (s, 3H), 4.17-4.24 (m, 1H), 4.79-4.87 (m, 1H), 5.00 (d, J = 12.6 Hz, 1H), 5.04 (d, J = 12.1 Hz, 1H), 5.65 (d, J = 8.4 Hz, 1H), 6.64 (s, 1H), 7.17-7.31 (m, 5H), 7.59 (d, J = 7.6 Hz, 1H). ^{13}C NMR (125 MHz) in CDCl₃, δ = 14.00, 22.43, 27.56, 28.23, 33.06, 33.31, 38.39, 40.49, 48.59, 53.53, 55.00, 61.64, 66.87, 128.07, 128.11, 128.54, 136.52, 156.11, 171.86, 172.46, 180.03.

Benzyl ((S)-3-cyclopropyl-1-((((S)-1-(methoxy(methyl)amino)-1-oxo-3-((S)-2-oxopyrrolidin-3-yl)propan-2-yl)amino)-1-oxopropan-2-yl)carbamate (8e)
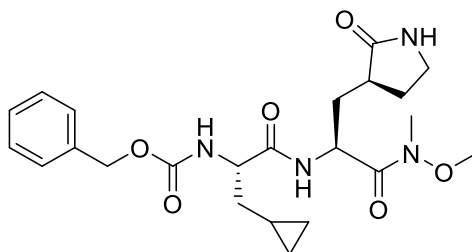
In this reaction Cbz-Cpa-OH **7e** was used as the acid. Eluent mixture: EtOAc/MeOH, 19:1. Consistency = pale yellow solid; Yield = 77%. R_f = 0.35 in EtOAc/MeOH 19:1. ^{1}H NMR (500 MHz) in CDCl₃, δ = 0.01-0.11 (m, 2H), 0.32-0.48 (m, 2H), 0.65-0.79 (m, 1H), 1.51-1.82 (m, 4H), 2.05-2.20 (m, 1H), 2.25-2.49 (m, 2H), 3.07-3.28 (m, 2H), 3.17 (s, 3H), 3.78 (s, 3H), 4.27-4.39 (m, 1H), 4.80-4.94 (m, 1H), 5.06 (d, J = 13.1 Hz, 1H), 5.09 (d, J = 12.3 Hz, 1H), 5.79 (d, J = 8.0 Hz, 1H), 6.67-6.75 (bs, 1H), 7.20-7.36 (m, 5H), 7.65 (d, J = 7.3 Hz, 1H). ^{13}C NMR (125 MHz) in CDCl₃, δ = 4.39, 4.51, 7.31, 28.25, 33.44, 38.11, 38.38, 40.47, 48.57, 53.53, 55.50, 61.65, 66.82, 127.76, 128.07, 128.53, 136.55, 155.97, 171.80, 172.17, 180.00.

Benzyl ((S)-1-((((S)-1-(methoxy(methyl)amino)-1-oxo-3-((S)-2-oxopyrrolidin-3-yl)propan-2-yl)amino)-4,4-dimethyl-1-oxopentan-2-yl)carbamate (8f)

In this reaction Cbz-Tba-OH **7f** was used as the acid. Eluent mixture: EtOAc/MeOH, 19:1. Consistency = pale yellow solid; Yield = 73%. R_f = 0.34 in EtOAc/MeOH 19:1. ^{1}H NMR (500 MHz) in CDCl₃, δ = 0.80-0.97 (s, 9H), 1.37-1.50 (m, 1H), 1.60-1.84 (m, 2H), 2.05-2.18 (m, 1H), 2.23-2.47 (m, 2H), 2.67-2.75 (m, 1H), 3.15 (s, 3H), 3.14-3.35 (m, 2H), 3.75 (s, 3H), 4.22-4.35 (m, 1H), 4.76-4.91 (m, 1H), 5.03 (d, J = 12.3 Hz, 1H), 5.08 (d, J = 11.8 Hz, 1H), 5.73 (d, J = 8.8 Hz, 1H), 6.92 (bs, 1H), 7.12-7.33 (m, 5H), 7.61 (d, J = 7.6 Hz, 1H). ^{13}C NMR (125

MHz) in CDCl₃, δ = 28.09, 29.71, 30.57, 33.39, 38.31, 38.62, 40.44, 46.35, 48.38, 52.97, 61.56, 66.80, 127.93, 128.02, 128.46, 136.50, 155.80, 171.79, 173.37, 180.02.

Benzyl ((S)-3-cyclohexyl-1-(((S)-1-(methoxy(methyl)amino)-1-oxo-3-((S)-2-oxopyrrolidin-3-yl)propan-2-yl)amino)-1-oxopropan-2-yl)carbamate (8g)
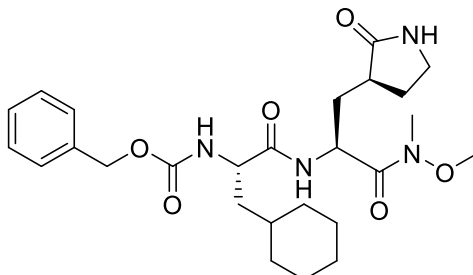
In this reaction Cbz-Cha-OH **7g** was used as the acid. Eluent mixture: EtOAc/MeOH, 19:1. Consistency = pale yellow solid; Yield = 83%. R_f = 0.40 in EtOAc/MeOH 19:1. ¹H NMR (500 MHz) in CDCl₃, δ = 0.76-1.00 (m, 2H), 1.03-1.26 (m, 3H), 1.26-1.40 (m, 1H), 1.41-1.52 (m, 1H), 1.53-1.85 (m, 7H), 2.06-2.23 (m, 2H), 2.29-2.49 (m, 2H), 3.18 (s, 3H), 3.20-3.29 (m, 2H), 3.78 (s, 3H), 4.22-4.37 (m, 1H), 4.81-4.94 (m, 1H), 5.05 (d, J = 12.5 Hz, 1H), 5.12 (d, J = 12.0 Hz, 1H), 5.54 (d, J = 8.3 Hz, 1H), 6.51 (s, 1H), 7.18-7.39 (m, 5H), 7.54 (d, J = 7.8 Hz, 1H). ¹³C NMR (125 MHz) in CDCl₃, δ = 26.14, 26.32, 26.51, 28.27, 32.43, 33.39, 33.85, 34.03, 38.36, 38.69, 40.49, 40.79, 48.51, 52.92, 61.65, 66.89, 128.05, 128.13, 128.56, 136.53, 156.13, 171.84, 172.99, 180.00.

General Procedure for the Warhead Incorporation in SPR35-SPR44

In a round-bottom flask, the intermediate **8a–g** (1 eq.) was solubilized in dry THF (20 mL/mmol), cooled down to -10 °C with an ice/salt bath, and vigorously stirred. LiAlH₄ (1 eq.) was added each 30 min until the TLC monitoring (DCM/MeOH 19:1) did not show the presence of starting material (usually, 2 or 3 eq. of LiAlH₄ were added). Cold temperature was kept. Aldehydes were detected by the treatment of the TLC with 2,4-dinitrophenylhydrazine TLC stain. Afterwards, the unreacted LiAlH₄ was quenched with 1 M KHSO₄ and the ice-bath was removed. The suspension was moved in a separatory funnel, DCM was added, and the two phases were separated. The organic phase was further extracted with DCM (x 3). Subsequently, the merged organic phases were washed with NaHCO₃ saturated solution (x 2), 1 M KHSO₄ (x 2) and brine (x 2), dried over Na₂SO₄ and concentrated. The obtained residues were used for the next step without further purification. In a round-bottom flask, the aldehydes were solubilized in DCM (5 mL/mmol) and the appropriate Wittig reagent (1 eq.) was added in one portion. The reaction was stirred at rt for 2 h. After that, the solvent was removed *in vacuo* and the desired products were purified by column chromatography using the appropriate eluent below described.

Benzyl ((S)-1-oxo-1-(((S,E)-5-oxo-1-((S)-2-oxopyrrolidin-3-yl)hex-3-en-2-yl)amino)pentan-2-yl)carbamate (SPR35)

In this reaction **8a** and 1-(triphenylphosphoranylidene)-2-propanone were used as the intermediate and Wittig reagent, respectively. Eluent mixture: EtOAc/MeOH, 25:1. Consistency = pale yellow solid; Yield = 41% (two steps). R_f = 0.30 in EtOAc/MeOH 25:1. ^{1}H NMR (500 MHz) in CDCl$_3$, δ = 0.89-0.97 (m, 3H), 1.30-1.44 (m, 2H), 1.55-1.70 (m, 2H), 1.72-1.87 (m, 2H), 1.99-2.11 (m, 1H), 2.22 (s, 3H), 2.29-2.39 (m, 1H), 2.39-2.48 (m, 1H), 3.21-3.35 (m, 2H), 4.28-4.38 (m, 1H), 4.53-4.61 (m, 1H), 5.09 (s, 2H), 5.64 (d, J = 8.7 Hz, 1H), 6.16 (d, J = 15.9 Hz, 1H), 6.41 (s, 1H), 6.65 (dd, J = 16.0, 6.0 Hz, 1H), 7.26-7.36 (m, 5H), 7.93 (d, J = 7.4 Hz, 1H). ^{13}C NMR (125 MHz) in CDCl$_3$, δ = 13.88, 18.90, 27.66, 28.66, 35.08, 35.71, 38.64, 40.66, 49.44, 54.92, 67.01, 128.08, 128.26, 128.65, 129.88, 136.49, 146.26, 156.25, 172.53, 180.31, 198.33. Elemental analysis for C$_{23}$H$_{31}$N$_3$O$_5$, calculated: C, 64.32; H, 7.27; N, 9.78; found: C, 63.98; H, 7.33; N, 9.86.

Benzyl ((S)-3,3-dimethyl-1-oxo-1-(((S,E)-5-oxo-1-((S)-2-oxopyrrolidin-3-yl)hex-3-en-2-yl)amino)butan-2-yl)carbamate (SPR36)
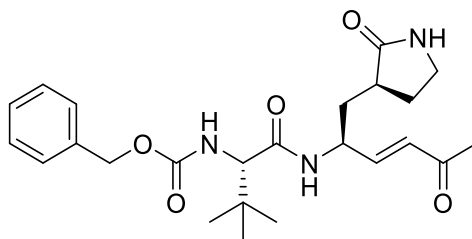
In this reaction **8b** and 1-(triphenylphosphoranylidene)-2-propanone were used as the intermediate and Wittig reagent, respectively. In this reaction methyl (triphenylphosphoranylidene)-2-propanone was used as the Wittig reagent. Eluent mixture: EtOAc/MeOH, 25:1. Consistency = pale yellow solid. Yield = 27% (two steps). R_f = 0.25 in EtOAc/MeOH 25:1. ^{1}H NMR (500 MHz) in CDCl$_3$, δ = 0.93 (s, 9H), 1.43-1.55 (m, 1H), 1.63-1.74 (m, 1H), 2.04-2.13 (m, 1H), 2.13-2.20 (m, 1H), 2.16 (s, 3H), 2.20-2.38 (m, 2H), 4.12 (d, J = 9.7 Hz, 1H), 4.39-4.50 (m 1H), 5.02 (s, 1H), 5.63 (d, J = 9.7 Hz, 1H), 6.15 (d, J = 16.2 Hz, 1H), 6.59 (dd, J = 16.0, 6.2 Hz, 1H), 6.63 (s, 1H), 7.21-7.32 (m, 5H), 7.99 (d, J = 6.9 Hz, 1H). ^{13}C NMR (125 MHz) in CDCl$_3$, δ = 26.81, 27.50, 28.46, 29.82, 34.99, 38.45, 40.65, 49.50, 62.61, 67.00, 127.99, 128.26, 128.65, 130.40, 136.49, 146.32, 156.54, 171.14, 180.17, 198.43. Elemental analysis for C$_{24}$H$_{33}$N$_3$O$_5$, calculated: C, 64.99; H, 7.50; N, 9.47; found: C, 65.24; H, 7.67; N, 9.34.

Benzyl ((S)-4-methyl-1-oxo-1-(((S,E)-5-oxo-1-((S)-2-oxopyrrolidin-3-yl)hex-3-en-2-yl)amino)pentan-2-yl)carbamate (SPR37)
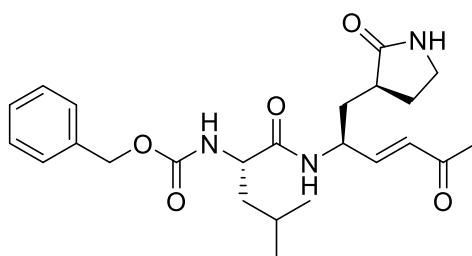
In this reaction **8c** and 1-(triphenylphosphoranylidene)-2-propanone were used as the intermediate and Wittig reagent, respectively. Eluent mixture: EtOAc/MeOH, 25:1. Consistency = pale yellow solid. Yield = 31% (two steps). R_f = 0.30 in EtOAc/MeOH 25:1. ^{1}H NMR (500 MHz) in CDCl$_3$, δ = 0.94 (s, 3H), 0.96 (s, 3H), 1.44-1.59 (m, 1H), 1.59-1.74 (m, 2H), 1.73-1.85 (m, 2H), 1.99-2.09 (m, 1H), 2.23 (s, 3H), 2.31-2.50 (m, 2H), 4.30-4.39 (m ,1H), 4.49-4.59 (m, 1H), 5.10 (s, 2H), 5.47 (d, J = 8.7 Hz, 1H), 6.16 (d, J = 15.8 Hz, 1H), 6.24 (s, 1H), 6.65 (dd, J = 16.0, 6.7 Hz, 2H), 7.27-7.35 (m, 5H), 7.94 (d, J = 7.4 Hz, 1H). ^{13}C NMR (125 MHz) in CDCl$_3$, δ = 22.07, 23.17, 24.97, 27.68, 28.78, 35.07, 38.64, 40.67, 42.62, 49.57, 53.74, 67.06, 128.06, 128.27, 128.66, 129.92, 136.49, 146.24, 156.28, 172.97, 180.29, 198.36. Elemental analysis for C$_{24}$H$_{33}$N$_3$O$_5$, calculated: C, 64.99; H, 7.50; N, 9.47; found: C, 65.17; H, 7.41; N, 9.30.

Benzyl ((S)-1-oxo-1-(((S,E)-5-oxo-1-((S)-2-oxopyrrolidin-3-yl)hex-3-en-2-yl)amino)hexan-2-yl)carbamate (SPR38)
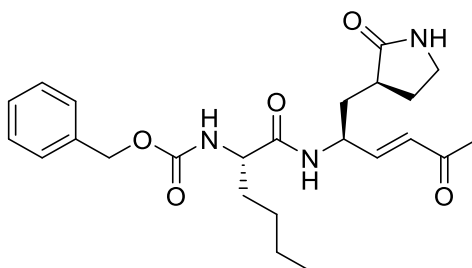
In this reaction **8d** and 1-(triphenylphosphoranylidene)-2-propanone were used as the intermediate and Wittig reagent, respectively. Eluent mixture: EtOAc/MeOH, 25:1. Consistency = pale yellow solid. Yield = 19% (two steps). R_f = 0.27 in EtOAc/MeOH 25:1. ^{1}H NMR (500 MHz) in CDCl$_3$, δ = 0.86-0.91 (m, 3H), 1.29-1.35 (m, 3H), 1.37-1.50 (m, 1H), 1.58-1.69 (m, 1H), 1.72-1.86 (m, 4H), 1.99-2.06 (m, 1H), 2.22 (s, 3H), 2.31-2.48 (m, 1H), 3.26-3.32 (m, 2H), 4.25-4.33 (m, 1H), 4.51-4.61 (m, 1H), 5.10 (s, 2H), 5.57 (d, J = 8.2 Hz, 1H), 6.16 (d, J = 15.9 Hz, 1H), 6.19 (s, 1H), 6.65 (dd, J = 15.9, 5.3 Hz, 1H), 7.26-7.37 (m, 5H), 7.93 (d, J = 7.3 Hz, 1H). ^{13}C NMR (125 MHz) in CDCl$_3$, δ = 14.06, 22.49, 27.61, 27.68, 28.49, 33.28, 35.10, 38.55, 40.64, 49.21, 55.06, 66.97, 128.03, 128.24, 128.63, 129.84, 136.46, 146.31,

156.24, 172.53, 180.31, 198.34. Elemental analysis for $C_{24}H_{33}N_3O_5$, calculated: C, 64.99; H, 7.50; N, 9.47; found: C, 64.73; H, 7.67; N, 9.28.

Benzyl ((S)-3-cyclopropyl-1-oxo-1-(((S,E)-5-oxo-1-((S)-2-oxopyrrolidin-3-yl)hex-3-en-2-yl)amino)propan-2-yl)carbamate (SPR39)
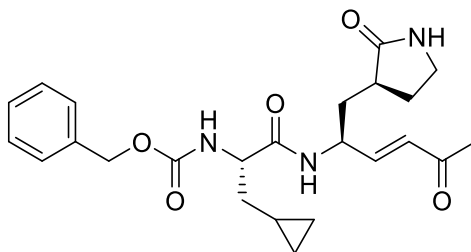
In this reaction **8e** and 1-(triphenylphosphoranylidene)-2-propanone were used as the intermediate and Wittig reagent, respectively. In this reaction methyl (triphenylphosphoranylidene)-2-propanone was used as the Wittig reagent. Eluent mixture: EtOAc/MeOH, 25:1. Consistency = pale yellow solid; Yield = 43% (two steps). R_f = 0.21 in EtOAc/MeOH 25:1. ^{1}H NMR (500 MHz) in CDCl$_3$, δ = 0.06-0.16 (m, 2H), 0.41-0.50 (m, 2H), 0.66-0.75 (m, 1H), 1.59-1.69 (m, 2H), 1.75-1.88 (m, 1H), 1.98-2.08 (m, 1H), 2.23 (s, 3H), 2.30-2.50 (m 2H), 3.24-3.38 (m, 2H), 4.31-4.40 (m, 1H), 4.52-4.61 (m, 1H), 5.11 (s, 2H), 5.63 (d, J = 9.0 Hz, 1H), 6.06 (s, 1H), 6.17 (d, J = 16.1 Hz, 1H), 6.65 (d, J = 15.7 Hz, 1H), 7.28-7.39 (m, 5H), 7.95 (d, J = 8.5 Hz, 1H). ^{13}C NMR (125 MHz) in CDCl$_3$, δ = 4.54, 4.66, 7.44, 27.69, 28.96, 35.01, 38.08, 38.69, 40.69, 49.83, 55.78, 67.04, 128.12, 128.27, 128.66, 130.03, 136.50, 146.07, 156.16, 172.31, 180.34, 198.34. Elemental analysis for $C_{24}H_{31}N_3O_5$, calculated: C, 65.29; H, 7.08; N, 9.52; found: C, 65.40; H, 7.19; N, 9.37.

Benzyl ((S)-4,4-dimethyl-1-oxo-1-(((S,E)-5-oxo-1-((S)-2-oxopyrrolidin-3-yl)hex-3-en-2-yl)amino)pentan-2-yl)carbamate (SPR40)
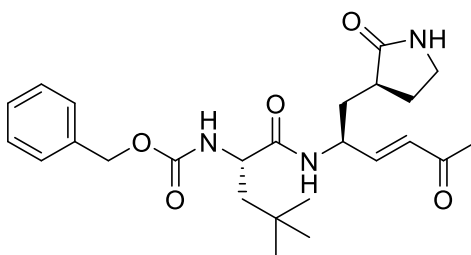
In this reaction **8f** and 1-(triphenylphosphoranylidene)-2-propanone were used as the intermediate and Wittig reagent, respectively. Eluent mixture: EtOAc/MeOH, 25:1. Consistency = pale yellow solid. Yield = 56% (two steps). R_f = 0.20 in EtOAc/MeOH 25:1. ^{1}H NMR (500 MHz) in CDCl$_3$, δ = 0.96 (s, 9H), 1.45 (dd, J = 14.4, 9.2 Hz, 1H),1.57-1.64, (m, 1H), 1.74-1.82 (m, 2H), 2.05 (ddd, J = 14.2, 11.9, 5.0 Hz, 1H), 2.21 (s, 3H), 2.28-2.37 (m, 1H), 2.38-2.46 (m, 1H), 3.22-3.32 (m, 2H), 4.32-4.40 (m, 1H), 1.45-4.57 (m, 1H), 5.10 (s, 2H), 5.51 (d, J = 8.8 Hz, 1H), 6.15 (d, J = 16.0 Hz, 1H), 6.46 (s, 1H), 6.63 (dd, J = 16.0, 5.5 Hz, 1H),

7.27-7.34 (m, 5H), 7.88 (d, J = 7.0 Hz, 1H). ^{13}C NMR (125 MHz) in CDCl$_3$, δ = 27.68, 28.62, 29.85, 30.71, 35.12, 38.56, 40.65, 46.83, 49.41, 53.17, 67.03, 127.96, 128.24, 128.64, 129.98, 136.52, 146.17, 155.97, 173.52, 180.32, 198.40. Elemental analysis calculated for C$_{25}$H$_{35}$N$_3$O$_5$: C, 65.62; H, 7.71; N, 9.18; found: C, 65.79; H, 7.57; N, 9.10.

Benzyl ((S)-3-cyclohexyl-1-oxo-1-(((S,E)-5-oxo-1-((S)-2-oxopyrrolidin-3-yl)hex-3-en-2-yl)amino)propan-2-yl)carbamate (SPR41)
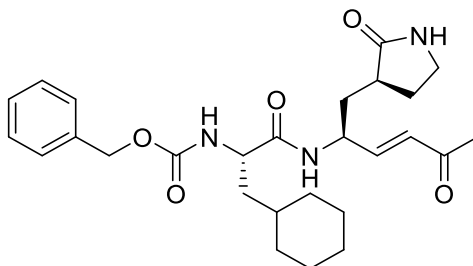
In this reaction **8g** and 1-(triphenylphosphoranylidene)-2-propanone were used as the intermediate and Wittig reagent, respectively. Eluent mixture: EtOAc/MeOH, 25:1. Consistency = pale yellow solid. Yield = 45% (two steps). R_f = 0.23 in EtOAc/MeOH 25:1. ^{1}H NMR (500 MHz) in CDCl$_3$, δ = 0.84-1.03 (m, 2H), 1.09-1.25 (m 3H), 1.31-1.39 (m, 1H), 1.46-1.54 (m, 1H), 1.61-1.72 (m, 5H), 1.77-1.85 (m, 3H), 1.99-2.08 (m, 1H), 2.24 (s, 3H), 2.31-2.40 (m, 1H), 2.40-2.48 (m, 1H), 3.24-3.36 (m, 2H), 4.30-4.39 (m, 1H), 4.50-4.62 (m, 1H), 5.09 (d, J = 12.5 Hz, 1H), 5.13 (d, J = 12.3 Hz, 1H), 6.17 (d, J = 16.0 Hz, 1H), 6.21 (s, 1H), 6.66 (dd, J = 16.0, 5.0 Hz, 1H), 7.28-7.38 (m, 5H), 7.91 (d, J = 6.9 Hz, 1H). ^{13}C NMR (125 MHz) in CDCl$_3$, δ = 26.21, 26.39, 26.51, 27.68, 28.81, 32.73, 33.81, 34.28, 35.06, 38.63, 40.67, 41.01, 49.56, 53.17, 67.03, 128.04, 128.26, 128.66, 129.91, 136.55, 146.22, 156.24, 173.05, 180.33, 198.32. Elemental analysis calculated for C$_{27}$H$_{37}$N$_3$O$_5$: C, 67.06; H, 7.71; N, 8.69; found: C, 67.32; H, 7.53; N, 8.44.

(S,E)-Methyl 4-((S)-2-(((benzyloxy)carbonyl)amino)hexanamido)-5-((S)-2-oxopyrrolidin-3-yl)pent-2-enoate (SPR42)
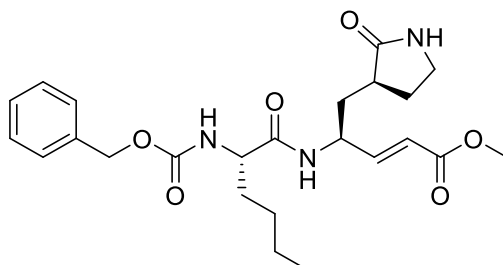

In this reaction **8d** and methyl (triphenylphosphoranylidene)-acetate were used as the intermediate and Wittig reagent, respectively. Eluent mixture: EtOAc/MeOH, 100:1. Consistency = pale yellow solid. Yield = 38% (two steps). R_f = 0.34 in EtOAc/MeOH 100:1. ^{1}H NMR (500 MHz) in CDCl$_3$, δ = 0.81-0.92 (m, 3H), 1.27-1.38 (m, 4H), 1.55-1.68 (m, 2H),

1.73-1.87 (m, 4H), 1.97-2.07 (m, 1H), 2.30-2.48 (m, 2H), 3.71 (s, 3H), 4.24-4.34 (m, 1H), 4.52-4.60 (m, 1H), 5.09 (s, 2H), 5.61 (d, J = 8.2 Hz, 1H), 5.93 (d, J = 15.7 Hz, 1H), 6.23 (s, 1H), 6.83 (dd, J = 15.7, 5.3 Hz, 1H), 7.27-7.37 (m, 5H), 7.85 (d, J = 6.9 Hz, 1H). ^{13}C NMR (125 MHz) in CDCl$_3$, δ = 14.04, 22.52, 27.67, 28.64, 33.37, 35.10, 38.60, 40.64, 49.35, 51.75, 55.07, 67.01, 120.84, 128.13, 128.25, 128.64, 136.50, 147.80, 156.21, 166.79, 172.41, 180.29. Elemental analysis calculated for C$_{24}$H$_{33}$N$_3$O$_6$: C, 62.73; H, 7.24; N, 9.14; found: C, 62.87; H, 7.02; N, 8.96.

(S,E)-Methyl 4-((S)-2-((((benzyloxy)carbonyl)amino)-4,4-dimethylpentanamido)-5-((S)-2-oxopyrrolidin-3-yl)pent-2-enoate (SPR43)
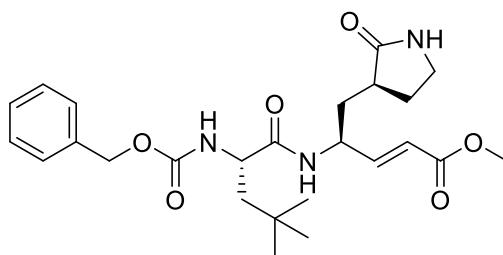
In this reaction **8f** and methyl (triphenylphosphoranylidene)-acetate were used as the intermediate and Wittig reagent, respectively. Eluent mixture: EtOAc/MeOH, 100:1. Consistency = pale yellow solid. Yield = 29% (two steps). R_f = 0.33 in EtOAc/MeOH 100:1. ^{1}H NMR (500 MHz) in CDCl$_3$, δ = 0.96 (s, 9H), 1.43 (dd, J = 14.4, 9.3 Hz, 1H), 1.57-1.66 (m, 1H), 1.74-1.83 (m 2H), 2.02 (ddd, J = 14.3, 11.9, 5.3 Hz, 1H), 2.30-2.46 (m, 2H), 3.20-3.35 (m, 2H), 3.72 (s, 3H), 4.25-4.36 (m, 1H), 4.47-4.58 (m, 1H), 5.10 (s, 2H), 5.40 (d, J = 8.7 Hz, 1H), 5.93 (d, J = 15.6 Hz, 1H), 6.15 (s, 1H), 6.82 (dd, J = 15.7, 5.6 Hz, 1H), 7.27-7.36 (m, 5H), 7.77 (d, J = 7.2 Hz, 1H). ^{13}C NMR (125 MHz) in CDCl$_3$, δ = 28.78, 29.87, 30.74, 35.14, 38.57, 40.63, 46.83, 49.52, 51.75, 53.20, 67.08, 120.99, 128.08, 128.24, 128.63, 136.53, 147.70, 155.98, 166.84, 173.43, 180.27. 43. Elemental analysis calculated for C$_{25}$H$_{35}$N$_3$O$_6$: C, 63.41; H, 7.45; N, 8.87; found: C, 63.59; H, 7.60; N, 8.72.

(S,E)-Methyl 4-((S)-2-((((benzyloxy)carbonyl)amino)-3-cyclohexylpropanamido)-5-((S)-2-oxopyrrolidin-3-yl)pent-2-enoate (SPR44)
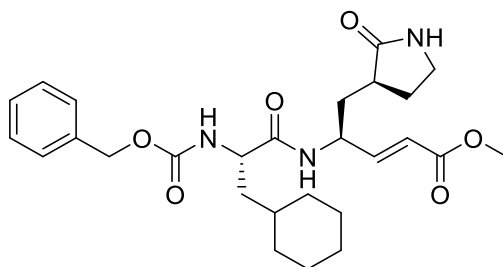
In this reaction **8g** and methyl (triphenylphosphoranylidene)-acetate were used as the intermediate and Wittig reagent, respectively. Eluent mixture: EtOAc/MeOH, 100:1. Consistency = pale yellow solid. Yield = 35% (two steps). R_f = 0.26 in EtOAc/MeOH 100:1. ^{1}H NMR (500 MHz) in CDCl$_3$, δ = 0.84-0.99 (m, 3H), 1.09-1.24 (m, 3H), 1.29-1.38 (m, 1H), 1.57-1.73 (m, 7H), 1.73-1.84 (m, 1H), 2.02 (ddd, J = 14.2, 12.0, 5.3 Hz, 1H), 2.30-2.46 (m, 2H), 3.22-3.34 (m, 2H), 3.72 (s, 3H), 4.29-4.38 (m, 1H), 4.50-4.60 (m, 1H), 5.08 (d, J = 12.6 Hz, 1H), 5.11 (d, J = 12.0 Hz, 1H), 5.45 (d, J = 8.4 Hz, 1H), 5.93 (d, J = 15.7 Hz, 1H), 6.16 (s, 1H), 6.83 (dd, J = 15.6, 5.3 Hz, 1H), 4.27-4.37 (m, 5H), 7.80 (d, J = 6.9 Hz, 1H). ^{13}C NMR (125 MHz) in CDCl$_3$, δ = 26.19, 26.34, 26.54, 28.72, 32.76, 33.79, 34.26, 35.12, 38.56, 40.64, 41.10, 49.36, 51.75, 53.13, 67.02, 120.85, 128.10, 128.25, 128.64, 136.55, 147.79, 156.22, 166.81, 172.97, 180.31. Elemental analysis calculated for C$_{27}$H$_{37}$N$_3$O$_6$: C, 64.91; H, 7.46; N, 8.41; found: C, 64.83; H, 7.22; N, 8.67.

9.1.2. Synthesis of Compounds SPR47-SPR64.

General Procedure for the Synthesis of Intermediates 10a-f.

In a round bottom flask (A), the appropriate commercially available *N*-Boc-protected amino acid **9a-f** (1.5 eq.) was dissolved in DCM (10 mL/mmol) and cooled down to 0 °C with an ice bath. TBTU (1.5 eq.) and NMM (2 eq.) were added, and the reaction was kept in vigorously stirring for 30 min. Meanwhile, the trifluoroacetate salt **6** (1 eq.) was suspended in DCM (10 mL/mmol) and NMM (2eq.) was added at 0 °C. The pH was checked (>8) and the resulting solution was added dropwise to the flask A at 0°C. After that, the reaction was maintained in stirring on at rt. Subsequently, a few mL of distilled water were added and DCM was removed *in vacuo*. The organic phase was extracted with EtOAc (x 3) and subsequently washed with 1 M HCl (x 2), NaHCO$_3$ saturated solution (x 2), and brine (x 2), dried over Na$_2$SO$_4$, and concentrated *in vacuo*. The obtained crude was purified using the appropriate eluent mixture below described.

tert-butyl ((S)-1-(((S)-1-(Methoxy(methyl)amino)-1-oxo-3-((S)-2-oxopyrrolidin-3-yl)propan-2-yl)amino)-1-oxopentan-2-yl)carbamate (10a)
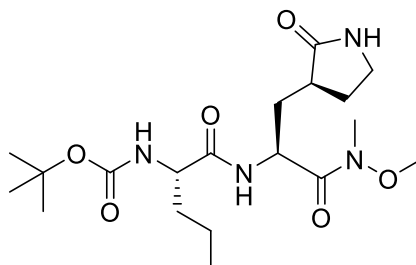
In this reaction Boc-Nva-OH **9a** was used as the acid. Yield = 72%. R_f and eluent mixture = 0.30 in EtOAc/MeOH 95:5. Consistency = white poder. ^{1}H NMR (500 MHz, CDCl$_3$) δ = 0.91 (t, J = 7.3 Hz, 3H), 1.31-1.47 (m, 2H), 1.42 (s, 9H), 1.50-1.60 (m, 1H), 1.68-1.85 (m, 3H), 2.15 (ddd, J = 14.1, 10.4, 3.5 Hz, 1H), 2.39-2.49 (m, 2H), 3.18 (s, 3H), 3.27-3.35 (m, 2H), 3.79 (s,

3H), 4.09-4.17 (m, 1H), 4.88-4.94 (m, 1H), 5.11 (d, J = 8.2 Hz, 1H), 6.26 (bs, 1H), 7.37 (d, J = 7.9 Hz, 1H). ^{13}C NMR (126 MHz, CDCl$_3$) δ = 13.57, 18.64, 28.18, 32.21, 33.41, 35.11, 38.10, 38.53, 40.26, 48.39, 54.47, 61.63, 79.87, 156.04, 172.43, 173.27, 180.39.

tert-butyl ((S)-1-(((S)-1-(Methoxy(methyl)amino)-1-oxo-3-((S)-2-oxopyrrolidin-3-yl)propan-2-yl)amino)-4-methyl-1-oxopentan-2-yl)carbamate (10b)
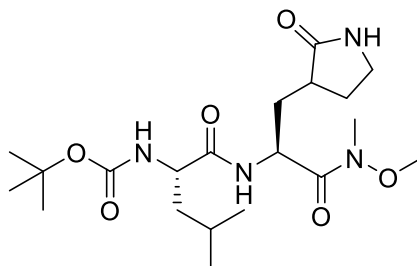
In this reaction Boc-Leu-OH **9b** was used as the acid. Yield = 64%; R_f and eluent mixture 0.37 in EtOAc/MeOH 19:1. Consistency = white poder. ^{1}H NMR (500 MHz, CDCl$_3$) δ = 0.91 (d, J = 2.3 Hz, 3H), 0.93 (d, J = 2.1 Hz, 3H), 1.41 (s, 9H), 1.44-1.49 (m, 1H), 1.58-1.65 (m, 1H), 1.66-1.74 (m, 2H), 1.76-1.84 (m, 1H), 2.37-2.49 (m, 2H), 3.17 (s, 3H), 3.26-3.34 (m, 2H), 3.78 (s, 3H), 4.13-4.21 (m, 2H), 4.90 (d, J = 9.6 Hz, 1H), 5.04 (d, J = 9.0 Hz, 1H), 6.42 (bs, 1H), 7.37 (d, J = 7.8 Hz, 1H); ^{13}C NMR (126 MHz, CDCl$_3$) δ = 21.70, 22.87, 24.56, 28.12, 28.16, 32.10, 33.42, 38.03, 40.29, 41.88, 48.29, 53.13, 61.62, 79.90, 156.03, 173.78, 175.71, 180.49.

tert-butyl ((S)-3-Cyclopropyl-1-(((S)-1-(methoxy(methyl)amino)-1-oxo-3-((S)-2-oxopyrrolidin-3-yl)propan-2-yl)amino)-1-oxopropan-2-yl)carbamate (10c)
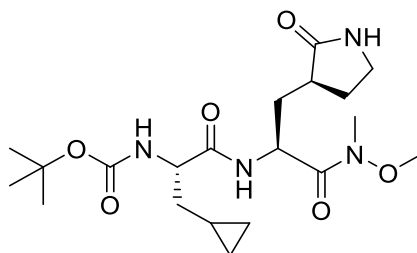
In this reaction Boc-Cpa-OH **9c** was used as the acid. Yield = 71%. R_f and eluent mixture 0.30 in EtOAc/MeOH 19:1. Consistency = white powder. ^{1}H NMR (500 MHz, CDCl$_3$) δ = 0.03-0.13 (m, 2H), 0.40-0.50 (m, 2H), 0.68-0.78 (m, 1H), 1.42 (s, 9H), 1.53-1.61 (m, 1H), 1.62-1.75 (m, 2H), 1.76-1.85 (m, 1H), 2.15 (dddd, J = 14.3, 10.7, 3.9, 1.4 Hz, 1H), 2.40-2.50 (m, 2H), 3.18 (s, 3H), 3.27-3-35 (m, 2H), 3.78 (s, 3H), 4.21 (q, J = 7.3 Hz, 1H), 4.94 (ddd, J = 11.3, 8.1, 3.4 Hz, 1H), 5.26 (d, J = 8.3 Hz, 1H), 6.43 (bs, 1H), 7.36 (d, J = 8.4 Hz, 1H). ^{13}C NMR (126 MHz, CDCl$_3$) δ = 4.21, 7.06, 20.75, 28.19, 32.14, 33.54, 37.66, 38.12, 38.52, 40.34, 48.28, 55.16, 61.66, 79.91, 155.92, 166.18, 173.05, 180.63.

tert-butyl ((S)-1-(((S)-1-(Methoxy(methyl)amino)-1-oxo-3-((S)-2-oxopyrrolidin-3-yl)propan-2-yl)amino)-4,4-dimethyl-1-oxopentan-2-yl)carbamate (10d)
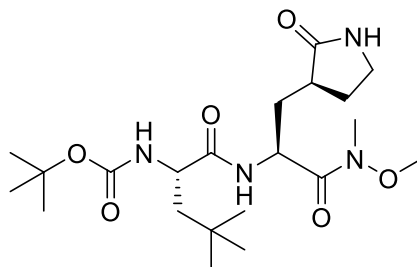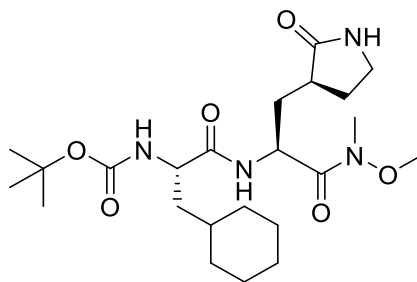

In this reaction Boc-Tba-OH **9d** was used as the acid. Yield = 55%. R_f and eluent mixture = 0.31 in EtOAc/MeOH 19:1. Consistency = white powder. ^{1}H NMR (500 MHz, CDCl$_3$) δ = 0.95 (s, 9H), 1.37-1.47 (m, 1H), 1.42 (s, 9H), 1.71 (ddd, J = 13.7, 9.6, 3.7 Hz, 1H), 1.77-1.86 (m, 2H), 2.16 (ddd, J = 14.0, 10.3, 3.7 Hz, 1H), 2.36-2.49 (m, 2H), 3.18 (s, 3H), 3.27-3.34 (m, 2H), 3.78 (s, 3H), 4.19 (dq, J = 9.2, 3.0 Hz, 1H), 4.91 (ddd, J = 11.2, 8.0, 3.5 Hz, 1H), 4.96 (d, J = 8.4 Hz, 1H), 6.27 (bs, 1H), 7.31 (d, J = 8.4 Hz, 1H). ^{13}C NMR (126 MHz, CDCl$_3$) δ = 28.21, 29.55, 30.40, 33.58, 38.02, 38.52, 40.24, 46.19, 48.27, 52.48, 61.63, 80.07, 156.75, 171.04, 174.08, 180.39.

tert-butyl ((S)-1-(((S)-1-(Methoxy(methyl)amino)-1-oxo-3-((S)-2-oxopyrrolidin-3-yl)propan-2-yl)amino)-1-oxohexan-2-yl)carbamate (10e)
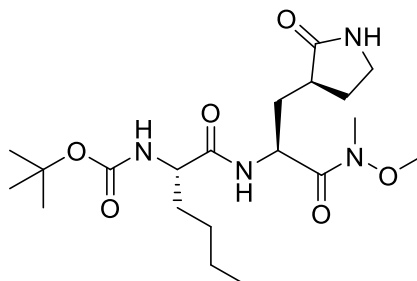
In this reaction Boc-Nle-OH **9e** was used as the acid. Yield = 76%. R_f and eluent mixture = 0.39 in EtOAc/MeOH 19:1. Consistency = white poder. ^{1}H NMR (500 MHz, CDCl$_3$) δ = 0.84-0.91 (m, 3H), 1.27-1.37 (m, 4H), 1.42 (s, 9H), 1.52-1.61 (m, 1H), 1.72 (ddd, J = 13.6, 9.2, 3.7 Hz, 1H), 1.77-1.84 (m, 2H), 2.11-2.19 (m, 1H), 2.40-2.50 (m, 2H), 3.18 (s, 3H), 3.29-3.36 (m, 2H), 3.78 (s, 3H), 4.11 (q, J = 7.6 Hz, 1H), 4.93 (ddd, J = 11.2, 8.1, 3.5 Hz, 1H), 5.09 (d, J = 8.3 Hz, 1H), 6.24 (bs, 1H), 7.30 (d, J = 8.0 Hz, 1H). ^{13}C NMR (126 MHz, CDCl$_3$) δ = 13.71, 22.20, 23.90, 27.51, 28.18, 32.55, 33.47, 38.07, 38.54, 40.30, 48.32, 54.72, 61.65, 79.85, 156.07, 169.49, 173.27, 180.50.
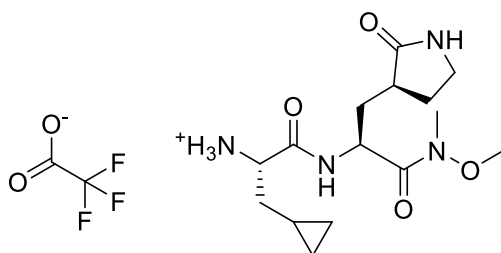
tert-butyl ((S)-3-Cyclohexyl-1-(((S)-1-(methoxy(methyl)amino)-1-oxo-3-((S)-2-oxopyrrolidin-3-yl)propan-2-yl)amino)-1-oxopropan-2-yl)carbamate (10f)

In this reaction Boc-Cha-OH **9f** was used as the acid. Yield = 66%. R_f and eluent mixture 0.42 in EtOAc/MeOH 19:1. Consistency = white powder. ^{1}H NMR (500 MHz, CDCl$_3$) δ = 0.80-1.00 (m, 2H), 1.05-1.27 (m, 4H), 1.28-1.37 (m, 1H), 1.42 (s, 9H), 1.57-1.75 (m, 6H), 1.75-1.85 (m, 2H), 2.15 (ddd, J = 13.9, 10.4, 3.6 Hz, 1H), 2.37-2.50 (m, 2H), 3.18 (s, 3H), 3.25-3-34 (m, 2H), 3.78 (s, 3H), 4.14-4.24 (m, 1H), 4.92 (ddd, J = 11.2, 8.1, 3.5 Hz, 1H), 4.97 (d, J = 8.3 Hz, 1H), 6.16 (bs, 1H), 7.26 (bs,1H). ^{13}C NMR (126 MHz, CDCl$_3$) δ = 25.94, 26.14, 26.29, 28.17, 32.11, 32.32, 33.56, 33.70, 34.01, 40.23, 40.45, 48.21, 52.52, 61.64, 79.97, 153.32, 171.40, 173.72, 180.34.

General Procedure to Obtain the Intermediates 11a-f.

In a round-bottom flask, the appropriate N-Boc-protected dipeptide **10a-f** (1 eq.) was dissolved in DCM (70% v/v) and cooled-down at 0°C. TFA (10 eq., 30% v/v) was then added dropwise. The reaction was vigorously stirred at rt until the TLC monitoring no showed the presence of the starting material. The TLC was performed using the same eluent mixture employed for the N-Boc-protected dipeptide purification. After that, volatiles were removed by co-evaporation with toluene (x 3), chloroform (x 1), and Et$_2$O (x 1). The resulting residue was triturated in Et$_2$O and used for the next step without purification.

(S)-1-(((S)-1-(Methoxy(methyl)amino)-1-oxo-3-((S)-2-oxopyrrolidin-3-yl)propan-2-yl)amino)-1-oxopentan-2-aminium 2,2,2-trifluoroacetate (11a)
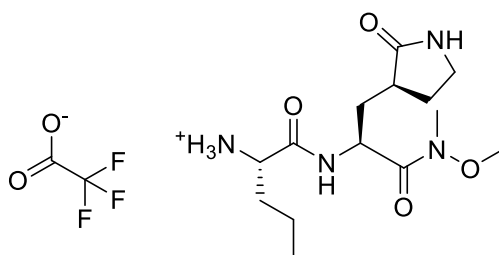
In this reaction the intermediate **10a** was used as the starting material. Yield = 94%. Consistency = White poder. ^{1}H NMR (500 MHz, MeOD) δ = 1.00 (t, J = 7.3 Hz, 3H), 1.43-1.49 (m, 3H), 1.75-1.87 (m, 3H), 2.07 (ddd, J = 14.0, 10.8, 4.2 Hz, 1H), 2.35-2.42 (m, 1H), 2.47-2.54 (m, 1H), 3.21 (s, 3H), 3.33-3.37 (m, 2H), 3.85 (s, 3H), 3.86-3.90 (m, 1H), 4.92-4.97 (m, 1H).

(S)-1-(((S)-1-(Methoxy(methyl)amino)-1-oxo-3-((S)-2-oxopyrrolidin-3-yl)propan-2-yl)amino)-4-methyl-1-oxopentan-2-aminium 2,2,2-trifluoroacetate (11b)
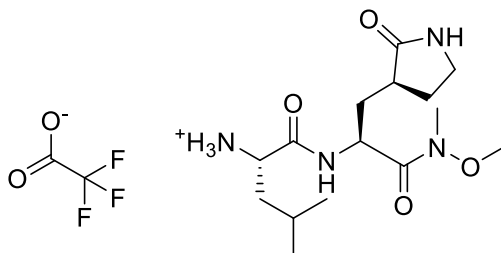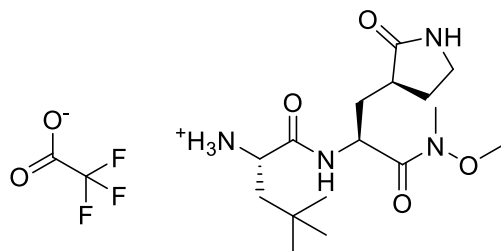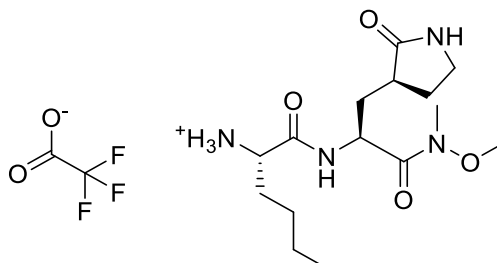

In this reaction the intermediate **10b** was used as the starting material. Yield = 88%. Consistency = white poder. ¹H NMR (500 MHz, MeOD) δ = 1.00 (d, J = 6.1 Hz, 3H), 1.02 (d, J = 6.2 Hz, 3H), 1.60-1.69 (m, 1H), 1.70-1.80 (m, 3H), 1.80-1.90 (m, 1H), 2.04-2.11 (m, 1H), 2.35-2.43 (m, 1H), 2.47-2.56 (m, 1H), 3.21 (s, 3H), 3.32-3.40 (m, 2H), 3.84 (s, 3H), 3.87-3.93 (m, 1H), 4.91-4.99 (m, 1H).

(S)-3-Cyclopropyl-1-(((S)-1-(methoxy(methyl)amino)-1-oxo-3-((S)-2-oxopyrrolidin-3-yl)propan-2-yl)amino)-1-oxopropan-2-aminium 2,2,2-trifluoroacetate (11c)


In this reaction the intermediate **10c** was used as the starting material. Yield = 91%. Consistency = white poder. ¹H NMR (500 MHz, MeOD) δ = 0.15-0.23 (m, 2H), 0.57 (dd, J = 13.7, 8.3 Hz, 2H), 0.77-0.85 (m, 1H), 1.69-1.89 (m, 4H), 2.36-2.44 (m, 1H), 2.46-2.55 (m, 1H), 3.20 (s, 3H), 3.32-3.41 (m, 2H), 3.84 (s, 3H), 3.95 (t, J = 6.7 Hz, 1H), 4.95-5.03 (m, 2H).

(S)-1-(((S)-1-(Methoxy(methyl)amino)-1-oxo-3-((S)-2-oxopyrrolidin-3-yl)propan-2-yl)amino)-4,4-dimethyl-1-oxopentan-2-aminium 2,2,2-trifluoroacetate (11d)

In this reaction the intermediate **10d** was used as the starting material. Yield = 90%. Consistency = White poder. ¹H NMR (500 MHz, MeOD) δ = 1.00 (s, 9H), 1.56-1.61 (m, 1H), 1.69-1.77 (m, 1H), 1.80-1.89 (m, 1H), 1.97-2.02 (m, 1H), 2.05-2.12 (m, 1H), 2.36-2.44 (m, 1H), 2.49-2.58

(m, 1H), 3.20 (s, 3H), 3.32-3.40 (m, 2H), 3.84 (s, 3H), 3.91 (q, *J* = 5.5 Hz, 1H), 4.96-5.02 (m, 1H).

(S)-1-(((S)-1-(Methoxy(methyl)amino)-1-oxo-3-((S)-2-oxopyrrolidin-3-yl)propan-2-yl)amino)-1-oxohexan-2-aminium 2,2,2-trifluoroacetate (11e)

In this reaction the intermediate **10e** was used as the starting material. Yield = 87%. Consistency = white poder. ^{1}H NMR (500 MHz, MeOD) δ = 0.93-0.99 (m, 3H), 1.36-1.47(m, 4H), 1.74 (ddd, *J* = 13.9, 10.0, 3.8 Hz, 1H), 1.79-1.93 (m, 3H), 2.04-2.11 (m, 1H), 2.34-2.42(m, 1H), 2.46-2.55 (m, 1H), 3.21 (s, 3H), 3.32-3.40 (m, 2H), 3.85 (s, 3H), 3.86-3-90 (m, 1H), 4.90-4.99 (m, 1H).

(S)-3-Cyclohexyl-1-(((S)-1-(methoxy(methyl)amino)-1-oxo-3-((S)-2-oxopyrrolidin-3-yl)propan-2-yl)amino)-1-oxopropan-2-aminium 2,2,2-trifluoroacetate (11f)
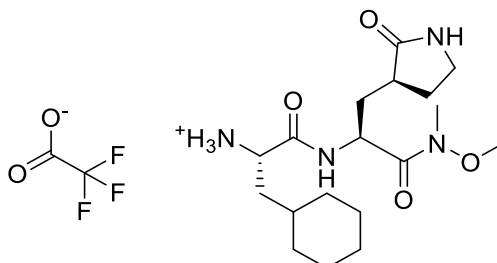
In this reaction the intermediate **10f** was used as the starting material. Yield = 93%. Consistency = white poder. ^{1}H NMR (500 MHz, MeOD) δ = 0.94-1.05 (m, 2H), 1.15-1.26 (m, 1H), 1.26-1.38 (m, 2H), 1.40-1.49 (m, 2H), 1.59-1.89 (m, 8H), 2.03-2.12 (m, 1H), 2.35-2.43 (m, 1H), 2.46-2.55 (m, 1H), 3.21 (s, 3H), 3.32-3.40 (m, 2H), 3.84 (s, 3H), 3.92 (t, *J* = 7.1, 1H), 4.96 (d, *J* = 10.6 Hz, 1H).

General Procedure to Obtain Intermediates 15a-f/17a-f

In a round bottom flask (A), the appropriate commercially available 2-,3- or 4-F-benzoic acid **12-14** (1.5 eq.) was dissolved in a mixture of DCM and DMF (10 mL/mmol, 1:1) and cooled down up to 0°C with an ice bath. TBTU (1.5 eq.) and NMM (2 eq.) were added, and the reaction was kept in vigorously stirring for 30 min. Meanwhile, the appropriate trifluoroacetate salt **11a-f** (1 eq.) was dissolved in DCM/DMF (10 mL/mmol, 1:1) and NMM (2eq.) was added at 0°C. The pH was checked (>8) and the resulting solution was added dropwise to the flask A. After

that, the reaction was left in stirring at rt on. Subsequently, a few mL of distilled water were added and solvents were removed *in vacuo*. The residue was dissolved in EtOAc and washed with 1 M HCl (x 2), NaHCO₃ saturated solution (x 2), and brine (x 2), dried over Na₂SO₄, and concentrated *in vacuo*. The obtained crude was purified using the appropriate eluent mixture below described.

2-Fluoro-N-((S)-1-(((S)-1-(methoxy(methyl)amino)-1-oxo-3-((S)-2-oxopyrrolidin-3-yl)propan-2-yl)amino)-1-oxopentan-2-yl)benzamide (15a)
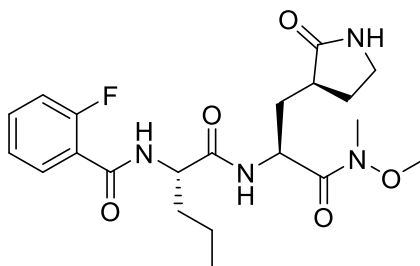
In this reaction 2-F-benzoic acid **12** and trifluoroacetate **11a** were used as the acid and amine, respectively. Yield = 82%; R_f and eluent mixture = 0.14 in EtOAc/MeOH 19:1; Consistency = white powder; ¹H NMR (500 MHz, CDCl₃) δ = 0.92 (t, J = 7.7 Hz, 3H), 1.35-1.50 (m, 2H), 1.65-1.85 (m, 3H), 1.85-1.96 (m, 1H), 2.11-2.23 (m, 1H), 2.32-2.43 (m, 1H), 2.43-2.55 (m, 1H), 3.19 (s, 3H), 3.24-3.35 (m, 2H), 3.79 (s, 3H), 4.70-4.82 (m, 1H), 4.85-4.96 (m, 1H), 6.87 (bs, 1H), 7.03-7.14 (m, 1H), 7.16-7.25 (m, 1H), 7.29-7.38 (m, 1H), 7.39-7.48 (m, 1H), 7.81 (d, J = 7.5 Hz, 1H), 7.95-8.06 (m, 1H). ¹³C NMR (126 MHz, CDCl₃) δ = 13.58, 18.49, 27.96, 32.17, 32.90, 35.06, 38.29, 40.49, 48.66, 53.49, 61.63, 116.36 (d, J = 24.2 Hz), 121.90 (d, J = 3.3 Hz), 125.00 (d, J = 3.2 Hz), 132.25 (d, J = 1.7 Hz), 133.71 (d, J = 8.5 Hz), 161.22 (d, J = 247.0 Hz), 163.63 (d, J = 3.4 Hz), 172.76, 178.53, 180.91.

2-Fluoro-N-((S)-1-(((S)-1-(methoxy(methyl)amino)-1-oxo-3-((S)-2-oxopyrrolidin-3-yl)propan-2-yl)amino)-4-methyl-1-oxopentan-2-yl)benzamide (15b)
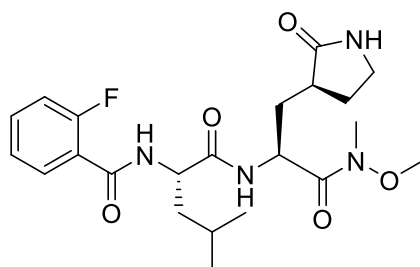
In this reaction 2-F-benzoic acid **12** and trifluoroacetate **11b** were used as the acid and amine, respectively. Yield = 75%; R_f and eluent mixture = 0.22 in EtOAc/MeOH 19:1; Consistency = white powder; ¹H NMR (500 MHz, CDCl₃) δ = 0.94 (d, J = 3.2, 3H), 0.95 (d, J = 2.9, 3H), 1.58-1.84 (m, 5H), 2.10-2.24 (m, 1H), 2.32-2.51 (m, 2H), 3.18 (s, 3H), 3.23-3.33 (m, 2H), 3.78 (s, 3H), 4.77-4.85 (m, 1H), 4.85-4.94 (m, 1H), 6.72 (bs, 1H), 7.08 (dd, J = 11.9, 8.2 Hz, 1H), 7.16-7.25 (m, 2H), 7.38-7.47 (m, 1H), 7.77 (d, J = 7.6 Hz, 1H), 7.96-8.04 (m, 1H). ¹³C NMR (126 MHz, CDCl₃) δ = 21.82, 22.83, 24.64, 28.06, 32.19, 32.88, 38.23, 40.37, 42.03, 48.69, 52.14, 61.58, 116.38 (d, J = 24.4 Hz), 121.35 (d, J = 0.8 Hz), 125.02 (d, J = 3.1 Hz), 132.29 (d,

J = 1.7 Hz), 133.76 (d, J = 9.2 Hz), 161.20 (d, J = 248.3 Hz), 163.67 (d, J = 3.2 Hz), 173.06, 176.93, 180.58.

N-((S)-3-Cyclopropyl-1-(((S)-1-(methoxy(methyl)amino)-1-oxo-3-((S)-2-oxopyrrolidin-3-yl)propan-2-yl)amino)-1-oxopropan-2-yl)-2-fluorobenzamide (15c)
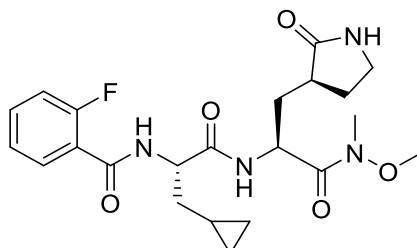
In this reaction 2-F-benzoic acid **12** and trifluoroacetate **11c** were used as the acid and amine, respectively. Yield = 70%; R_f and eluent mixture = 0.23 in EtOAc/MeOH 19:1; Consistency = white powder; ^{1}H NMR (500 MHz, CDCl$_3$) δ = 0.05-0.15 (m, 2H), 0.39-0.50 (m, 2H), 0.74-0.86 (m, 1H), 1.64-1.87 (m, 4H), 2.14 (ddd, J = 14.0, 10.8, 4.3 Hz, 1H), 2.33-2.51 (m, 2H), 3.17 (s, 3H), 3.22-3.34 (m, 2H), 3.78 (s, 3H), 4.76-4.86 (m, 1H), 4.90 (ddd, J = 11.0, 7.7, 3.5 Hz, 1H), 6.72 (bs, 1H), 7.08 (ddd, J = 11.9, 8.3, 1.1 Hz, 1H), 7.20 (td, J = 7.5, 1.1 Hz, 1H), 7.38-7.46 (m, 1H), 7.51 (dd, J = 11.7, 7.5 Hz, 1H), 7.85 (d, J = 7.7 Hz, 1H), 8.00 (td, J = 7.8, 1.9 Hz, 1H). ^{13}C NMR (126 MHz, CDCl$_3$) δ = 3.90, 4.12, 6.86, 27.98, 32.09, 32.97, 37.61, 38.18, 40.32, 48.58, 54.10, 61.59, 116.36 (d, J = 24.4 Hz), 121.34 (d, J = 11.6 Hz), 124.97 (d, J = 3.3 Hz), 132.17 (d, J = 2.2 Hz), 133.69 (d, J = 9.3 Hz), 161.21 (d, J = 248.4 Hz), 163.46 (d, J = 2.9 Hz), 172.49, 180.21, 180.55.

2-Fluoro-N-((S)-1-(((S)-1-(methoxy(methyl)amino)-1-oxo-3-((S)-2-oxopyrrolidin-3-yl)propan-2-yl)amino)-4,4-dimethyl-1-oxopentan-2-yl)benzamide (15d)
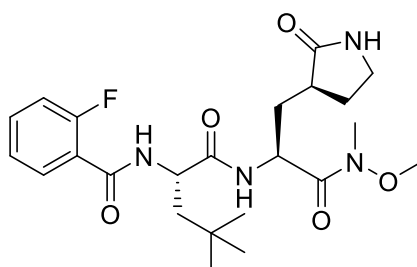
In this reaction 2-F-benzoic acid **11** and trifluoroacetate **11d** were used as the acid and amine, respectively. Yield = 68%; R_f and eluent mixture = 0.17 in EtOAc/MeOH 19:1; Consistency = white powder; ^{1}H NMR (500 MHz, CDCl$_3$) δ = 0.95 (s, 9H), 1.59 (dd, J = 14.6, 9.3 Hz, 1H), 1.62-1.78 (m, 2H), 1.90 (dd, J = 14.6, 3.2 Hz, 1H), 2.14 (ddd, J = 14.5, 10.7, 4.1 Hz, 1H), 2.28-2.47 (m, 2H), 3.15 (s, 3H), 3.18-3.29 (m, 2H), 3.75 (s, 3H), 4.75-4.89 (m, 2H), 6.92 (bs, 1H), 7.07 (ddd, J = 12.0, 8.3, 1.1 Hz, 1H), 7.11-7.22 (m, 2H), 7.36-7.46 (m, 1H), 7.75 (d, J = 7.6 Hz, 1H), 7.98 (td, J = 7.8, 1.9 Hz, 1H). ^{13}C NMR (126 MHz, CDCl$_3$) δ = 27.94, 29.50, 30.48, 32.07, 32.84, 38.14, 40.30, 46.13, 48.52, 51.34, 61.52, 116.36 (d, J = 24.7 Hz), 121.20 (d, J = 11.4

Hz), 125.00 (d, J = 3.2 Hz), 132.23 (d, J = 1.9 Hz), 133.77 (d, J = 9.2 Hz), 161.16 (d, J = 248.1 Hz), 163.47 (d, J = 3.0 Hz), 173.48, 178.61, 180.49.

2-Fluoro-N-((S)-1-(((S)-1-(methoxy(methyl)amino)-1-oxo-3-((S)-2-oxopyrrolidin-3-yl)propan-2-yl)amino)-1-oxohexan-2-yl)benzamide (15e)
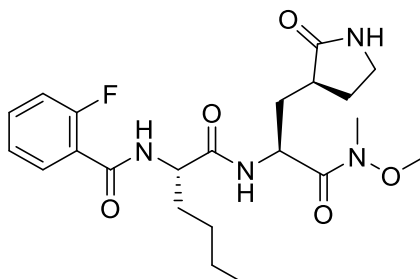
In this reaction 2-F-benzoic acid **12** and trifluoroacetate **11e** were used as the acid and amine, respectively. Yield = 65%; R_f and eluent mixture = 0.21 in EtOAc/MeOH 19:1; Consistency = white powder; ^{1}H NMR (500 MHz, CDCl$_3$) δ = 0.85 (t, J = 7.1 Hz, 3H), 1.28-1.41 (m, 4H), 1.67-1.83 (m, 3H), 1.88-2.00 (m, 1H), 2.16 (ddd, J = 13.9, 10.7, 4.4 Hz, 1H), 2.33-2.50 (m, 2H), 3.18 (s, 3H), 3.23-3.33 (m, 2H), 3.79 (s, 3H), 4.71-4.80 (m, 1H), 4.89 (ddd, J = 10.9, 7.5, 3.5 Hz, 1H), 6.74 (bs, 1H), 7.08 (ddd, J = 11.9, 8.3, 1.1 Hz, 1H), 7.20 (td, J = 7.6, 1.1 Hz, 1H), 7.34 (dd, J = 11.6, 7.8 Hz, 1H), 7.39-7.47 (m, 1H), 7.78 (d, J = 7.6 Hz, 1H), 8.00 (td, J = 7.8, 1.9 Hz, 1H). ^{13}C NMR (126 MHz, CDCl$_3$) δ = 13.65, 22.18, 27.26, 28.04, 32.15, 32.88, 38.23, 38.48, 40.36, 48.67, 53.59, 61.59, 116.37 (d, J = 24.5 Hz), 121.41 (d, J = 11.5 Hz), 124.99 (d, J = 3.2 Hz), 132.23 (d, J = 2.3 Hz), 133.68 (d, J = 9.4 Hz), 161.19 (d, J = 248.4 Hz), 163.57 (d, J = 3.3 Hz), 172.69, 178.67, 180.60.

N-((S)-3-Cyclohexyl-1-(((S)-1-(methoxy(methyl)amino)-1-oxo-3-((S)-2-oxopyrrolidin-3-yl)propan-2-yl)amino)-1-oxopropan-2-yl)-2-fluorobenzamide (15f)
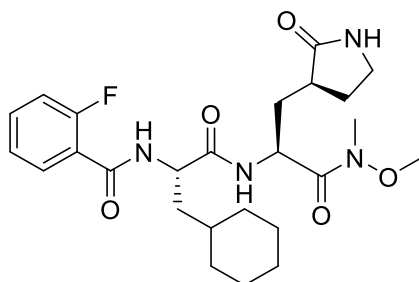
In this reaction 2-F-benzoic acid **12** and trifluoroacetate **11f** were used as the acid and amine, respectively. Yield = 70%; R_f and eluent mixture = 0.21 in EtOAc/MeOH 19:1; Consistency = white powder; ^{1}H NMR (500 MHz, CDCl$_3$) δ = 0.83-1.01 (m, 2H), 1.03-1.26 (m, 3H), 1.33-1.44 (m, 1H), 1.55-1.80 (m, 8H), 1.80-1.88 (m, 1H), 2.15 (ddd, J = 14.6, 10.6, 4.2 Hz, 1H), 2.31-2.48 (m, 2H), 3.17 (s, 3H), 3.22-3.32 (m, 2H), 3.77 (s, 3H), 4.76-4.85 (m, 1H), 4.89 (ddd, J = 11.0, 7.6, 3.5 Hz, 1H), 6.73 (bs, 1H), 7.09 (ddd, J = 11.9, 8.3, 1.1 Hz, 1H), 7.13-7.24 (m, 2H), 7.38-7.48 (m, 1H), 7.69 (d, J = 7.7 Hz, 1H), 7.99 (td, J = 7.8, 1.9 Hz, 1H). ^{13}C NMR (126 MHz, CDCl$_3$) δ = 25.86, 26.01, 26.21, 28.02, 32.09, 32.37, 32.94, 33.56, 38.15, 40.32, 48.54,

51.54, 61.57, 116.37 (d, J = 24.7 Hz), 121.36 (d, J = 11.5 Hz), 125.00 (d, J = 3.3 Hz), 132.25 (d, J = 2.3 Hz), 133.71 (d, J = 9.4 Hz), 161.17 (d, J = 248.4 Hz), 163.68 (d, J = 3.1 Hz), 173.13, 180.41, 180.54.

3-Fluoro-N-((S)-1-(((S)-1-(methoxy(methyl)amino)-1-oxo-3-((S)-2-oxopyrrolidin-3-yl)propan-2-yl)amino)-1-oxopentan-2-yl)benzamide (16a)
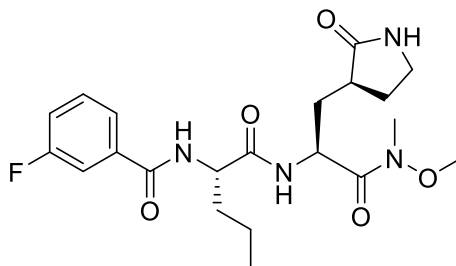
In this reaction 3-F-benzoic **13** acid and trifluoroacetate **11a** were used as the acid and amine, respectively. Yield = 73%; R_f and eluent mixture = 0.15 in EtOAc/MeOH 19:1; Consistency = white powder; ¹H NMR (500 MHz, CDCl₃) δ = 0.90 (t, J = 7.3, 3H), 1.35-1.48 (m, 2H), 1.65-1.83 (m, 3H), 1.85-1.93 (m, 1H), 2.16 (ddd, J = 15.0, 10.9, 4.6 Hz, 1H), 2.30-2.40 (m, 1H), 2.40-2.50 (m, 1H), 3.19 (s, 3H), 3.23-3.35 (m, 2H), 3.80 (s, 3H), 4.75 (q, J = 5.2 Hz, 1H), 4.87 (ddd, J = 11.0, 7.4, 3.5 Hz, 1H), 6.87 (bs, 1H), 7.09-7.18 (m, 1H), 7.29-7.38 (m, 2H), 7.47-7.55 (m, 1H), 7.57 (dd, J = 7.7, 1.3 Hz, 1H), 8.09 (d, J = 7.3 Hz, 1H); ¹³C NMR (126 MHz, CDCl₃) δ = 13.58, 18.57, 28.05, 32.13, 32.72, 35.14, 38.37, 40.45, 48.87, 53.41, 61.58, 114.86 (d, J = 22.9 Hz), 118.80 (d, J = 21.3 Hz), 123.06 (d, J = 2.9 Hz), 130.47 (d, J = 8.0 Hz), 136.80 (d, J = 6.6 Hz), 162.24, 165.28 (d, J = 267.9 Hz), 173.12, 180.15, 180.72.

3-Fluoro-N-((S)-1-(((S)-1-(methoxy(methyl)amino)-1-oxo-3-((S)-2-oxopyrrolidin-3-yl)propan-2-yl)amino)-4-methyl-1-oxopentan-2-yl)benzamide (16b)
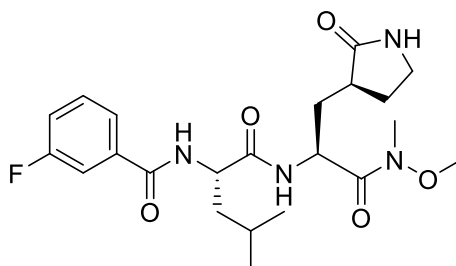
In this reaction 3-F-benzoic acid **13** and trifluoroacetate **11b** were used as the acid and amine, respectively. Yield = 66%; R_f and eluent mixture = 0.23 in EtOAc/MeOH, 19:1; Consistency = White powder; ¹H NMR (500 MHz, CDCl₃) δ = 0.93 (d, J = 5.5 Hz, 3H), 0.95 (d, J = 5.7 Hz, 3H), 1.60-1.85 (m, 6H), 2.16 (ddd, J = 15.0, 10.5, 4.6 Hz, 1H), 2.32-2.50 (m, 1H) 3.19 (s, 3H), 3.24-3.36 (m, 2H), 3.80 (s, 3H), 4.76-4.83 (m, 1H), 4.87 (ddd, J = 10.9, 7.2, 3.4 Hz, 1H), 6.69 (bs, 1H), 7.15 (td, J = 8.3, 2.6 Hz, 1H), 7.22 (d, J = 8.4 Hz, 1H), 7.31-7.39 (m, 1H), 7.50-7.55 (m, 1H), 7.57 (dd, J = 7.6, 1.4 Hz, 1H), 8.01 (d, J = 7.5 Hz, 1H). ¹³C NMR (126 MHz, CDCl₃) δ = 21.81, 22.88, 24.72, 28.10, 32.16, 32.75, 38.31, 40.43, 42.05, 48.86, 52.16, 61.60, 114.90

(d, *J* = 23.0 Hz), 118.86 (d, *J* = 21.0 Hz), 123.08 (d, *J* = 2.9 Hz), 130.51 (d, *J* = 8.0 Hz), 136.76 (d, *J* = 6.8 Hz), 163.26 (d, *J* = 247.1 Hz), 166.45 (d, *J* = 2.6 Hz), 173.51, 180.09, 180.65.

N-((S)-3-Cyclopropyl-1-(((S)-1-(methoxy(methyl)amino)-1-oxo-3-((S)-2-oxopyrrolidin-3-yl)propan-2-yl)amino)-1-oxopropan-2-yl)-3-fluorobenzamide (16c)
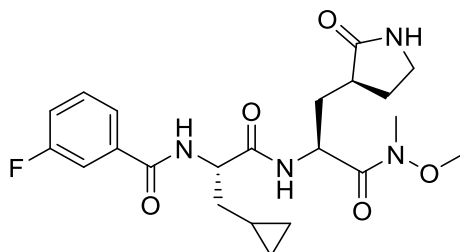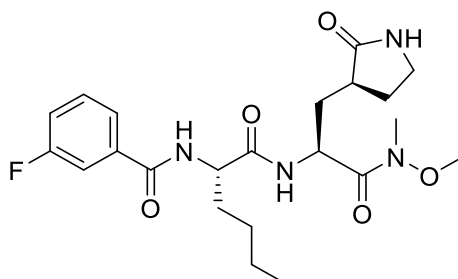

In this reaction 3-F-benzoic acid **13** and trifluoroacetate **11c** were used as the acid and amine, respectively. Yield = 74%; R_f and eluent mixture = 0.19 in EtOAc/MeOH 19:1; Consistency = white powder; ^{1}H NMR (500 MHz, CDCl₃) δ = 0.01-0.10 (m, 2H), 0.32-0.438 (m, 2H), 0.69-0.81 (m, 1H), 1.58-1.79 (m, 4H), 2.06-2.16 (m, 1H), 2.26-2.36 (m, 1H), 2.37-2.47 (m, 1H), 3.14 (s, 3H), 3.17-3.30 (m, 2H), 3.74 (s, 3H), 4.77 (q, *J* = 6.0 Hz, 1H), 4.86 (ddd, *J* = 11.0, 7.6, 3.5 Hz, 1H), 7.05 (s, 1H), 7.09 (tdd, *J* = 8.3, 2.6, 1.0 Hz, 1H), 7.29 (td, *J* = 8.0, 5.6 Hz, 1H), 7.46-7.51 (m, 1H), 7.51-7.55 (dt, *J* = 7.7, 1.3 Hz, 1H), 7.57 (d, *J* = 8.0 Hz, 1H), 8.11 (d, *J* = 7.6 Hz, 1H). ^{13}C NMR (126 MHz, CDCl₃) δ = 3.93, 3.95, 6.97, 27.76, 31.99, 32.78, 37.51, 38.17, 40.29, 48.48, 54.01, 61.44, 114.68 (d, *J* = 22.9 Hz), 118.61 (d, *J* = 21.3 Hz), 122.97 (d, *J* = 3.1 Hz), 130.34 (d, *J* = 7.7 Hz), 136.72 (d, *J* = 6.9 Hz), 163.06 (d, *J* = 247.0 Hz), 166.19 (d, *J* = 2.8 Hz), 172.34, 172.93, 180.55.

3-Fluoro-N-((S)-1-(((S)-1-(methoxy(methyl)amino)-1-oxo-3-((S)-2-oxopyrrolidin-3-yl)propan-2-yl)amino)-4,4-dimethyl-1-oxopentan-2-yl)benzamide (16d)
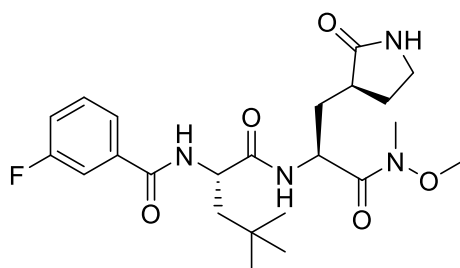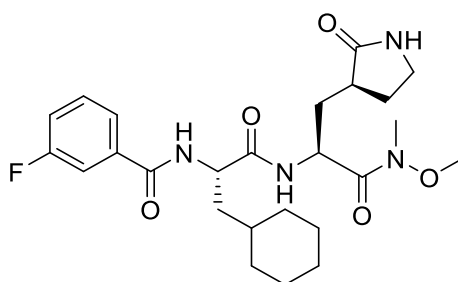

In this reaction 3-F-benzoic acid **13** and trifluoroacetate **11d** were used as the acid and amine, respectively. Yield = 68%; R_f and eluent mixture = 0.22 in EtOAc/MeOH 19:1; Consistency = white powder; ^{1}H NMR (500 MHz, CDCl₃) δ = 0.98 (s, 9H), 1.60-1.84 (m, 3H), 1.91 (dd, *J* = 14.6, 3.0 Hz, 1H), 2.11-2.20 (m, 1H), 2.33-2.50 (m, 2H), 3.19 (s, 3H), 3.24-3.34 (m, 2H), 3.79 (s, 3H), 4.74-4.82 (m, 1H), 4.82-4.90 (m, 1H), 6.45 (bs, 1H), 7.10-7.20 (m, 2H), 7.30-7.39 (m, 1H), 7.48-7.57 (m, 2H), 7.83 (d, *J* = 7.4 Hz, 1H). ^{13}C NMR (126 MHz, CDCl₃) δ = 28.21, 29.59, 30.58, 32.16, 32.73, 38.21, 40.36, 46.06, 48.88, 51.48, 61.60, 114.86 (d, *J* = 22.9 Hz), 118.87 (d, *J* = 21.5 Hz), 123.01 (d, *J* = 2.9 Hz), 130.55 (d, *J* = 8.2 Hz), 136.86 (d, *J* = 10.3 Hz), 163.28 (d, *J* = 247.0 Hz), 166.20 (d, *J* = 2.2 Hz), 173.83, 179.73, 180.45.

3-Fluoro-N-((S)-1-(((S)-1-(methoxy(methyl)amino)-1-oxo-3-((S)-2-oxopyrrolidin-3-yl)propan-2-yl)amino)-1-oxohexan-2-yl)benzamide (16e)

In this reaction 3-F-benzoic acid **13** and trifluoroacetate **11e** were used as the acid and amine, respectively. Yield = 67%; R_f and eluent mixture = 0.23 in EtOAc/MeOH, 19:1; Consistency = white powder; ^{1}H NMR (500 MHz, CDCl$_3$) δ = 0.85 (t, J = 7.1 Hz, 3H), 1.25-1.45 (m, 4H), 1.68-1.85 (m, 3H), 1.88-1.99 (m, 1H), 2.10-2.22 (m, 1H), 2.34-2.49 (m, 2H), 3.20 (s, 3H), 3.24-3.36 (m, 2H), 3.81 (s, 3H), 4.73 (td, J = 7.9, 5.3 Hz, 1H), 4.87 (ddd, J = 10.9, 7.3, 3.6 Hz, 1H), 6.62 (bs, 1H), 7.15 (tdd, J = 8.2, 2.6, 0.9 Hz, 1H), 7.22 (d, J = 8.0 Hz, 1H), 7.32-7.40 (m, 1H), 7.50-7.56 (m, 1H), 7.58 (d, J = 7.8, 1H), 7.99 (d, J = 7.4 Hz, 1H). ^{13}C NMR (126 MHz, CDCl$_3$) δ = 13.70, 22.23, 27.36, 28.23, 32.21, 32.78, 38.52, 38.37, 40.41, 48.98, 53.56, 61.60, 114.89 (d, J = 22.9 Hz), 118.84 (d, J = 21.1 Hz), 123.03 (d, J = 2.9 Hz), 130.51 (d, J = 7.8 Hz), 136.89 (d, J = 6.9 Hz), 163.28 (d, J = 247.5 Hz), 166.33 (d, J = 2.4 Hz), 172.96, 178.70, 180.58.

N-((S)-3-Cyclohexyl-1-(((S)-1-(methoxy(methyl)amino)-1-oxo-3-((S)-2-oxopyrrolidin-3-yl)propan-2-yl)amino)-1-oxopropan-2-yl)-3-fluorobenzamide (16f)

In this reaction 3-F-benzoic acid **13** and trifluoroacetate **11f** were used as the acid and amine, respectively. Yield = 64%; R_f and eluent mixture = 0.23 in EtOAc/MeOH, 19:1; Consistency = white powder; ^{1}H NMR (500 MHz, CDCl$_3$) δ = 0.82-1.01 (m, 2H), 1.03-1.27 (m, 3H), 1.32-1-43 (m, 1H)1.54-1.81 (m, 8H), 1.85 (d, J = 12.8 Hz, 1H), 2.14 (ddd, J = 14.7, 10.7, 4.5 Hz, 1H), 2.31-2.49 (m, 2H), 3.19 (s, 3H), 3.22-3.34 (m, 2H), 3.80 (s, 3H), 4.77 (td, J = 8.9, 4.9 Hz, 1H), 4.89 (ddd, J = 11.1, 7.6, 3.6 Hz, 1H), 6.70 (bs, 1H), 7.11-7.18 (m, 1H), 7.23-7.28 (m, 1H), 7.31-7.395 (m, 1H), 7.49-7.54 (m, 1H), 7.54-7.59 (m, 1H), 7.90 (d, J = 7.5 Hz, 1H); ^{13}C NMR (126 MHz, CDCl$_3$) δ = 25.92, 26.07, 26.25, 28.11, 32.14, 32.37, 32.76, 33.61, 38.25, 40.41, 48.75, 51.60, 61.61, 114.91 (d, J = 22.9 Hz), 118.81 (d, J = 21.5 Hz), 123.08 (d, J = 2.9 Hz), 130.48 (d, J = 7.8 Hz), 136.85 (d, J = 7.4 Hz), 163.25 (d, J = 247.4 Hz), 166.44 (d, J = 2.5 Hz) , 173.56, 178.52, 180.64.

4-Fluoro-N-((S)-1-(((S)-1-(methoxy(methyl)amino)-1-oxo-3-((S)-2-oxopyrrolidin-3-yl)propan-2-yl)amino)-1-oxopentan-2-yl)benzamide (17a)
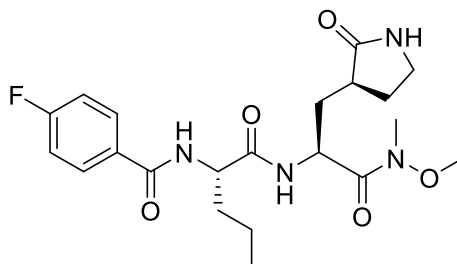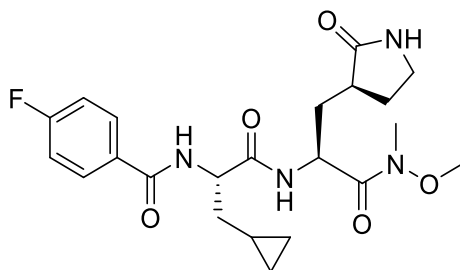

In this reaction 4-F-benzoic acid **14** and trifluoroacetate **11a** were used as the acid and amine, respectively. Yield = 71%; R_f and eluent mixture = 0.18 in EtOAc/MeOH 19:1; Consistency = white powder; ^{1}H NMR (500 MHz, CDCl$_3$) δ = 0.90 (t, J = 7.3 Hz, 3H), 1.35-1.47 (m, 2H), 1.64-1.83 (m, 3H), 1.83-1.94 (m, 1H), 2.15 (ddd, J = 20.0, 13.7, 6.8 Hz, 1H), 2.30-2.40 (m, 1H), 2.40-2.50 (m, 1H), 3.19 (s, 3H), 3.23-3.35 (m, 2H), 3.80 (s, 3H), 4.70-4.80 (m, 1H), 4.82-4.91 (m, 1H), 6.92 (bs, 1H), 7.05 (t, J = 8.4 Hz, 2H), 7.22-7.31 (m, 1H), 7.80-7.87 (m, 2H), 8.11 (d, J = 7.4 Hz, 1H). ^{13}C NMR (126 MHz, CDCl$_3$) δ = 13.57, 18.56, 27.99, 32.16, 32.73, 35.17, 38.35, 40.43, 48.80, 53.34, 61.56, 115.72 (d, J = 21.8 Hz), 129.96 (d, J = 8.8 Hz), 130.65 (d, J = 3.1 Hz), 165.31 (d, J = 251.8 Hz), 166.64, 173.25, 180.30, 180.70.

4-Fluoro-N-((S)-1-(((S)-1-(methoxy(methyl)amino)-1-oxo-3-((S)-2-oxopyrrolidin-3-yl)propan-2-yl)amino)-4-methyl-1-oxopentan-2-yl)benzamide (17b)
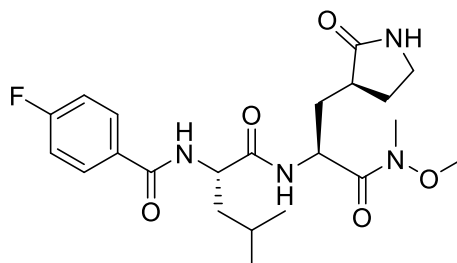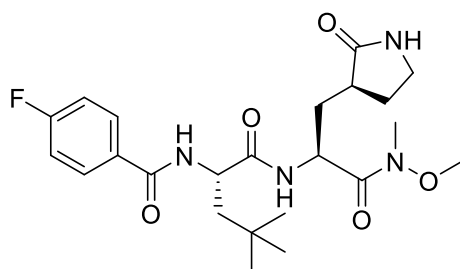

In this reaction 4-F-benzoic acid **14** and trifluoroacetate **11b** were used as the acid and amine, respectively. Yield = 69%; R_f and eluent mixture = 0.23 in EtOAc/MeOH 19:1; Consistency = white powder; ^{1}H NMR (500 MHz, CDCl$_3$) δ = 0.93 (d, J = 5.6 Hz, 3H), 0.95 (d, J = 5.7 Hz, 3H), 1.59-1.83 (m, 5H), 2.16 (ddd, J = 14.9, 10.9, 4.5 Hz, 1H), 2.32-2.40 (m, 1H), 2.40-2.48 (m, 1H), 3.19 (s, 3H), 3.22-3.35 (m, 2H), 3.79 (s, 3H), 4.77-4.89 (m, 2H), 6.75 (bs, 1H), 7.05 (t, J = 8.4 Hz, 2H), 7.11 (d, J = 8.4 Hz, 1H), 7.82 (dd, J = 8.4, 5.3 Hz, 2H), 7.98 (d, J = 7.4 Hz, 1H); ^{13}C NMR (126 MHz, CDCl$_3$) δ = 21.84, 22.87, 24.70, 28.11, 32.17, 32.77, 38.32, 40.39, 42.18, 48.86, 52.05, 61.57, 115.77 (d, J = 21.9 Hz), 129.97 (d, J = 9.0 Hz), 130.84 (d, J = 3.2 Hz), 165.36 (d, J = 251.9 Hz), 166.65, 173.57, 179.11, 180.52.

N-((S)-3-Cyclopropyl-1-(((S)-1-(methoxy(methyl)amino)-1-oxo-3-((S)-2-oxopyrrolidin-3-yl)propan-2-yl)amino)-1-oxopropan-2-yl)-4-fluorobenzamide (17c)
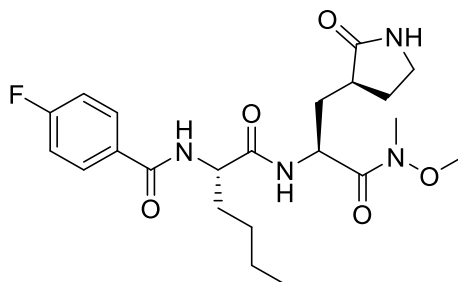
In this reaction 4-F-benzoic acid **14** and trifluoroacetate **11c** were used as the acid and amine, respectively. Yield = 66%; R_f and eluent mixture = 0.20 in EtOAc/MeOH 19:1; Consistency = white powder; ^{1}H NMR (500 MHz, CDCl₃) δ = 0.02-0.13 (m, 2H), 0.37-0.48 (m, 2H), 0.74-0.87 (m, 1H), 1.65-1.74 (m, 2H), 1.74-1.83 (m, 2H), 2.15 (ddd, J = 14.1, 10.8, 4.6 Hz, 1H), 2.32-2.40 (m, 1H), 2.40-2.50 (m, 1H), 3.18 (s, 3H), 3.22-3.33 (m, 2H), 3.79 (s, 3H), 4.77-4.85 (m, 1H), 4.89 (ddd, J = 11.0, 7.4, 3.6 Hz, 1H), 6.87 (bs, 1H), 7.01-7.09 (m, 2H), 7.29 (d, J = 7.9 Hz, 1H), 7.78-7.86 (m, 2H), 8.03 (d, J = 7.5 Hz, 1H). ^{13}C NMR (126 MHz, CDCl₃) δ = 3.95, 4.20, 6.98, 28.08, 32.13, 32.89, 37.79, 38.34, 40.39, 48.78, 53.97, 61.57, 115.74 (d, J = 21.9 Hz), 129.89 (d, J = 9.0 Hz), 130.75 (d, J = 3.2 Hz), 165.29 (d, J = 251.3 Hz), 166.40, 172.35, 172.86, 180.59.

4-Fluoro-N-((S)-1-(((S)-1-(methoxy(methyl)amino)-1-oxo-3-((S)-2-oxopyrrolidin-3-yl)propan-2-yl)amino)-4,4-dimethyl-1-oxopentan-2-yl)benzamide (17d)
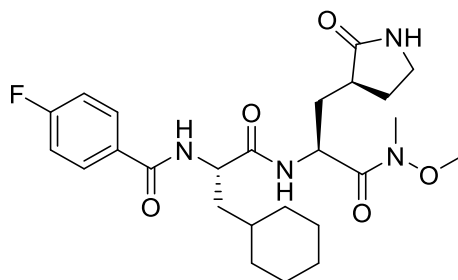

In this reaction 4-F-benzoic acid **14** and trifluoroacetate **11d** were used as the acid and amine, respectively. Yield = 71%; R_f and eluent mixture = 0.24 in EtOAc/MeOH 19:1; Consistency = white powder; ^{1}H NMR (500 MHz, CDCl₃) δ = 1.03 (s, 9H), 1.60-1.68 (m, 1H), 1.75-1.86 (m, 2H), 1.94-2.07 (m, 2H), 2.35-2.46 (m, 2H), 3.19 (s, 3H), 3.22-3.35 (m, 2H), 3.86 (s, 3H), 4.83 (ddd, J = 9.7, 8.5, 2.9 Hz, 1H), 4.97 (ddd, J = 11.3, 7.9, 3.6 Hz, 1H), 6.83 (bs, 1H), 7.22-7.31 (m, 2H), 7.86 (d, J = 7.5 Hz, 1H), 7.92 (d, J = 8.6 Hz, 1H), 8.02-8.08 (m, 2H). ^{13}C NMR (126 MHz, CDCl₃) δ = 29.59, 29.63, 30.59, 32.17, 32.85, 38.23, 40.32, 46.30, 48.86, 51.32, 62.70, 115.89 (d, J = 17.1 Hz), 129.94 (d, J = 8.9 Hz), 130.74 (d, J = 3.2 Hz), 165.41 (d, J = 252.1 Hz), 166.44, 172.29, 173.84, 180.35.

4-Fluoro-N-((S)-1-(((S)-1-(methoxy(methyl)amino)-1-oxo-3-((S)-2-oxopyrrolidin-3-yl)propan-2-yl)amino)-1-oxohexan-2-yl)benzamide (17e)

In this reaction 4-F-benzoic acid **14** and trifluoroacetate **11e** were used as the acid and amine, respectively. Yield = 67%; R_f and eluent mixture = 0.23 in EtOAc/MeOH 19:1; Consistency = white powder; ^{1}H NMR (500 MHz, CDCl$_3$) δ = 0.86 (t, J = 6.8 Hz, 3H), 1.27-1.40 (m, 4H), 1.69-1.85 (m, 3H), 1.88-1.99 (m, 1H), 2.17 (ddt, J = 15.0, 10.7, 4.7 Hz, 1H), 2.33-2.50 (m, 2H), 3.20 (s, 3H), 3.25-3.36 (m, 2H), 3.81 (s, 3H), 4.70-4.77 (m, 1H), 4.88 (ddd, J = 10.9, 7.3, 3.6 Hz, 1H), 6.74 (bs, 1H), 7.07 (t, J = 8.6, Hz, 2H), 7.17 (d, J = 8.0 Hz, 1H), 7.80-7.87 (m, 2H), 7.98 (d, J = 7.4 Hz, 1H). ^{13}C NMR (126 MHz, CDCl$_3$) δ = 13.70, 22.23, 27.37, 28.15, 32.14, 32.75, 38.51, 38.37, 40.43, 48.90, 53.49, 61.59, 115.78 (d, J = 21.7 Hz), 129.96 (d, J = 8.9 Hz), 130.72 (d, J = 3.0 Hz), 165.36 (d, J = 252.1 Hz), 166.61, 173.15, 175.30, 180.68.

N-((S)-3-Cyclohexyl-1-(((S)-1-(methoxy(methyl)amino)-1-oxo-3-((S)-2-oxopyrrolidin-3-yl)propan-2-yl)amino)-1-oxopropan-2-yl)-4-fluorobenzamide (17f)


In this reaction 4-F-benzoic acid **14** and trifluoroacetate **11f** were used as the acid and amine, respectively. Yield = 63%; R_f and eluent mixture = 0.25 in EtOAc/MeOH 19:1; Consistency = white powder; ^{1}H NMR (500 MHz, CDCl$_3$) δ = 0.84-1.02 (m, 2H), 1.06-1.27 (m, 4H), 1.32-1.43 (m, 1H), 1.55-1.90 (m, 8H), 2.16 (ddd, J = 14.8, 10.6, 4.5 Hz, 1H), 2.31-2.48 (m, 2H), 3.19 (s, 3H), 3.22-3.33 (m, 2H), 3.80 (s, 3H), 4.80 (td, J = 9.0, 4.9 Hz, 1H), 4.88 (ddd, J = 10.9, 7.4, 3.6 Hz, 1H), 6.74 (bs, 1H), 7.03-7.14 (m, 3H), 7.79 – 7.88 (m, 3H). ^{13}C NMR (126 MHz, CDCl$_3$) δ = 25.91, 26.06, 26.24, 32.14, 32.41, 32.82, 33.61, 34.07, 38.27, 40.41, 48.75, 51.48, 61.59, 115.77 (d, J = 21.6 Hz), 129.98 (d, J = 9.0 Hz), 130.71 (d, J = 3.0 Hz), 165.35 (d, J = 252.2 Hz), 166.67, 173.67, 178.51, 180.64.

General Procedure for the Synthesis of Final Compounds SPR47-SPR64

In a round-bottom flask, the appropriate intermediate **15a-f/17a-f** (1 eq.) was dissolved in dry THF (5 mL/mmol). An ice-bath was installed and the temperature was cooled-down up to -10°C by the addition of salt. A vigorous stirring was set, and LiAlH$_4$ (1 eq.) was added. TLC monitoring (starting material and reaction crude) was performed after 30 min using the same

eluent mixture employed for purification of the starting material in question. Considering the starting material was always detected after the first TLC monitoring, additional equivalents of LiAlH$_4$ (one equivalent at intervals of 30 min) were added until the starting material disappearance. After that, the reaction was quenched with 1M KHSO$_4$ and the ice-bath was removed. The organic phase was extracted with DCM (x 3), washed with 1M HCl (x 1), H$_2$O (x 1), and brine (x 1), dried over Na$_2$SO$_4$ and concentrated *in vacuo*. The obtained aldehyde (as crude, 1 eq.) was solubilized in DCM (10 mL/mmol) at rt, and 1-(triphenylphosphoranylidene)-2-propanone **16** (1.1 eq.) was added. The reaction was kept in stirring at rt for 2 h. After this time, DCM was removed *in vacuo* and the desired final compound was purified using the appropriate eluent mixture (see below).

2-Fluoro-N-((S)-1-oxo-1-(((S,E)-5-oxo-1-((S)-2-oxopyrrolidin-3-yl)hex-3-en-2-yl)amino)pentan-2-yl)benzamide (SPR47)
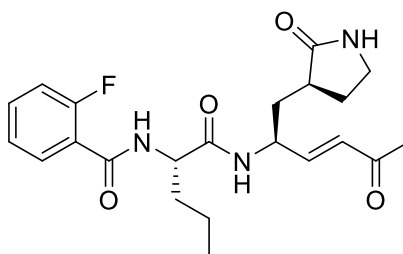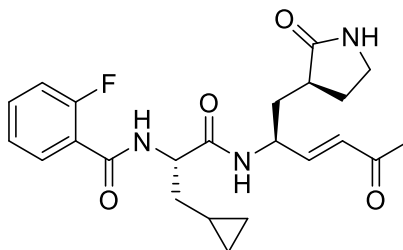

In this reaction the intermediate **15a** was used as the substrate. Yield = 29%; R_f and eluent mixture = 0.35 in EtOAc/ACN 3:2; Consistency = white powder. ^{1}H NMR in CDCl$_3$ (500 MHz), δ = 0.97 (t, J = 7.4 Hz, 3H), 1.40-1.50 (m, 2H), 1.63-1.68 (m, 1H), 1.74-1.84 (m, 2H), 1.90-1.99 (m, 1H), 2.03-2.13 (m, 1H), 2.25 (s, 3H), 2.35-2.42 (m, 1H), 2.43-2.51 (m, 1H), 3.29-3-37 (m, 2H), 4.54-4.62 (m, 1H), 4.78-4.85 (m, 1H), 6.20 (s, 1H), 6.20 (dd, J = 15.9, 1.1 Hz, 2H), 6.68 (dd, J = 16.0, 5.5 Hz, 1H), 7.12 (dd, J = 11.9, 8.2 Hz, 1H), 7.24 (t, J = 7.6 Hz, 1H), 7.36 (dd, J = 11.9, 7.7 Hz, 1H), 7.44-7.50 (m, 1H), 8.01 (td, J = 7.8, 1.7 Hz, 1H), 8.12 (d, J = 6.8 Hz, 1H). ^{13}C NMR in CDCl$_3$ (126 MHz), δ = 13.96, 18.98, 27.67, 28.87, 35.01, 35.51, 38.64, 40.69, 49.79, 53.72, 116.32 (d, J = 24.6 Hz), 121.03 (d, J = 11.4 Hz), 124.85 (d, J = 3.4 Hz), 130.01, 131.93 (d, J = 2.4 Hz), 133.63 (d, J = 9.2 Hz), 146.28, 160.87 (d, J = 248.4 Hz), 163.33 (d, J = 2.9 Hz), 172.25, 180.18, 198.33. Elemental analysis for C$_{22}$H$_{28}$FN$_3$O$_4$: calcd. = C, 63.29; H, 6.76; N, 10.07; found = C, 63.11; H, 7.02; N, 10.25.

2-Fluoro-N-((S)-4-methyl-1-oxo-1-(((S,E)-5-oxo-1-((S)-2-oxopyrrolidin-3-yl)hex-3-en-2-yl)amino)pentan-2-yl)benzamide (SPR48)
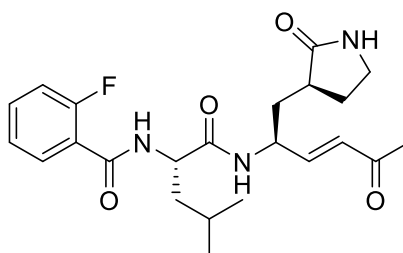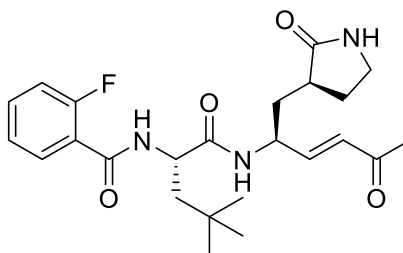
In this reaction the intermediate **15b** was used as the substrate. Yield = 36%; R_f and eluent mixture = 0.29 in EtOAc/ACN 4:1; Consistency = white powder. ^{1}H NMR in CDCl$_3$ (500 MHz), δ = 0.99 (d, J = 5.8 Hz, 6H), 1.59-1.66 (m, 1H), 1.67-1.83 (m, 4H), 2.06-2.14 (m, 1H), 2.25 (s, 3H), 2.31-2.39 (m, 1H), 2.41-2.49 (m, 1H), 3.24-3.39 (m, 2H), 4.53-4.61 (m, 1H), 4.85-4.92 (m, 1H), 6.20 (dd, J = 16.0, 1.3 Hz, 1H), 6.41 (s, 1H), 6.68 (dd, J = 15.9, 5.5 Hz, 1H), 7.08-7.15 (m, 1H), 7.20-7.26 (m, 2H), 7.43-7.50 (m, 1H), 8.00 (td, J = 7.8, 1.8 Hz, 1H), 8.11 (d, J = 7.0 Hz, 1H). ^{13}C NMR in CDCl$_3$ (126 MHz), δ = 22.27, 23.14, 25.13, 27.61, 28.68, 35.04, 38.53, 40.66, 42.56, 49.51, 52.41, 116.33 (d, J = 24.5 Hz), 120.96 (d, J = 11.4 Hz), 124.85 (d, J = 3.3 Hz), 130.01, 131.93 (d, J = 2.2 Hz), 133.68 (d, J = 9.4 Hz), 146.38, 160.84 (d, J = 248.4 Hz), 163.38 (d, J = 2.9 Hz), 172.62, 180.10, 198.40. Elemental analysis for C$_{23}$H$_{30}$FN$_3$O$_4$ = calcd. C, 64.02; H, 7.01; N, 9.74; found = C, 64.19; H, 7.26; N, 9.50.

N-((S)-3-Cyclopropyl-1-oxo-1-(((S,E)-5-oxo-1-((S)-2-oxopyrrolidin-3-yl)hex-3-en-2-yl)amino)propan-2-yl)-2-fluorobenzamide (SPR49)
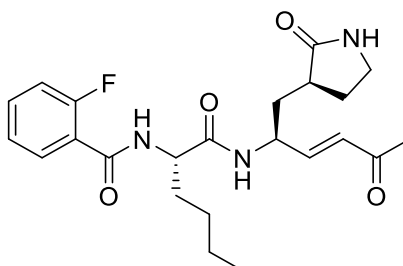

In this reaction the intermediate **15c** was used as the substrate. Yield = 26%; R_f and eluent mixture = 0.25 in EtOAc/ACN 7:3; Consistency = white powder. ^{1}H NMR in CDCl$_3$ (500 MHz), δ = 0.12-0.20 (m, 2H), 0.46.0.56 (m, 2H), 0.74-0.83 (m, 1H), 1.74-1.89 (m, 4H), 2.07 (ddd, J = 14.3, 11.8, 5.9 Hz, 1H), 2.25 (s, 3H), 2.35-2.43 (m, 1H), 2.44-2.58 (m, 1H), 3.28-3.38 (m, 2H), 4.54-4-65 (m, 1H), 4.74-4.86 (m, 1H), 6.04 (bs, 1H), 6.22 (dd, J = 15.9, 1.4 Hz, 1H), 6.68 (dd, J = 16.0, 5.7 Hz, 1H), 7.10-7.16 (m, 1H), 7.22-7.25 (m, 1H), 7.44-7.50 (m, 2H), 8.03 (td, J = 7.8, 1.9 Hz, 1H), 8.08 (d, J = 6.8 Hz, 1H). ^{13}C NMR in CDCl$_3$ (126 MHz), δ = 4.51, 4.72, 7.46, 27.66, 28.97, 29.84, 34.98, 37.84, 38.62, 40.68, 49.92, 54.54, 116.32 (d, J = 24.6 Hz), 120.99 (d, J = 11.4 Hz), 124.80, 124.86 (d, J = 3.3 Hz), 130.15, 131.98 (d, J = 1.9 Hz), 133.65 (d, J = 9.5 Hz), 160.91 (d, J = 248.6 Hz), 163.26 (d, J = 2.9 Hz), 172.03, 180.20, 198.36. Elemental analysis for C$_{23}$H$_{28}$FN$_3$O$_4$C, 64.32; H, 6.57; N, 9.78; found: C, 64.55; H, 6.31; N, 9.62.

N-((S)-4,4-Dimethyl-1-oxo-1-(((S,E)-5-oxo-1-((S)-2-oxopyrrolidin-3-yl)hex-3-en-2-yl)amino)pentan-2-yl)-2-fluorobenzamide (SPR50)
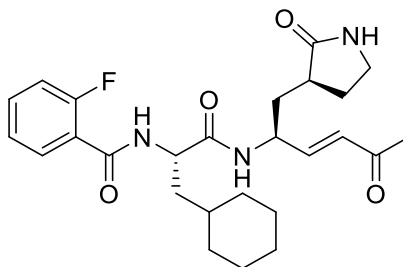
In this reaction the intermediate **15d** was used as the substrate. Yield = 33%; R_f and eluent mixture = 0.36 in EtOAc/ACN 3:2; Consistency = white powder. ^{1}H NMR in CDCl$_3$ (500 MHz), δ = 1.01 (s, 9H), 1.58-1.67 (m, 2H), 1.75-1.85 (m, 1H), 1.88-1.97 (m, 1H), 2.05-2-15 (m, 1H), 2.25 (s, 3H), 2.29-2.39 (m, 1H), 2.42-2.48 (m, 1H), 3.23-3.36 (m, 2H), 4.52-4.60 (m, 1H), 4.79-4.85 (m, 1H), 6.19 (s, 1H), 6.21 (d, J = 16.1 Hz, 1H), 6.67 (dd, J = 16.0, 5.6 Hz, 1H), 7.05-7.18 (m, 2H), 7.22-7.27 (m, 1H), 7.39-7.52 (m, 1H), 7.97 (d, J = 6.9 Hz, 1H), 8.05 – 8.00 (m, 1H). ^{13}C NMR in CDCl$_3$ (126 MHz), δ = 27.65, 28.78, 29.84, 29.89, 30.84, 35.00, 38.44, 40.61, 46.62, 49.58, 51.80, 116.33 (d, J = 24.7 Hz), 120.85 (d, J = 11.4 Hz), 124.93 (d, J = 3.2 Hz), 130.13, 132.00 (d, J = 1.9 Hz), 133.76 (d, J = 9.4 Hz), 146.26, 160.88 (d, J = 248.4 Hz), 163.26 (d, J = 3.1 Hz), 173.04, 180.08, 198.43. Elemental analysis for C$_{24}$H$_{32}$FN$_3$O$_4$: calcd. = C, 64.70; H, 7.24; N, 9.43; found = C, 64.82; H, 7.14; N, 9.68.

2-Fluoro-N-((S)-1-oxo-1-(((S,E)-5-oxo-1-((S)-2-oxopyrrolidin-3-yl)hex-3-en-2-yl)amino)hexan-2-yl)benzamide (SPR51)
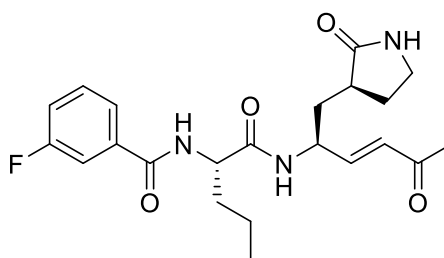

In this reaction the intermediate **15e** was used as the substrate. Yield = 37%; R_f and eluent mixture = 0.40 in EtOAc/ACN 3:2; Consistency = white powder. ^{1}H NMR in CDCl$_3$ (500 MHz), δ = 0.89 (t, J = 7.0 Hz, 3H), 1.32-1.43 (m, 4H), 1.65 (ddd, J = 14.3, 7.7, 3.8 Hz, 1H), 1.74-1.87 (m, 3H), 2.09 (ddd, J = 14.3, 11.9, 5.3 Hz, 1H), 2.24 (s, 3H), 2.32-2.41 (m, 1H), 2.42-2.50 (m, 1H), 3.25-3.38 (m, 2H), 4.50-4.65 (m, 1H), 4.74-4.87 (m, 1H), 6.21 (dd, J = 16.0, 1.5 Hz, 1H), 6.35 (s, 1H), 6.69 (dd, J = 16.0, 5.5 Hz, 1H), 7.12 (ddd, J = 11.9, 8.3, 1.1 Hz, 1H), 7.23 (td, J = 7.6, 1.1 Hz, 1H), 7.38 (dd, J = 11.9, 7.8 Hz, 1H), 7.51 – 7.42 (m, 1H), 8.00 (td, J = 7.8, 1.9 Hz, 1H), 8.12 (d, J = 7.1 Hz, 1H). ^{13}C NMR in CDCl$_3$ (126 MHz), δ = 14.08, 22.58, 27.63, 27.71, 28.71, 33.15, 35.05, 38.57, 40.67, 49.55, 53.84, 116.33 (d, J = 24.5 Hz), 121.04 (d, J = 11.4 Hz), 124.83 (d, J = 3.3 Hz), 129.98, 131.87 (d, J = 2.2 Hz), 133.62 (d, J = 9.3 Hz), 146.34, 160.85 (d, J = 248.7 Hz), 163.30 (d, J = 2.8 Hz), 172.22, 180.16, 198.32. Elemental analysis for C$_{23}$H$_{30}$FN$_3$O$_4$: calcd. = C, 64.02; H, 7.01; N, 9.74; found = C, 63.84; H, 6.90; N, 9.96.

N-((S)-3-Cyclohexyl-1-oxo-1-(((S,E)-5-oxo-1-((S)-2-oxopyrrolidin-3-yl)hex-3-en-2-yl)amino)propan-2-yl)-2-fluorobenzamide (SPR52)
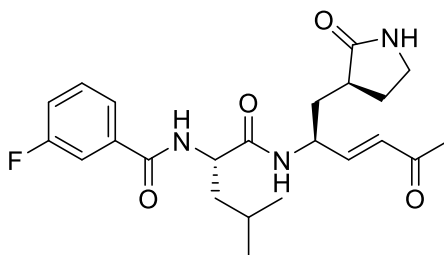

In this reaction the intermediate **15f** was used as the substrate. Yield = 25%; R_f and eluent mixture = 0.32 in EtOAc/ACN 1:1; Consistency = white powder. ^{1}H NMR in CDCl$_3$ (500 MHz), δ = 0.84-1.05 (m, 3H), 1.11-1.24 (m, 1H), 1.36-1.44 (m, 1H), 1.62-1.73 (m, 7H), 1.74-1.88 (m, 3H), 2.08 (ddd, J = 14.3, 11.8, 5.6 Hz, 1H), 2.25 (s, 3H), 2.32-2.40 (m, 1H), 2.42-2.51 (m, 1H), 3.26-3.37 (m, 2H), 4.54-4.63 (m, 1H), 4.80-4.87 (m, 1H), 6.10 (bs, 1H), 6.21 (dd, J = 16.0, 1.5 Hz, 1H), 6.68 (dd, J = 16.0, 5.5 Hz, 1H), 7.09-7.26 (m, 3H), 7.39-7.52 (m, 1H), 7.98-8.05 (m, 2H). ^{13}C NMR in CDCl$_3$ (126 MHz), δ = 26.24, 26.37, 26.52, 27.66, 28.86, 29.84, 32.93, 33.76, 34.47, 35.00, 38.53, 40.64, 40.78, 49.65, 51.99, 116.32 (d, J = 24.6 Hz), 121.02 (d, J = 11.4 Hz),124.88 (d, J = 3.4 Hz), 130.02, 131.97 (d, J = 1.9 Hz), 133.65 (d, J = 9.3 Hz), 146.30, 160.86 (d, J = 248.4 Hz), 163.40 (d, J = 2.9 Hz), 172.63, 180.11, 198.31. Elemental analysis for C$_{26}$H$_{34}$FN$_3$O$_4$: calcd. = C, 66.22; H, 7.27; N, 8.91; found = C, 66.04; H, 7.44; N, 9.13.

3-Fluoro-N-((S)-1-oxo-1-(((S,E)-5-oxo-1-((S)-2-oxopyrrolidin-3-yl)hex-3-en-2-yl)amino)pentan-2-yl)benzamide (SPR53)
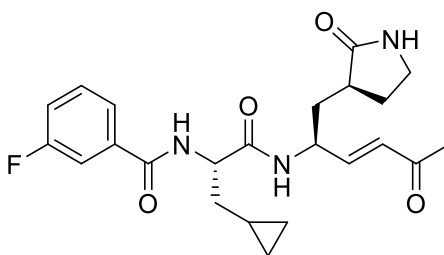

In this reaction the intermediate **16a** was used as the substrate. Yield = 38%; R_f and eluent mixture = 0.29 in EtOAc/ACN 7:3; Consistency = white powder. ^{1}H NMR in CDCl$_3$ (500 MHz), δ = 0.96 (t, J = 7.2 Hz, 3H), 1.49-1.37 (m, 2H), 1.64-1.80 (m, 3H), 1.80-1-89 (m, 1H), 1.89-1-98 (m, 1H), 2.01-2.10 (m, 1H), 2.25 (s, 3H), 2.31-2.53 (m, 2H), 3.26-3.41 (m, 2H), 4.49-4.60 (m, 1H), 4.80 (q, J = 7.5 Hz, 1H), 6.19 (d, J = 16.3 Hz, 2H), 6.67 (dd, J = 15.9, 5.3 Hz, 1H), 7.01 (d, J = 7.8 Hz, 1H), 7.19 (t, J = 7.1 Hz, 1H), 7.40 (q, J = 7.7 Hz, 1H), 7.56 (d, J = 9.2 Hz, 1H), 7.59 (d, J = 7.7 Hz, 1H), 8.32 (d, J = 6.1 Hz, 1H). ^{13}C NMR in CDCl$_3$ (126 MHz), δ = 13.95, 18.96, 27.67, 29.84, 34.93, 35.79, 38.84, 40.75, 50.16, 53.51, 114.70 (d, J = 22.9 Hz), 118.84 (d, J = 21.3 Hz), 122.72 (d, J = 3.0 Hz), 130.04, 130.37 (d, J = 7.9 Hz), 136.43 (d, J = 6.9 Hz), 146.12, 162.90 (d, J = 247.7 Hz), 165.95, 172.41, 180.29, 198.30. Elemental analysis for C$_{22}$H$_{28}$FN$_3$O$_4$: calcd. = C, 63.29; H, 6.76; N, 10.07; found = C, 63.32; H, 6.44; N, 10.37.

3-Fluoro-N-((S)-4-methyl-1-oxo-1-(((S,E)-5-oxo-1-((S)-2-oxopyrrolidin-3-yl)hex-3-en-2-yl)amino)pentan-2-yl)benzamide (SPR54)

In this reaction the intermediate **16b** was used as the substrate. Yield = 31%; R_f and eluent mixture = 0.33 in EtOAc/ACN 3:2; Consistency = white powder. ^{1}H NMR in CDCl$_3$ (500 MHz), δ = 0.99 (d, J = 6.3 Hz, 3H), 1.01 (d, J = 6.1 Hz, 3H), 1.62-1.79 (m, 4H), 1.79-1.89 (m, 1H), 1.98-2.09 (m, 1H), 2.25 (s, 3H), 2.35-2.43 (m, 1H), 2.43-2.51 (m, 1H), 3.29-3.41 (m, 2H), 4.48-4.57 (m, 1H), 4.78-4.87 (m, 1H), 6.07 (bs, 1H), 6.19 (dd, J = 15.9, 1.4 Hz, 1H), 6.66 (dd, J = 16.0, 5.6 Hz, 1H), 6.82 (d, J = 8.4 Hz, 1H), 7.20 (tdd, J = 8.3, 2.6, 0.9 Hz, 1H), 7.40 (td, J = 8.0, 5.6 Hz, 1H), 7.53-7.61 (m, 2H), 8.32 (d, J = 6.4 Hz, 1H). ^{13}C NMR in CDCl$_3$ (126 MHz), δ = 22.24, 23.21, 25.20, 27.70, 29.85, 34.83, 38.93, 40.77, 42.83, 50.46, 52.38, 91.10, 114.72 (d, J = 23.0 Hz), 118.86 (d, J = 21.2 Hz), 122.74 (d, J = 2.9 Hz), 130.38 (d, J = 7.9 Hz), 130.41, 136.40 (d, J = 7.1 Hz), 146.07, 162.91 (d, J = 248.0 Hz), 165.98 (d, J = 2.4 Hz), 172.79, 180.35, 198.33. Elemental analysis for C$_{23}$H$_{30}$FN$_3$O$_4$: calcd. = C, 64.02; H, 7.01; N, 9.74; found = C, 63.82; H, 7.07; N, 9.62.

N-((S)-3-Cyclopropyl-1-oxo-1-(((S,E)-5-oxo-1-((S)-2-oxopyrrolidin-3-yl)hex-3-en-2-yl)amino)propan-2-yl)-3-fluorobenzamide (SPR55)

In this reaction the intermediate **16c** was used as the substrate. Yield = 29%; R_f and eluent mixture = 0.44 in EtOAc/ACN 4:1; Consistency = white powder. ^{1}H NMR in CDCl$_3$ (500 MHz), δ = 0.04-0.15 (m, 2H), 0.45 (d, J = 8.1 Hz, 2H), 0.69-0.77 (m, 1H), 1.55-1.65 (m, 1H), 1.69-1.83 (m, 3H), 2.07-2.16 (m, 1H), 2.23 (s, 3H), 2.30-2.38 (m, 1H), 2.43-2.48 (m, 1H), 3.23-3.37 (m, 2H), 4.52-4.63 (m, 1H), 4.85-4.95 (m, 1H), 6.19 (dd, J = 16.0, 1.4 Hz, 1H), 6.67 (dd, J = 16.0, 5.7 Hz, 1H), 6.80 (s, 1H), 7.16 (tdd, J = 8.3, 2.6, 1.0 Hz, 1H), 7.32-7.40 (m, 2H), 7.52 (ddd, J = 9.4, 2.6, 1.6 Hz, 1H), 7.56 (dt, J = 7.8, 1.3 Hz, 1H), 8.30 (d, J = 7.2 Hz, 1H). ^{13}C NMR in CDCl$_3$ (126 MHz), δ = 4.52, 4.65, 7.50, 27.46, 28.48, 35.16, 38.21, 38.53, 40.68, 49.40, 54.20, 114.62 (d, J = 23.0 Hz), 118.74 (d, J = 21.3 Hz), 122.70, 122.76 (d, J = 3.0 Hz), 130.10, 130.31 (d, J = 7.4 Hz), 136.36 (d, J = 6.9 Hz), 146.30, 162.78 (d, J = 247.0 Hz), 165.90 (d, J = 2.9 Hz), 172.32, 180.18, 198.45. Elemental analysis for C$_{23}$H$_{28}$FN$_3$O$_4$: C, 64.32; H, 6.57; N, 9.78; found: C, 64.17; H, 6.72; N, 9.55.

N-((S)-4,4-Dimethyl-1-oxo-1-(((S,E)-5-oxo-1-((S)-2-oxopyrrolidin-3-yl)hex-3-en-2-yl)amino)pentan-2-yl)-3-fluorobenzamide (SPR56)
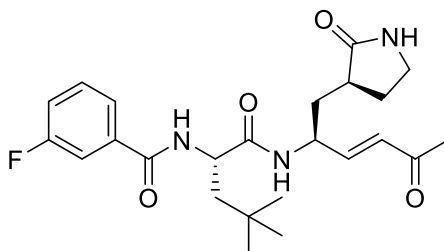
In this reaction the intermediate **16d** was used as the substrate. Yield = 22%; R_f and eluent mixture = 0.37 in EtOAc/ACN 7:3; Consistency = white powder. ^{1}H NMR in CDCl$_3$ (500 MHz), δ = 1.00 (s, 9H), 1.62-1.67 (m, 2H), 1.79-1.93 (m, 2H), 2.06 (ddd, J = 14.2, 12.2, 6.1 Hz, 1H), 2.25 (s, 3H), 2.30-2.37 (m, 1H), 2.41-2.48 (m, 1H), 3.30-3.35 (m, 2H), 4.47-4.55 (m, 1H), 4.85 (td, J = 8.9, 3.4 Hz, 1H), 6.19 (d, J = 15.2 Hz, 1H), 6.23 (bs, 1H), 6.66 (dd, J = 16.0, 5.7 Hz, 1H), 6.80 (d, J = 8.4 Hz, 1H), 7.19 (td, J = 8.5, 2.8 Hz, 1H), 7.40 (td, J = 7.8, 5.9 Hz, 1H), 7.61 – 7.51 (m, 2H), 8.23 (d, J = 6.5 Hz, 1H). ^{13}C NMR in CDCl$_3$ (126 MHz), δ = 27.66, 29.01, 29.89, 29.99, 30.90, 34.87, 38.72, 40.71, 47.02, 50.08, 51.69, 114.67 (d, J = 23.0 Hz), 118.90 (d, J = 21.3 Hz), 122.71 (d, J = 3.0 Hz), 130.14, 130.43 (d, J = 7.9 Hz), 136.38 (d, J = 6.8 Hz), 146.14, 162.89 (d, J = 247.7 Hz), 165.78 (d, J = 2.3 Hz), 173.33, 180.24, 198.45. Elemental analysis for C$_{24}$H$_{32}$FN$_3$O$_4$: C, 64.70; H, 7.24; N, 9.43; found: C, 65.03; H, 7.17; N, 9.29.

3-Fluoro-N-((S)-1-oxo-1-(((S,E)-5-oxo-1-((S)-2-oxopyrrolidin-3-yl)hex-3-en-2-yl)amino)hexan-2-yl)benzamide (SPR57)
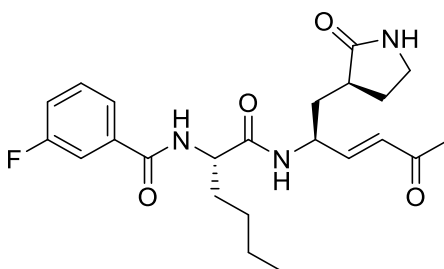
In this reaction the intermediate **16e** was used as the substrate. Yield = 25%; R_f and eluent mixture = 0.25 in EtOAc/MeOH 19:1; Consistency = white powder. ^{1}H NMR in CDCl$_3$ (500 MHz), δ = 0.85-0.89 (m, 3H), 1.32-1.38 (m, 4H), 1.63 (ddd, J = 14.3, 7.9, 3.7 Hz, 1H), 1.72-1.83 (m, 2H), 1.88-1.97 (m, 1H), 2.10 (ddd, J = 17.3, 13.1, 6.0 Hz, 1H), 2.24 (s, 3H), 2.30-2.40 (m, 1H), 2.41-2.49 (m, 1H), 3.27-3.39 (m, 2H), 4.52-4.61 (m, 1H), 4.78-4.86 (m, 1H), 6.19 (dd, J = 15.9, 1.4 Hz, 1H), 6.59 (s, 1H), 6.68 (dd, J = 16.0, 5.5 Hz, 1H), 7.12-7.23 (m, 2H), 7.34-7.43 (m, 1H), 7.50-7.55 (m, 1H), 7.57 (d, J = 7.8 Hz, 1H), 8.28 (d, J = 7.1 Hz, 1H). ^{13}C NMR in CDCl$_3$ (126 MHz), δ = 14.07, 22.56, 27.57, 27.76, 28.65, 33.37, 35.07, 38.64, 40.71, 49.58, 53.64, 114.68 (d, J = 22.9 Hz), 118.82 (d, J = 21.2 Hz), 122.75 (d, J = 3.0 Hz), 129.99, 130.34 (d, J = 7.8 Hz), 136.36 (d, J = 6.6 Hz), 146.29, 162.84 (d, J = 247.7 Hz), 165.96 (d, J = 2.7 Hz),

172.46, 180.19, 198.33. Elemental analysis for $C_{23}H_{30}FN_3O_4$: C, 64.02; H, 7.01; N, 9.74; found: C, 63.85; H, 7.27; N, 9.50.

N-((S)-3-Cyclohexyl-1-oxo-1-(((S,E)-5-oxo-1-((S)-2-oxopyrrolidin-3-yl)hex-3-en-2-yl)amino)propan-2-yl)-3-fluorobenzamide (SPR58)
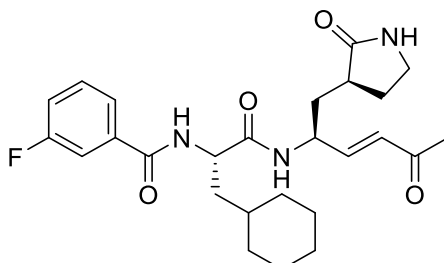
In this reaction the intermediate **16f** was used as the substrate. Yield = 28%; R_f and eluent mixture = 0.36 in EtOAc/ACN 7:3; Consistency = white powder. ^{1}H NMR in CDCl$_3$ (500 MHz), δ = 0.81-0.90 (m, 1H), 0.90-1.06 (m, 2H), 1.07-1.31 (m, 5H), 1.31-1.41 (m, 1H), 1.65-1.92 (m, 6H), 1.96-2.06 (m, 1H), 2.25 (s, 3H), 2.33-2.43 (m, 1H), 2.44-2.53 (m, 1H), 3.28-3.41 (m, 2H), 4.50-4.59 (m, 1H), 4.74-4.85 (m, 1H), 5.95 (s, 1H), 6.19 (dd, J = 16.1, 1.6 Hz, 1H), 6.66 (dd, J = 16.0, 5.5 Hz, 1H), 6.80 (d, J = 8.3 Hz, 1H), 7.20 (t, J = 8.0 Hz, 1H), 7.41 (q, J = 7.6 Hz, 1H), 7.51-7.64 (m, 2H), 8.27 (d, J = 6.5 Hz, 1H). ^{13}C NMR in CDCl$_3$ (126 MHz), δ = 26.24, 26.38, 26.50, 27.70, 29.26, 29.85, 32.90, 33.84, 34.50, 34.83, 38.89, 40.76, 41.19, 50.39, 51.85, 114.73 (d, J = 23.0 Hz), 118.85 (d, J = 21.4 Hz), 122.75 (d, J = 3.0 Hz), 130.05, 130.39 (d, J = 7.8 Hz), 136.41, 146.06, 162.92 (d, J = 247.5 Hz), 165.99 (d, J = 2.4 Hz),172.85, 180.36, 198.30. Elemental analysis for $C_{26}H_{34}FN_3O_4$ = calcd. C, 66.22; H, 7.27; N, 8.91; found: C, 66.49; H, 7.13; N, 8.81.

4-Fluoro-N-((S)-1-oxo-1-(((S,E)-5-oxo-1-((S)-2-oxopyrrolidin-3-yl)hex-3-en-2-yl)amino)pentan-2-yl)benzamide (SPR59)
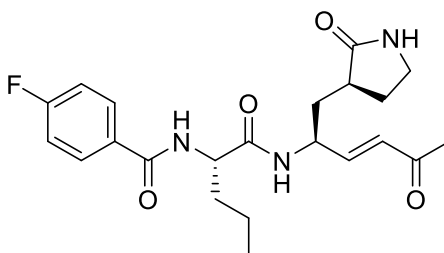
In this reaction the intermediate **17a** was used as the substrate. Yield = 31%; R_f and eluent mixture = 0.21 in EtOAc/ACN 1:1; Consistency = white powder. ^{1}H NMR in CDCl$_3$ (500 MHz), δ = 0.97 (t, J = 7.3 Hz, 3H), 1.40-1.47 (m, 2H), 1.67-1.78 (m, 2H), 1.80-1.90 (m, 1H), 1.99-2.04 (m, 1H), 2.25 (s, 3H), 2.35-2.54 (m, 2H), 3.31-3.39 (m, 2H), 4.51-4.60 (m, 1H), 4.76 (q, J = 7.2 Hz, 1H), 5.99 (s, 1H), 6.19 (d, J = 15.8 Hz, 1H), 6.67 (dd, J = 16.3, 5.6 Hz, 1H), 6.91 (d, J = 8.0 Hz, 1H), 7.10 (t, J = 8.4 Hz, 2H), 7.82-7.90 (m, 2H), 8.32 (d, J = 6.2 Hz, 1H). ^{13}C NMR in CDCl$_3$ (126 MHz), δ = 13.97, 18.96, 27.71, 29.25, 34.85, 35.74, 38.94, 40.77, 50.44, 53.53, 115.75 (d, J = 21.9 Hz), 129.64 (d, J = 9.0 Hz), 130.04, 130.34, 146.05, 165.02 (d, J =

252.9 Hz), 166.18, 172.50, 180.37, 198.29. Elemental analysis for $C_{22}H_{28}FN_3O_4$: calcd. = C, 63.29; H, 6.76; N, 10.07; found = C, 63.10; H, 6.65; N, 10.19.

4-Fluoro-N-((S)-4-methyl-1-oxo-1-(((S,E)-5-oxo-1-((S)-2-oxopyrrolidin-3-yl)hex-3-en-2-yl)amino)pentan-2-yl)benzamide (SPR60)
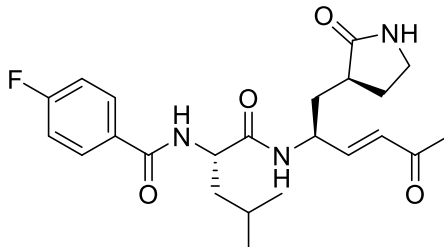
In this reaction the intermediate **17b** was used as the substrate. Yield = 38%; R_f and eluent mixture = 0.29 in EtOAc/ACN 1:1; Consistency = white powder. ^{1}H NMR in CDCl$_3$ (500 MHz), δ = 0.98 (d, J = 6.1 Hz, 3H), 1.00 (d, J = 5.7 Hz, 3H), 1.60-1.70 (m, 2H), 1.70-1.77 (m, 2H), 1.77-1.87 (m, 1H), 2.07 (ddd, J = 14.2, 12.0, 5.8 Hz, 1H), 2.25 (s, 3H), 2.33-2.41 (m, 1H), 2.41-2.50 (m, 1H), 3.28-3.41 (m, 2H), 4.50-4.58 (m, 1H), 4.82-4.91 (m, 1H), 6.18 (dd, J = 16.0, 1.5 Hz, 1H), 6.28 (bs, 1H), 6.67 (dd, J = 16.0, 5.5 Hz, 1H), 6.82 (d, J = 8.5 Hz, 1H), 7.10 (t, J = 8.6 Hz, 2H), 7.79-7.88 (m, 2H), 8.28 (d, J = 6.6 Hz, 1H). ^{13}C NMR in CDCl$_3$ (126 MHz), δ = 22.25, 23.19, 25.17, 27.64, 28.97, 34.95, 38.76, 40.73, 42.92, 50.02, 52.22, 115.76 (d, J = 21.9 Hz), 129.65 (d, J = 9.0 Hz), 130.06, 130.24 (d, J = 2.9 Hz), 146.18, 165.03 (d, J = 252.2 Hz), 166.23, 172.96, 180.22, 198.36. Elemental analysis for $C_{22}H_{30}FN_3O_4$: calcd. = C, 64.02; H, 7.01; F, 4.40; N, 9.74; found = C, 63.88; H, 7.35; N, 9.69.

N-((S)-3-Cyclopropyl-1-oxo-1-(((S,E)-5-oxo-1-((S)-2-oxopyrrolidin-3-yl)hex-3-en-2-yl)amino)propan-2-yl)-4-fluorobenzamide (SPR61)
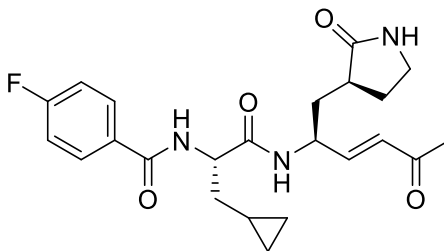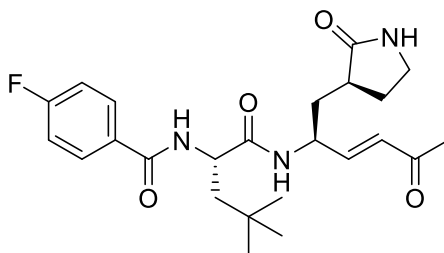

In this reaction the intermediate **17c** was used as the substrate. Yield = 27%; R_f and eluent mixture = 0.39 in EtOAc/ACN 3:2; Consistency = white powder. ^{1}H NMR in CDCl$_3$ (500 MHz), δ = 0.04-0.16 (m, 2H), 0.40-0.51 (m, 2H), 0.68-0.79 (m, 1H), 1.62 (ddd, J = 13.9, 8.0, 3.6 Hz, 1H), 1.69-1.83 (m, 3H), 2.07-2.15 (m, 1H), 2.23 (s, 3H), 2.31-2-39 (m, 1H), 2.41-2.49 (m, 1H), 3.25-3.73 (m, 2H), 4.53-4.61 (m, 1H), 4.87-4.94 (m, 1H), 6.19 (d, J = 16.0 Hz, 1H), 6.67 (dd, J = 15.8, 5.9 Hz, 1H), 6.68 (bs, 1H), 7.08 (t, J = 8.4 Hz, 2H), 7.18 (d, J = 8.1 Hz, 1H), 7.82 (dd, J = 8.4, 5.4 Hz, 2H), 8.28 (d, J = 7.1 Hz, 1H). ^{13}C NMR in CDCl$_3$ (126 MHz), δ = 4.52, 4.72, 7.49, 27.51, 28.61, 35.15, 38.36, 38.59, 40.69, 49.54, 54.10, 115.71 (d, J = 21.9 Hz), 129.60 (d, J = 9.0 Hz), 130.14, 130.30 (d, J = 3.0 Hz), 146.24, 164.95 (d, J = 252.3 Hz), 166.10, 172.35, 180.14, 198.39. Elemental analysis for $C_{23}H_{28}FN_3O_4$: C, 64.32; H, 6.57; N, 9.78; found: C, 64.46; H, 6.33; N, 9.93.

N-((S)-4,4-Dimethyl-1-oxo-1-(((S,E)-5-oxo-1-((S)-2-oxopyrrolidin-3-yl)hex-3-en-2-yl)amino)pentan-2-yl)-4-fluorobenzamide (SPR62)
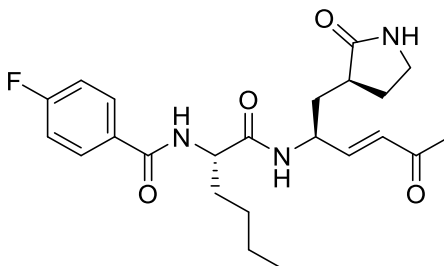

In this reaction the intermediate **17d** was used as the substrate. Yield = 20%; R_f and eluent mixture = 0.29 in EtOAc/MeOH 19:1; Consistency = white powder. ^{1}H NMR in CDCl$_3$ (500 MHz), δ = 0.99 (s, 9H), 1.58-1.66 (m, 2H), 1.71-1.83 (m, 1H), 1.87 (dd, J = 14.4, 3.5 Hz, 1H), 2.09 (ddd, J = 14.4, 12.0, 5.5 Hz, 1H), 2.24 (s, 3H), 2.30-2.38 (m, 1H), 2.39-2.48 (m, 1H), 3.25-3.38 (m, 2H), 4.45-4.56 (m, 1H), 4.89 (td, J = 8.9, 3.5 Hz, 1H), 6.19 (dd, J = 16.0, 1.4 Hz, 1H), 6.41 (bs, 1H), 6.66 (dd, J = 16.0, 5.7 Hz, 1H), 6.78 (d, J = 8.8 Hz, 1H), 7.03-7.14 (m, 2H), 7.79-7.86 (m, 2H), 8.20 (d, J = 6.7 Hz, 1H). ^{13}C NMR in CDCl$_3$ (126 MHz), δ = 27.61, 28.85, 29.90, 30.89, 34.94, 38.62, 40.68, 47.12, 49.82, 51.55, 115.80 (d, J = 21.9 Hz), 129.62 (d, J = 9.1 Hz), 130.16, 130.28 (d, J = 3.3 Hz), 146.20, 165.04 (d, J = 252.7 Hz), 165.99, 173.46, 180.10, 198.42. Elemental analysis for C$_{24}$H$_{32}$FN$_3$O$_4$: C, 64.70; H, 7.24; N, 9.43; found: C, 64.83; H, 7.39; F, 4.26; N, 9.22.

4-Fluoro-N-((S)-1-oxo-1-(((S,E)-5-oxo-1-((S)-2-oxopyrrolidin-3-yl)hex-3-en-2-yl)amino)hexan-2-yl)benzamide (SPR63)

In this reaction the intermediate **17e** was used as the substrate. Yield = 23%; R_f and eluent mixture = 0.27 in EtOAc/ACN 1:1; Consistency = white powder. ^{1}H NMR in CDCl$_3$ (500 MHz), δ = 0.89 (t, J = 7.0 Hz, 3H), 1.32-1.39 (m, 5H), 1.68 (ddd, J = 14.4, 6.4, 4.0 Hz, 1H), 1.77-1.87 (m, 1H), 1.91-1.99 (m, 1H), 2.05 (ddd, J = 14.1, 12.1, 6.1 Hz, 1H), 2.25 (s, 3H), 2.33-2.41 (m, 1H), 2.43-2.50 (m, 1H), 3.29-3.38 (m, 2H), 4.51-4.61 (m, 1H), 4.75-4.82 (m, 1H), 6.20 (d, J = 15.9 Hz, 1H), 6.21 (bs, 1H), 6.67 (dd, J = 16.0, 5.6 Hz, 1H), 6.96 (d, J = 8.0 Hz, 1H), 7.10 (t, J = 8.5 Hz, 2H), 7.81-7.88 (m, 2H), 8.28 (d, J = 6.7 Hz, 1H). ^{13}C NMR in CDCl$_3$ (126 MHz), δ = 14.10, 22.60, 27.66, 27.73, 29.01, 33.40, 34.93, 38.81, 40.74, 50.07, 53.62, 115.75 (d, J = 21.9 Hz), 129.64 (d, J = 9.0 Hz), 130.03, 130.65 (d, J = 3.2 Hz), 146.14, 165.02 (d, J = 252.2 Hz), 166.16, 172.50, 180.27, 198.28. Elemental analysis for C$_{23}$H$_{30}$FN$_3$O$_4$: calcd. = C, 64.02; H, 7.01; N, 9.74; found: C, 63.81; H, 7.30; N, 9.92.

N-((S)-3-Cyclohexyl-1-oxo-1-(((S,E)-5-oxo-1-((S)-2-oxopyrrolidin-3-yl)hex-3-en-2-yl)amino)propan-2-yl)-4-fluorobenzamide (SPR64)
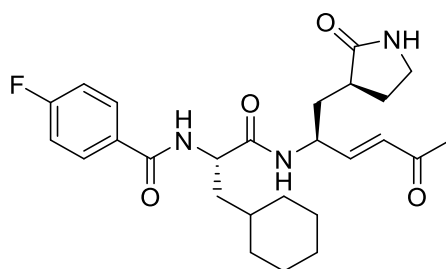
In this reaction the intermediate **17f** was used as the substrate. Yield = 32%; R_f and eluent mixture = 0.35 in EtOAc/MeOH 19:1; Consistency = white powder. ^{1}H NMR in CDCl$_3$ (500 MHz), δ = 0.87-1.06 (m, 3H), 1.08-1.35 (m, 4H), 1.58-2.03 (m, 8H), 2.09 (ddd, J = 14.3, 12.0, 5.4 Hz, 1H), 2.25 (s, 3H), 2.30-2.39 (m, 1H), 2.40-2.49 (m, 1H), 3.25-3.38 (m, 2H), 4.51-4.60 (m, 1H), 4.85-4.91 (m, 1H), 6.19 (dd, J = 16.0, 1.4 Hz, 1H), 6.47 (s, 1H), 6.67 (dd, J = 16.0, 5.5 Hz, 1H), 6.89 (d, J = 8.5 Hz, 1H), 7.04 (m, 2H), 7.78-7.86 (m, 2H), 8.21 (d, J = 7.0 Hz, 1H). ^{13}C NMR in CDCl$_3$ (126 MHz), δ = 26.24, 26.37, 26.49, 27.60, 28.85, 32.93, 33.77, 34.47, 34.98, 38.67, 40.70, 41.34, 49.77, 51.66, 115.75 (d, J = 21.9 Hz), 129.65 (d, J = 8.9 Hz), 130.04, 130.29 (d, J = 3.1 Hz), 146.27, 165.02 (d, J = 252.3 Hz), 166.21, 173.02, 180.16, 198.34. Elemental analysis for C$_{26}$H$_{34}$FN$_3$O$_4$: calcd. = C, 66.22; H, 7.27; N, 8.91; found: C, 66.46; H, 7.33; N, 8.70.

9.1.3. Synthesis of Compounds EC1- EC8

General Procedure for the Insertion of the Weinreb Amides in 20,21

In a round bottom flask (A), the appropriate commercially available *N*-Boc-amino acids **18,19** (1 eq.) were dissolved in DCM (10 mL/mmol) and cooled down to 0 °C with an ice bath. TBTU (1.2 eq) and DIPEA (4 eq.) were added, and the reaction was kept in vigorously stirring for 15 min. After this time, *N,O*-dimethylhydroxylamine hydrochloride (1.2 eq.) was added portion-wise, and the pH was checked (>8). The reaction was vigorously stirred at rt on. Subsequently, DCM was removed *in vacuo*. The organic phase was dissolved with EtOAc (x 3) and washed with 1 M HCl (x 2), NaHCO$_3$ saturated solution (x 2), and brine (x 2), dried over Na$_2$SO$_4$, and concentrated *in vacuo*. The obtained crude was purified using the appropriate eluent mixture below described.

tert-butyl (S)-(1-(Methoxy(methyl)amino)-1-oxopentan-2-yl)carbamate (20)
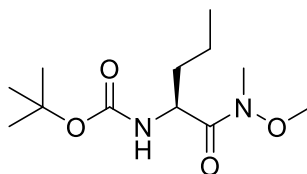
In this reaction Boc-Nva-OH **(19)** was used as the acid. Yield = 28%; R_f = 0.50 in Ex/EtOAc 6:4; Consistency = colorless oil ; ^{1}H NMR (500 MHz, CDCl$_3$): δ = 0.80 (t, J = 7.2 Hz, 3H), 1.15 – 1.44 (m, 12H), 1.44 – 1.62 (m, 1H), 3.07 (s, 3H), 3.65 (s, 3H), 4.55 (d, J = 3.3 Hz, 1H), 5.15 (d, J = 8.9 Hz, 1H); ^{13}C NMR (125 MHz, CDCl$_3$): δ = 13.58, 18.56, 28.21, 34.87, 50.02, 61.41, 79.17, 155.47, 173.28.

tert-butyl (S)-(1-(Methoxy(methyl)amino)-1-oxohexan-2-yl)carbamate (21)
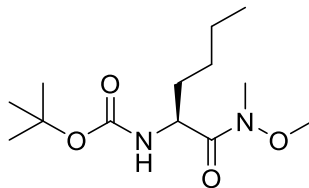
In this reaction Boc-Nle-OH **(18)** was used as the acid. Yield = 86%; R_f = 0.45 in Ex/EtOAc 7:3; Consistency = colorless oil ; ^{1}H NMR (500 MHz, CDCl$_3$): δ = 0.95 (dd, J = 9.2, 4.8 Hz, 3H), 1.33 – 1.46 (m, 4H), 1.50 (s, 9H), 1.58 (ddd, J = 13.7, 10.0, 5.3 Hz, 1H), 1.71 – 1.84 (m, 1H), 3.27 (s, 3H), 3.84 (s, 3H), 4.72 (s, 1H), 5.20 (d, J = 8.7 Hz, 1H); ^{13}C NMR (125 MHz, CDCl$_3$): δ = 13.88, 22.36, 27.47, 28.37, 32.10, 32.65, 50.33, 61.59, 79.47, 155.60, 173.49.

General Procedure for the Synthesis of Intermediates 26-29

In a round-bottom flask, the appropriate N-Boc-protected intermediates **20,21** (1 eq.) were dissolved in DCM (70% *v/v*) and cooled to 0°C. TFA (10 eq., 30% *v/v*) was then added dropwise. The reaction mixture was stirred vigorously at room temperature until TLC monitoring (using the same eluent mixture as for the purification of the starting compound) indicated the disappearance of the starting material. Subsequently, the volatiles were removed by co-evaporation with toluene (3x), chloroform (1x), and Et$_2$O (1x). The resulting residue was triturated in Et$_2$O and used for the next step without further purification.

In a round bottom flask (A), the commercially available *N*-Cbz-amino acids **24,25** (1.2 eq.) were dissolved in DCM (10 mL/mmol) and cooled down up to 0 °C with an ice bath. TBTU (1.2 eq.) and DIPEA (2 eq.) were added and the reaction was kept in vigorously stirring for 30 min. Meanwhile, the trifluoroacetate salts **22,23** (1 eq.) were suspended in DCM (10 mL/mmol) and DIPEA (2eq.) was added at 0 °C. The pH was checked (>8) and the resulting solution was added dropwise to the flask A. After that, the reaction was left in stirring at rt on. Subsequently, DCM vas removed *in vacuo*, and the residue was dissolved in EtOAc and washed with 1 M HCl (x 2), NaHCO$_3$ saturated solution (x 2), and brine (x 2), dried over Na$_2$SO$_4$, and concentrated *in vacuo*. The obtained crude was purified using the appropriate eluent mixture below described.

Benzyl ((S)-1-(((S)-1-(methoxy(methyl)amino)-1-oxopentan-2-yl)amino)-4-methyl-1-oxopentan-2-yl)carbamate (26)
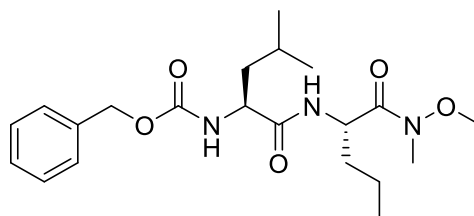
In this reaction Cbz-Leu-OH **24** was used as the acid and the trifluoroacetate salts **22** was used as amine. Consistency = white powder; Yield = 88%; R_f = 0.29 in Ex/EtOAc 3:2. ^{1}H NMR (500 MHz) in CDCl$_3$, d = 0.62 (dd, J = 12.9, 6.9 Hz, 9H), 0.98 - 1.18 (m, 4H), 1.25 – 1.37 (m, 3H), 1.37 – 1.51 (m, 2H), 2.92 (s, 3H), 3.50 (s, 3H), 4.16 (td, J = 9.1, 5.6 Hz, 1H), 4.79 (d, J = 12.5

Hz, 2H), 4.85 (d, J = 12.3 Hz, 1H), 5.94 (d, J = 8.7 Hz, 1H), 7.08 – 6.92 (m, 5H), 7.32 (d, J = 8.2 Hz, 1H); ^{13}C NMR (125 MHz, CDCl$_3$): δ = 13.72, 18.54, 21.77, 23.01, 24.61, 32.11, 34.65, 48.98, 53.48, 61.55, 66.92, 125.68, 128.09, 128.48, 136.26, 156.05, 171.96, 172.42.

Benzyl ((S)-1-(((S)-1-(methoxy(methyl)amino)-1-oxopentan-2-yl)amino)-1-oxo-3-phenylpropan-2-yl)carbamate (27)
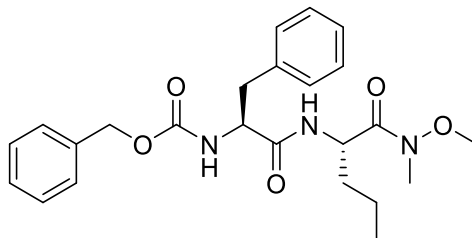
In this reaction Cbz-Phe-OH **25** was used as the acid and the trifluoroacetate salts **22** was used as amine. Consistency = yellow powder; Yield = 66%; R_f = 0.30 in Ex/EtOAc 3:2. ^{1}H NMR (500 MHz) in CDCl$_3$, d = 0.87 (t, J = 7.3 Hz, 3H), 1.11 (d, J = 5.6 Hz, 1H), 1.17 – 1.32 (m, 3H), 1.46 – 1.58 (m, 1H), 1.60 – 1.73 (m, 1H), 3.18 (s, 3H), 3.74 (s, 3H), 4.49 (d, J = 6.4 Hz, 1H), 4.94 (s, 1H), 5.02 – 5.12 (m, 2H), 5.34 (d, J = 7.5 Hz, 1H), 6.60 (d, J = 6.1 Hz, 1H), 7.13 – 7.38 (m, 10H); ^{13}C NMR (125 MHz, CDCl$_3$): δ = 13.70, 18.46, 31.86, 34.66, 38.47, 48.95, 55.94, 61.59, 66.98, 126.94, 128.00, 128.11, 128.48, 128.56, 129.36, 129.63, 136.23, 155.82, 170.43, 172.15.
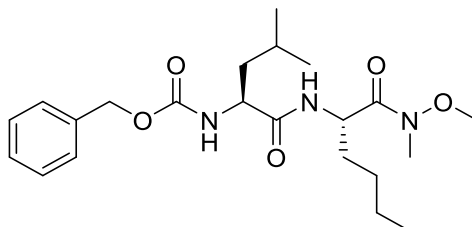
Benzyl ((S)-1-(((S)-1-(methoxy(methyl)amino)-1-oxohexan-2-yl)amino)-4-methyl-1-oxopentan-2-yl)carbamate (28)

In this reaction Cbz-Leu-OH **24** was used as the acid and the trifluoroacetate salts **23** was used as amine. Consistency = white powder; Yield = 99%; R_f = 0.37 in Ex/EtOAc 3:2. ^{1}H NMR (500 MHz) in CDCl$_3$, d = 0.87 (t, J = 6.5 Hz, 3H), 0.93 (t, J = 5.9 Hz, 6H), 1.22 – 1.36 (m, 4H), 1.46 – 1.80 (m, 5H), 3.20 (s, 3H), 3.76 (s, 3H), 4.23 (d, J = 5.0 Hz, 1H), 4.95 (s, 1H), 5.04 – 5.15 (m, 2H), 5.21 (d, J = 8.2 Hz, 1H), 6.59 (d, J = 7.6 Hz, 1H), 7.26 – 7.39 (m, 5H); ^{13}C NMR (125 MHz, CDCl$_3$): δ = 13.82, 21.88, 22.30, 23.00, 24.61, 27.26, 32.10, 32.21, 41.80, 49.15, 53.50, 61.58, 66.98, 128.01, 128.11, 128.49, 136.23, 156.06, 171.88, 172.34.

Benzyl ((S)-1-(((S)-1-(methoxy(methyl)amino)-1-oxohexan-2-yl)amino)-1-oxo-3-phenylpropan-2-yl)carbamate (29)
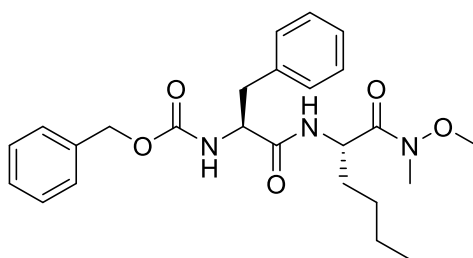
In this reaction Cbz-Phe-OH **25** was used as the acid and the trifluoroacetate salts **23** was used as amine. Consistency = colorless oil; Yield = 64%; R_f = 0.47 in Ex/EtOAc 1:1. ^{1}H NMR (500 MHz) in CDCl$_3$, d = 0.85 (t, J = 7.1 Hz, 3H), 1.16 – 1.36 (m, 4H), 1.47 – 1.59 (m, 1H), 1.65 – 1.75 (m, 1H), 3.02 – 3.13 (m, 2H), 3.18 (s, 3H), 3.74 (s, 3H), 4.50 (d, J = 6.7 Hz, 1H), 4.94 (d, J = 5.1 Hz, 1H), 5.02 – 5.14 (m, 2H), 5.34 (d, J = 7.4 Hz, 1H), 6.60 (d, J = 6.9 Hz, 1H), 7.10 – 7.38 (m, 10H); ^{13}C NMR (125 MHz, CDCl$_3$): δ = 13.82, 22.32, 27.18, 31.97, 32.23, 38.46, 49.16, 55.90, 61.51, 66.98, 126.95, 128.01, 128.12, 128.49, 128.56, 129.37, 136.23, 155.82, 170.40, 172.05.

General Procedure for the Warhead Incorporation in 30-33

In a round-bottom flask, the intermediates **26-29** (1 eq.) were solubilized in dry THF (20 mL/mmol), cooled down to -10 °C with an ice/salt bath, and vigorously stirred. LiAlH$_4$ (1 eq.) was added each 30 min until the TLC monitoring (DCM/MeOH 19:1) did not show the presence of starting material. Cold temperature was kept. Afterwards, the unreacted LiAlH$_4$ was quenched with 1 M KHSO$_4$ and the ice-bath was removed. The suspension was moved in a separatory funnel, DCM was added, and the two phases were separated. The organic phase was further extracted with DCM (x 3). Subsequently, the merged organic phases were washed with NaHCO$_3$ saturated solution (x 2), 1 M KHSO$_4$ (x 2) and brine (x 2), dried over Na$_2$SO$_4$ and concentrated. The obtained residues were used for the next step without further purification. In a round-bottom flask, the aldehydes were solubilized in DCM (5 mL/mmol) and the appropriate Wittig reagent (1 eq.) was added in one portion. The reaction was stirred at rt for 2 h. After that, the solvent was removed *in vacuo* and the desired products were purified by column chromatography using the appropriate eluent below described.

Methyl (S,E)-4-((S)-2-(((benzyloxy)carbonyl)amino)-4-methylpentanamido)hept-2-enoate (30)
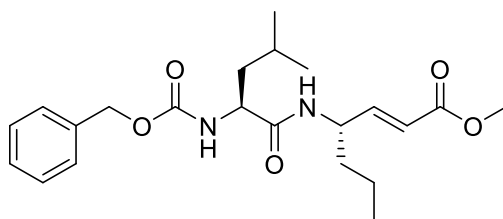
In this reaction the intermediate **26** was used as substrate. Consistency = white powder; Yield = 87%; R_f = 0.32 in Ex/EtOAc 7:3. ^{1}H NMR (500 MHz) in CDCl$_3$, d = 0.84 – 0.97 (m, 9H), 1.23 – 1.38 (m, 3H), 1.40 – 1.60 (m, 2H), 1.60 – 1.70 (m, 2H), 3.72 (s, 3H), 4.17 (d, J = 4.3 Hz, 1H), 4.58 (dt, J = 12.7, 6.3 Hz, 1H), 5.05 – 5.15 (m, 2H), 5.23 (d, J = 8.2 Hz, 1H), 5.89 (d, J = 15.6 Hz, 1H), 6.30 (d, J = 6.6 Hz, 1H), 6.82 (dd, J = 15.7, 5.5 Hz, 1H), 7.28 – 7.37 (m, 5H);

^{13}C NMR (125 MHz, CDCl$_3$): δ = 13.68, 18.82, 21.97, 22.89, 24.69, 36.30, 40.95, 49.80, 51.62, 53.50, 67.16, 120.61, 128.00, 128.25, 128.53, 136.02, 147.81, 155.97, 166.57, 171.66. Elemental analysis for C$_{22}$H$_{32}$N$_2$O$_5$, C, 65.32; H, 7.97; N, 6.93; found: C, 65.49; H, 7.76; N, 7.15.

Methyl (S,E)-4-((S)-2-(((benzyloxy)carbonyl)amino)-3-phenylpropanamido)hept-2-enoate (31)
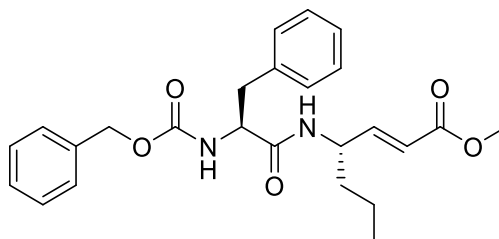
In this reaction the intermediate **27** was used as substrate. Consistency = white powder; Yield = 77%; R_f = 0.30 in Ex/EtOAc 7:3. ^{1}H NMR (500 MHz) in CDCl$_3$, d = 0.86 (t, J = 7.3 Hz, 3H), 1.30 – 1.13 (m, 2H), 1.37 (dt, J = 13.5, 8.2 Hz, 1H), 1.41 – 1.52 (m, 1H), 3.01 (dd, J = 13.7, 7.9 Hz, 1H), 3.11 (dd, J = 13.6, 6.1 Hz, 1H), 3.73 (s, 3H), 4.37 (d, J = 7.0 Hz, 1H), 4.47 – 4.57 (m, 1H), 5.08 (q, J = 12.3 Hz, 2H), 5.38 (s, 1H), 5.66 (d, J = 15.7 Hz, 1H), 5.79 (s, 1H), 6.63 (dd, J = 15.7, 5.8 Hz, 1H), 7.14 – 7.38 (m, 10H); ^{13}C NMR (125 MHz, CDCl$_3$): δ = 13.63, 18.71, 36.18, 38.52, 49.83, 51.58, 56.24, 67.08, 120.75, 127.20, 128.05, 128.20, 128.27, 128.55, 128.82, 129.27, 135.98, 136.16, 147.29, 155.93, 166.55, 170.24. Elemental analysis for C$_{25}$H$_{30}$N$_2$O$_5$, C, 68.47; H, 6.90; N, 6.39; found: C, 68.32; H, 6.83; N, 6.51.

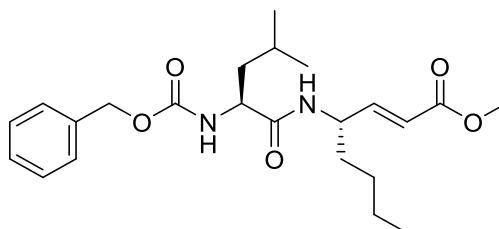***Methyl (S,E)-4-((S)-2-(((benzyloxy)carbonyl)amino)-4-methylpentanamido)oct-2-enoate (32)***

In this reaction the intermediate **28** was used as substrate. Consistency = white powder; Yield = 87%; R_f = 0.42 in Ex/EtOAc 7:3. ^{1}H NMR (500 MHz) in CDCl$_3$, d = 0.86 (t, J = 6.4 Hz, 3H), 0.92 (t, J = 5.6 Hz, 6H), 1.28 (s, 4H), 1.53 (dd, J = 17.3, 8.6 Hz, 3H), 1.59 – 1.71 (m, 2H), 3.72 (s, 3H), 4.17 (s, 1H), 4.50 – 4.61 (m, 1H), 5.09 (s, 2H), 5.30 (d, J = 8.1 Hz, 1H), 5.89 (d, J = 15.7 Hz, 1H), 6.39 (d, J = 6.4 Hz, 1H), 6.83 (dd, J = 15.6, 4.8 Hz, 1H), 7.37 – 7.27 (m, 5H); ^{13}C NMR (125 MHz, CDCl$_3$): δ = 13.86, 22.00, 22.29, 22.88, 24.68, 27.65, 33.93, 41.01, 50.01, 51.62, 53.58, 67.15, 120.61, 127.98, 128.24, 128.53, 135.81, 147.87, 156.29, 166.67, 171.70. Elemental analysis for C$_{23}$H$_{34}$N$_2$O$_5$, C, 66.00; H, 8.19; N, 6.69; found: C, 65.79; H, 8.45; N, 6.82.

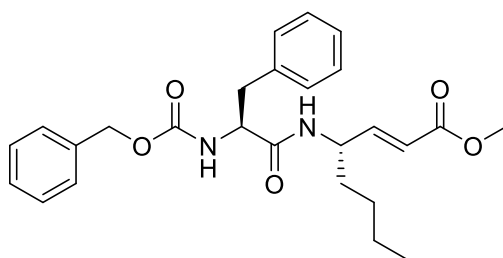***Methyl (S,E)-4-((S)-2-(((benzyloxy)carbonyl)amino)-3-phenylpropanamido)oct-2-enoate (33)***

In this reaction the intermediate **29** was used as substrate. Consistency = white powder; Yield = 81%; R_f = 0.32 in Ex/EtOAc 7:3. ^{1}H NMR (500 MHz) in CDCl$_3$, d = 0.84 (t, J = 7.1 Hz, 3H), 1.12 – 1.31 (m, 4H), 1.40 (dd, J = 14.4, 7.4 Hz, 1H), 1.48 (td, J = 14.1, 7.0 Hz, 1H), 3.00 (dd, J = 13.7, 7.7 Hz, 1H), 3.11 (dd, J = 13.5, 6.1 Hz, 1H), 3.73 (s, 3H), 4.38 (d, J = 7.0 Hz, 1H), 4.44 – 4.55 (m, 1H), 5.03 – 5.13 (m, 2H), 5.41 (s, 1H), 5.67 (d, J = 15.7 Hz, 1H), 5.86 (s, 1H), 6.63 (dd, J = 15.7, 5.6 Hz, 1H), 7.10 – 7.38 (m, 11H); ^{13}C NMR (125 MHz, CDCl$_3$): δ = 13.83, 22.26, 27.54, 33.84, 38.57, 50.06, 51.58, 56.52, 67.15, 120.76, 127.19, 128.04, 128.27, 128.29, 128.55, 128.81, 135.99, 136.17, 147.34, 166.56, 170.24. Elemental analysis for C$_{26}$H$_{33}$N$_2$O$_5$, C, 69.01; H, 7.13; N, 6.19; found: C, 69.17; H, 7.25; N, 6.02.

General Procedure for the Hydrolysis to Produce 34-37

In a round bottom flask (A), the esters **30-33** (1 eq.) were dissolve in MeOH and THF (solvent mix = 1 mmol/ 10 mL) and cooled down up to 0 °C with ice bath. After this H$_2$O and LiOH (2.5 eq) were added. The reaction was maintained in stirring on until TLC monitoring (using the same eluent mixture as for the purification of the starting compound) showed the disappearance of the starting material. Solvents were removed *in vacuo*. Subsequently, the resulting residue was dissolved in water and the aqueous phase was washed with Et$_2$O (x 2). The resulting aqueous phase was acidified with 1 M HCl up to pH 2, the organic phase was extracted with EtOAc (x 3) and washed with brine, dried over Na$_2$SO$_4$ and concentrated *in vacuo*. The resulting residue was used for the next step without further purification.

(S,E)-4-((S)-2-((((Benzyloxy)carbonyl)amino)-4-methylpentanamido)hept-2-enoic acid (34)
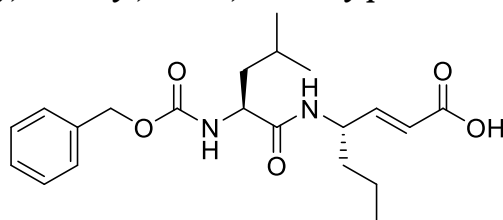
In this reaction the ester **30** was used as substrate. Consistency = colorless oil; Yield = 87%; R_f = 0.44 in DCM/MeOH 9:1. ^{1}H NMR (500 MHz) in CDCl$_3$, d = 0.84 – 0.99 (m, 9H), 1.24 – 1.36 (m, 3H), 1.42 – 1.68 (m, 4H), 4.20-4.30 (m, 1H), 4.54-4.64 (m, 1H), 5.08 (s, 2H), 5.80 (d, J = 8.2 Hz, 1H), 5.89 (dd, J = 15.4, 7.6 Hz, 1H), 5.90-5.96 (m, 1H), 7.28 – 7.36 (m, 5H); ^{13}C NMR (125 MHz, CDCl$_3$): δ = 13.68, 18.80, 21.98, 22.76, 24.66, 36.19, 41.00, 49.95, 53.58, 67.18, 120.54, 127.90, 128.21, 128.53, 136.01, 149.50, 156.69, 169.98, 172.37. Elemental analysis for C$_{21}$H$_{30}$N$_2$O$_5$, C, 64.60; H, 7.74; N, 7.17; found: C, 64.74; H, 7.49; N, 7.28.

(S,E)-4-((S)-2-((((Benzyloxy)carbonyl)amino)-3-phenylpropanamido)hept-2-enoic acid (35)
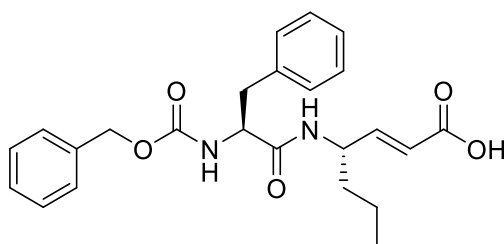
In this reaction the ester **31** was used as substrate. Consistency = white powder; Yield = 65%; R_f = 0.53 in DCM/MeOH 95:5. ^{1}H NMR (500 MHz) in CDCl$_3$, d = 0.86 (t, J = 7.3 Hz, 3H), 1.23-1.28 (m, 2H), 1.35-1.51 (m, 2H), 2.97-3.05 (m, 1H), 3.10 (dd, J = 13.7, 6.4 Hz, 1H), 4.35-4.43 (m, 1H), 4.49-4.57 (m, 1H), 5.07 (d, J = 12.0 Hz, 1H), 5.11 (d, J = 12.2 Hz, 1H), 5.55 (d, J = 7.7 Hz, 1H), 5.62 (d, J = 16.2 Hz, 1H), 5.95-6.02 (m, 1H), 6.70 (dd, J = 15.8, 5.3 Hz, 1H), 7.13-7.21 (m, 3H), 7.21-7.38 (m, 8H). Elemental analysis for C$_{24}$H$_{28}$N$_2$O$_5$, C, 67.91; H, 6.65; N, 6.60; found: C, 67.76; H, 6.95; N, 6.82.

(S,E)-4-((S)-2-((((Benzyloxy)carbonyl)amino)-4-methylpentanamido)oct-2-enoic acid (36)
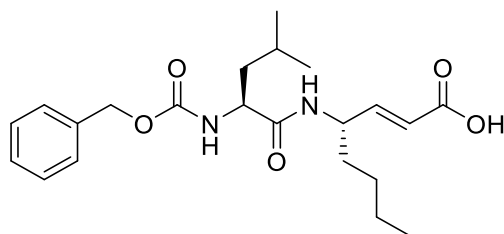
In this reaction the ester **32** was used as substrate. Consistency = colorless oil; Yield = 83%; R_f = 0.51 in DCM/MeOH 95:5. ^{1}H NMR (500 MHz) in CDCl$_3$, d = 0.84 (t, J = 6.4 Hz, 3H), 0.90-0.99 (m, 6H), 1.28 (bs, 4H), 1.53 (dd, J = 17.3, 8.6 Hz, 3H), 1.59-1.71 (m, 2H), 4.24 (bs, 1H), 4.53 – 4.62 (m, 1H), 5.12 (s, 2H), 5.61 (d, J = 8.1 Hz, 1H), 5.90 (dd, J = 15.9, 7.1 Hz, 1H), 6.75 (d, J = 6.4 Hz, 1H), 6.87-6.95 (m, 1H), 7.25 – 7.38 (m, 5H); ^{13}C NMR (125 MHz, CDCl$_3$): δ = 13.86, 22.00, 22.29, 22.78, 24.67, 27.62, 33.83, 40.91, 50.13, 53.60, 67.25, 120.46, 127.97, 128.26, 128.55, 136.04, 149.69, 156.63, 171.23, 172.14. Elemental analysis for C$_{22}$H$_{32}$N$_2$O$_5$, C, 65.32; H, 7.97; N, 6.93; found: C, 64.98; H, 7.81; N, 7.22.

(S,E)-4-((S)-2-((((Benzyloxy)carbonyl)amino)-3-phenylpropanamido)oct-2-enoic acid (37)
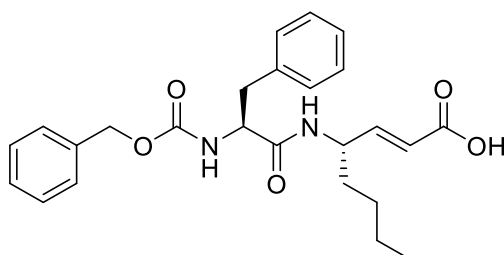
In this reaction the ester **33** was used as substrate. Consistency = white powder; Yield = 87%; R_f = 0.72 in DCM/MeOH 9:1. ^{1}H NMR (500 MHz) in CDCl$_3$, d = 0.84 (t, J = 6.9 Hz, 3H), 1.12-1.32 (m, 4H), 1.36-1.45 (m, 1H), 1.45-1.54 (m, 1H), 2.95-3.20 (m, 2H), 4.38-4.56 (m, 2H), 5.06 (s, 2H), 5.62 (d, J = 15.2 Hz, 1H), 5.80 (bs, 1H), 6.32 (bs, 1H), 6.71 (dd, J = 15.6, 5.3 Hz, 1H), 6.71 (dd, J = 15.6, 5.3 Hz, 1H), 7.09-7.38 (m, 10H). ^{13}C NMR (125 MHz) in CDCl$_3$, d = 13.98, 22.40, 27.69, 33.89, 38.68, 50.31, 56.72, 67.38, 120.67, 127.40, 128.15, 128.41, 128.70,

128.94, 129.41, 136.09, 136.21, 149.35, 156.41, 170.27, 170.98. Elemental analysis for $C_{25}H_{30}N_2O_5$, C, 68.47; H, 6.90; N, 6.39; found: C, 68.76; H, 6.81; N, 6.13.

General Procedure for the Synthesis of Final Compounds EC1-EC8

In a round bottom flask (A), the intermediates **34-37** (1.2 eq.) were dissolved in DCM (10 mL/mmol) and cooled down up to 0 °C with an ice bath. TBTU (1.2 eq.) and DIPEA (2.5 eq.) were added and the reaction was kept in vigorously stirring for 30 min. Meanwhile, the appropriate amine (1 eq) was added at 0 °C. The pH was checked (>8) and the resulting solution was added dropwise to the flask A. After that, the reaction was left in stirring at rt on. Subsequently, DCM vas removed *in vacuo*, and the residue was dissolved in EtOAc and washed with 1 M HCl (x 2), NaHCO₃ saturated solution (x 2), and brine (x 2), dried over Na₂SO₄, and concentrated *in vacuo*. The obtained crude was purified using the appropriate eluent mixture below described.

*Benzyl ((S)-4-methyl-1-oxo-1-(((S,E)-1-oxo-1-(phenylamino)hept-2-en-4-yl)amino)pentan-2-yl)carbamate (EC1)*
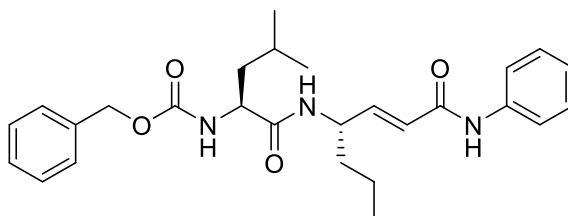
In this reaction the acid **34** was used as substrate. Consistency = white powder; Yield = 52%; R_f = 0.35 in CHCl₃/MeOH 10:0.1. ¹H NMR (500 MHz) in MeOD, d = 0.80-0.91 (m, 9H), 1.20-1.31 (m, 2H), 1.42-1.59 (m, 3H), 1.62–1.77 (m, 2H), 4.28-4.34 (m, 1H), 4.42-4.56 (m, 1H), 5.26 (s, 2H), 5.74 (d, J = 15.4 Hz, 1H), 6.53 (dd, J = 15.4, 6.3 Hz, 1H), 7.14-7.19 (m, 2H), 7.24-7.30 (m, 5H), 7.32-7.39 (m, 6H). ¹³C NMR (125 MHz) in MeOD, d = 12.64, 21.89, 22.20, 23.19, 25.31, 33.47, 40.65, 50.17, 56.68, 66.12, 123.18, 126.74, 127.30, 127.65, 128.22, 128.24, 129.10, 136.67, 138.33, 143.19, 166.60, 172.21, 177.13. Elemental analysis for $C_{27}H_{35}N_3O_4$: calculated = C, 69.65; H, 7.58; N, 9.03; found = C, 69.50, H, 7.29, N, 9.26.

Benzyl ((S)-1-oxo-1-(((S,E)-1-oxo-1-(phenylamino)hept-2-en-4-yl)amino)-3-phenylpropan-2-yl)carbamate (EC2)
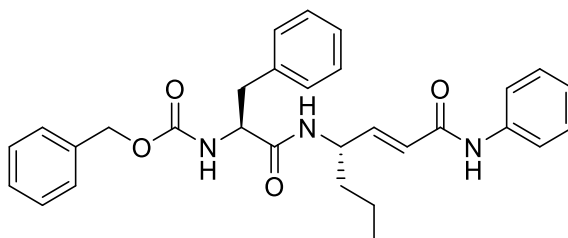
In this reaction the acid **35** was used as substrate. Consistency = white powder; Yield = 56%; R_f = 0.41 in CHCl₃/MeOH 10:0.1. ¹H NMR (500 MHz) in MeOD, d = 0.83-0.90 (m, 3H), 1.22-1.31 (m, 2H), 1.48-1.57 (m, 2H), 2.90 (dd, J = 13.5, 6.9 Hz, 1H), 3.09 (dd, J = 13.5, 6.9 Hz, 1H), 4.30-4.38 (m, 1H), 4.38-4.45 (m, 1H), 5.12 (d, J = 12.8 Hz, 1H), 5.14 (d, J = 12.6 Hz, 1H), 5.84 (d, J = 15.5 Hz, 1H), 6.49 (dd, J = 15.5, 6.3 Hz, 1H), 7.05-7.12 (m, 2H), 7.12-7.20 (m,

5H), 7.29-7.35 (m, 11H). ^{13}C NMR (125 MHz) in MeOD, d = 12.98, 22.07, 31.32, 37.68, 50.26, 56.49, 66.12, 123.34, 126.32, 126.74, 127.45, 127.58, 127.73, 128.23, 128.34, 128.52, 129.34, 136.89, 137.03, 138.64, 143.53, 166.78, 172.23, 177.34. Elemental analysis for $C_{30}H_{33}N_3O_4$: calculated = C, 72.12; H, 6.66; N, 8.41; found = C, 72.03, H, 6.98, N, 8.71.

Benzyl ((S)-4-methyl-1-oxo-1-(((S,E)-1-oxo-1-(phenylamino)oct-2-en-4-yl)amino)pentan-2-yl)carbamate (EC3)
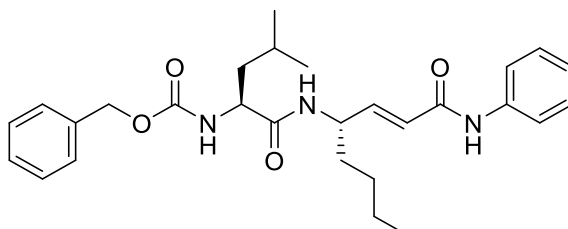
In this reaction the acid **36** was used as substrate. Consistency = white powder; Yield = 54%; R_f = 0.39 in CHCl$_3$/MeOH 10:0.1. ^{1}H NMR (500 MHz) in MeOD, d = 0.82-0.98 (m, 9H), 1.24-1.35 (m, 4H), 1.43-1.61 (m, 3H), 1.70–1.83 (m, 2H), 4.33-4.39 (m, 1H), 4.45-4.51 (m, 1H), 5.13 (s, 2H), 5.89 (d, J = 15.4 Hz, 1H), 6.63 (dd, J = 15.4, 6.3 Hz, 1H), 7.12-7.29 (m, 2H), 7.21-7.25 (m, 5H), 7.27-7.40 (m, 6H). ^{13}C NMR (125 MHz) in MeOD, d = 12.81, 21.99, 22.06, 23.20, 25.14, 27.77, 33.47, 40.65, 50.17, 56.63, 66.12, 123.03, 126.85, 127.24, 127.51, 128.04, 128.18, 129.00, 136.71, 138.39, 143.13, 166.59, 172.10, 177.11. Elemental analysis for $C_{28}H_{37}N_3O_4$: calculated = C, 70.12; H, 7.78; N, 8.76; found = C, 70.33, H, 7.94, N, 8.62.

Benzyl ((S)-1-oxo-1-(((S,E)-1-oxo-1-(phenylamino)oct-2-en-4-yl)amino)-3-phenylpropan-2-yl)carbamate (EC4)
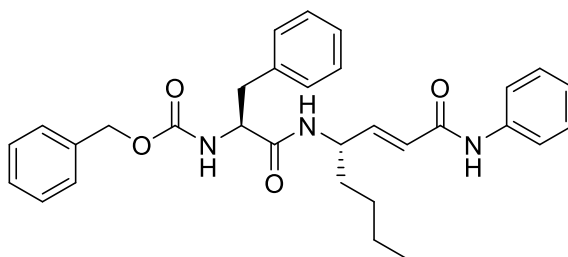
In this reaction the acid **37** was used as substrate. Consistency = white powder; Yield = 53%; R_f = 0.39 in CHCl$_3$/MeOH 10:0.1. ^{1}H NMR (500 MHz) in MeOD, d = 0.86-0.99 (m, 3H), 1.27-1.38 (m, 4H), 1.51-1.64 (m, 2H), 2.89 (dd, J = 13.6, 6.7 Hz, 1H), 3.11 (dd, J = 13.6, 6.7 Hz, 1H), 4.35-4.41 (m, 1H), 4.42-4.49 (m, 1H), 5.04 (d, J = 12.9 Hz, 1H), 5.07 (d, J = 12.5 Hz, 1H), 5.88 (d, J = 15.4 Hz, 1H), 6.57 (dd, J = 15.4, 6.3 Hz, 1H), 7.12-7.19 (m, 2H), 7.18-7.26 (m, 5H), 7.27-7.37 (m, 11H). ^{13}C NMR (125 MHz) in MeOD, d = 12.83, 21.95, 27.71, 33.44, 37.90, 50.13, 56.59, 66.19, 123.07, 126.30, 126.88, 127.29, 127.31, 127.56, 128.05, 128.09, 128.13, 129.05, 136.74, 136.95, 138.42, 143.12, 166.51, 172.03, 177.07. Elemental analysis for $C_{31}H_{35}N_3O_4$: calculated = C, 72.49; H, 6.87; N, 8.18; found = C, 72.54, H, 7.12, N, 7.94.

Benzyl ((S)-1-(((S,E)-1-(benzylamino)-1-oxohept-2-en-4-yl)amino)-4-methyl-1-oxopentan-2-yl)carbamate (EC5)
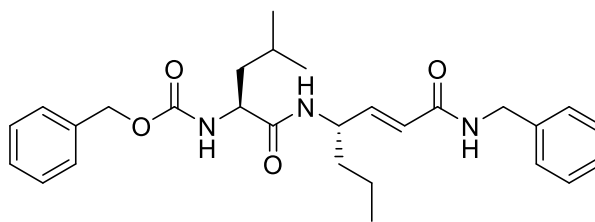
In this reaction the acid **34** was used as substrate. Consistency = white powder; Yield = 67%; R_f = 0.37 in CHCl₃/MeOH 10:0.1. ¹H NMR (500 MHz) in MeOD, *d* = 0.82-0.95 (m, 9H), 1.23-1.34 (m, 2H), 1.40-1.58 (m, 3H), 1.65–1.73 (m, 2H), 4.27-4.36 (m, 1H), 4.44-4.51 (m, 1H), 4.53 (s, 2H), 5.23 (s, 2H), 5.78 (d, *J* = 15.4 Hz, 1H), 6.59 (dd, *J* = 15.4, 6.3 Hz, 1H), 7.10-7.16 (m, 2H), 7.27-7.32 (m, 5H), 7.33-7.40 (m, 6H). ¹³C NMR (125 MHz) in MeOD, *d* = 12.67, 21.81, 22.02, 23.14, 25.23, 33.41, 40.69, 43.82, 50.18, 56.61, 66.08, 123.12, 126.70, 127.34, 127.69, 128.20, 128.23, 129.01, 136.65, 138.39, 143.13, 166.64, 172.12, 177.07. Elemental analysis for C₂₈H₃₇N₃O₄: calculated = C, 70.12; H, 7.78; N, 8.76; found = C, 69.98, H, 7.95, N, 9.02.

Benzyl ((S)-1-(((S,E)-1-(benzylamino)-1-oxohept-2-en-4-yl)amino)-1-oxo-3-phenylpropan-2-yl)carbamate (EC6)
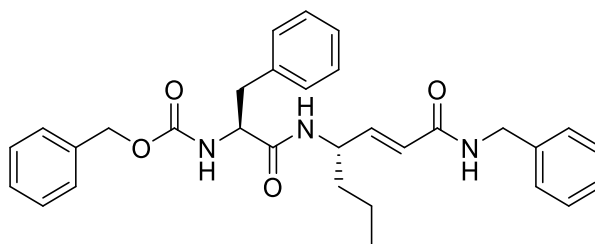
In this reaction the acid **35** was used as substrate. Consistency = white powder; Yield = 69%; R_f = 0.34 in CHCl₃/MeOH 10:0.1. ¹H NMR (500 MHz) in MeOD, *d* = 0.78-0.85 (m, 3H), 1.22-1.30 (m, 2H), 1.43-1.51 (m, 2H), 2.86 (dd, *J* = 13.5, 6.7 Hz, 1H), 3.06 (dd, *J* = 13.5, 6.7 Hz, 1H), 4.25-4.32 (m, 1H), 4.32-4.39 (m, 1H), 4.42 (s, 2H), 5.08 (d, *J* = 12.8 Hz, 1H), 5.13 (d, *J* = 12.6 Hz, 1H), 5.76 (d, *J* = 15.5 Hz, 1H), 6.38 (dd, *J* = 15.5, 6.3 Hz, 1H), 7.07-7.17 (m, 2H), 7.19-7.25 (m, 5H), 7.26-7.34 (m, 11H). ¹³C NMR (125 MHz) in MeOD, *d* = 13.05, 22.23, 31.41, 37.74, 42.87, 50.34, 56.58, 66.23, 123.25, 126.12, 126.34, 127.38, 127.41, 127.89, 128.10, 128.19, 128.28, 129.12, 136.74, 137.14, 138.89, 143.54, 166.98, 172.45, 177.13. Elemental analysis for C₃₁H₃₅N₃O₄: calculated = C, 72.49; H, 6.87; N, 8.18; found = C, 72.23, H, 6.62, N, 8.35.

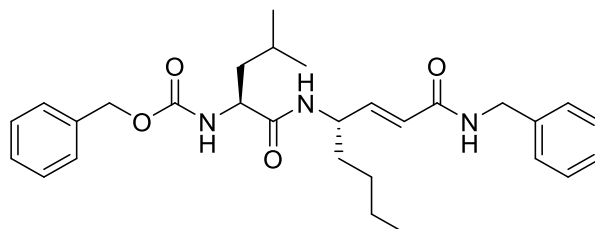**Benzyl ((S)-1-(((S,E)-1-(benzylamino)-1-oxooct-2-en-4-yl)amino)-4-methyl-1-oxopentan-2-yl)carbamate (EC7)**

In this reaction the acid **36** was used as substrate. Consistency = white powder; Yield = 70%; R_f = 0.36 in CHCl₃/MeOH 10:0.1. ¹H NMR (500 MHz) in MeOD, *d* = 0.86-1.02 (m, 9H), 1.27-

1.38 (m, 4H), 1.46-1.64 (m, 3H), 1.72–1.82 (m, 2H), 4.30-4.38 (m, 1H), 4.42-4.49 (m, 1H), 4.52 (s, 2H), 5.19 (s, 2H), 5.85 (d, J = 15.4 Hz, 1H), 6.59 (dd, J = 15.4, 6.3 Hz, 1H), 7.15-7.20 (m, 2H), 7.23-7.29 (m, 5H), 7.29-7.39 (m, 6H). ^{13}C NMR (125 MHz) in MeOD, d = 12.83, 21.95, 22.09, 23.19, 25.11, 27.71, 33.44, 40.61, 43.78, 50.13, 56.59, 66.19, 123.07, 126.88, 127.29, 127.56, 128.09, 128.13, 129.05, 136.74, 138.42, 143.12, 166.51, 172.03, 177.07. Elemental analysis for $C_{29}H_{39}N_3O_4$: calculated = C, 70.56; H, 7.96; N, 8.51; found = C, 70.39, H, 7.90, N, 8.67.

Benzyl ((S)-1-(((S,E)-1-(benzylamino)-1-oxooct-2-en-4-yl)amino)-1-oxo-3-phenylpropan-2-yl)carbamate (EC8)
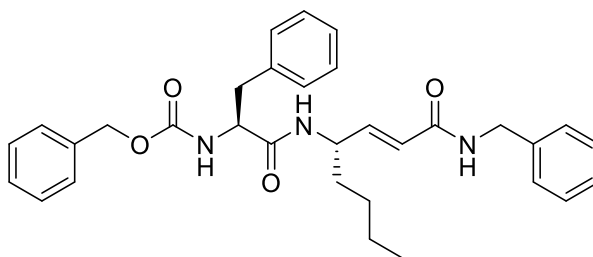
In this reaction the acid **37** was used as substrate. Consistency = white powder; Yield = 64%; R_f = 0.37 in CHCl$_3$/MeOH 10:0.1. ^{1}H NMR (500 MHz) in MeOD, d = 0.81-0.93 (m, 3H), 1.23-1.35 (m, 4H), 1.47-1.60 (m, 2H), 2.87 (dd, J = 13.5, 8.6 Hz, 1H), 3.07 (dd, J = 13.6, 6.6 Hz, 1H), 4.32-4.38 (m, 1H), 4.38-4.46 (m, 1H), 4.41 (s, 2H), 5.00 (d, J = 12.9 Hz, 1H), 5.04 (d, J = 12.5 Hz, 1H), 5.85 (d, J = 15.4 Hz, 1H), 6.54 (dd, J = 15.4, 6.3 Hz, 1H), 7.08-7.14 (m, 2H), 7.14-7.22 (m, 5H), 7.22-7.34 (m, 11H). ^{13}C NMR (125 MHz) in MeOD, d = 12.86, 21.93, 27.68, 33.40, 37.91, 42.80, 50.17, 56.56, 66.15, 123.02, 126.36, 126.90, 127.27, 127.33, 127.52, 128.01, 128.04, 128.16, 129.00, 136.74, 136.91, 138.44, 143.15, 166.48, 172.07, 176.99. Elemental analysis for $C_{32}H_{37}N_3O_4$: calculated = C, 72.84, H, 7.07, N, 7.96; found = C, 72.62, H, 7.32, N, 7.88.

9.1.4. Synthesis of Compounds SPR81-SPR102

General Procedure for Coupling Reactions (GP1)

In a round bottom flask (A), the appropriate acid (1.5 eq.) was dissolved in DCM (10 mL/mmol) and cooled down up to 0 °C with an ice bath. TBTU (1.5 eq.) and DIPEA (2 eq.) were added and the reaction was kept in vigorously stirring for 20 min. Meanwhile, the appropriate amine (1 eq.) was suspended in DCM (10 mL/mmol) and DIPEA (2eq.) was added at 0 °C. The pH was checked (>8) and the resulting solution was added dropwise to the flask A. After that, the reaction was left in stirring at rt on. Subsequently, DCM vas removed *in vacuo*, and the residue was dissolved in EtOAc and washed with 1 M HCl (x 2), NaHCO$_3$ saturated solution (x 2), and brine (x 2), dried over Na$_2$SO$_4$, and concentrated *in vacuo*. The obtained crudes were purified using the appropriate eluent mixture.

General Procedure for the Hydrolysis Reaction (GP2)

In a round bottom flask (A), the appropriate ester (1 eq.) was dissolved in MeOH and Dioxane (1:1, solvent mix = 1 mmol/ 10 mL) and cooled down up to 0 °C with ice bath. After this H_2O (1 mmol/ 10 mL) and LiOH (3 eq) were added. The reaction was maintained in stirring until TLC monitoring showed the disappearance of the starting material (normally overnight). Solvents were removed *in vacuo*. Subsequently, the resulting residue was dissolved in water and the aqueous phase was washed with Et_2O. The resulting aqueous phase was acidified with 1 M HCl up to pH 1, and the organic phase was extracted with EtOAc (x 3), dried over Na_2SO_4 and concentrated *in vacuo*. The resulting residues were used for the next step without further purification.

General Procedure for the Synthesis of Weinreb Amides (GP3)

In a round-bottom flask, the appropriate *N*-Boc amino acid (1 eq.) was dissolved in DCM (10 mL/mmol) and stirred at 0 °C. TBTU (1.2 eq.) and DIPEA (3 eq.) were added and the reaction was maintained in stirring for 30 min at 0 °C. After this time, N,O-dimethylhydroxylamine hydrochloride (1.2 eq.) was added portion-wise, and the pH was checked (>8). The reaction was vigorously stirred at rt on. After this time, DCM vas removed *in vacuo*, and the resulting residue was dissolved in EtOAc washed with 1 M HCl (x 2), $NaHCO_3$ saturated solution (x 2), and brine (x 2), dried over Na_2SO_4, and concentrated. The crude was purified using the appropriate eluent mixture.

General Procedure for the Warhead Incorporation (GP4)

In a round-bottom flask, the appropriate intermediate (1 eq.) were solubilized in dry THF (20 mL/mmol), cooled down to -10 °C with an ice/salt bath, and vigorously stirred. $LiAlH_4$ (1 eq.) was added over 30 min. After this period TLC monitoring did not show the presence of starting material. Cold temperature was kept. Aldehydes were detected by the treatment of the TLC with 2,4-dinitrophenylhydrazine TLC stain. Afterwards, the unreacted $LiAlH_4$ was quenched with 1 M $KHSO_4$ and the ice-bath was removed. The suspension was moved in a separatory funnel, DCM was added, and the two phases were separated. The organic phase was further extracted with DCM (x 3). Subsequently, the merged organic phases were washed with $NaHCO_3$ saturated solution (x 2), 1 M $KHSO_4$ (x 2) and brine (x 2), dried over Na_2SO_4 and concentrated. The obtained residue was used for the next step without further purification. In a round-bottom flask, the aldehyde was solubilized in DCM (5 mL/mmol) and the appropriate Wittig reagent (1 eq.) was added in one portion. The reaction was stirred at rt for 2 h. After that, the solvent was removed *in vacuo* and the desired product was purified using the appropriate eluent mixture.

General Procedure for the *N*-Boc-deprotection (GP5)

In a round-bottom flask, the appropriate *N*-Boc-protected intermediate (1 eq.) was dissolved in DCM (70% *v/v*) and cooled to 0°C. TFA (10 eq., 30% *v/v*) was then added dropwise. The reaction mixture was stirred vigorously at room temperature until TLC monitoring (using the

same eluent mixture as for the purification of the starting compound) indicated the disappearance of the starting material. Subsequently, the volatiles were removed by co-evaporation with toluene (3x), chloroform (1x), and Et₂O (1x). The resulting residues were triturated in Et₂O and used for the next step without further purification.

General Procedure for the Synthesis of Final Compounds SPR92-SPR102 (GP6)

In a round bottom flask (A), the trifluoroacetate salts of **SPR81-SPR91** (1 eq.) were dissolved in DCM (10 mL/mmol) and cooled down up to 0 °C with an ice bath. DIPEA (4 eq.) was added and the reaction was kept in vigorously stirring for 10 min. Later, acetic anhydride (1.5 eq.) was added at 0 °C. The pH was checked (>8) and the reaction was left in stirring at rt on. Subsequently, DCM vas removed *in vacuo*, and the residue was dissolved in EtOAc and washed with 1 M HCl (x 2), NaHCO₃ saturated solution (x 2), and brine (x 2), dried over Na₂SO₄, and concentrated *in vacuo*. The obtained crudes were purified using the appropriate eluent mixture below described.

Synthesis of Intermediates to Obtain the Final Compounds SPR81-SPR102

Methyl (tert-butoxycarbonyl)phenylalanylglycinate (43)
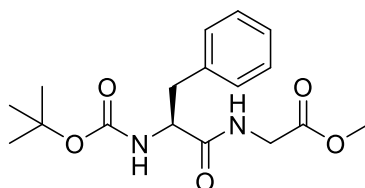
In this reaction Boc-Phe-OH **38** was used as the acid and H-Gly-OMe HCl **40** as the amine following the GP1. Consistency = White powder; Yield = 69%; R_f = 0.32 in EtOAc/light petroleum 3:2. ¹H NMR (500 MHz) in CDCl₃, d = 1.39 (s, 9H), 2.98 - 3.08 (m, 1H), 3.08 – 3.18 (m, 1H), 3.73 (d, J = 2.3 Hz, 3H), 3.94 (dd, J = 18.2, 5.0 Hz, 1H), 4.04 (ddd, J = 18.2, 5.5, 1.8 Hz, 1H), 4.42 (s, 1H), 5.04 (s, 1H), 6.48 (d, J = 5.6 Hz, 1H), 7.16 – 7.26 (m, 3H), 7.26 – 7.35 (m, 2H); ¹³C NMR (125 MHz) in , d = 28.11, 38.23, 41.11, 52.34, 55.65, 127.35, 129.07, 129.71, 137.02, 170.49, 172.18, 175.91.

Methyl 3-(2-((tert-butoxycarbonyl)amino)-3-phenylpropanamido)propanoate (44)
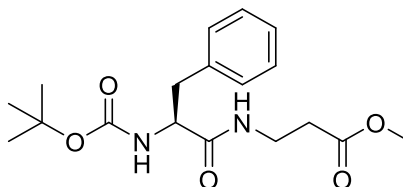
In this reaction Boc-Phe-OH **38** was used as the acid and H-β-Ala-OMe HCl **41** as the amine following the GP1. Consistency = White powder; Yield = 50%; R_f = 0.32 in EtOAc/light petroleum 3:2. ¹H NMR (500 MHz) in CDCl₃, d = 1.42 (q, J = 2.2, 1.6 Hz, 9H), 2.37 (s, 1H), 2.45 (d, J = 17.3 Hz, 1H), 2.91 - 3.03 (m, 1H), 3.07 (d, J = 7.0 Hz, 1H), 3.31 – 3.43 (m, 1H), 3.43 – 3.56 (m, 1H), 3.65 (s, 3H), 4.28 (s, 1H), 5.05 (s, 1H), 6.22 (s, 1H), 7.12 – 7.27 (m, 3H),

7.22 – 7.34 (m, 2H); ^{13}C NMR (125 MHz) in , d = 127.32, 129.08, 129.69, 137.99, 171.68, 173.22, 174.69.

Methyl (S)-(2-((tert-butoxycarbonyl)amino)-4-phenylbutanoyl)glycinate (45)
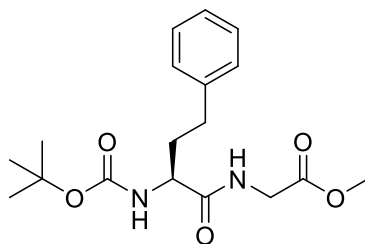
In this reaction Boc-hPhe-OH **39** was used as the acid and H-Gly-OMe HCl **40** as the amine following the GP1. Consistency = pale yellow oil; Yield = 98%; R_f = 0.48 in EtOAc/light petroleum 3:2. ^{1}H NMR (500 MHz) in CDCl$_3$, d = 1.44 (s, 9H), 1.82-2.03 (m, 1H), 2.08-2.31 (m, 1H), 2.69 (t, J = 7.9 Hz, 2H), 3.74 (s, 3H), 4.03 (dd, J = 5.4, 1.5 Hz, 2H), 4.15 (s, 1H), 5.06 (d, J = 8.1 Hz, 1H), 6.64 (s, 1H), 7.12 – 7.23 (m, 3H), 7.22 – 7.36 (m, 2H); ^{13}C NMR (125 MHz) in , d = 28.19, 31.64, 33.87, 41.09, 52.38, 54.02, 79.11, 126.56, 128.84, 128.94, 133.82, 170.68, 172.83, 176.57.

Methyl (S)-3-(2-((tert-butoxycarbonyl)amino)-4-phenylbutanamido)propanoate (46)
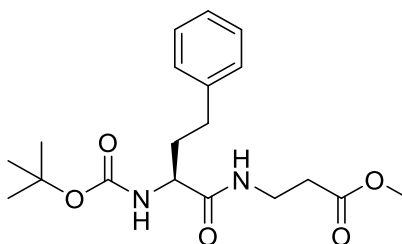
In this reaction Boc-hPhe-OH **39** was used as the acid and H-β-Ala-OMe HCl **41** as the amine following the GP1. Consistency = White crystals; Yield = 90%; R_f = 0.38 in EtOAc/light petroleum 3:2. ^{1}H NMR (500 MHz) in CDCl$_3$, d = 1.42 (s, 9H), 1.82 – 1.93 (m, 1H), 2.06 – 2.18 (m, 1H), 2.49 – 2.55 (m, 2H), 2.64 (t, J = 8.0 Hz, 2H), 3.42 – 3.58 (m, 2H), 3.66 (s, 3H), 4.05 (d, J = 7.7 Hz, 1H), 5.12 (d, J = 8.2 Hz, 1H), 6.64 (t, J = 6.2 Hz, 1H), 7.10 – 7.21 (m, 3H), 7.22 – 7.32 (m, 2H); ^{13}C NMR (125 MHz) in , d = 28.16, 31.69, 33.64, 34.08, 34.81, 51.78, 54.22, 126.51, 128.76, 128.89, 141.34, 172.56, 173.37, 178.57.

Methyl (S)-4-(2-((tert-butoxycarbonyl)amino)-4-phenylbutanamido)butanoate (47)
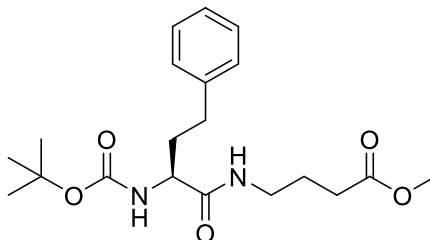
In this reaction Boc-hPhe-OH **39** was used as the acid and H-GABA-OMe HCl **42** as the amine following the GP1. Consistency = White crystals; Yield = 90%; R_f = 0.43 in EtOAc/light petroleum 3:2. ^{1}H NMR (500 MHz) in CDCl$_3$, d = 1.42 (s, 1H), 1.81 (p, J = 7.1 Hz, 2H), 1.83 – 1.96 (m, 1H), 2.06 – 2.18 (m, 1H), 2.33 (t, J = 7.3 Hz, 2H), 2.65 (t, J = 7.9 Hz, 2H), 3.27 (q,

$J = 6.6$ Hz, 2H), 3.64 (s, 3H), 4.04 (d, $J = 7.8$ Hz, 1H), 5.09 (d, $J = 8.3$ Hz, 1H), 6.38 (t, $J = 5.7$ Hz, 1H), 7.10 – 7.21 (m, 3H), 7.21 – 7.33 (m, 2H); ^{13}C NMR (125 MHz) in , d = 24.44, 28.17, 31.18, 31.77, 33.93, 38.74, 51.68, 54.23, 126.52, 128.79, 128.91, 141.35, 172.64, 174.31, 176.39.

(tert-Butoxycarbonyl)phenylalanylglycine (48)
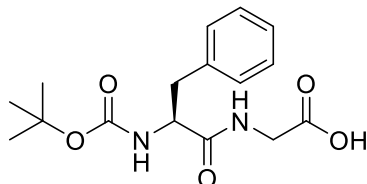
In this reaction the ester **43** was used as substrate following the GP2. Consistency = colorless oil. R_f = 0.0 in EtOAc/light petroleum (3:2). Yield: 84%. ^{1}H NMR (500 MHz) in MeOD, d = 1.34 (s, 9H), 2.81 (dd, $J = 13.9, 9.7$ Hz, 1H), 3.10 – 3.21 (m, 1H), 3.92 (d, $J = 2.5$ Hz, 2H), 4.36 (dd, $J = 9.6, 4.9$ Hz, 1H), 7.20 (td, $J = 6.1, 2.5$ Hz, 1H), 7.22 – 7.36 (m, 5H).

3-(2-((tert-Butoxycarbonyl)amino)-3-phenylpropanamido)propanoic acid (49)
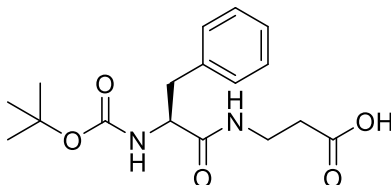
In this reaction the ester **44** was used as substrate following the GP2. Consistency = pale yellow oil. R_f = 0.0 in EtOAc/light petroleum (3:2). Yield: 96%. ^{1}H NMR (500 MHz) in CDCl$_3$, d = 1.35 (s, 9H), 2.43 (dq, $J = 13.3, 6.8$ Hz, 2H), 2.83 (dd, $J = 13.7, 8.8$ Hz, 1H), 3.06 (dd, $J = 13.7, 6.0$ Hz, 1H), 3.32 – 3.40 (m, 1H), 3.44 (dt, $J = 13.4, 6.6$ Hz, 1H), 4.28 (dd, $J = 8.7, 6.0$ Hz, 1H), 7.31 – 7.16 (m, 6H).

(S)-(2-((tert-Butoxycarbonyl)amino)-4-phenylbutanoyl)glycine (50)
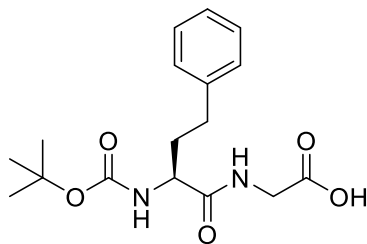
In this reaction the ester **45** was used as substrate following the GP2. Consistency = white foamy powder. R_f = 0.0 in EtOAc/light petroleum (3:2). Yield: 90%. ^{1}H NMR (500 MHz) in CDCl$_3$, d = 1.42 (s, 9H), 1.92 (dd, $J = 14.5, 7.2$ Hz, 1H), 2.09 (d, $J = 17.3$ Hz, 1H), 2.59 – 2.76 (m, 2H), 4.01 (dd, $J = 12.3, 5.0$ Hz, 2H), 4.32 (d, $J = 7.5$ Hz, 1H), 5.51 (d, $J = 8.6$ Hz, 1H), 7.12 – 7.21 (m, 4H), 7.22 – 7.32 (m, 2H).

(S)-3-(2-((tert-Butoxycarbonyl)amino)-4-phenylbutanamido)propanoic acid (51)
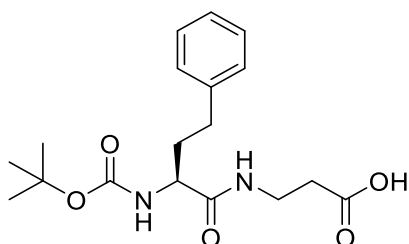
In this reaction the ester **46** was used as substrate following the GP2. Consistency = white powder. R_f = 0.0 in EtOAc/light petroleum (3:2). Yield: 94%. ^{1}H NMR (500 MHz) in CDCl$_3$, d = 1.42 (s, 9H), 1.92 (dd, J = 14.5, 7.2 Hz, 1H), 1.98 – 2.11 (m, 1H), 2.52 (dd, J = 6.5, 4.4 Hz, 1H), 2.63 (q, J = 8.5 Hz, 1H), 3.45 (d, J = 7.0 Hz, 1H), 3.57 (dd, J = 13.2, 6.7 Hz, 1H), 4.23 – 4.35 (m, 1H), 5.52 (d, J = 9.1 Hz, 1H), 7.11 – 7.20 (m, 3H), 7.21 – 7.29 (m, 2H), 7.33 (s, 1H).

(S)-4-(2-((tert-Butoxycarbonyl)amino)-4-phenylbutanamido)butanoic acid (52)
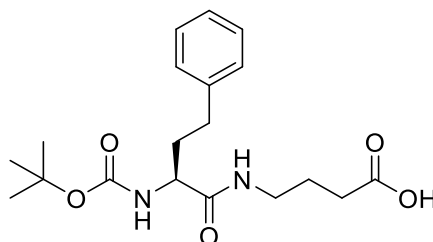
In this reaction the ester **47** was used as substrate following the GP2. Consistency = colorless oil. R_f = 0.0 in EtOAc/light petroleum (3:2). Yield: 90%. ^{1}H NMR (500 MHz) in CDCl$_3$, d = 1.43 (s, 9H), 1.76 – 1.86 (m, 2H), 1.92 (s, 1H), 2.06 (s, 1H), 2.35 (t, J = 7.2 Hz, 2H), 2.65 (q, J = 8.5, 7.0 Hz, 2H), 3.28 (q, J = 6.7 Hz, 2H), 4.14 (dd, J = 8.6, 5.0 Hz, 1H), 5.64 (d, J = 8.5 Hz, 1H), 7.00 (t, J = 5.9 Hz, 1H), 7.12 – 7.21 (m, 3H), 7.22 – 7.31 (m, 2H).

tert-butyl (2-(Methoxy(methyl)amino)-2-oxoethyl)carbamate (55)
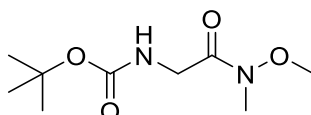
In this reaction Boc-Gly-OH **53** was used as the acid following the GP3. Consistency = white powder; Yield = 50%; R_f = 0.55 in light petroleum/EtOAc 7:3. ^{1}H NMR (500 MHz) in CDCl$_3$, d = 1.40 (s, 9H), 3.15 (s, 3H), 3.67 (s, 3H), 4.03 (d, J = 5.5 Hz, 2H), 5.26 (s, 1H); ^{13}C NMR (125 MHz) in , d = 28.14, 32.19, 41.57, 61.41, 79.66, 156.39, 170.78

tert-butyl (3-(Methoxy(methyl)amino)-3-oxopropyl)carbamate (56)
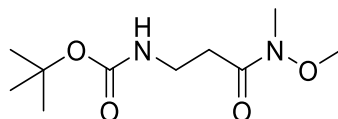
In this reaction Boc-βAla-OH **54** was used as the acid following the GP3. Consistency = yellow oil; Yield = 57%; R_f = 0.48 in light petroleum/EtOAc 7:3. ^{1}H NMR (500 MHz) in CDCl$_3$, d = 1.40 (s, 9H), 2.61 (d, J = 6.2 Hz, 2H), 3.15 (s, 3H), 3.39 (q, J = 6.1 Hz, 2H), 3.65 (s, 3H), 5.21 (s, 1H); ^{13}C NMR (125 MHz) in CDCl$_3$, d = 28.26, 32.16, 35.71, 61.23, 79.17, 156.51, 171.75

Methyl (E)-4-((tert-butoxycarbonyl)amino)but-2-enoate (57)
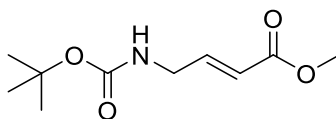
In this reaction **55** was used as the starting material following the condition described as GP4. Consistency = colorless oil; Yield = 50%; R_f = 0.55 in light petroleum/EtOAc 1:1. ^{1}H NMR (500 MHz) in CDCl$_3$, d = 1.43 (s, 9H), 3.72 (s, 3H), 3.90 (d, J = 6.0 Hz, 2H), 4.75 (s, 1H), 5.93 (dt, J = 15.7, 1.9 Hz, 1H), 6.90 (dt, J = 15.7, 4.9 Hz, 1H); ^{13}C NMR (125 MHz) in CDCl$_3$, d = 28.60, 41.67, 52.01, 80.44, 121.65, 146.00, 156.52, 167.55

Methyl (E)-5-((tert-butoxycarbonyl)amino)pent-2-enoate (58)
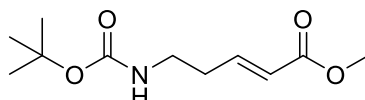
In this reaction **56** was used as the starting material following the condition described as GP4. Consistency = colorless oil; Yield = 59%; R_f = 0.48 in light petroleum/EtOAc 4:1. ^{1}H NMR (500 MHz) in CDCl$_3$, d = 1.40 (s, 9H), 2.38 (q, J = 6.8 Hz, 2H), 3.23 (q, J = 6.6 Hz, 2H), 3.70 (s, 3H), 4.65 (s, 1H), 5.86 (dt, J = 15.6, 1.5 Hz, 1H), 6.88 (dt, J = 15.7, 7.1 Hz, 1H); ^{13}C NMR (125 MHz) in CDCl$_3$, d = 28.19, 32.64, 38.93, 51.46, 79.54, 123.29, 146.18, 156.30, 167.25

Methyl (E)-4-(2-((tert-butoxycarbonyl)amino)acetamido)but-2-enoate (59)
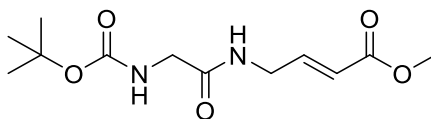
The *N*-Boc-deprotected trifluoroacetate salt of the intermediate **57** was obtained following the GP5. The titled compound **59** was obtained through coupling reaction between the Boc-Gly-OH **53** and the above reported trifluoroacetate salt of the intermediate **57**, which correspond to the acid and amine respectively, following the GP1. Consistency = white powder; Yield = 54%; R_f = 0.31 in EtOAc/light petroleum 7:3. ^{1}H NMR (500 MHz) in CDCl$_3$, d = 1.45 (s, 9H), 3.72 (s, 3H), 3.82 (dd, J = 6.0, 1.6 Hz, 2H), 4.06 (dq, J = 6.5, 1.8 Hz, 2H), 5.20 (s, 1H), 5.92 (dq, J = 15.7, 1.9 Hz, 1H), 6.56 (s, 1H), 6.90 (dtd, J = 15.9, 4.9, 1.6 Hz, 1H); ^{13}C NMR (125 MHz) in CDCl$_3$, d = 28.16, 39.87, 44.59, 51.66, 80.52, 121.84, 144.29, 166.99, 170.26, 173.28

Methyl (E)-4-(3-((tert-butoxycarbonyl)amino)propanamido)but-2-enoate (60)
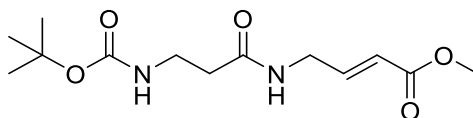
The *N*-Boc-deprotected trifluoroacetate salt of the intermediate **57** was obtained following the GP5. The titled compound **60** was obtained through coupling reaction between the Boc-Gly-OH **53** and the above reported trifluoroacetate salt of the intermediate **57**, which correspond to the acid and amine respectively, following the GP1. Consistency = white powder; Yield = 50%; R_f = 0.40 in EtOAc/light petroleum 7:3. ^{1}H NMR (500 MHz) in CDCl$_3$, d = 1.34 (s, 9H), 2.39 (t, J = 6.1 Hz, 2H), 3.31 (dd, J = 12.3, 6.2 Hz, 2H), 3.64 (s, 3H), 3.94 (td, J = 5.6, 1.8 Hz, 2H), 5.34 (s, 1H), 5.83 (dt, J = 15.7, 1.8 Hz, 1H), 6.81 (dt, J = 15.7, 5.0 Hz, 1H), 6.96 (s, 1H). [13]C

NMR (125 MHz) in CDCl₃, *d* = 28.27, 36.10, 36.61, 40.00, 51.54, 79.31, 121.10, 144.38, 156.24, 166.44, 171.58.

Methyl (E)-5-(2-((tert-butoxycarbonyl)amino)acetamido)pent-2-enoate (61)
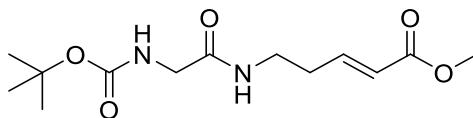
The *N*-Boc-deprotected trifluoroacetate salt of the intermediate **58** was obtained following the GP5. The titled compound **61** was obtained through coupling reaction between the Boc-Gly-OH **53** and the above reported trifluoroacetate salt of the intermediate **58**, which correspond to the acid and amine respectively, following the GP1. Consistency = white powder; Yield = 57%; R_f = 0.32 in EtOAc/light petroleum 7:3. ¹H NMR (500 MHz) in CDCl₃, *d* = 1.40 (s, 9H), 2.40 (qd, *J* = 6.9, 1.4 Hz, 2H), 3.37 (q, *J* = 6.6 Hz, 2H), 3.69 (s, 3H), 3.73 (d, *J* = 5.8 Hz, 2H), 5.33 (dt, *J* = 46.1, 5.6 Hz, 1H), 5.85 (dt, *J* = 15.7, 1.5 Hz, 1H), 6.63 (s, 1H), 6.86 (dt, *J* = 15.7, 7.1 Hz, 1H); ¹³C NMR (125 MHz) in CDCl₃, *d* = 28.24, 32.13, 37.80, 44.32, 51.48, 80.17, 122.97, 145.33, 156.15, 166.59, 169.68.

Synthesis of Final Compounds SPR81-SPR91

Methyl (S,E)-2,2-dimethyl-4,7,10-trioxo-6-phenethyl-3-oxa-5,8,11-triazapentadec-13-en-15-oate (SPR81)
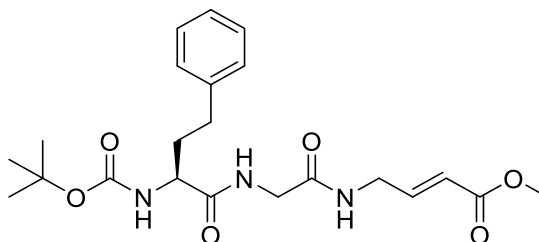
The *N*-Boc-deprotected trifluoroacetate salt of the intermediate **57** was obtained following the GP5. The next reaction was carried-out using Boc-hPhe-Gly-OH **50** and the trifluoroacetate salts of **57** as the acid and the amine, respectively, following the GP1. Consistency = white powder; Yield = 48%; R_f = 0.45 in EtOAc/methanol 9:1. ¹H NMR (500 MHz) in CDCl₃, *d* = 1.41 (s, 9H), 1.94 (ddd, *J* = 22.7, 15.4, 7.7 Hz, 1H), 2.15 (dt, *J* = 13.9, 7.6 Hz, 1H), 2.70 (td, *J* = 8.1, 7.4, 2.6 Hz, 2H), 3.69 (s, 3H), 3.92 – 4.09 (m, 4H), 5.23 (d, *J* = 4.8 Hz, 1H), 5.91 (dt, *J* = 15.7, 1.8 Hz, 1H), 6.88 (dt, *J* = 15.7, 5.0 Hz, 1H), 6.96 (s, 1H), 7.14 – 7.23 (m, 3H), 7.24 – 7.31 (m, 2H); ¹³C NMR (125 MHz) in CDCl₃, *d* = 28.40, 32.06, 33.38, 40.29, 43.39, 51.86, 55.34, 81.12, 122.03, 126.98, 129.01, 129.27, 141.08, 144.67, 157.01, 167.34, 169.90, 173.65. Elemental analysis for C₂₂H₃₁N₃O₆, C, 60.95; H, 7.21; N, 9.69; found: C, 61.14; H, 7.29; N, 9.51.

Methyl (S,E)-2,2-dimethyl-4,7,11-trioxo-6-phenethyl-3-oxa-5,8,12-triazahexadec-14-en-16-oate (SPR82)
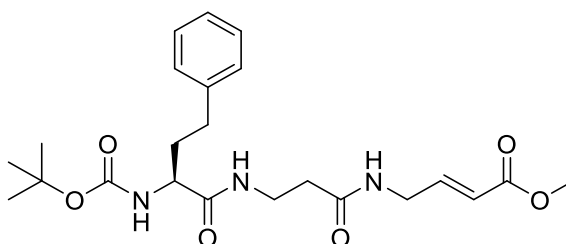
The *N*-Boc-deprotected trifluoroacetate salt of the intermediate **57** was obtained following the GP5. The next reaction was carried-out using Boc-hPhe-β-Ala-OH **51** and the trifluoroacetate salts of **57** as the acid and the amine, respectively, following the GP1. Consistency = white powder; Yield = 67%; R_f = 0.26 in EtOAc/methanol 9:1. ^{1}H NMR (500 MHz) in CDCl₃, *d* = 1.42 (s, 9H), 1.79 – 1.94 (m, 1H), 2.03 – 2.15 (m, 1H), 2.38 – 2.52 (m, 2H), 2.57 – 2.72 (m, 2H), 3.43 – 3.59 (m, 2H), 3.70 (s, 3H), 3.93 (dtd, *J* = 17.5, 5.5, 1.9 Hz, 1H), 3.98 – 4.02 (m, 1H), 4.02 – 4.09 (m, 1H), 5.44 (d, *J* = 7.0 Hz, 1H), 5.87 (dt, *J* = 15.7, 1.8 Hz, 1H), 6.74 (t, *J* = 5.8 Hz, 1H), 6.86 (dt, *J* = 15.7, 5.0 Hz, 1H), 7.03 (t, *J* = 6.1 Hz, 1H), 7.12 – 7.19 (m, 3H), 7.22 – 7.29 (m, 2H); ^{13}C NMR (125 MHz) in CDCl₃, *d* = 28.45, 32.04, 34.29, 35.92, 40.31, 51.91, 54.75, 80.48, 121.93, 126.79, 129.00, 129.16, 141.56, 144.96, 156.55, 167.30, 173.56. Elemental analysis for C₂₃H₃₃N₃O₆, C, 61.73; H, 7.43; N, 9.39; found: C, 62.01; H, 7.39; N, 9.31.

Methyl (S,E)-2,2-dimethyl-4,7,12-trioxo-6-phenethyl-3-oxa-5,8,13-triazaheptadec-15-en-17-oate (SPR83)

The *N*-Boc-deprotected trifluoroacetate salt of the intermediate **57** was obtained following the GP5. The next reaction was carried-out using Boc-hPhe-GABA-OH **52** and the trifluoroacetate salts of **57** as the acid and the amine, respectively, following the GP1. Consistency = white powder; Yield = 69%; R_f = 0.23 in EtOAc/methanol 9:1. ^{1}H NMR (500 MHz) in CDCl₃, *d* = 1.43 (s, 9H), 1.75 – 1.84 (m, 2H), 1.89 (ddd, *J* = 27.5, 13.9, 7.5 Hz, 1H), 2.10 (dt, *J* = 14.4, 7.8 Hz, 1H), 2.22 (t, *J* = 6.9 Hz, 1H), 2.58 – 2.73 (m, 2H), 2.73 – 2.58 (m, 2H), 3.70 (s, 3H), 3.99 (dd, *J* = 14.0, 8.7 Hz, 2H), 4.08 (d, *J* = 4.8 Hz, 1H), 5.32 (d, *J* = 6.4 Hz, 1H), 5.93 (dt, *J* = 15.7, 1.9 Hz, 1H), 6.82 – 6.94 (m, 2H), 6.98 (s, 1H), 7.17 (dd, *J* = 16.0, 7.4 Hz, 3H), 7.12 – 7.21 (m, 2H); ^{13}C NMR (125 MHz) in CDCl₃, *d* = 25.86, 28.47, 32.09, 33.47, 34.37, 38.89, 40.33, 51.86, 54.76, 80.60, 121.84, 126.82, 129.01, 129.18, 141.51, 145.27, 156.65, 167.41, 173.60, 173.78. Elemental analysis for C₂₄H₃₅N₃O₆, C, 62.45; H, 7.64; N, 9.10; found: C, 62.71; H, 7.53; N, 9.36.

Methyl (S,E)-2,2-dimethyl-4,7,10-trioxo-6-phenethyl-3-oxa-5,8,11-triazahexadec-14-en-16-oate (SPR84)

The *N*-Boc-deprotected trifluoroacetate salt of the intermediate **58** was obtained following the GP5. The next reaction was carried-out using Boc-hPhe-Gly-OH **50** and the trifluoroacetate salts of **58** as the acid and the amine, respectively, following the GP1. Consistency = white powder; Yield = 73%; R_f = 0.23 in EtOAc/methanol 9:1. ^{1}H NMR (500 MHz) in CDCl$_3$, d = 1.43 (s, 9H), 1.94 (dt, J = 14.8, 8.1 Hz, 1H), 2.08 – 2.20 (m, 1H), 2.37 – 2.45 (m, 2H), 2.63 – 2.74 (m, 2H), 3.29 (dd, J = 13.0, 6.3 Hz, 1H), 3.40 (td, J = 13.4, 6.8 Hz, 1H), 3.70 (s, 3H), 3.83 (dd, J = 16.6, 5.4 Hz, 1H), 3.94 – 4.07 (m, 2H), 5.36 (d, J = 5.3 Hz, 1H), 5.86 (dt, J = 15.7, 1.4 Hz, 1H), 6.88 (dt, J = 15.7, 7.0 Hz, 1H), 7.02 (d, J = 15.9 Hz, 2H), 7.14 – 7.22 (m, 3H), 7.25 – 7.31 (m, 2H); ^{13}C NMR (125 MHz) in CDCl$_3$, d = 28.45, 32.07, 32.22, 33.56, 38.16, 43.44, 51.80, 55.09, 80.88, 123.50, 126.92, 129.03, 129.24, 141.26, 146.20, 156.89, 167.63, 169.86, 173.57. Elemental analysis for C$_{23}$H$_{33}$N$_3$O$_6$, C, 61.73; H, 7.43; N, 9.39; found: C, 62.03; H, 7.27; N, 9.56.

Methyl (S,E)-2,2-dimethyl-4,7,11-trioxo-6-phenethyl-3-oxa-5,8,12-triazaheptadec-15-en-17-oate (SPR85)
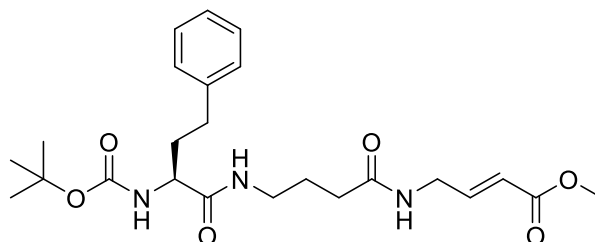

The *N*-Boc-deprotected trifluoroacetate salt of the intermediate **58** was obtained following the GP5. The next reaction was carried-out using Boc-hPhe-β-Ala-OH **51** and the trifluoroacetate salts of **58** as the acid and the amine, respectively, following the GP1. Consistency = white powder; Yield = 67%; R_f = 0.24 in EtOAc/methanol 9:1. ^{1}H NMR (500 MHz) in CDCl$_3$, d = 1.45 (s, 9H), 1.91 (dt, J = 14.6, 8.1 Hz, 1H), 2.05 – 2.17 (m, 1H), 2.33 – 2.49 (m, 4H), 2.66 (dd, J = 18.2, 11.0 Hz, 2H), 3.36 (dtt, J = 32.8, 13.1, 6.3 Hz, 2H), 3.45 – 3.61 (m, 2H), 3.73 (s, 3H), 4.09 (s, 1H), 5.46 (d, J = 6.3 Hz, 1H), 5.88 (dt, J = 15.7, 1.4 Hz, 1H), 6.51 (s, 1H), 6.90 (dt, J = 15.7, 7.0 Hz, 1H), 7.05 (t, J = 5.5 Hz, 1H), 7.15 – 7.22 (m, 3H), 7.24 – 7.31 (m, 2H); ^{13}C NMR (125 MHz) in CDCl$_3$, d = 28.47, 32.05, 32.23, 34.44, 35.91, 35.99, 38.13, 38.80, 51.83, 54.79, 80.39, 123.47, 126.79, 129.01, 129..17, 141.64, 146.40, 156.53, 167.64, 172.26, 173.42. Elemental analysis for C$_{24}$H$_{35}$N$_3$O$_6$, C, 62.45; H, 7.64; N, 9.10; found: C, 62.19; H, 7.87; N, 8.93.

Methyl (S,E)-2,2-dimethyl-4,7,12-trioxo-6-phenethyl-3-oxa-5,8,13-triazaoctadec-16-en-18-oate (SPR86)
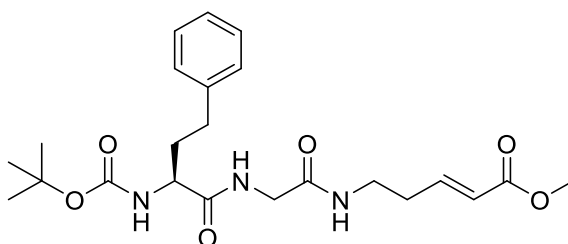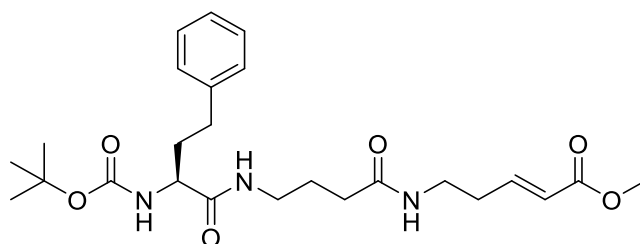
The *N*-Boc-deprotected trifluoroacetate salt of the intermediate **58** was obtained following the GP5. The next reaction was carried-out using Boc-hPhe-GABA-OH **52** and the trifluoroacetate salts of **58** as the acid and the amine, respectively, following the GP1. Consistency = white powder; Yield = 67%; R_f = 0.28 in EtOAc/methanol 95:5. ^{1}H NMR (500 MHz) in CDCl₃, *d* = 1.42 (s, 9H), 1.77 (tq, *J* = 13.7, 7.0 Hz, 2H), 1.91 (dd, *J* = 14.2, 7.8 Hz, 1H), 2.03 – 2.20 (m, 3H), 2.41 (dd, *J* = 13.6, 6.8 Hz, 2H), 2.65 (dd, *J* = 18.5, 11.0 Hz, 2H), 3.14 – 3.44 (m, 4H), 3.69 (s, 3H), 4.09 (s, 1H), 5.40 (d, *J* = 7.8 Hz, 1H), 5.88 (d, *J* = 15.7 Hz, 1H), 6.76 (s, 1H), 6.92 (dd, *J* = 15.7, 7.5 Hz, 2H), 7.10 – 7.21 (m, 3H), 7.21 – 7.33 (m, 2H); ^{13}C NMR (125 MHz) in CDCl₃, *d* = 25.68, 28.48, 32.10, 32.33, 33.56, 34.42, 38.12, 38.85, 51.78, 54.73, 80.47, 123.45, 126.80, 129.02, 129.16, 141.58, 146.64, 156.69, 167.68, 173.61, 173.79. Elemental analysis for $C_{25}H_{37}N_3O_6$, C, 63.14; H, 7.84; N, 8.84; found: C, 63.41; H, 7.56; N, 8.62.

Methyl (S,E)-2,2-dimethyl-4,7,10,13-tetraoxo-6-phenethyl-3-oxa-5,8,11,14-tetraazaoctadec-16-en-18-oate (SPR87)
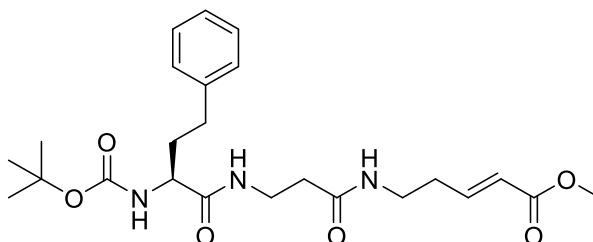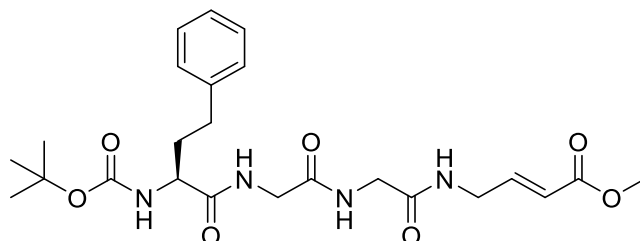

The *N*-Boc-deprotected trifluoroacetate salt of the intermediate **59** was obtained following the GP5. The next reaction was carried-out using Boc-hPhe-Gly-OH **50** and the trifluoroacetate salts of **59** as the acid and the amine, respectively, following the GP1. Consistency = white powder; Yield = 20%; R_f = 0.29 in EtOAc/methanol 98:2. ^{1}H NMR (500 MHz) in CDCl₃, *d* = 1.49 (s, 9H), 2.04 (dt, *J* = 14.4, 8.0 Hz, 1H), 2.20 (qd, *J* = 19.8, 13.1 Hz, 1H), 2.76 (dt, *J* = 14.1, 7.6 Hz, 2H), 3.78 (s, 3H), 3.91 – 4.19 (m, 7H), 5.85 (d, *J* = 5.8 Hz, 1H), 6.07 (d, *J* = 15.7 Hz, 1H), 7.00 (dt, *J* = 15.7, 4.6 Hz, 1H), 7.21 – 7.31 (m, 3H), 7.31 – 7.39 (m, 2H), 7.44 (t, *J* = 5.4 Hz, 1H), 7.72 (d, *J* = 19.4 Hz, 1H); ^{13}C NMR (125 MHz) in CDCl₃, *d* = 28.40, 31.95, 33.22, 40.13, 43.22, 43.89, 51.91, 55.30, 81.28, 121.95, 127.00, 129.02, 129.26, 141.07, 144.90, 157.42, 167.71, 169.95, 170.29, 174.95. Elemental analysis for $C_{24}H_{34}N_4O_7$, C, 58.76; H, 6.99; N, 11.42; found: C, 58.93; H, 6.79; N, 11.63.

Methyl (S,E)-6-benzyl-2,2-dimethyl-4,7,10,13-tetraoxo-3-oxa-5,8,11,14-tetraazaoctadec-16-en-18-oate (SPR88)
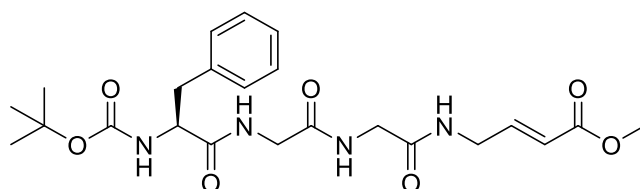
The *N*-Boc-deprotected trifluoroacetate salt of the intermediate **59** was obtained following the GP5. The next reaction was carried-out using Boc-Phe-Gly-OH **48** and the trifluoroacetate salts of **59** as the acid and the amine, respectively, following the GP1. Consistency = white powder; Yield = 51%; R_f = 0.29 in EtOAc/methanol 98:2. ^{1}H NMR (500 MHz) in CDCl$_3$, d = 1.33 (s, 9H), 2.92 (dd, J = 13.6, 8.3 Hz, 1H), 3.10 (dd, J = 13.7, 6.1 Hz, 1H), 3.68 (s, 3H), 3.77 – 4.10 (m, 6H), 4.32 (dt, J = 8.2, 6.4 Hz, 1H), 5.58 (d, J = 6.0 Hz, 1H), 5.97 (d, J = 15.7 Hz, 1H), 6.90 (dt, J = 15.7, 4.9 Hz, 1H), 7.15 – 7.25 (m, 3H), 7.25 – 7.30 (m, 2H), 7.32 (t, J = 5.3 Hz, 1H), 7.48 – 7.60 (m, 2H). ^{13}C NMR (125 MHz) in CDCl$_3$, d = 28.37, 38.17, 40.17, 43.22, 43.76, 51.89, 56.74, 81.08, 121.91, 127.74, 129.34, 129.87, 137.04, 144.96, 157.04, 167.62, 170.07, 170.42, 174.28. Elemental analysis for C$_{23}$H$_{32}$N$_4$O$_7$, C, 57.97; H, 6.77; N, 11.76; found: C, 58.16; H, 6.94; N, 11.53.

Methyl (S,E)-6-benzyl-2,2-dimethyl-4,7,11,14-tetraoxo-3-oxa-5,8,12,15-tetraazanonadec-17-en-19-oate (SPR89)

The *N*-Boc-deprotected trifluoroacetate salt of the intermediate **59** was obtained following the GP5. The next reaction was carried-out using Boc-Phe-β-Ala-OH **49** and the trifluoroacetate salts of **59** as the acid and the amine, respectively, following the GP1. Consistency = white powder; Yield = 36%; R_f = 0.25 in EtOAc/methanol 97:3. ^{1}H NMR (500 MHz) in CDCl$_3$, d = 1.34 (s, 1H), 2.31 (ddd, J = 16.1, 10.3, 3.8 Hz, 1H), 2.42 (ddd, J = 12.9, 8.3, 4.5 Hz, 1H), 2.93 (dd, J = 13.5, 7.7 Hz, 1H), 3.03 (dd, J = 13.2, 5.9 Hz, 1H), 3.38 (s, 1H), 3.38 (s, 1H), 3.50 – 3.61 (m, 1H), 3.69 (s, 3H), 3.81 (dd, J = 16.5, 5.1 Hz, 1H), 3.92 – 4.06 (m, 3H), 4.34 (d, J = 6.6 Hz, 1H), 5.46 (d, J = 7.3 Hz, 1H), 5.92 (dt, J = 15.7, 1.8 Hz, 1H), 6.87 (dt, J = 15.7, 5.0 Hz, 1H), 6.95 (s, 1H), 7.13 – 7.22 (m, 2H), 7.22 – 7.28 (m, 3H), 7.38 (s, 1H); ^{13}C NMR (125 MHz) in CDCl$_3$, d = 28.25, 35.84, 36.05, 38.81, 40.11, 43.15, 51.65, 55.90, 80.00, 121.37, 126.77, 128.42, 129.37, 136.80, 144.02, 155.65, 166.49, 169.31, 171.98, 172.42. Elemental analysis for C$_{24}$H$_{34}$N$_4$O$_7$, C, 58.76; H, 6.99; N, 11.42; found: C, 58.97; H, 6.81; N, 11.66.

### *Methyl (S,E)-6-benzyl-2,2-dimethyl-4,7,10,13-tetraoxo-3-oxa-5,8,11,14-tetraazanonadec-17-en-19-oate (SPR90)*

The *N*-Boc-deprotected trifluoroacetate salt of the intermediate **61** was obtained following the GP5. The next reaction was carried-out using Boc-Phe-Gly-OH **48** and the trifluoroacetate salts of **61** as the acid and the amine, respectively, following the GP1. Consistency = white powder; Yield = 75%; R_f = 0.23 in EtOAc/methanol 98:2. ^{1}H NMR (500 MHz) in CDCl$_3$, d = 1.32 (s, J = 13.8 Hz, 9H), 2.41 (q, J = 6.6 Hz, 2H), 2.71 (s, 2H), 2.94 (dd, J = 13.6, 8.3 Hz, 1H), 3.09 (dd, J = 13.6, 6.2 Hz, 1H), 3.33 (dtt, J = 19.9, 13.1, 6.5 Hz, 2H), 3.68 (s, 3H) 3.70 – 3.81 (m, 2H), 3.85 – 3.98 (m, 2H), 4.29 (dd, J = 14.2, 6.6 Hz, 1H), 5.71 (d, J = 6.0 Hz, 1H), 5.89 (d, J = 15.7 Hz, 1H), 6.89 – 7.01 (m, 1H), 7.16 – 7.24 (m, 4H), 7.25 – 7.30 (m, 2H), 7.52 (d, J = 15.6 Hz, 1H), 7.62 (t, J = 5.5 Hz, 1H); ^{13}C NMR (125 MHz) in CDCl$_3$, d = 28.36, 32.05, 37.97, 38.26, 43.27, 43.69, 51.82, 56.87, 80.97, 123.32, 127.73, 129.34, 129.86, 137.07, 146.95, 157.12, 168.02, 170.30, 170.50, 174.52. Elemental analysis for C$_{24}$H$_{34}$N$_4$O$_7$, C, 58.76; H, 6.99; N, 11.42; found: C, 58.62; H, 6.82; N, 11.61.

Methyl (S,E)-6-benzyl-2,2-dimethyl-4,7,10,14-tetraoxo-3-oxa-5,8,11,15-tetraazanonadec-17-en-19-oate (SPR91)
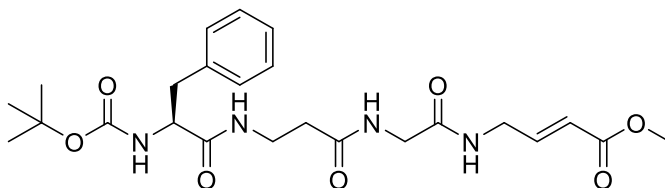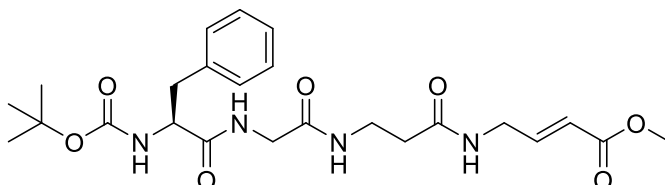

The *N*-Boc-deprotected trifluoroacetate salt of the intermediate **60** was obtained following the GP5. The next reaction was carried-out using Boc-Phe-Gly-OH **48** and the trifluoroacetate salts of **60** as the acid and the amine, respectively, following the GP1. Consistency = white powder; Yield = 76%; R_f = 0.33 in EtOAc/methanol 96:4. ^{1}H NMR (500 MHz) in CDCl$_3$, d = 1.33 (s, 9H), 2.82 (s, 1H), 2.86 – 2.96 (m, 1H), 3.03 – 3.16 (m, 1H), 3.33 – 3.45 (m, 1H), 3.50 (dt, J = 23.6, 11.9 Hz, 1H), 3.67 (s, 3H), 3.69 – 3.78 (m, 1H), 3.84 – 4.02 (m, 3H), 4.33 (dd, J = 13.8, 7.2 Hz, 1H), 5.54 (d, J = 5.7 Hz, 1H), 5.86 (d, J = 15.7 Hz, 1H), 6.86 (dt, J = 15.7, 4.8 Hz, 1H), 7.18 (dd, J = 19.2, 7.1 Hz, 3H), 7.24 (t, J = 6.5 Hz, 2H), 7.33 (t, J = 5.3 Hz, 1H), 7.59 (s, 1H); ^{13}C NMR (125 MHz) in CDCl$_3$, d = 28.25, 35.72, 36.02, 38.17, 40.10, 43.08, 51.69, 56.14, 80.27, 120.90, 126.92, 128.55, 129.19, 136.54, 144.76, 155.91, 166.74, 169.58, 171.42, 172.55. Elemental analysis for C$_{24}$H$_{34}$N$_4$O$_7$, C, 58.76; H, 6.99; N, 11.42; found: C, 58.89; H, 6.73; N, 11.22.

Synthesis of Final Compounds SPR92-SPR102

Methyl (S,E)-4-(2-(2-acetamido-4-phenylbutanamido)acetamido)but-2-enoate (SPR92)
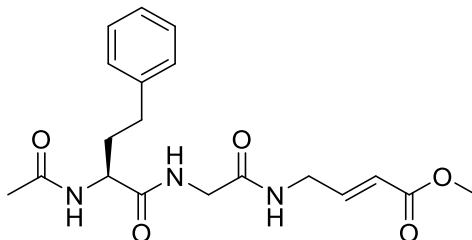
The *N*-Boc-deprotected trifluoroacetate salt of **SPR81** was obtained following the GP5. The next reaction was carried-out following the GP6. Consistency = white powder; Yield = 76%; R_f = 0.52 in EtOAc/methanol 9:1. ^{1}H NMR (500 MHz) in CDCl$_3$, d = 1.85 – 1.94 (m, 1H), 2.00 (s, 3H), 2.04 (dtdd, J = 9.2, 7.8, 4.6, 2.9 Hz, 1H), 2.44 (t, J = 6.7 Hz, 2H), 2.72 – 2.56 (m, 2H), 3.69 (s, 3H), 3.93 (dt, J = 5.0, 1.8 Hz, 2H), 4.23 (dd, J = 9.0, 5.2 Hz, 1H), 5.90 (dt, J = 15.7, 1.9 Hz, 1H), 6.88 (dt, J = 15.7, 5.0 Hz, 1H), 7.13 – 7.20 (m, 3H), 7.25 (dt, J = 9.0, 1.6 Hz, 2H). ^{13}C NMR (125 MHz) in CDCl$_3$, d = 21.05, 31.73, 33.51, 39.56, 50.67, 53.35, 120.42, 125.68, 128.03, 128.05, 140.92, 144.66, 166.77, 172.04, 172.30, 173.01. Elemental analysis for C$_{19}$H$_{25}$N$_3$O$_5$, C, 60.79; H, 6.71; N, 11.19; found: C, 60.93; H, 6.49; N, 10.95.

Methyl (S,E)-4-(3-(2-acetamido-4-phenylbutanamido)propanamido)but-2-enoate (SPR93)
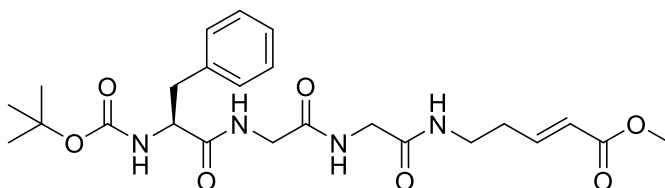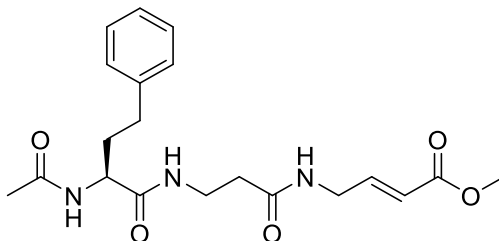

The *N*-Boc-deprotected trifluoroacetate salt of **SPR82** was obtained following the GP5. The next reaction was carried-out following the GP6. Consistency = white powder; Yield = 92%; R_f = 0.40 in EtOAc/methanol 9:1. ^{1}H NMR (500 MHz) in CDCl$_3$, d = 1.96 (ddd, J = 12.4, 9.1, 4.3 Hz, 1H), 2.01 (s, J = 1.5 Hz, 3H), 2.06 – 2.17 (m, 1H), 2.61 – 2.69 (m, 1H), 2.70 – 2.78 (m, 1H), 3.69 (s, J = 1.1 Hz, 3H), 3.80 (d, J = 16.8 Hz, 1H), 3.92 (d, J = 16.8 Hz, 2H), 3.99 (dd, J = 14.1, 4.7 Hz, 2H), 4.09 (ddd, J = 14.2, 7.1, 1.0 Hz, 1H), 4.20 (dd, J = 8.5, 5.7 Hz, 1H), 4.34 (dtd, J = 8.2, 6.8, 1.1 Hz, 1H), 5.93 (dd, J = 8.8, 8.1 Hz, 1H), 6.89 (dt, J = 15.7, 4.7 Hz, 1H), 7.13 – 7.23 (m, 3H), 7.26 (dd, J = 11.0, 4.1 Hz, 2H). ^{13}C NMR (125 MHz) in CDCl$_3$, d = 21.02, 22.28, 31.64, 33.17, 39.47, 50.63, 53.39, 120.38, 125.72, 128.08, 128.43, 140.82, 144.46, 166.81, 170.26, 172.71, 173.75. Elemental analysis for C$_{20}$H$_{27}$N$_3$O$_5$, C, 61.68; H, 6.99; N, 10.79; found: C, 61.98; H, 6.68; N, 10.46.

*Methyl (S,E)-4-(4-(2-acetamido-4-phenylbutanamido)butanamido)but-2-enoate (SPR94)*

The *N*-Boc-deprotected trifluoroacetate salt of **SPR83** was obtained following the GP5. The next reaction was carried-out following the GP6. Consistency = white powder; Yield = 92%; R_f = 0.39 in EtOAc/methanol 9:1. ^{1}H NMR (500 MHz) in CDCl$_3$, d = 1.77 – 1.84 (m, 2H), 1.87 – 1.97 (m, 1H), 2.01 (s, 3H), 2.11 – 2.02 (m, 1H), 2.22 – 2.28 (m, 2H), 2.57 – 2.66 (m, 1H), 2.66 – 2.75 (m, 1H), 3.17 – 3.25 (m, 2H), 3.70 (s, 3H), 3.94 (d, J = 4.9 Hz, 1H), 4.24 (dd, J = 8.9, 5.2 Hz, 1H), 5.92 (dd, J = 15.7, 1.9 Hz, 1H), 6.89 (dt, J = 9.2, 4.9 Hz, 1H), 7.13 – 7.21 (m, 3H), 7.26 (dd, J = 11.2, 3.7 Hz, 2H). ^{13}C NMR (125 MHz) in CDCl$_3$, d = 21.11, 25.14, 31.79, 32.66, 33.50, 38.40, 39,54, 50.67, 53.49, 120.36, 125.70, 128, 04, 128.08, 140.92, 144.78, 166.77, 172.11, 173.04, 174.06. Elemental analysis for C$_{21}$H$_{29}$N$_3$O$_5$, C, 62.51; H, 7.24; N, 10.41; found: C, 62.34; H, 7.12; N, 10.59.

Methyl (S,E)-5-(2-(2-acetamido-4-phenylbutanamido)acetamido)pent-2-enoate (SPR95)
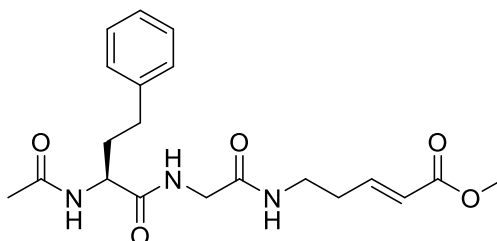
The *N*-Boc-deprotected trifluoroacetate salt of **SPR84** was obtained following the GP5. The next reaction was carried-out following the GP6. Consistency = white powder; Yield = 96%; R_f = 0.48 in EtOAc/methanol 9:1. ^{1}H NMR (500 MHz) in CDCl$_3$, d = 1.90 – 1.99 (m, 1H), 2.02 (s, 3H), 2.05 – 2.16 (m, 1H), 2.42 (q, J = 6.8 Hz, 2H), 2.61 – 2.69 (m, 1H), 2.69 – 2.78 (m, 1H), 3.33 (dd, J = 13.4, 4.7 Hz, 3H), 3.68 (s, 3H), 3.75 (dd, J = 16.8, 1.6 Hz, 1H), 3.86 (dd, J = 16.8, 1.6 Hz, 1H), 4.15 – 4.21 (m, 1H), 5.89 (dd, J = 15.7, 1.4 Hz, 1H), 6.91 (dt, J = 15.8, 6.0 Hz, 1H), 7.13 – 7.22 (m, 3H), 7.22 – 7.31 (m, 2H). ^{13}C NMR (125 MHz) in CDCl$_3$, d = 21.03, 31.48, 31.65, 32.74, 37.58, 42.09, 50.54, 54.06, 122.14, 125.73, 128.06, 128,08, 140.81, 146.02, 167.00, 170.26, 172.74, 173.63. Elemental analysis for C$_{20}$H$_{27}$N$_3$O$_5$, C, 61.68; H, 6.99; N, 10.79; found: C, 61.45; H, 7.21; N, 10.53.

Methyl (S,E)-5-(3-(2-acetamido-4-phenylbutanamido)propanamido)pent-2-enoate (SPR96)

The *N*-Boc-deprotected trifluoroacetate salt of **SPR85** was obtained following the GP5. The next reaction was carried-out following the GP6. Consistency = white powder; Yield = 83%;

$R_f = 0.41$ in EtOAc/methanol 9:1. ^{1}H NMR (500 MHz) in CDCl$_3$, d = 1.85 – 1.95 (m, 1H), 2.00 (s, 3H), 2.01 – 2.09 (m, 1H), 2.33 – 2.41 (m, 4H), 2.57 – 2.65 (m, 2H), 3.36 – 3.48 (m, 2H), 3.70 (s, 3H), 4.23 (dd, J = 8.9, 5.2 Hz, 1H), 5.87 (dd, J = 15.7, 1.4 Hz, 1H), 6.90 (dt, J = 14.6, 7.0 Hz, 1H), 7.16 (dd, J = 15.3, 7.7 Hz, 3H), 7.25 (t, J = 7.3 Hz, 2H). ^{13}C NMR (125 MHz) in CDCl$_3$, d = 21.08, 31.60, 31.76, 33.57, 35.02, 35.60, 50.56, 53.36, 122.04, 125.70, 128.03, 128.07, 140.95, 146.12, 166.98, 172.0, 172.27, 172.97. Elemental analysis for C$_{21}$H$_{29}$N$_3$O$_5$, C, 62.51; H, 7.24; N, 10.41; found: C, 62.64; H, 7.03; N, 10.76.

Methyl (S,E)-5-(4-(2-acetamido-4-phenylbutanamido)butanamido)pent-2-enoate (SPR97)
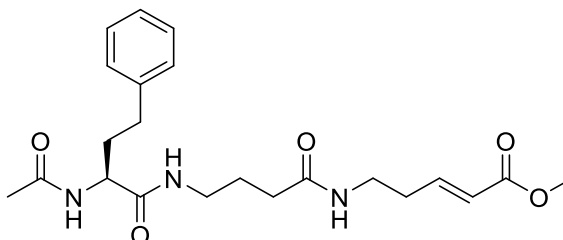
The N-Boc-deprotected trifluoroacetate salt of **SPR86** was obtained following the GP5. The next reaction was carried-out following the GP6. Consistency = white powder; Yield = 76%; $R_f = 0.35$ in EtOAc/methanol 9:1. ^{1}H NMR (500 MHz) in CDCl$_3$, d = 2.42 (q, J = 6.7 Hz, 2H), 2.58 – 2.67 (m, 1H), 2.67 – 2.76 (m, 1H), 3.28 – 3.36 (m, 3H), 3.68 (s, 3H), 4.10 (q, J = 7.0 Hz, 2H), 4.22 – 4.28 (m, 1H), 5.90 (dd, J = 15.7, 1.4 Hz, 1H), 6.87 – 6.97 (m, 1H), 7.13 – 7.21 (m, 3H), 7.23 – 7.28 (m, 2H). ^{13}C NMR (125 MHz) in CDCl$_3$, d = 21.10, 25.24, 31.67, 31.79, 32.81, 33.53, 37.45, 38.36, 50.54, 53.45, 122.12, 125.68, 128.03, 128.07, 140.93, 146.16, 166.49, 172.05, 172.98, 174.06. Elemental analysis for C$_{22}$H$_{31}$N$_3$O$_5$, C, 63.29; H, 7.48; N, 10.06; found: C, 63.54; H, 7.23; N, 10.24.

Methyl (S,E)-2,5,8,11-tetraoxo-4-phenethyl-3,6,9,12-tetraazahexadec-14-en-16-oate (SPR98)
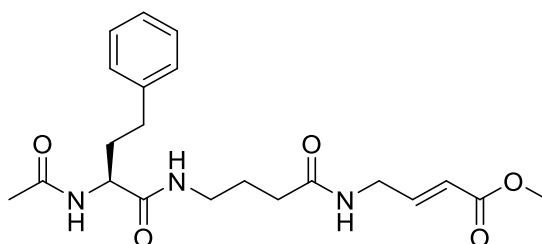

)The N-Boc-deprotected trifluoroacetate salt of **SPR87** was obtained following the GP5. The next reaction was carried-out following the GP6. Consistency = orange powder; Yield = %; R_f = 0.46 in EtOAc/methanol 8:2. ^{1}H NMR (500 MHz) in CDCl$_3$, d = 1.84 – 1.97 (m, 1H), 2.01 (s, 3H), 2.05 – 2.16 (m, 1H), 2.61 – 2.77 (m, 2H), 3.67 – 3.70 (m, 3H), 3.80 – 3.85 (m, 1H), 3.89 (s, 3H), 3.98 (dt, J = 4.6, 1.8 Hz, 2H), 4.21 (dd, J = 8.8, 5.4 Hz, 1H), 5.95 (dt, J = 15.7, 2.0 Hz, 1H), 6.89 (dt, J = 15.7, 4.7 Hz, 1H), 7.13 – 7.21 (m, 3H), 7.26 (dt, J = 8.9, 1.6 Hz, 2H). ^{13}C NMR (125 MHz) in CDCl$_3$, d = 21.05, 31.62, 32.81, 39.53, 42.04, 42.53, 50.63, 53.83, 120.45, 125.72, 128.07, 140.81, 144.43, 166.82, 170.30, 170.72, 170.88, 174.11. Elemental analysis for C$_{21}$H$_{28}$N$_4$O$_6$, C, 58.32; H, 6.53; N, 12.96; found: C, 58.12; H, 6.64; N, 12.79.

### Methyl (S,E)-4-benzyl-2,5,8,11-tetraoxo-3,6,9,12-tetraazahexadec-14-en-16-oate (SPR99)

The *N*-Boc-deprotected trifluoroacetate salt of **SPR88** was obtained following the GP5. The next reaction was carried-out following the GP6. Consistency = white powder; Yield = 63%; R_f = 0.43 in EtOAc/methanol 8:2. ^{1}H NMR (500 MHz) in CDCl$_3$, d = 1.92 (s, 3H), 2.88 – 2.97 (m, 1H), 3.11 – 3.18 (m, 1H), 3.68 (s, 3H), 3.71 – 3.77 (m, 1H), 3.85 – 3.94 (m, 3H), 3.99 (dd, J = 4.8, 1.8 Hz, 2H), 4.47 – 4.52 (m, 1H), 5.96 (dt, J = 15.8, 1.8 Hz, 1H), 6.90 (dtd, J = 15.8, 4.8, 1.4 Hz, 1H), 7.18 – 7.25 (m, 3H), 7.28 (dd, J = 11.2, 4.5 Hz, 2H). ^{13}C NMR (125 MHz) in CDCl$_3$, d = 20.98, 36.89, 39.54, 42.05, 42.54, 50.63, 55.46, 120.47, 126.43, 128.08, 128.80, 136.94, 144.45, 166.80, 170.24, 170.77, 172.32, 173.47. Elemental analysis for C$_{21}$H$_{28}$N$_4$O$_6$, C, 57.41; H, 6.26; N, 13.39; found: C, 57.69; H, 6.32; N, 13.16.

Methyl (S,E)-4-benzyl-2,5,9,12-tetraoxo-3,6,10,13-tetraazaheptadec-15-en-17-oate (SPR100)
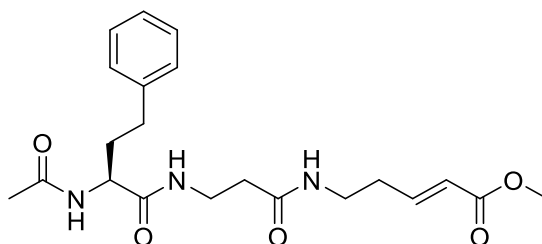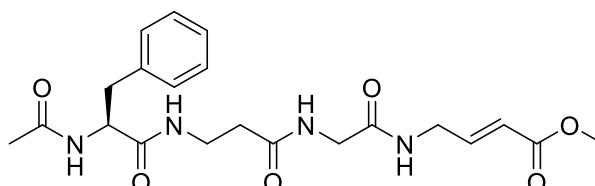

The *N*-Boc-deprotected trifluoroacetate salt of **SPR89** was obtained following the GP5. The next reaction was carried-out following the GP6. Consistency = white powder; Yield = 85%; R_f = 0.36 in EtOAc/methanol 8:2. ^{1}H NMR (500 MHz) in CDCl$_3$, d = 1.89 (s, 3H), 2.31 – 2.47 (m, 2H), 2.85 (dd, J = 13.8, 9.0 Hz, 1H), 3.09 (dd, J = 13.8, 6.1 Hz, 1H), 3.35 – 3.43 (m, 1H), 3.42 – 3.50 (m, 1H), 3.69 (s, 3H), 3.80 – 3.94 (m, 2H), 3.99 (dd, J = 4.8, 1.9 Hz, 2H), 4.49 (dd, J = 9.0, 6.1 Hz, 1H), 5.95 (dt, J = 15.7, 1.9 Hz, 1H), 6.90 (dt, J = 15.7, 4.8 Hz, 1H), 7.16 – 7.24 (m, 3H), 7.24 – 7.29 (m, 2H). ^{13}C NMR (125 MHz) in CDCl$_3$, d = 21.05, 31.62, 32.81, 39.53, 42.04, 42.53, 50.63, 53.83, 120.45, 125.72, 128.07, 140.81, 144.43, 166.82, 170.30, 170.88, 172.72, 174.11. Elemental analysis for C$_{21}$H$_{28}$N$_4$O$_6$, C, 58.32; H, 6.53; N, 12.96; found: C, 58.61; H, 6.29; N, 12.78.

Methyl (S,E)-4-benzyl-2,5,8,12-tetraoxo-3,6,9,13-tetraazaheptadec-15-en-17-oate (SPR101)
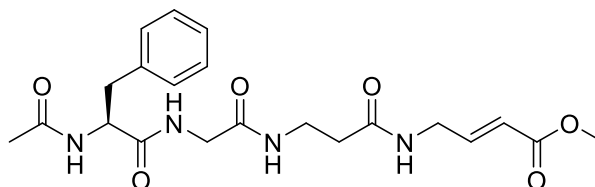
The *N*-Boc-deprotected trifluoroacetate salt of **SPR90** was obtained following the GP5. The next reaction was carried-out following the GP6. Consistency = white powder; Yield = 92%; R_f = 0.50 in EtOAc/methanol 8:2. ^{1}H NMR (500 MHz) in CDCl$_3$, d = 1.92 (s, 3H), 2.45 (dd, J = 6.8, 5.4 Hz, 1H), 2.89 – 2.96 (m, 2H), 3.13 (dd, J = 13.8, 5.2 Hz, 1H), 3.30 (d, J = 0.7 Hz, 1H), 3.45 (t, J = 6.7 Hz, 2H), 3.61 – 3.67 (m, 1H), 3.70 (s, 3H), 3.85 (dd, J = 16.8, 1.5 Hz, 1H), 3.92 – 3.98 (m, 2H), 4.48 (t, J = 6.8 Hz, 1H), 5.92 (dd, J = 15.8, 1.8 Hz, 1H), 6.90 (ddd, J =

7.9, 6.3, 3.9 Hz, 1H), 7.22 (dd, J = 16.4, 7.9 Hz, 3H), 7.28 (dd, J = 10.8, 4.0 Hz, 2H). ^{13}C NMR (125 MHz) in CDCl$_3$, d = 23.00, 35.53, 36.43, 37.40, 40.04, 43.19, 51.89, 55.74, 120.64, 127.02, 128.78, 129.02, 135.89, 145.18, 167.21, 169.43, 171.52, 171.60, 172.21. Elemental analysis for C$_{21}$H$_{28}$N$_4$O$_6$, C, 58.32; H, 6.53; N, 12.96; found: C, 58.59; H, 6.27; N, 12.76.

Methyl (S,E)-4-benzyl-2,5,8,11-tetraoxo-3,6,9,12-tetraazaheptadec-15-en-17-oate (SPR102)
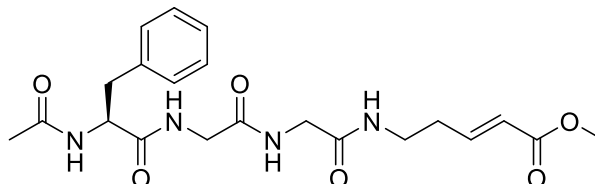
The *N*-Boc-deprotected trifluoroacetate salt of **SPR91** was obtained following the GP5. The next reaction was carried-out f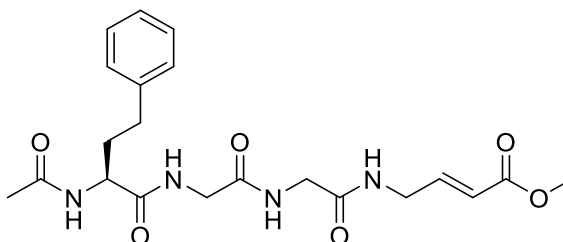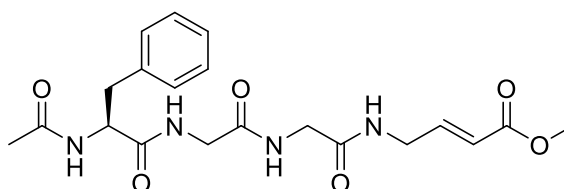ollowing the GP6. Consistency = white powder; Yield = 98%; R_f = 0.49 in EtOAc/methanol 8:2. ^{1}H NMR (500 MHz) in CDCl$_3$, d = 1.92 (s, 3H), 2.44 (q, J = 6.8 Hz, 2H), 2.95 (ddd, J = 13.8, 8.8, 1.6 Hz, 1H), 3.12 – 3.18 (m, 1H), 3.32 – 3.39 (m, 2H), 3.69 (s, 3H), 3.70 – 3.75 (m, 1H), 3.83 (dd, J = 5.4, 1.6 Hz, 2H), 3.88 (dd, J = 16.6, 2.0 Hz, 1H), 4.46 – 4.53 (m, 1H), 5.91 (dd, J = 15.7, 1.4 Hz, 1H), 6.94 (ddd, J = 9.1, 8.0, 2.0 Hz, 1H), 7.18 – 7.31 (m, 5H). ^{13}C NMR (125 MHz) in CDCl$_3$, d = 21.02, 31.56, 36. 85, 37.58, 42.04, 42.52, 50.59, 55.59, 122.18, 126.46, 128.10, 128.81, 136.92, 146.06, 167.05, 170.20, 170.72, 172.41, 173.50. Elemental analysis for C$_{21}$H$_{28}$N$_4$O$_6$, C, 58.32; H, 6.53; N, 12.96; found: C, 58.47; H, 6.56; N, 12.87.

9.2. Biological Evaluations

9.2.1. Enzyme Expression and Preparation

SARS-CoV-2 M^{pro}

The expression of SARS-CoV-2 M^{pro} was performed exactly as described previously.[115] Briefly, pMal-c2 plasmid DNA (New England Biolabs) containing the entire SARS-CoV-2 M^{pro} coding sequence flanked, at the 5' end, by a short sequence specifying the 5 C-terminal residues of nonstructural protein 4 and, at the 3' end, 6 histidine codons at the 3' end. The plasmid construct was transformed in *Escherichia coli* (*E. coli*) BL21-Gold (DE3) (Agilent Technologies, Santa Clara, CA, USA) cells. After growing the bacterial culture in LB medium with ampicillin to an OD$_{600}$ of ~0.5 and induction with isopropyl-β-D- thiogalactopyranoside (IPTG), M^{pro} was produced at 18 °C for 16 h. Cell pellets obtained by centrifugation were resuspended in lysis buffer (20 mM Tris−HCl pH 7.8, 150 mM NaCl, 20 mM imidazole) and lysed by sonication (Sonoplus HD 2200; Bandelin, Berlin, Germany). The cleared lysate was subjected to immobilized metal affinity chromatography (IMAC) on a HisTrap HP 5 ml column (Cytiva Europe GmbH, Freiburg im Breisgau. Germany). After washing with IMAC buffer A

(20 mM Tris−HCl pH 7.8, 200 mM NaCl, 20 mM imidazole), M^{pro} was eluted with IMAC buffer B (20 mM Tris−HCl pH 7.8, 200 mM NaCl, 500 mM imidazole). The collected fractions containing M^{pro}, were subjected to a gel filtration step (HiLoad 16/600 Superdex 75 pg column; GE Healthcare, Chicago, IL, USA) in SEC buffer (20 mM Tris−HCl pH 7.8, 150 mM NaCl, 1 mM ethylenediaminetetraacetic acid (EDTA), 1 mM dithiothreitol (DTT)). After dilution to 10 μM and adjustment to 10% (v/v) glycerol, M^{pro} was shock frozen in liquid N_2 and stored at -80 °C.

SARS-CoV-2 PL^{pro}

The SARS-CoV-2 PL^{pro} was prepared exactly as described previously.[153]

Dengue Virus NS2B/NS3

The glycine linked dengue virus 2 NS2B/NS3 protease was prepared exactly as described previously.[154]

Human Cathepsins

Human Cathepsin L was purchased by Sigma Adrich (St. Louis, Missouri, USA). Human Cathepsin B and Human Cathepsin S were purchased from Merck (Darmstadt, Germany).

9.2.2. Enzyme Inhibition Assays

Nirmatrelvir was purchased from AOBIUS (Gloucester, Massachusetts, USA). Inhibitory activity was determined using either a FRET-substrate (SARS-CoV-2 M^{pro}),[115] or fluorogenic AMC-substrates (NS2B/NS3),[154] PL^{pro},[153] hCatL,[155] and hCatB.[156] Assays were performed in white flat-bottom 96-well microtiter plates (Greiner bio-one, Kremsmünster, Austria) on a TECAN Infinite F2000 PRO plate reader (Agilent Technologies, Santa Clara, USA) for SARS-CoV-2 M^{pro} or a TECAN Spark 10M (Agilent Technologies) for assays using AMC-substrates. As a general procedure, inhibitors were dissolved as 20 mM DMSO-stock solutions. Substrates were also dissolved in DMSO. After an initial screening at 20 μM for SARS-CoV M^{pro} or 100 μM for all other proteases, IC_{50} values of active inhibitors were determined. Therefore.

half-logarithmic dilution series of active inhibitors were prepared (eg. final concentrations: 100, 30, 10, 3, 1, 0.3, 0.1 µM and DMSO as control). For each well, 185 µL of the respective buffer was supplemented with 5 µL of the enzyme-solutions, followed by 10 µL of the Inhibitors. Reactions were initiated without further incubation by addition of 5 µL of the substrate-solutions and vigorous mixing. Measurements were performed in at technical triplicates. The fluorescence was recorded in intervals of 30 s for 10 min at 25 °C (EDANS: λ_{ex} 335 nm; λ_{em} 493 nm; AMC: λ_{ex} 380 nm; λ_{em} 460). IC_{50} values were calculated with GraFit (Version 6.0.12; Erithacus Software Limited, East Grinstead, West Sussex, UK),[157] by fitting the enzymatic activities against the respective inhibitor concentration to the four-parameter equation. To correct for substrate competition, K_i values calculated by the Cheng-Prusoff equation.

9.2.3. Dilution Assay

Experiments shifting the inhibitor concentrations from 5-fold the respective IC_{50} to 0.1-fold the IC_{50}, were performed for SARS-CoV-2 M^{pro} and hCatL mainly as described previously.[158,159] The 5-fold IC_{50} solutions were as described for enzyme activity assays without addition of the substrate but with 50-fold the SARS-CoV-2 M^{pro} or 10-fold the hCatL concentration. Samples were incubated for 60 min at rt to ensure potent inhibition. After incubation, one sample per enzyme was diluted 50-fold to achieve inhibitor concentrations of 0.1-fold the IC_{50}. Enzymatic activities of 58.5 µL samples initiated with 1.5 µL of the respective substrate concentration were recorded in triplicates before and after dilution and were normalized to similar treated control experiment with DMSO instead of inhibitor solutions.

9.2.4. Dialysis Assay

Experiments extracting unbound or reversibly bound inhibitors from SARS-CoV-2 M^{pro} were performed using a custom-built dialysis chamber allowing the parallel examination of five samples mainly as described previously.[158,159]

In brief, a dialysis membrane (cut off 13 kDa MW) connected the sample containing wells with a chamber of continuously flowing assay buffer supplemented with 7.5% (v/v) DMSO (flowrate: ~200 mL/h). Samples were prepared similar to the enzymatic activity assay conditions without substrate (5-fold the volumes). To potently inhibit SARS-CoV-2 M^{pro} activity, inhibitors were used at a concentration 10-fold the IC_{50}. To compensate for loss of enzymatic activity during dialysis, SARS-CoV-2 M^{pro} was used in a final concentration of

250 nM, exceeding the concentration of Nirmatrelvir, so that activity could not be fully inhibited by Nirmatrelvir. Activity control measurements were performed using pure DMSO instead of the inhibitor solutions. Hence, 975 µL reaction mixtures were incubated for 60 min at rt to allow covalent reaction (if possible). After that, the first samples (t = 0 min) were drawn, and the rest was put in the wells of the dialysis device. Samples of 58.5 µL were drawn in duplicates at seven different time points (0, 30, 60, 150, 300, 600 and 1500 min). Enzymatic cleavage reactions were initiated by the addition of 1.5 µL of substrate solution in a final concentration of 25 µM. Fluorescence was recorded over 10 min as described for enzymatic activity assays.

9.2.5. Cell-Based Antiviral Activity and Cytotoxicity Assays

Cells and Viruses

Huh-7 cells overexpressing human angiotensin-converting enzyme 2 (ACE2) (Huh-7-ACE2; kindly provided by Friedemann Weber, Institute of Virology, Justus Liebig University Giessen) were grown in Dulbecco's modified Eagle's medium (DMEM) supplemented with 10% fetal bovine serum (FBS) and antibiotics (100 U/mL penicillin and 100 µg/mL streptomycin) at 37 °C in an atmosphere containing 5% CO_2. The SARS-CoV-2 isolate Munich 929,[160] was kindly provided by Christian Drosten (Institute of Virology, Charité-Universitätsmedizin, Berlin).

Cell Toxicity

Cytotoxic concentrations 50% (CC_{50}) of the compounds used in antiviral activity assays were determined using MTT assays as described previously.[161]

Antiviral Activity

To determine effective concentrations 50% (EC_{50}) of the respective compounds, Huh-7-ACE2 cells were inoculated with SARS-CoV-2 at a multiplicity of infection (MOI) of 0.1 plaque-forming units (pfu) per cell. After incubation for 1 h at 33 °C, the virus inoculum was replaced with fresh cell culture medium containing the test compounds at the indicated concentration. After 23 h at 33 °C, the cell culture supernatants were collected and virus titers were determined by virus plaque assay as described previously.[153]

9.3. Molecular Modeling Methods

9.3.1. Docking

AutoDock4 (AD4) was employed for molecular docking calculations.[162] The formation of the covalent adduct between ligand and protein was modeled using the covalent docking protocol devised by Bianco et al. known as the "flexible side chain method".[143] Using the Maestro suite, the ligands were modeled with two extra atoms where the alkylation would take place. Namely, a sulfur and a carbon atom, in order to match the corresponding atoms Cys145 of the protein. The X-ray structures of M^{pro} (for **SPR39** and **SPR62**) and hCatL (for **SPR62**) with the PDB code 7BQY,[123] and 3OF9,[145] were sourced from the RCSB PDB database and underwent preliminary adjustments for docking purposes using the Protein Preparation Wizard integrated into the Schrödinger suite.[163] The overlay of the ligand with the reactive cysteines was attained using the scripts offered by the AD4 website. The AutoGrid4 software was used to prepare the protein grid maps using the ligand atom types as probes. The enzyme grid box with a size of 60 Å × 60 Å × 60 Å and 0.375 Å spacing was centered on the coordinates of the cognate c7BQY o-crystal ligand. The docking calculations were performed by treating the modified cysteine/ligand residue as flexible. The Lamarckian Genetic Algorithm (LGA) was employed for the docking simulations. 100 runs of LGA were executed. The docking run consisted of 20 million energy evaluations using the Lamarckian genetic algorithm local search (GALS) method. The GALS method evaluates a population of possible docking solutions and propagates the most successful individuals from each generation into the subsequent generation of possible solutions. A low-frequency local search according to the method of Solis and Wets is applied to docking trials to ensure that the final solution represents a local minimum. The docking experiment was performed with a population size of 150, and 300 rounds of Solis and Wets local search were applied with a probability of 0.06. A mutation rate of 0.02 and a crossover rate of 0.8 were used to generate new docking trials for subsequent generations, and the best individual from each generation was propagated over the next generation. All the other settings were left at their default value. The docking results from the calculation were clustered on the basis of root-mean-square deviation (solutions differing by less than 2.0 Å) between the Cartesian coordinates of the atoms and were ranked on the basis of free energy of binding (ΔG_{AD4}). Finally, the **SPR39** and **SPR62** docking poses with the best-predicted ΔG_{AD4} were selected. All the images were rendered using the UCSF Chimera X software.[164]

9.3.2. Molecular Dynamics Simulations

The complex obtained from the docking results was subjected to a molecular dynamics (MD) simulation by means of the Desmond module of the Schrödinger software package.[165,166] As a first step, the system builder panel was used to prepare the system for the MD calculation. Each complex was embedded in a parallelepiped box by solvating it with TIP3P water model.[167] The initial −3 negative charge was neutralized using 3 Na^+ ions. Then, the system was equilibrated by employing the NPT ensemble with the default Desmond protocol that includes eight steps. The first 7 are short simulations known as the equilibration phase, where the system temperature is gradually increased and the solute is partially restrained. After the first 7 steps, the equilibrated systems were subjected to the 100 ns MD final production run with PBC conditions and NPT ensemble. The system was set to 300 K temperature and 1 atm pressure throughout the simulation utilizing the Martyna−Tobias−Klein barostat,[168] and Nose−Hoover chain thermostat.[169] The OPLSe force field,[170] was used for all the MD simulation steps.

9.4. Solubility Experiments

The determination of **SPR62** solubility was carried out using a Varian Cary 50 UV–Vis spectrophotometer, furnished with a fixed path length (1 cm) optical fiber probe. The acquisition of absorbance (A) signal vs. wavelength (λ/nm) was performed by means of the Varian Cary WinUV 3.00 software, set up on a computer connected to the instrument.[146] Saturated aqueous solutions of **SPR62** were prepared by addition of little amounts of the solid product to 0.50 mL of deionized water and later sonication, using an Argo Lab digital ultrasonic bath (mod. DU-45) at $t = 37\pm1°C$, until the solid did not further dissolve. At the same temperature, the saturated solutions were centrifuged at 12000 rpm for 40 min by means of a Neya-8 Remi laboratory centrifuge and the supernatants were separated from the solid residues. The first set up of the experiments consisted in UV-Vis scans of diluted 1:100 solutions, at t = 37.0±0.1°C, in the λ range = 200-800 nm, with $\Delta\lambda = 1$ nm among two consecutive signal readings (Figure 43). After identifying the wavelength of maximum absorption, the absorbance was measured for each **SPR62** sample at fixed λ = 226 nm (Figure 44). The compound solubilities in the diluted solutions were calculated using the calibration straight line obtained measuring the absorbance signal at the mentioned wavelength, of five standards solutions prepared in the range of $c_{SPR62} = 0.013$-0.064 mM, starting from a stock solution at $c_{SPR62} = 1.28$ mM.
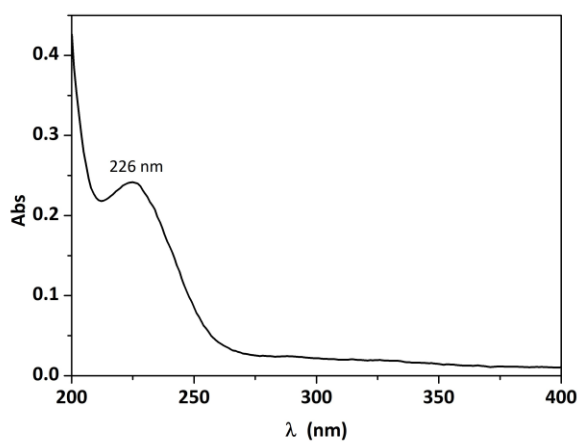
Figure 43. UV-Vis spectrum of **SPR62** at $c_{SPR62} = 0.013$ mM in water.
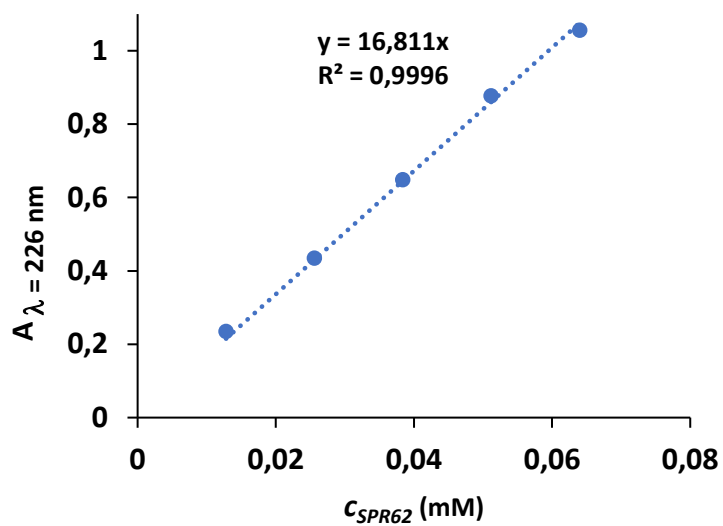
Figure 44. Absorbance of **SPR62** at different concentrations (range $c_{SPR62} = 0.013$-0.064 mM) and $\lambda = 226$ nm.

10. SUPPLEMENT

Identification of constrained peptidomimetics carrying a Michael acceptor warhead as antitrypanosomal agents

10.1. Introduction and aim of research

Human African Trypanosomiasis (HAT), also known as sleeping sickness, is a disease transmitted by vectors and caused by two subspecies of Trypanosoma brucei: T. b. gambiense and T. b. rhodesiense.[171] Following a tsetse fly bite, the protozoa enter the bloodstream, leading to flu-like symptoms such as fever, headache, weakness, and muscle soreness.[172] The protozoa then cross the Blood-Brain Barrier (BBB), resulting in various neurological disorders, including disruptions to the sleep-wake cycle, which is how the disease got its name. If not treated, HAT is fatal.[173] While both subspecies of T. brucei cause similar clinical symptoms, they differ significantly in the disease's progression time: T. b. gambiense (gHAT) progresses over 2-3 years, whereas T. b. rhodesiense (rHAT) advances within a few weeks.

In recent decades, significant efforts by the World Health Organization (WHO), its partners, and charitable foundations have resulted in a substantial decrease in HAT cases.[171] However, the large number of people still at risk of infection, the limited selection of available drugs, and the emergence of resistant strains remain significant challenges for the control and treatment of the disease.[173] The development of an effective vaccine is hindered by the presence of Variant Surface Glycoproteins (VSGs) on the Trypanosoma's coat.[174] As a result, chemotherapy is the only available treatment strategy for HAT. Except for fexinidazole, recently approved for non-severe forms of gHAT, the other drugs are old, toxic, and have a narrow spectrum of activity.[175] Consequently, developing new antitrypanosomal agents remains a critical challenge for the scientific community.

At the turn of the millennium, rhodesain was identified as a promising target for the treatment of HAT.[176] This enzyme is a lysosomal L-cathepsin-like cysteine protease, with its proteolytic activity mediated by the catalytic triad Cys25/His162/Asn182. Rhodesain is crucial for both the survival of Trypanosoma and the progression of the disease, as it is involved in disrupting the BBB and in the turnover of VSGs.[177,178] The crystal structures of rhodesain in complex with vinyl sulfones **K11777**[179] and **K11002**,[180] as well as macrolactam **62**,[181] have been deposited in the Protein Data Bank (PDB) archive, along with the crystal structure of pro-rhodesain (Figure 45).[182]
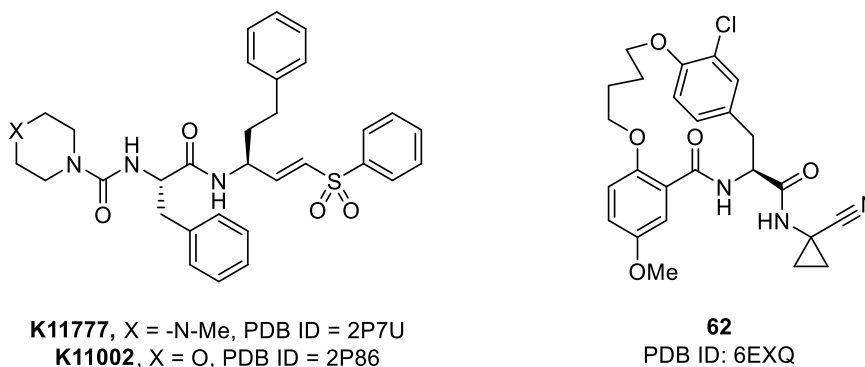
Figure 45. Structures of compound with which rhodesain was co-crystallized.

Building on the valuable information provided by the crystal structures, a modest number of Structure-Activity Relationship (SAR) studies have been conducted over the past 20 years.[183–185] Our research group, in particular, identified a series of peptidomimetics (*i.e.*, **63a-m**, Figure 46) featuring a methyl ketone warhead, homophenylalanine (hPhe) at the P1 site, phenylalanine (Phe) at the P2 position, and various substituents at the P3 position.[186–190] Among the strategies to enhance the inhibitory properties of peptide-based compounds and peptidomimetics, incorporating conformationally constrained amino acids has shown benefits in terms of affinity, selectivity, and proteolytic stability, among other factors.[191] Incorporating constrained amino acids at the P2 position yielded promising results for rhodesain inhibition and antitrypanosomal properties.[192,193] Given rhodesain's strong preference for Phe at the P2 site, we developed a new series of peptidomimetics (**SPR65-SPR77**) featuring the 1,2,3,4-tetrahydroisoquinoline-3-carboxylic acid (Tic) at this position. The Tic residue, a well-known constrained analogue of Phe, provides the classic β-amino acid pattern, which can modulate the biological properties, conformation, proteolytic susceptibility, and dynamics of the parent peptides.[194,195] All new Tic analogues were designed with a methyl vinyl ketone warhead and an hPhe residue at the P1 position, due to rhodesain's high affinity for both components.[190] Lastly, various substituents were incorporated at the P3 position via amide, urea, and carbamoyl bonds. Fluorine-containing phenyl rings at P3 produced potent rhodesain inhibitors, with the fluorine atom's position significantly affecting potency.[188,189,196] Consequently, compounds **SPR67-SPR71**, featuring monofluoro substitutions at the *ortho*, *meta*, and *para* positions, as well as 2,4- and 2,6-difluoro substitutions, were developed. The introduction of a urea bond between the P2 and P3 residues was found to be well-tolerated, particularly in terms of antitrypanosomal activity.[187] Therefore, analogues **SPR72-SPR73**, which include the most promising urea substituents, were synthesized. The P3 pocket demonstrated a significant preference for bulky amino acids, while the presence of smaller residues led to reduced rhodesain inhibition.[186] Thus, N-Cbz-tripeptides

SPR75-SPR77, which contain amino acids with bulky side chains (*e.g.*, Leu, Cha, and Phe), were developed. Additionally, the Ala-analogue **SPR74** was synthesized to further explore the impact of bulky amino acids at P3 on binding affinity to the target. Lastly, Boc- and Cbz-containing derivatives (**SPR65** and **SPR66**, respectively) were synthesized.

	P3
a, **SPR65**	= Boc
b, **SPR66**	= Cbz
c, **SPR67**	= -2-F-benzoyl
d, **SPR68**	= -3-F-benzoyl
e, **SPR69**	= -4-F-benzoyl
f, **SPR70**	= -2,4-F$_2$-benzoyl
g, **SPR71**	= -2,6-F$_2$-bezoyl
h, **SPR72**	= -CO-NH-Ph-4-Me
i, **SPR73**	= -CO-NH-Ph-2-Me,4-Cl
j, **SPR74**	= Cbz-Ala
k, **SPR75**	= Cbz-Leu
l, **SPR76**	= Cbz-Cha
m, **SPR77**	= Cbz-Phe

63a-m
Parent compounds
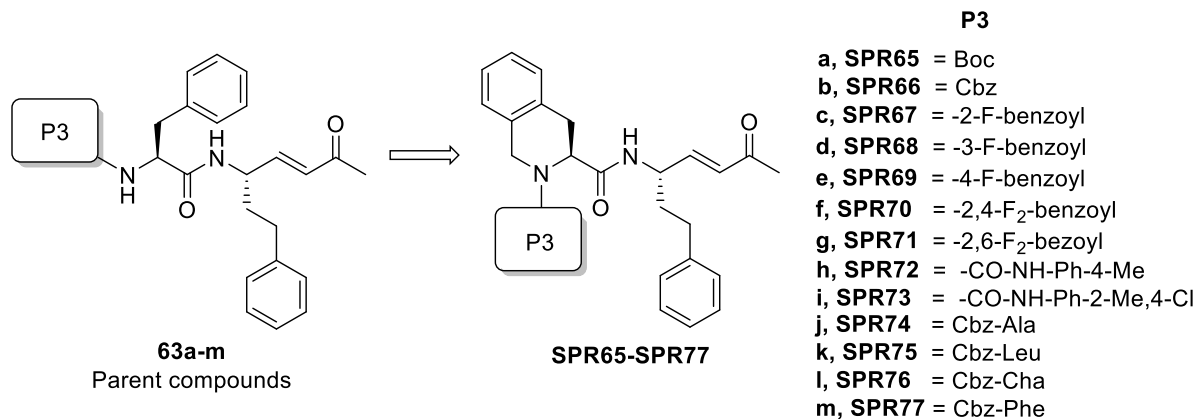
SPR65-SPR77

Figure 46. Design of novel peptidomimetics **SPR65-SPR77** carrying Tic at the P2 site starting from parent compounds reported in the literature.[186–190]

10.2. Results and Discussion

10.2.1. Synthesis

The newly designed Tic-analogues were synthesized in solution using Boc-chemistry (Scheme 7). Initially, the commercially available Boc-hPhe-OH **64** was converted into the corresponding Weinreb amide **65** through a coupling with *N,O*-dimethylhydroxylamine hydrochloride. The amino group of this amide was deprotected by treatment with trifluoroacetic acid (TFA), as previously reported.[197] The resulting intermediate **66** was coupled with Boc-Tic-OH **67** to yield compound **68**. Spectroscopic characterization using ^{1}H-NMR revealed a spectrum with broad signals and unresolved multiplets, making interpretation difficult. Therefore, LC-MS analysis was performed to confirm the identity of intermediate **68**. Subsequent treatment with TFA produced amine **69**, which exhibited a well-resolved ^{1}H-NMR spectrum.

Intermediate **69** was then coupled with fluorine-containing benzoic acids **70b-f** and N-Cbz-protected amino acids **70i-l** to produce intermediates **71b-f** and **71i-l**. The N-Cbz analogue **71a** was synthesized by treating amine **69** with Cbz-Cl under alkaline conditions, while urea derivatives **71g-h** were obtained using the appropriate isocyanates in the presence of TEA. Similar to intermediate **68**, the ^{1}H-NMR spectra of compounds **71a-l** were challenging to analyze due to unresolved multiplets and double peaks. This complexity arises from the rotational isomerism of the peptide bond involving the endocyclic nitrogen of the Tic residue

and the carbonyl group of the P3 substituents. The partial double-bond character of the P2-P3 bond leads to cis and trans isomers, with their N-substituents being geometrically and magnetically nonequivalent, as documented in the literature.[198–200] Finally, the vinyl methyl ketone warhead was incorporated by reducing intermediates **71a-l** to the corresponding aldehydes with LiAlH$_4$, followed by a Wittig reaction with 1-(triphenylphosphoranylidene)-2-propanone.

	X		X
a, SPR66 = Cbz		**g, SPR72** = -CO-NH-Ph-4-Me	
b, SPR67 = 2-F-benzoyl		**h, SPR73** = -CO-NH-Ph-2-Me,4-Cl	
c, SPR68 = 3-F-benzoyl		**i, SPR74** = Cbz-Ala-	
d, SPR69 = 4-F-benzoyl		**j, SPR75** = Cbz-Leu-	
e, SPR70 = 2,4-F$_2$-benzoyl		**k, SPR76** = Cbz-Cha-	
f, SPR71 = 2,6-F$_2$-benzoyl		**l, SPR77** = Cbz-Phe-	
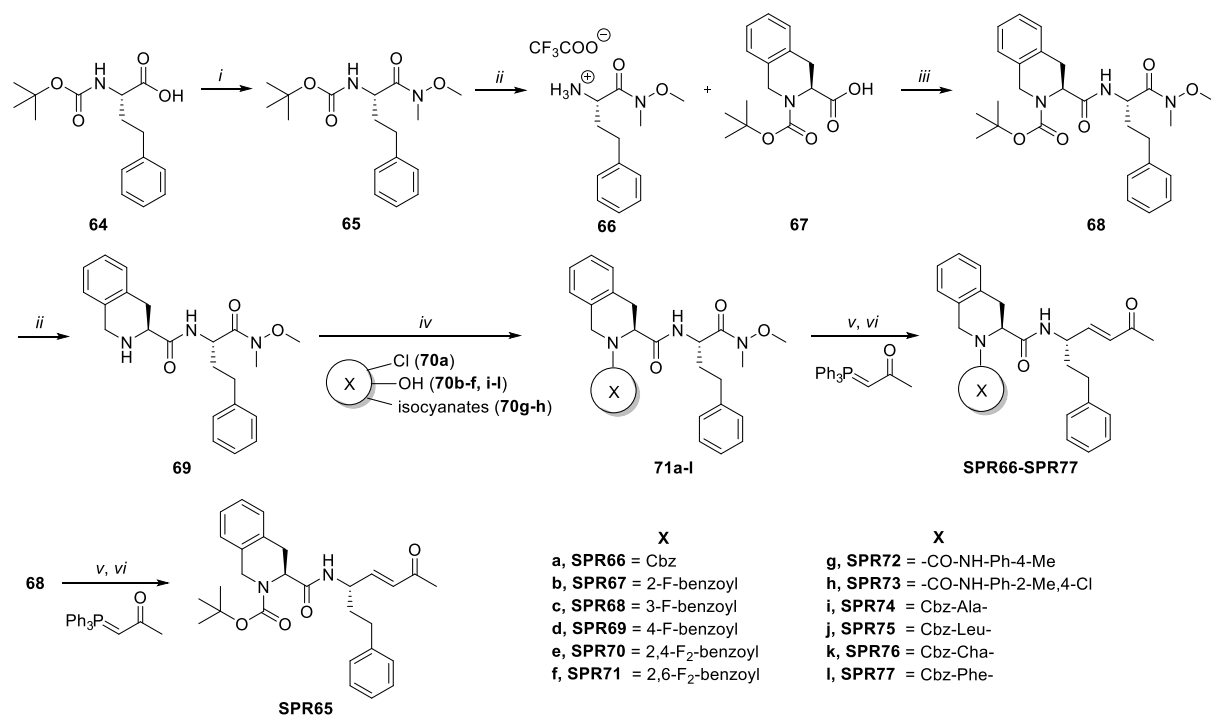
Scheme 7. Reagents and conditions: *i*) DCM, TBTU, DIPEA, 0°C, 20 min, then *N,O-dimethylhydroxylamine hydrochloride*, rt, 12h; *ii*) 30%TFA in DCM, 0° C, then ta, 12h; *iii*) DCM, TBTU, DIPEA, 0°C, 20 min, then rt, 12h; *iv*) for **71a**: dioxane/H$_2$O (1:10), K$_2$CO$_3$, 20 min, rt, then 0°C, **70a**, then rt, 12h; for **71b-f, 71i-l**: appropriate **70b-f, 70i-l**, DCM, TBTU, DIPEA, 0°C, 20 min, then **69**, rt, 12h; for **71g-h**: dry THF, TEA, 20 min, rt then appropriate isocyanate **70g-h**, rt, 12h; *v*) LiAlH$_4$, dry THF, -15° C, 4h; *vi*) DCM, rt, 2h.

10.2.2. Biology evaluation

All the new Tic analogues were screened at 20 μM against rhodesain using Cbz-Phe-Arg-AMC as the fluorogenic substrate (Table 7). Eight compounds exhibited over 50% inhibition, and their k_{inact} (min^{-1}), K_i (μM), and k_{2nd} (x 10^3 M^{-1} min^{-1}) values were determined. Analogue **SPR70**, featuring the 2,4-difluorophenyl ring at P3, showed the highest k_{2nd} value against the target. In contrast, **SPR71**, which differs from **SPR70** only by having the fluorine atom at the *para* position, demonstrated weak inhibitory properties. Among the monofluorine analogues **SPR67-**

SPR69, only modest k_{2nd} values were observed, highlighting the importance of fluorine atom positioning for rhodesain inhibition.

Table 7. Biological characterization of **SPR65-SPR77** towards rhodesain.				

SPR65-SPR77

Cmpd	X	Rhodesain		
		k_{inact} (min^{-1})	K_i (µM)	k_{2nd} (x 10^3 M^{-1} min^{-1})
SPR65	Boc	18 ± 2.3%[a]		
SPR66	Cbz	0.0048 ± 0.0001	0.72 ± 0.012	6.7 ± 0.2
SPR67	2-F-benzoyl	0.019 ± 0.007	4.88 ± 2.19	4.1 ± 0.4
SPR68	3-F-benzoyl	0.021 ± 0.002	0.70 ± 0.13	30.1 ± 2.7
SPR69	4-F-benzoyl	0.015 ± 0.003	1.92 ± 0.58	8.0 ± 0.6
SPR70	2,4-F$_2$-benzoyl	0.012 ± 0.004	0.09 ± 0.043	146.1 ± 23.4
SPR71	2,6-F$_2$-benzoyl	32 ± 4.3%[a]		
SPR72	CO-NH-Ph-4-Me	14 ± 1.6%[a]		
SPR73	CO-NH-Ph-4-Cl,2-Me	40 ± 3.2%[a]		
SPR74	Cbz-Ala-	26 ± 3.5%[a]		
SPR75	Cbz-Leu-	0.0008 ± 0.0001	0.016 ± 0.008	68.5 ± 32.5
SPR76	Cbz-Cha-	0.0009 ± 0.0001	0.022 ± 0.007	47.9 ± 13.7
SPR77	Cbz-Phe-	0.0007 ± 0.0001	0.011 ± 0.003	75.6 ± 25.4
[a] % of inhibition at the screening concentration (20 µM)				

N-Cbz-tripeptides **SPR74-SPR77** exhibited inhibitory properties consistent with previous SAR studies.[186] Specifically, the Ala derivative **SPR74** was inactive, while the presence of bulky amino acids at the P3 position (Leu in **SPR75**, Cha in **SPR76**, and Phe in **SPR77**) resulted in notable k_{2nd} values. The incorporation of a urea bond between the P3 site and the Tic residue in compounds **SPR72** and **SPR73** rendered them inactive, indicating that additional rigidity negatively impacts binding affinity. Lastly, the presence of Boc (**SPR65**) and Cbz (**SPR66**)

groups was unproductive, resulting in weak inhibition percentages and single-digit k_{2nd} values, respectively.

To further investigate the role of the Tic residue, the hPhe of the best newly identified rhodesain inhibitor (**SPR70**) was replaced with amino acids having smaller side chains: Gly (**SPR78**), Ala (**SPR79**), and Phe (**SPR80**). These **SPR70** analogues were synthesized as shown at the Scheme 8, starting from Boc-Gly-OH, Boc-Ala-OH, and Boc-Phe-OH. The 2,4-difluorobenzoic acid (**70e**) was used in the coupling reaction to incorporate the P3 substituent.
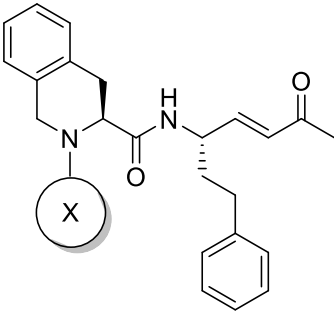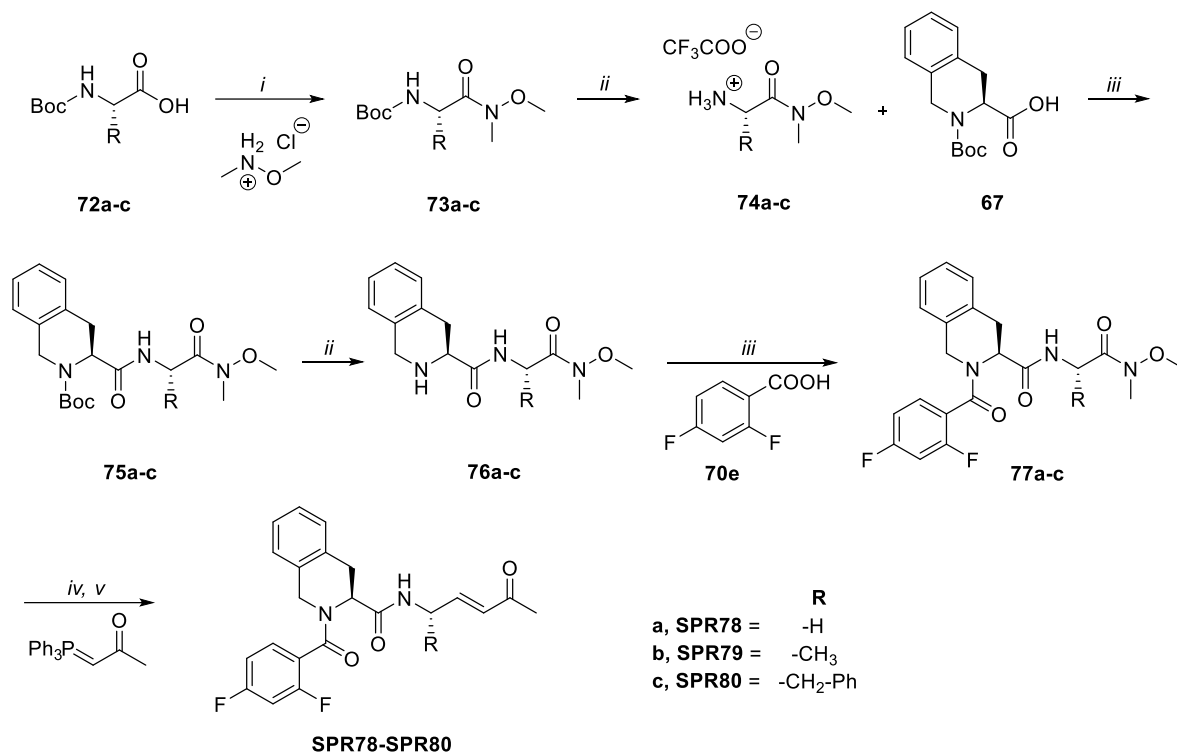

Scheme 8. Reagents and conditions: *i*) DCM, TBTU, DIPEA, 0°C, 20 min, then *N,O*-dimethylhydroxylamine hydrochloride, rt, 12h; *ii*) 30%TFA in DCM, 0° C, then ta, 12h; *iii*) DCM, TBTU, DIPEA, 0°C to rt, 12h; *iv*) LiAlH₄, dry THF, -15° C, 4h; *v*) DCM, rt, 2h.

In biological evaluations against rhodesain, **SPR78**, **SPR79**, and **SPR80** exhibited poor inhibition percentages at the screening concentration, with values of $11.0 \pm 1.5\%$, $20.2 \pm 1.8\%$, and $18.4 \pm 0.3\%$, respectively.

Overall, eight novel Michael acceptors containing the Tic residue at the P2 site showed inhibitory properties against rhodesain. Compared to their Phe-containing counterparts, these analogues exhibited lower affinities towards the target, likely due to the rigidity of the Tic residue and its binding characteristics within the S2 pocket. The substituent at the P3 position was found to be crucial for binding affinity. Replacing hPhe at the P1 site was poorly tolerated,

suggesting a strong correlation not only between the P3 substituents and the Phe-hPhe building block but also between the Tic residue and the P1 residues.

All the newly identified rhodesain inhibitors were tested against T. b. brucei cultures (Table 8). Remarkably, these compounds exhibited EC_{50} values in the low micromolar to sub-micromolar range, from 0.42 to 1.35 µM. Unlike the significant variations observed in rhodesain inhibition, the antiprotozoal effects of the new compounds were relatively uniform. There was no perfect correlation between target inhibition and antiprotozoal activity. Notably, the EC_{50} values of the new SPRs were comparable to or slightly better than those of the parent compounds with Phe at the P2 site.

Table 8. Comparison between the new Tic-analogues and corresponding Phe derivatives in terms of rhodesain inhibition and antitrypanosomal effect.

Cmpd	Rhodesain k_{2nd} x 10^3 M^{-1} min^{-1}	T. b. brucei EC_{50} (µM)
SPR66	6.7 ± 0.2	0.67 ± 0.05
63b[190]	67 000	3.18
SPR67	4.1 ± 0.4	0.91 ± 0.00
63c[189]	230 300	n.a.
SPR68	30.1 ± 2.7	1.35 ± 0.11
63d[189]	149 200	n.a.
SPR69	8.0 ± 0.6	0.85 ± 0.01
63e[189]	881 100	3.6
SPR70	146.1 ± 23.4	1.21 ± 0.02
63f[189]	107 100	0.67
SPR75	68.5 ± 32.5	0.58 ± 0.02
63k[186]	13 000	3.1
SPR76	47.9 ± 13.7	0.57 ± 0.00
63l[186]	11 900	1.3
SPR77	75.6 ± 25.4	0.42 ± 0.04
63m[186]	13 800	2.6
n.a.: not available		

These results might be attributed to several factors: i) inhibition of alternative targets, such as TbCatB,[201,202] ii) increased accumulation in lysosomes where rhodesain is located, and iii) enhanced resistance to proteolytic degradation due to the presence of the unnatural and

constrained Tic amino acid.[203] Overall, the incorporation of the Tic residue at the P2 site in peptidomimetics with a Michael acceptor warhead appears to provide promising antitrypanosomal effects.

10.2.3. Conclusion

In this SAR study, a small series of new Tic-containing Michael acceptors were developed. Incorporating the Tic residue at the P2 site resulted in eight novel rhodesain inhibitors with k_{2nd} values ranging from 4.1 to 146.1 × 10^3 M^{-1} min^{-1}. Compared to the analogues with Phe at the P2 site, these new constrained peptidomimetics showed reduced inhibitory properties towards the target enzyme, likely due to the rigidity of the Tic residue.

However, promising EC_{50} values ranging from 0.42 to 1.35 µM were observed in cell-based assays against T. b. brucei cultures. In contrast to the target inhibition, the antitrypanosomal effects of these Tic-containing peptidomimetics were comparable to or slightly better than those of the parent compounds.

These findings suggest that while the Tic residue was less effective for rhodesain inhibition, its presence in peptidomimetics with the vinyl methyl ketone warhead generally yielded interesting antitrypanosomal effects. This indicates potential for further investigation in future SAR studies.

10.3. Experimental section

10.3.1 Chemistry

All the reagents and solvents used for the synthesis of the compounds reported here were purchased from commercial suppliers. Boc-Tic-OH, the amino acids incorporated at the P1 and P3 sites, TBTU, N,O-dimethylhydroxylamine hydrochloride, and DIPEA were purchased from Fluorochem. The fluorinated aromatic rings, the isocyanates, $LiAlH_4$, and the Wittig reagent (1-(triphenylphosphoranylidene)-2-propanone) were obtained from Merck. The silica gel plates 60 F254 for monitoring reactions and purifications and the silica gel used for purifications (200-400 mesh) were obtained from Merck. All ^1H, ^{13}C, COSY, and HSQC spectra were recorded on a Varian 500 MHz instrument equipped with a ONE NME probe and operating at 499.74 and 125.73 MHz for ^1H and ^{13}C, respectively. The deuterated solvents ($CDCl_3$ and MeOD) were obtained from Merck, and the solvent signals (7.26 ppm and 3.30 ppm) were used as internal standards. The multiplicity of the signals is reported as singlet (s), doublet (d), doublet of

doublets (dd), triplet (t), quartet (q), multiples (m), and broad singlet (bs). Chemical shifts are expressed in ppm and coupling constants (J) in Hz. All novel compounds were analysed with a LC/MS system consisted of a Waters Alliance 2690 HPLC, coupled to a ZQ spectrometer (Manchester, UK) fitted with an electrospray source operated in the positive ionization mode (ESI$^+$). All the analyses were carried out using a C_{18} Chromolith Flash 25 x 4.6 mm column operated at a flow rate of 3 mL/min, in gradient from of 0% to 100% of ACN with 0.1% of TFA. Positive-ion electrospray mass spectra were acquired at a solvent flow rate of 100-200 µL/min. Nitrogen was used for both the nebulizing and drying gas. The data were obtained in a scan mode ranging from 200 to 1700 m/z in 0.1 s intervals. High Resolution Mass Spectra (HRMS) were performed at the "Laboratoire de Mesures Physiques" of University of Montpellier (France) on a Micromass Q-Tof spectrometer equipped with electrospray source ionization (ESI), using phosphoric acid as an internal standard.

tert-butyl (S)-(1-(Methoxy(methyl)amino)-1-oxo-4-phenylbutan-2-yl)carbamate (65)
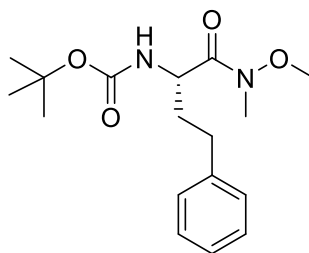
In a round bottom flask (A), the appropriate commercially available Boc-hPhe-OH **64** (1.5 eq.) was dissolved in DCM (10 mL/mmol) and cooled down to 0 °C with an ice bath. TBTU (1.5 eq) and DIPEA (2.5 eq.) were added, and the reaction was kept in vigorously stirring for 30 min. After this time, *N,O*-dimethylhydroxylamine hydrochloride (1 eq.) was added portion-wise, and the pH was checked (>8). The reaction was vigorously stirred at rt on. Subsequently, DCM was removed *in vacuo*. The organic phase was dissolved with EtOAc (x 3) and washed with 1 M HCl (x 2), NaHCO$_3$ saturated solution (x 2), and brine (x 2), dried over Na$_2$SO$_4$, and concentrated *in vacuo*. The obtained crude was purified using the eluent mixture light petroleum /EtOAc (4:1). Yield = 90%; R_f = 0.45 (light petroleum /EtOAc 4:1); Consistency = colorless oil. ^{1}H NMR (75 MHz, CDCl$_3$): δ = 1.42 (s, 9H), 1.80-1.91 (m, 1H), 2.01-2.16 (m, 1H), 2.60-2.74 (m, 1H), 2.74-2.83 (m, 1H), 3.18 (s, 3H), 3.65 (s, 3H), 4.68-4.79 (m, 1H), 5.26 (d, J = 8.3 Hz, 1H), 7.21-7.26 (m, 3H), 7.30-7.38 (m, 2H).

(S)-1-(Methoxy(methyl)amino)-1-oxo-4-phenylbutan-2-aminium 2,2,2-trifluoroacetate (66)
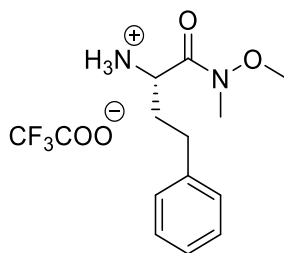
In a round-bottom flask, the Weinreb amide **65** (1 eq.) was dissolved in DCM (70% *v/v*) and cooled to 0°C. TFA (10 eq., 30% *v/v*) was then added dropwise. The reaction mixture was stirred vigorously at room temperature until TLC monitoring (light petroleum /EtOAc 4:1) indicated the disappearance of the starting material. Subsequently, the volatiles were removed by co-evaporation with toluene (3x), chloroform (1x), and Et$_2$O (1x). The resulting residues were triturated in Et$_2$O and used for the next step without further purification. ^{1}H NMR (75 MHz, MeOD): δ = 2.10-2.27 (m, 2H), 2.71-2.83 (m, 2H), 3.23 (s, 3H), 3.66 (s, 3H), 4.28-4.35 (m, 1H), 7.19-7.33 (m, 3H), 7.34-7.40 (m, 2H).

tert-butyl (S)-3-(((S)-1-(Methoxy(methyl)amino)-1-oxo-4-phenylbutan-2-yl)carbamoyl)-3,4-dihydroisoquinoline-2(1H)-carboxylate (68)
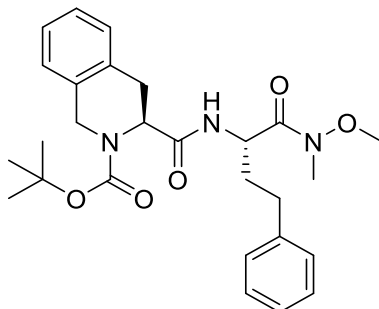
In a round bottom flask (A), Boc-Tic-OH **67** (1.5 eq.) was dissolved in DCM (10 mL/mmol) and cooled down up to 0 °C with an ice bath. TBTU (1.5 eq.) and DIPEA (2.5 eq.) were added and the reaction was kept in vigorously stirring for 30 min. Meanwhile, in a different flask (B) the intermediate **66** (1 eq.) was suspended in DCM (10 mL/mmol) and DIPEA (2eq.) was added at 0 °C. The pH was checked in both flasks (>8) and the solution of the flask B was added dropwise to the flask A. After that, the reaction was left in stirring at rt on. Subsequently, DCM was removed *in vacuo*, and the resulting residue was dissolved in EtOAc, washed with 1 M HCl (x 2), NaHCO$_3$ saturated solution (x 2), and brine (x 2), dried over Na$_2$SO$_4$, and concentrated *in vacuo*. The obtained crude was purified using light petroleum /EtOAc 3:2 as the eluent mixture. Yield = 85%; R_f = 0.25 (light petroleum /EtOAc 3:2); Consistency = White powder. ^{1}H NMR (75 MHz, CDCl$_3$): δ = 1.45-1.59 (m, 10H), 1.70-1.89 (m, 1H), 1.96-2.19 (m, 2H), 3.02-3.13 (m, 4H), 3.29-3.41 (m, 1H), 3.56 (s, 3H), 4.47-4.75 (m, 3H), 4.78-4.88 (m, 1H), 6.47 (bs, 0.5H), 6.77 (bs, 0,5H), 6.92 (bs, 2H), 7.09-7.25 (m, 7H). RT at the LC/MS system = 3.77 min. Exact mass for C$_{27}$H$_{35}$N$_3$O$_5$ = calculated 481.257; found mass: 482.4 [M + H]$^+$. Fragments: 426.4 [M - tBu], 421.4 [M – NH(CH$_3$)O(CH$_3$)], 382.4 [M - Boc].

(S)-N-((S)-1-(methoxy(methyl)amino)-1-oxo-4-phenylbutan-2-yl)-1,2,3,4-tetrahydroisoquinoline-3-carboxamide (69)
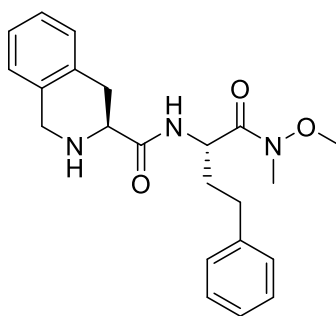
In a round-bottom flask, the Weinreb amide **68** (1 eq.) was dissolved in DCM (70% *v/v*) and cooled to 0°C with an ice-bath. TFA (10 eq., 30% *v/v*) was then added dropwise. The reaction mixture was vigorously stirred at rt until the disappearance of the starting material, which was monitored by TLC using a mixture of light petroleum /EtOAc 3:2. Subsequently, the volatiles were removed by co-evaporation with toluene (x 3), chloroform (x 1), and Et$_2$O (x 1). The resulting residue was triturated in Et$_2$O and used for the next step without further purification. Yield = 98%; Consistency = pale yellow solid. ^{1}H NMR (75 MHz, CDCl$_3$): δ = 1.68 (bs, 1H), 1,87-1.97 (m, 1H), 2.03-2.13 (m, 1H), 2.52-2.67 (m, 2H), 2.85 (dd, *J* = 16.2, 9.9 Hz, 1H), 3.16-3.22 (m, 1H), 3.18 (s, 3H), 3.57 (dd, *J* = 10.0, 5.2 Hz, 1H), 3.67 (s, 3H), 3.95-4.05 (m, 2H), 4.97-5.08 (m, 1H), 7.03-7.09 (m, 1H), 7.12-7.18 (m, 6H), 7.23-7.29 (m, 2H), 7.73 (d, *J* = 8.9 Hz, 1H). ^{13}C NMR (126 MHz, CDCl$_3$): δ = 31.33, 31.87, 34.10, 47.40, 48.60, 56.49, 61.64, 125.76, 126.08, 126.37, 126.69, 128.48, 128.63, 129.19, 134.39, 136.20, 141.20, 173.34. RT at the LC/MS system = 1.98 min. Exact mass for C$_{22}$H$_{27}$N$_3$O$_3$ = calculated 381.205; found mass: 382.3 [M + H]$^+$, 384.3 [M + 2H]$^{2+}$. Fragments: 321.3 [M – NH(CH$_3$)O(CH$_3$)].

Benzyl (S)-3-(((S)-1-(methoxy(methyl)amino)-1-oxo-4-phenylbutan-2-yl)carbamoyl)-3,4-dihydroisoquinoline-2(1H)-carboxylate (71a)
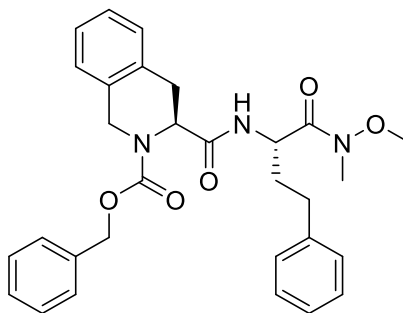
In a round bottom flask, amine **69** (1 eq.) was solubilized in a mixture of dioxane/H$_2$O (1:10, 5mL/mmol) at rt and K$_2$CO$_3$ (3 eq.) was added. The reaction was left in stirring for 15 min. After that, an ice bath was installed and Cbz-Cl **70a** (1.1 eq.) was added dropwise. The ice bath was removed and the reaction was kept in vigorously stirring on at rt. After this time, 1 M HCl was added and dioxane was removed *in vacuo*, and the organic phase was extracted with EtOAc (x 3), dried over Na$_2$SO$_4$ and concentrated. The intermediate was purified using a mixture of light petroleum /EtOAc 3:2 by column chromatography. Yield: 71%. R_f = 0.29 (light petroleum /EtOAc 3:2); Consistency = opalescent solid. ^{1}H NMR (75 MHz, CDCl$_3$): δ = 1.58-1.69 (m, 0.5H), 1.72-1.92 (m, 1H), 2.00-2.25 (m, 2.5H), 3.05-3.17 (m, 4H), 3.37 (dd, *J* = 29.9, 15.2 Hz, 1H), 3.47-3.61 (m, 3H), 4.52-4.89 (m, 3.5H), 4.98 (bs, 0.5H), 5.16-5.30 (m, 2H), 6.56 (d, *J* = 8.9 Hz, 0.5H), 6.80 (d, *J* = 8.6 Hz, 0.5H), 6.85-6.98 (m, 2H), 6.98-7.06 (m, 0.5H), 7.06-7.26 (m, 7.5H), 7.26-7.48 (m, 4H). RT at the LC/MS system = 3.82 min. Exact mass for C$_{30}$H$_{33}$N$_3$O$_5$

= calculated 515.242; found mass: 516.4 [M + H]$^+$, 538.3 [M + Na]$^+$ .Fragments: 455.3 [M - NH(CH$_3$)O(CH$_3$)], 294.2 [M - NH(CH$_3$)O(CH$_3$) - hPhe]

**General Procedure for the Synthesis of Intermediates 71b-f and 71i-l**

In a round bottom flask (A), the appropriate acid **70b-f** and **70i-l** (1.5 eq.) was dissolved in DCM (10 mL/mmol) and cooled down up to 0 °C with an ice bath. TBTU (1.5 eq.) and DIPEA (2.5 eq.) were added and the reaction was kept in vigorously stirring for 30 min. Meanwhile, the intermediate **69** (1 eq.) was added at 0 °C. The pH was checked (>8) and the reaction was left in stirring at rt on. Subsequently, DCM vas removed *in vacuo*, and the residue was dissolved in EtOAc and washed with 1 M HCl (x 2), NaHCO$_3$ saturated solution (x 2), and brine (x 2), dried over Na$_2$SO$_4$, and concentrated *in vacuo*. The obtained crudes were purified using the appropriate eluent mixture.

*(S)-2-(2-Fluorobenzoyl)-N-((S)-1-(methoxy(methyl)amino)-1-oxo-4-phenylbutan-2-yl)-1,2,3,4-tetrahydroisoquinoline-3-carboxamide (71b)*
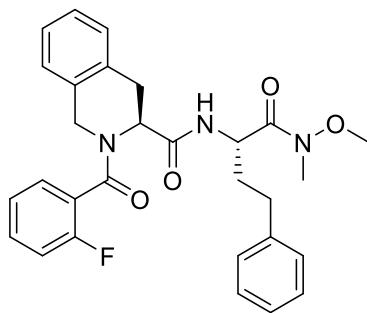
In this reaction **70b** was used as the acid. Yield: 77%. R_f = 0.35 (light petroleum /EtOAc 3:2); Consistency = Opalescent solid. ^{1}H NMR (75 MHz, CDCl$_3$): δ = 1.60-1.69 (m, 0.5), 1.69-1.82 (m, 0.5H), 1.81-1.90 (m, 0.5H) 1.93-2.04 (m, 0.5H), 2.14-2.24 (m, 0.5H) 2.30-2.46 (m, 1.5H), 3.11-3.21 (m, 4H), 3.45-3.53 (m, 4H), 4.48 (d, J = 15.3 Hz, 0.5H), 4.54-4.62 (m, 1H), 4.67-4.74 (m, 1H), 4.81 (d, J = 17.6 Hz, 0.5H), 4.88-4.96 (m, 0.5H), 5.23 (d, J = 16.7 Hz, 0.5H), 5.31-5.43 (m, 1H), 6.53-6.60 (m, 0.5H), 6.86 (d, J = 7.1 Hz, 0.5H), 6.95 (d, J = 7.3 Hz, 1H), 7.04 (d, J = 7.0 Hz, 1H), 7.11-7.17 (m, 2H), 7.19-7.26 (m, 7H), 7.38-7.44 (m, 0.5H), 7.44-7.55 (m, 1.5H). RT at the LC/MS system = 3.49 min. Exact mass for C$_{29}$H$_{30}$FN$_3$O$_4$ = calculated: 503.222; found mass: 504.3 [M + H]$^+$, 526.3 [M + Na]$^+$. Fragments: 282.2 [M – hPhe-NH(CH$_3$)O(CH$_3$)].

(S)-2-(3-Fluorobenzoyl)-N-((S)-1-(methoxy(methyl)amino)-1-oxo-4-phenylbutan-2-yl)-1,2,3,4-tetrahydroisoquinoline-3-carboxamide (71c)
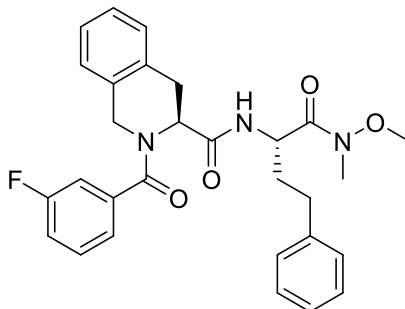
In this reaction **70c** was used as the acid. Yield: 72%. R_f = 0.34 (light petroleum /EtOAc 3:2); Consistency = Opalescent solid. ^{1}H NMR (75 MHz, CDCl$_3$): δ = 1.60-1.69 (m, 0.5), 1.71-1.85 (m, 0.5H), 1.86-1.90 (m, 0.5H), 1.93-2.01 (m, 0.5H), 2.15-2.25 (m, 0.5H) 2.30-2.44 (m, 1.5H), 3.13-3.24 (m, 4H), 3.44-3.57 (m, 4H), 4.50 (d, J = 15.2 Hz, 0.5H), 4.56-4.64 (m, 1H), 4.71-4.76 (m, 1H), 4.84 (d, J = 17.4 Hz, 0.5H), 4.90-4.96 (m, 0.5H), 5.22 (d, J = 16.6 Hz, 0.5H), 5.30-5.41 (m, 1H), 6.54-6.63 (m, 0.5H), 6.86-6.92 (m, 0.5H), 6.95-7.00 (m, 1H), 7.04-7.171 (m, 3H), 7.19-7.26 (m, 7H), 7.38-7.49 (m, 2H). RT at the LC/MS system = 3.49 min. Exact mass for C$_{29}$H$_{30}$FN$_3$O$_4$ = calculated: 503.222; found mass: 504.2 [M + H]$^+$, 526.2 [M + Na]$^+$. Fragments: 282.2 [M – hPhe-NH(CH$_3$)O(CH$_3$)].

(S)-2-(4-Fluorobenzoyl)-N-((S)-1-(methoxy(methyl)amino)-1-oxo-4-phenylbutan-2-yl)-1,2,3,4-tetrahydroisoquinoline-3-carboxamide (71d)

In this reaction **70d** was used as the acid. Yield: 67%. R_f = 0.33 (light petroleum /EtOAc 2:3); Consistency = Opalescent solid. ^{1}H NMR (75 MHz, CDCl$_3$): δ = 1.67-1.83 (m, 1H), 1.89-2.06 (m, 1H), 2.14-2.33 (m, 0.5H) 2.36-2.53 (m, 1.5HH), 2.98-3.22 (m, 1H), 3.14 (s, 3H), 3.39 (dd, J = 15.6, 4.6 Hz, 1H), 3.45 (s, 1H) 3.60 (s, 2H), 4.50-4.83 (m, 0.5H), 4.86-5.01 (m, 3.5H), 5.05-5.21 (m, 1H), 6.56-7.32 (m, 12H), 7.55 (bs, 2H). RT at the LC/MS system = 3.51 min. Exact mass for C$_{29}$H$_{30}$FN$_3$O$_4$: 503.222. Found mass: 504.4 [M + H]$^+$, 526.2 [M + Na]$^+$. Fragments: 443.3 [M – NH(CH$_3$)O(CH$_3$)], 282.2 [M – hPhe-NH(CH$_3$)O(CH$_3$)].

(S)-2-(2,4-Difluorobenzoyl)-N-((S)-1-(methoxy(methyl)amino)-1-oxo-4-phenylbutan-2-yl)-1,2,3,4-tetrahydroisoquinoline-3-carboxamide (71e)

In this reaction **70e** was used as the acid. Yield: 58%. R_f = 0.51 (light petroleum /EtOAc 1:1); Consistency = Opalescent solid. ^{1}H NMR (75 MHz, CDCl$_3$): δ = 1.69-1.79 (m, 0.5H), 1.81-1.90 (m, 0.5H), 1.92-2.04 (m, 1H), 2.13-2.21 (m, 0.5H), 2.30-2.45 (m, 1.5H), 3.11 (s, 1H), 3.15 (s, 2H), 3.18 (dd, J = 15.9, 6.5 Hz, 1H), 3.41-3.48 (m, 1H), 3.45 (s, 1H), 3.60 (s, 2H), 4.47 (d, J = 15.5 Hz, 1H), 4.52-4.63 (m, 1H), 4.64-4.72 (m, 0.5H), 4.82 (d, J = 17.3 Hz, 0.5H), 4.87-4.95 (m, 0.5H) 5.17 (d, J = 17.1 Hz, 0.5H), 6.51 (d, J = 7.4 Hz, 1H), 6.75-7.07 (m, 4H), 7.11-7.28 (m, 7H), 7.45-7.60 (m, 1H). RT at the LC/MS system = 3.57 min. Exact mass for

C$_{29}$H$_{29}$F$_2$N$_3$O$_4$ = 521.212. Found mass: 522.4 [M + H]$^+$, 544.4 [M + Na]$^+$. Fragments: 461.3 [M – NH(CH$_3$)O(CH$_3$)], 300.2 [M – hPhe-NH(CH$_3$)O(CH$_3$)], 142.3 [M – Tic-hPhe-NH(CH$_3$)O(CH$_3$)].

(S)-2-(2,6-Difluorobenzoyl)-N-((S)-1-(methoxy(methyl)amino)-1-oxo-4-phenylbutan-2-yl)-1,2,3,4-tetrahydroisoquinoline-3-carboxamide (71f)
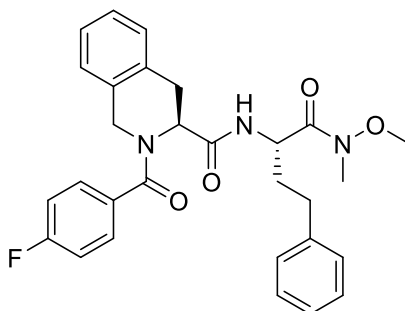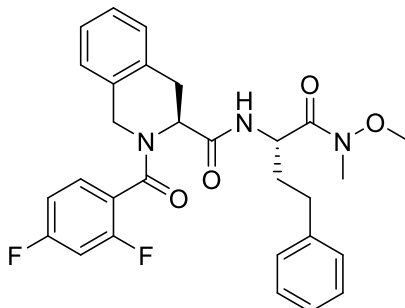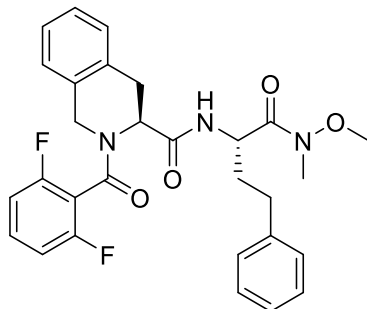

In this reaction **70f** was used as the acid. Yield: 56%; R_f = 0.47 (light petroleum /EtOAc 1:1); Consistency = Opalescent solid. ^{1}H NMR (75 MHz, CDCl$_3$): δ = 1.63-1.70 (m, 0.5H), 1.71-1.80 (m, 0.5H), 1.84-1.92 (m, 0.5H) 1.93-2.01 (m, 0.5H), 2.06-2.14 (m, 0.5H), 2.23-2.44 (m, 1.5H), 3.10 (s, 1H), 3.14 (s, 2H) 3.12-3.18 (m, 1H), 3.42-3.54 (m, 1H), 3.47 (s, 1H), 3.58 (s, 2H), 4.47 (d, *J* = 15.6 Hz, 0.5H), 4.65-4.72 (m, 1H), 4.54-4.61 (m, 1H), 4.78 (d, *J* = 17.7 Hz, 0.5H), 4.88-4.95 (m, 0.5H), 5.32 (d, *J* = 17.6 Hz, 0.5H), 5.45 (t, *J* = 5.1 Hz, 0.5H), 6.60 (d, *J* = 7.8 Hz, 1.5H), 6.95-7.08 (m, 2.5H), 6.86 (dd, *J* = 15.6, 7.9 Hz, 1H), 7.11-7.23 (m, 6H), 7.26-7.28 (m, 1H), 7.36-7.48 (m, 1H). RT at the LC/MS system = 3.51 min. Exact mass for C$_{29}$H$_{29}$F$_2$N$_3$O$_4$ = 521.212. Found mass: 522.4 [M + H]$^+$, 544.4 [M + Na]$^+$. Fragments: 461.3 [M – NH(CH$_3$)O(CH$_3$)], 300.2 [M – hPhe-NH(CH$_3$)O(CH$_3$)], 142.3 [M – Tic-hPhe-NH(CH$_3$)O(CH$_3$)].

Benzyl ((S)-1-((S)-3-(((S)-1-(methoxy(methyl)amino)-1-oxo-4-phenylbutan-2-yl)carbamoyl)-3,4-dihydroisoquinolin-2(1H)-yl)-1-oxopropan-2-yl)carbamate (71i)
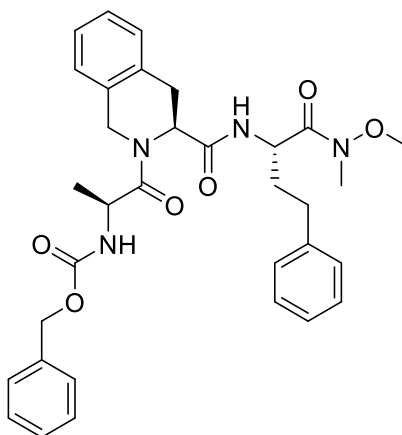
In this reaction **70i** was used as the acid. Yield: 63%. R_f = 0.20 (light petroleum /EtOAc 3:7); Consistency = Opalescent solid. ^{1}H NMR (75 MHz, CDCl$_3$): δ = 1.28 (d, *J* = 5.5 Hz, 2H), 1.41 (d, *J* = 6.7 Hz, 1H), 1.60-1.69 (m, 0.5H), 1.69-1.78 (m, 0.5H), 1.79-1.86 (m, 0.5H), 2.01-2.07 (m, 0.5H), 2.21-2.32 (m, 1.5H), 2.98 (s, 1H), 3.04-3.09 (m, 1H), 3.11 (s, 2H), 3.34 (d, *J* = 5.2 Hz, 0.5H), 3.37 (s, 1H), 3.49 (s, 0.5H), 3.56 (s, 2H), 4.61-4.79 (m, 2H), 4.79-4.92 (m, 2H), 4.96 (d, *J* = 12.6 Hz, 1H), 5.05-5.15 (m, 2H), 5.62-5.67 (m, 0.5H), 5.77 (d, *J* = 7.4 Hz, 0.5H), 6.55

(d, J = 8.1 Hz, 0.5H), 6.88 (d, J = 7.1 Hz, 0.5H), 7.01 (d, J = 7.3 Hz, 1H), 7.09-7.24 (m, 6H), 7.56-7.37 (m, 8H). RT at the LC/MS system = 3.66 min. Exact mass for $C_{33}H_{38}N_4O_6$ = calculated: 586.279; found: 587.4 [M+H]$^+$, 609.4 [M+Na]$^+$. Fragments: 526.4 [M - N(CH$_3$)O-CH$_3$], 365.2 [M - N(CH$_3$)O-CH$_3$ -hPhe].

Benzyl   ((S)-1-((S)-3-(((S)-1-(methoxy(methyl)amino)-1-oxo-4-phenylbutan-2-yl)carbamoyl)-3,4-dihydroisoquinolin-2(1H)-yl)-4-methyl-1-oxopentan-2-yl)carbamate (71j)
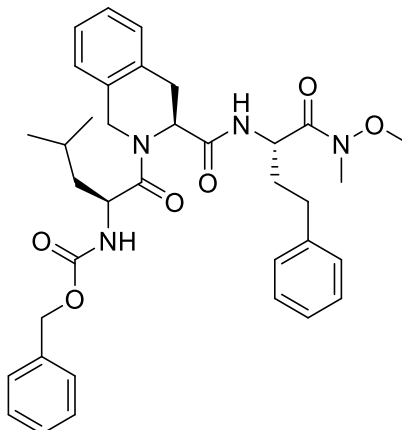
In this reaction **70i** was used as the acid. Yield: 70%. R_f = 0.29 (light petroleum /EtOAc 2:3); Consistency = Opalescent solid. ^{1}H NMR (75 MHz, CDCl$_3$): δ = 0.98 (dt, J = 13.3, 6.5 Hz, 4H), 1.11 (d, J = 6.5 Hz, 2H), 1.60-1.65 (m, 2H), 1.65-1.72 (m, 1H), 1.72-1.80 (m, 1H), 1.80-1.88 (m, 1H), 1.88-1.97 (m, 1H), 2.25-2.39 (m, 2H), 3.01 (s, 1H), 3.04-3.10 (m, 1H), 3.11 (s, 2H), 3.32 (dd, J = 15.6, 5.2 Hz, 1H), 3.44 (s, 1H), 3.55 (s, 2H), 4.54-4.71 (m, 2H), 4.79-4.95 (m, 3H), 5.02-5.09 (m, 2H), 5.44-5.50 (m, 1H), 6.55 (d, J = 8.3 Hz, 1H), 6.92 (d, J = 7.5 Hz, 0.5H), 7.04 (d, J = 7.1 Hz, 1.5H), 7.13-7.24 (m, 7H), 7.30-7.35 (m, 4H). RT at the LC/MS system = 4.11 min. Exact mass for $C_{36}H_{44}N_4O_6$ = calculated: 628.770; found: 629.5 [M+H]$^+$, 651.5 [M+Na]$^+$. Fragments: 568.4 [M - N(CH$_3$)O-CH$_3$], 407.3 [M - N(CH$_3$)O-CH$_3$ -hPhe].

Benzyl ((S)-3-cyclohexyl-1-((S)-3-(((S)-1-(methoxy(methyl)amino)-1-oxo-4-phenylbutan-2-yl)carbamoyl)-3,4-dihydroisoquinolin-2(1H)-yl)-1-oxopropan-2-yl)carbamate (71k)
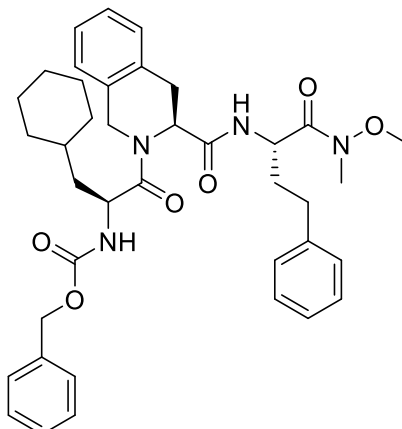
In this reaction **70k** was used as the acid. Yield: 67%. R_f = 0.40 (light petroleum /EtOAc 2:3); Consistency = Opalescent solid. ^{1}H NMR (75 MHz, CDCl$_3$): δ = 0.81-0.93 (m, 1H), 0.95-1.07 (m, 2H), 1.13-1.24 (m, 2H), 1.44-1.57 (m, 2H), 1.61-1.80 (m, 6H), 1.88-1.96 (m, 1H), 2.06-2.20 (m, 1H), 2.24-2.39 (m, 2H), 3.03 (s, 1H), 3.05-3.10 (m, 1H), 3.11 (s, 2H), 3.33 (dd, J =

15.5, 5.0 Hz, 1H), 3.46 (s, 1H), 3.55 (s, 2H), 4.59-4.65 (m, 1H), 4.78-4.86 (m, 2H), 4.91-4.97 (m, 1.5H), 5.03-5.10 (m, 1.5H), 5.12 (d, J = 12.3 Hz, 1H), 5.39-5.49 (m, 1H), 6.55 (d, J = 8.3 Hz, 1H), 6.93 (d, J = 7.3 Hz, 1H), 7.03 (d, J = 7.4 Hz, 1H), 7.11-7.25 (m, 7H), 7.28-7.37 (m, 5H). RT at the LC/MS system = 4.44 min. Exact mass for $C_{39}H_{48}N_4O_6$ = calculated: 668.357; found: 669.5 [M+H]$^+$, 691.5 [M+Na]$^+$. Fragments: 608.5 [M - N(CH$_3$)O-CH$_3$], 447.4 [M - N(CH$_3$)O-CH$_3$ -hPhe].

Benzyl   ((S)-1-((S)-3-(((S)-1-(methoxy(methyl)amino)-1-oxo-4-phenylbutan-2-yl)carbamoyl)-3,4-dihydroisoquinolin-2(1H)-yl)-1-oxo-3-phenylpropan-2-yl)carbamate (71l)
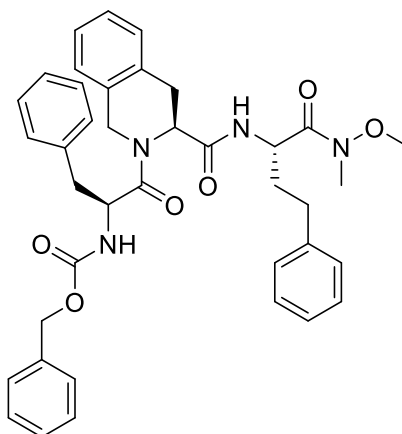
In this reaction **70l** was used as the acid. Yield: 59%. R_f = 0.30 (light petroleum /EtOAc 2:3); Consistency = Opalescent solid. ^{1}H NMR (75 MHz, CDCl$_3$): δ = 1.62-1.71 (m, 1H), 1.71-1.80 (m, 1H), 1.79-1.87 (m, 1H), 1.87-1.96 (m, 1H), 2.06-2.13 (m, 0.5H), 2.21-2.31 (m, 1.5H), 3.02 (s, 2H), 3.04-3.11 (m, 2.5H), 3.11-3.15 (m, 0.5H), 3.13 (s, 1H), 3.24 (dd, J = 13.8, 7.1 Hz, 0.5H), 3.31 (dd, J = 15.3, 5.1 Hz, 0.5H), 3.44 (s, 1.5H), 3.57 (s, 1.5H), 4.22-4.30 (m, 1H), 4.47-4.55 (m, 0.5H), 4.59 (d, J = 16.8 Hz, 0.5H), 4.68 (d, J = 14.6 Hz, 0.5H), 4.76-4.87 (m, 1.5H), 4.90-4.97 (m, 1H), 4.99-5.12 (m, 2H), 5.63-5.73 (m, 1H), 6.52 (d, J = 8.7 Hz, 0.5H), 6.87 (d, J = 7.2 Hz, 1H), 6.95 (d, J = 7.3 Hz, 0.5H), 6.99-7.09 (m, 1H), 7.10-7.20 (m, 4H), 7.21-7.36 (m, 10H), 7.37-7.46 (m, 1H). RT at the LC/MS system = 4.10 min. Exact mass for $C_{39}H_{42}N_4O_6$ = calculated: 662.310; found: 663.5 [M+H]$^+$, 685.4 [M+Na]$^+$. Fragments: 602.4 [M - N(CH$_3$)O-CH$_3$], 441.4 [M - N(CH$_3$)O-CH$_3$ -hPhe].

General procedure for the synthesis of urea intermediates 71g-h

In a round bottom flask, intermediate **69** (1.2 eq.) was solubilized in dry THF (2 mL/mmol), and TEA (1.3 eq.) was added, pH checked (>7) and the reaction was maintained in stirring for 5 min at rt. After that, the appropriate isocyanate **70g-h** (1 eq.) was diluted in dry THF and added drop-wise to the reaction, which was kept in stirring on at rt. A few drops of 1 M HCl were added to the flask, and the solution was moved in a separatory funnel. A few mL of 1 M HCl were added and the organic phase was extracted with EtOAc (x 3), dried over Na$_2$SO$_4$ and concentrated *in vacuo*. The desired compound was purified by column chromatography using the appropriate eluent (see details in the below section).

(S)-N3-((S)-1-(methoxy(methyl)amino)-1-oxo-4-phenylbutan-2-yl)-N2-(p-tolyl)-3,4-dihydroisoquinoline-2,3(1H)-dicarboxamide (71g)
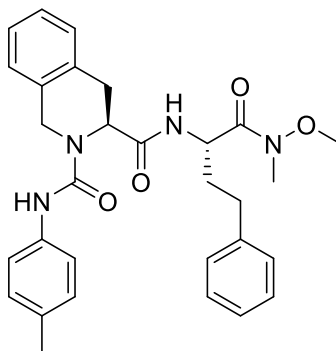
In this reaction **70g** was used as the isocyanate. Yield: 68%. R_f = 0.23 (light petroleum /EtOAc 1:1); Consistency = Opalescent solid. ^{1}H NMR (75 MHz, CDCl$_3$): δ = 1.60-1.67 (m, 1H), 1.90-2.01 (m, 2H), 2.25-2.29 (m, 1H), 2.30 (s, 3H), 3.12 (s, 3H), 3.18 (dd, J = 15.0, 6.1 Hz, 1H), 3.40 (dd, J = 15.0, 2.9 Hz, 1H), 3.49 (s, 3H), 4.46-4.52 (m, 1H), 4.54 (d, J = 14.5 Hz, 1H), 4.69 (d, J = 14.5 Hz, 1H), 4.73-4.77 (m, 1H), 6.57 (d, J = 8.2 Hz, 1H), 6.84 (d, J = 7.0 Hz, 2H), 7.07-7.13 (m, 3H), 7.14-7.18 (m, 1H), 7.19-7.30 (m, 6H), 7.36-7.40 (m, 2H). RT at the LC/MS system = 3.64 min. Exact mass for C$_{30}$H$_{34}$N$_4$O$_4$ = calculated: 514.258; found: 515.5 [M+H]$^+$, 537.4 [M+Na]$^+$. Fragments: 454.3 [M - N(CH$_3$)O-CH$_3$], 407.3 [M - 4-Me-Ph-NH-CO], 393.2 [M - N(CH$_3$)O-CH$_3$ -hPhe].

(S)-N2-(4-chloro-2-methylphenyl)-N3-((S)-1-(methoxy(methyl)amino)-1-oxo-4-phenylbutan-2-yl)-3,4-dihydroisoquinoline-2,3(1H)-dicarboxamide (71h)
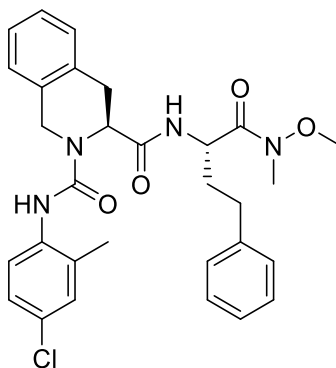
In this reaction **70h** was used as the isocyanate. Yield: 77%. R_f = 0.27 (light petroleum /EtOAc 1:1); Consistency = Opalescent solid. ^{1}H NMR (75 MHz, CDCl$_3$): δ = 1.60-1.64 (m, 1H), 1.85-1.94 (m, 1H), 1.97-2.06 (m, 1H), 2.17-2.25 (m, 1H), 2.23 (s, 3H), 3.08 (s, 3H), 3.20 (dd, J = 15.2, 6.1 Hz, 1H), 3.40 (dd, J = 15.1, 2.9 Hz, 1H), 3.50 (s, 3H), 4.56 (d, J = 14.5 Hz, 1H), 4.59-4.66 (m, 1H), 4.75 (d, J = 14.5 Hz, 1H), 4.80-4.85 (m, 1H), 6.59 (d, J = 8.3 Hz, 1H), 6.77 (s, 1H), 6.87-6.20 (m, 2H), 7.12-7.19 (m, 2H), 7.19-7.31 (m, 7H), 7.60 (d, J = 8.3 Hz, 1H). RT at the LC/MS system = 3.77 min. Exact mass for C$_{30}$H$_{33}$N$_4$O$_4$ = calculated: 548.219; found: 549.3 [M+H]$^+$. Fragments: 488.3 [M - N(CH$_3$)O-CH$_3$], 407.3 [M - 4-Cl,2-Me-Ph-NH-CO], 327.3 [M - N(CH$_3$)O-CH$_3$ -hPhe].

General Procedure for the Synthesis of Final Compounds SPR65-SPR77

In a round-bottom flask, the appropriate intermediate **71a-l** (1 eq.) was solubilized in dry THF (5 mL/mmol), cooled down to -15 °C with an ice/salt bath, and vigorously stirred. LiAlH$_4$ (1 eq.) was added over 30 min. After this period TLC monitoring did not show the presence of starting material. Cold temperature was kept. Afterwards, the unreacted LiAlH$_4$ was quenched with 1 M KHSO$_4$ and the ice-bath was removed. The suspension was moved in a separatory funnel, DCM was added, and the two phases were separated. The organic phase was further extracted with DCM (x 3). Subsequently, the merged organic phases were washed with NaHCO$_3$ saturated solution (x 2), 1 M KHSO$_4$ (x 2) and brine (x 2), dried over Na$_2$SO$_4$ and concentrated. The obtained residue was used for the next step without further purification. In a round-bottom flask, the aldehyde was solubilized in DCM (5 mL/mmol) and the appropriate Wittig reagent (1 eq.) was added in one portion. The reaction was stirred at rt for 2 h. After that, the solvent was removed *in vacuo* and the desired product was purified using the appropriate eluent mixture.

tert-Butyl (S)-3-(((S,E)-6-oxo-1-phenylhept-4-en-3-yl)carbamoyl)-3,4-dihydroisoquinoline-2(1H)-carboxylate (SPR65)
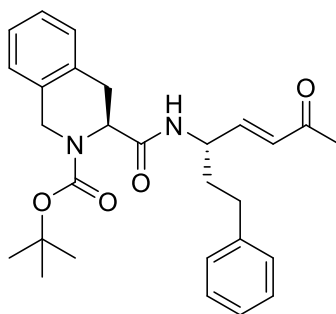
In this reaction **68** was used as the starting material. R_f = 0.42 in light petroleum /EtOAc 3:2; Consistency = white powder; Yield = 33%. ^{1}H NMR (75 MHz, CDCl$_3$): δ = 1.41-1.47 (m, 1H), 1.53 (s, 9H) 1.61-1.69 (m, 1H), 1.69-1.79 (m, 0.5H), 1.87-2.00 (m, 1H), 2.18 (s, 3H), 2.20-2.27 (m, 0.5H), 3.03-3.15 (m, 1H), 3.37 (dd, J = 15.2, 3.1 Hz, 1H), 4.47 (bs, 2.5H), 4.63-4.88 (m, 1.5H), 5.70 (bs, 0.5H), 6.01-6.20 (m, 1.5H), 6.53 (bs, 1H), 6.80-7.02 (m, 2H), 7.13-7.30 (m, 7H). RT at the LC/MS system = 3.72 min. Exact mass for C$_{28}$H$_{34}$N$_2$O$_4$ = calculated: 462.2519; found: 463.4 [M+H]$^+$, 485.4 [M+Na]$^+$. Fragments: 407.3 [M – tBu], 363.3 [M - Boc]. HRMS, found mass = 463.2582 [M+H]$^+$.

Benzyl (S)-3-(((S,E)-6-oxo-1-phenylhept-4-en-3-yl)carbamoyl)-3,4-dihydroisoquinoline-2(1H)-carboxylate (SPR66)
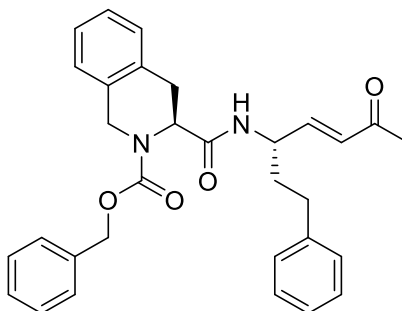
In this reaction **71a** was used as the starting material. $R_f = 0.53$ in light petroleum /EtOAc 1:1; Consistency = pale yellow powder; Yield = 31%. ^{1}H NMR (75 MHz, CDCl_3): $\delta = 1.49$-1.57 (m, 1H), 1.60-1.71 (m, 0.5H), 1.71-1.81 (m, 0.5H), 1.96 (bs, 1H), 2.07 (bs, 2H), 2.19 (bs, 2H), 3.09 (bs, 1H), 3.38 (d, $J = 14.6$ Hz, 1H), 4.43 (bs, 1H), 4.55 (bs, 1H), 4.61-4.81 (m, 1H), 4.86 (bs, 1H), 5.22 (d, $J = 12.6$ Hz, 1H), 5.27-5.37 (m, 1H), 5.66 (m, 0.5H), 5.87-6.13 (m, 1.5H), 6.36-6.60 (m, 1H), 6.78-6.99 (m, 2H), 7.08-7.28 (m, 8H), 7.28-7.45 (m, 4H). RT at the LC/MS system = 3.75 min. Exact mass for $C_{31}H_{32}N_2O_4$ = calculated: 496.2362; found: 497.4 [M+H]$^+$, 519.3 [M+Na]$^+$. Fragments: 294.3 [M – Cbz-Tic]. HRMS: determined: 479.2434; found mass: 497.2435 [M+H]$^+$.

(S)-2-(2-Fluorobenzoyl)-N-((S,E)-6-oxo-1-phenylhept-4-en-3-yl)-1,2,3,4-tetrahydroisoquinoline-3-carboxamide (SPR67)
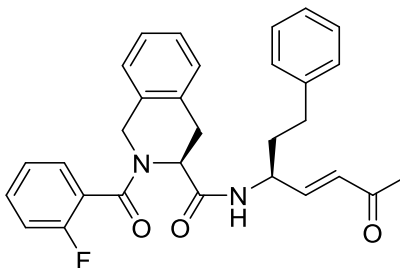
In this reaction **71b** was used as the starting material. $R_f = 0.32$ in light petroleum /EtOAc 1:1; Consistency = pale yellow powder; Yield = 39%. ^{1}H NMR (75 MHz, CDCl_3) $\delta = 1.70$-1.80 (m, 1H), 1.84-1.92 (m, 1H), 2.17 (s, 1H) 2.20 (s, 2H), 2.22-2.29 (m, 0.5H), 2.38-2.53 (m, 1.5H), 3.16 (dd, $J = 15.8, 6.6$ Hz, 1H), 3.52 ($J = 15.8, 4.9$ Hz, 1H), 4.43 (d, $J = 15.4$ Hz, 1H), 4.50 (d, $J = 15.3$ Hz, 1H), 4.53-4.59 (m, 1H), 5.37-5.40 (m, 1H), 6.16 (dd, $J = 16.0, 1.6$ Hz, 1H), 6.46-6.53 (m, 1H), 6.62 (dd, $J = 16.0, 5.2$ Hz, 1H), 6.85 (d, $J = 7.0$ Hz, 0.5H), 6.95 (d, $J = 7.5$ Hz, 1H), 7.04 (d, $J = 7.1$ Hz, 1.5H), 7.13-7.31 (m, 9H), 7.35-7.42 (m, 1H), 7.43-7.53 (m, 1H). RT at the LC/MS system = 3.45 min. Exact mass for $C_{30}H_{29}FN_2O_3$ = calculated: 484.2162; found mass: 485.3 [M + H]$^+$, 507.3 [M + Na]$^+$. Fragments: 303.3 [M - hPhe-CH=CH-COCH_3 + H + Na]$^{+2}$, 283.20 [M - hPhe-CH=CH-COCH_3 + H]$^+$, 282.0 [M - hPhe-CH=CH-COCH_3], 254.1 [M - -CO-hPhe-CH=CH-COCH_3]. HRMS, determined: 485.2234; found: 485.2235 [M+H]$^+$.

(S)-2-(3-Fluorobenzoyl)-N-((S,E)-6-oxo-1-phenylhept-4-en-3-yl)-1,2,3,4-tetrahydroisoquinoline-3-carboxamide (SPR68)

In this reaction **71c** was used as the starting material. $R_f = 0.33$ in light petroleum /EtOAc 1:1; Consistency = pale yellow powder; Yield = 22%. ^{1}H NMR (75 MHz, CDCl_3) $\delta = 1.80$-1.91 (m, 1H), 1.91-2.01 (m, 1H), 2.23 (s, 3H), 2.55-2.67 (m, 2H), 3.02-3.19 (m, 1H), 3.43-3.52 (m, 1H), 4.43 (d, $J = 15.0$ Hz, 1H), 4.55 (d, $J = 15.6$ Hz, 1H), 4.61-4.68 (m, 1H), 5.05-5.14 (m, 1H), 6.15 (d, $J = 15.9$ Hz, 1H), 6.66 (dd, $J = 16.4, 5.1$ Hz, 1H), 6.79 (d, $J = 7.0$ Hz, 1H), 6.95 (d, $J = 6.5$

Hz, 1H), 7.07-7.31 (m, 11H), 7.37-7.46 (m, 1H). RT at the LC/MS system = 3.46 min. Exact mass: 484.216. Found mass: 485.3 [M + H]$^+$, 507.3 [M + Na]$^+$, 508.3 [M + H + Na]$^{+2}$ Fragments: 303.3 [M - hPhe-CH=CH-COCH$_3$ + H + Na]$^{+2}$, 283.2 [M - hPhe-CH=CH-COCH$_3$ + H]$^+$, 282.0 [M - hPhe-CH=CH-COCH$_3$], 254.1 [M - -CO-hPhe-CH=CH-COCH$_3$]. HRMS: Calculated mass for C$_{30}$H$_{29}$FN$_2$O$_3$: 484.2162; Determined: 485.2; Found mass: 485.2 [M+H]$^+$.

(S)-2-(4-Fluorobenzoyl)-N-((S,E)-6-oxo-1-phenylhept-4-en-3-yl)-1,2,3,4-tetrahydroisoquinoline-3-carboxamide (SPR69)

In this reaction **71d** was used as the starting material. R_f = 0.31 in light petroleum /EtOAc 1:1; Consistency = pale yellow powder; Yield = 50%. ^{1}H NMR (75 MHz, CDCl$_3$) δ = 1.77-1.91 (m, 1H), 1.92-2.00 (m, 1H), 2.22 (s, 3H), 2.47-2.75 (m, 2H), 3.05-3.20 (m, 1H), 3.40-3.56 (m, 1H), 5.35-4.50 (m, 1H), 4.52-4.73 (m, 2H), 5.04-5.18 (m, 1H), 6.15 (d, J = 15.1 Hz, 1H), 6.66 (d, J = 15.1, 5.0 Hz, 1H), 6.74 (bs, 1H), 6.88-7.01 (m, 1H), 7.04-7.35 (m, 10H), 7.39-7.50 (m, 2H). RT at the LC/MS system = 3.46 min. Exact mass: 484.216. Found mass: 485.3 [M + H]$^+$, 507.3 [M + Na]$^+$, 508.3 [M + H + Na]$^{+2}$ Fragments: 303.3 [M – hPhe-CH=CH-COCH$_3$ + H + Na]$^{+2}$, 283.2 [M – hPhe-CH=CH-COCH$_3$ + H]$^+$, 282.0 [M – hPhe-CH=CH-COCH$_3$], 254.1 [M – -CO-hPhe-CH=CH-COCH$_3$]. HRMS: Calculated mass for C$_{30}$H$_{29}$FN$_2$O$_3$: 484.2162; Determined: 485.2234; Found mass: 485.2235 [M+H]$^+$.

(S)-2-(2,4-Difluorobenzoyl)-N-((S,E)-6-oxo-1-phenylhept-4-en-3-yl)-1,2,3,4-tetrahydroisoquinoline-3-carboxamide (SPR70)
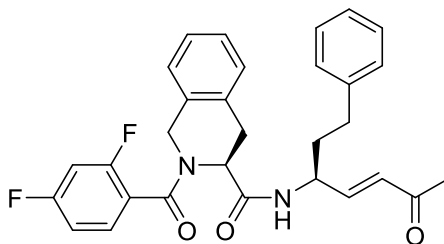
In this reaction **71e** was used as the starting material. R_f = 0.43 in light petroleum /EtOAc 1:1; Consistency = pale yellow powder; Yield = 25%. ^{1}H NMR (75 MHz, CDCl$_3$) δ = 1.70-1.81 (m, 1H), 1.85-1.93 (m, 1H), 2.21 (s, 3H), 2.41-2.55 (m, 2H), 3.15 (dd, J = 15.9, 6.6 Hz, 1H), 3.51 (dd, J = 16.0, 5.1 Hz, 1H), 4.42 (d, J = 15.2 Hz, 1H), 4.49 (d, J = 15.3 Hz, 1H), 4.53-4.62 (m, 1H), 5.24-5.33 (m, 1H), 6.14 (d, J = 15.9 Hz, 1H), 6.43 (d, J = 8.5 Hz, 1H), 6.62 (dd, J = 16.0, 5.2 Hz, 1H), 6.91-6.99 (m, 2H), 6.99-7.07 (m, 3H), 7.14-7.31 (m, 7H), 7.40 (q, J = 8.0 Hz, 1H). LC-MS: RT = 3.51 min. Exact mass: 502.207. Found mass: 503.3 [M + H]$^+$, 525.2 [M + Na]$^+$, 526.2 [M + H + Na]$^{+2}$ Fragments: 300.2 [M – hPhe-CH=CH-COCH$_3$ + H]$^+$, 272.1 [M – -CO-hPhe-CH=CH-COCH$_3$]. HRMS: Calculated mass for C$_{30}$H$_{28}$F$_2$N$_2$O$_3$: 502.2068; Determined: 503.2139; Found mass: 503.2141 [M+H]$^+$.

(S)-2-(2,6-Difluorobenzoyl)-N-((S,E)-6-oxo-1-phenylhept-4-en-3-yl)-1,2,3,4-tetrahydroisoquinoline-3-carboxamide (SPR71)
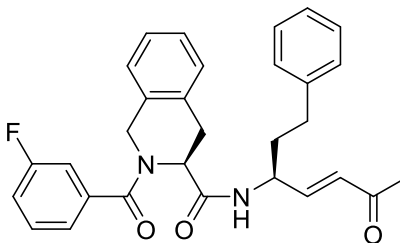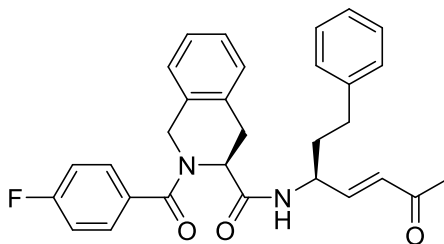

In this reaction **71f** was used as the starting material. R_f = 0.41 in light petroleum /EtOAc 1:1; Consistency = pale yellow powder; Yield = 61%. ^{1}H NMR (75 MHz, CDCl$_3$) δ = 1.58-1.74 (m, 1H), 1.79-1.89 (m, 1H), 2.06-2.14 (m, 0.5H), 2.17 (s, 1H), 2.20 (s, 2H), 2.28-2.44 (m, 1.5H), 3.08-3.19 (m, 1H), 3.48-3.59 (m, 1H), 4.30-4.40 (m, 0.3H) 4.44-4.47 (m, 0.7H), 4.47-4.51 (m, 0.7H), 4.51-4.58 (m, 0.7H), 4.58-4.63 (m, 0.3H), 4.84 (d, J = 17.5 Hz, 0.3H), 5.15 (d, J = 17.3 Hz, 0.3H), 5.36-5.44 (m, 0.7H), 5.92 (d, J = 16.1 Hz, 0.3H), 6.02 (d, J = 8.4 Hz, 0.3H), 6.17 (d, J = 16.0 Hz, 0.7H), 6.33 (d, J = 8.4 Hz, 0.7H), 6.47 (dd, J = 16.1, 5.8 Hz, 0.3H), 6.60 (dd, J = 16.0, 5.1 Hz, 0.7H), 6.81 (d, J = 7.9 Hz, 0.6H), 6.96-7.13 (m, 4H), 7.13-7.37 (m, 7H), 7.40-7.53 (m, 1H). LC-MS: RT = 3.49 min. Exact mass: 502.207. Found mass: 503.3 [M + H]$^+$, 525.2 [M + Na]$^+$, 526.2 [M + H + Na]$^{+2}$ Fragments: 300.2 [M – hPhe-CH=CH-COCH$_3$ + H]$^+$, 272.1 [M – -CO-hPhe-CH=CH-COCH$_3$]. HRMS: Calculated mass for C$_{30}$H$_{28}$F$_2$N$_2$O$_3$: 502.2068; Determined: 503.2; Found mass: 503.2 [M+H]$^+$.

(S)-N3-((S,E)-6-oxo-1-phenylhept-4-en-3-yl)-N2-(p-tolyl)-3,4-dihydroisoquinoline-2,3(1H)-dicarboxamide (SPR72)

In this reaction **71g** was used as the starting material. R_f = 0.22 in light petroleum /EtOAc 1:1; Consistency = pale yellow powder; Yield = 43%. ^{1}H NMR (75 MHz, CDCl$_3$) δ = 1.48-1.58 (m, 1H), 1.67-1.76 (m, 1H), 2.04 (s, 3H), 2.15 (t, J = 7.9 Hz, 2H), 2.30 (s, 3H), 3.12 (dd, J = 15.3, 5.9 Hz, 1H), 3.38 (dd, J = 15.3, 2.7 Hz, 1H), 4.41-4.49 (m, 1H), 4.55 (d, J = 14.2 Hz, 1H), 4.74 (d, J = 14.2 Hz, 1H), 4.92-4.99 (m, 1H), 6.02 (dd, J = 15.9, 1.4 Hz, 1H), 6.36 (d, J = 8.6 Hz, 1H), 6.51 (dd, J = 15.9, 5.0 Hz, 1H), 6.84 (s, 1H), 6.89-6.95 (m, 2H), 7.10 (d, J = 8.2 Hz, 2H), 7.14-7.19 (m, 1H), 7.19-7.28 (m, 6H), 7.31 (d, J = 8.4 Hz, 2H). RT at the LC/MS system = 3.55 min. Exact mass calculated for C$_{31}$H$_{33}$N$_3$O$_3$ = 495.2522. Found at the LC/MS system = 496.4 [M + H]$^+$, 518.3 [M + Na]$^+$; fragments = 363.3 [M – hPhe-CHCHCOMe], 239.3 [M – 4-Me-Ph-NH-CO-Tic]. Exact mass determined for HRMS = 496.3; found = 496.3 [M+H]$^+$.

(S)-N2-(4-chloro-2-methylphenyl)-N3-((S,E)-6-oxo-1-phenylhept-4-en-3-yl)-3,4-dihydroisoquinoline-2,3(1H)-dicarboxamide (SPR73)

In this reaction **71h** was used as the starting material. R_f = 0.28 in light petroleum /EtOAc 1:1; Consistency = pale yellow powder; Yield = 46%. ^{1}H NMR (75 MHz, CDCl$_3$) δ = 1.49-1.60 (m, 1H), 1.70-1.78 (m, 1H), 2.08 (s, 3H), 2.22 (s, 3H), 2.24 (t, J = 7.9 Hz, 2H), 3.16 (dd, J = 15.4, 6.0 Hz, 1H), 3.34 (dd, J = 15.5, 3.1 Hz, 1H), 4.42-4.51 (m, 1H), 4.57 (d, J = 14.2 Hz, 1H), 4.74 (d, J = 14.3 Hz, 1H), 4.92 (dd, J = 6.0, 3.0 Hz, 1H), 5.95 (dd, J = 15.9, 1.6 Hz, 1H), 6.21 (d, J = 8.4 Hz, 1H), 6.50 (dd, J = 15.9, 5.3 Hz, 1H), 6.66 (bs, 1H), 6.93-6.98 (m, 2H), 7.13-7.20 (m, 3H), 7.21-7.32 (m, 7H). RT at the LC/MS system = 3.67 min. Exact mass calculated for C$_{31}$H$_{32}$ClN$_3$O$_3$ = 529.2132. Found at the LC/MS system = 530.3 [M + H]$^+$, 552.2 [M + Na]$^+$; fragments = 363.4 [M − 4-Cl,2-Me-Ph-NH-CO-], 327.2 [M − hPhe-CHCHCOMe]. Exact mass determined for HRMS = 530.2207; found = 530.2205 [M+H]$^+$.

Benzyl ((S)-1-oxo-1-((S)-3-(((S,E)-6-oxo-1-phenylhept-4-en-3-yl)carbamoyl)-3,4-dihydroisoquinolin-2(1H)-yl)propan-2-yl)carbamate (SPR74)
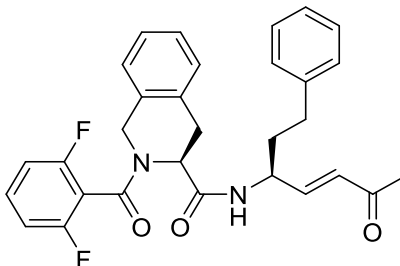

In this reaction **71i** was used as the starting material. R_f = 0.61 in light petroleum /EtOAc 3:7; Consistency = pale yellow powder; Yield = 26%. ^{1}H NMR (75 MHz, CDCl$_3$) δ = 1.41 (d, J = 7.0 Hz, 1.8H), 1.44 (d, J = 6.8 Hz, 1.2H), 1.67-1.81 (m, 1.5H), 1.81-1.91 (m, 0.5H), 2.12 (s, 1.5H), 2.19-2.26 (m, 0.5H), 2.20 (s, 1.5H), 2.28-2.36 (m, 0.5H), 2.39-2.52 (m, 1H), 2.97-3.09 (m, 1H), 3.33 (dd, J = 15.6, 5.7 Hz, 0.4H), 3.66 (dd, J = 15.4, 2.1 Hz, 0.6H), 4.29-4.38 (m, 0.5H), 4.48-4.58 (m, 2H), 4.71-4.78 (m, 1H), 4.82-4.89 (m, 0.5H), 4.93 (d, J = 17.2 Hz, 0.5H), 4.99 (d, J = 12.4 Hz, 0.5H), 4.99-5.02 (m, 0.5H), 5.10 (d, J = 4.4 Hz, 1H), 5.13 (bs, 0.5H), 5.38 (d, J = 6.6 Hz, 0.5H), 5.71 (d, J = 7.5 Hz, 0.5H), 6.03 (d, J = 16.0 Hz, 1H), 6.16 (d, J = 8.3 Hz, 0.5H), 6.58 (ddd, J = 16.0, 8.8, 5.9 Hz, 1H), 6.88 (d, J = 6.9 Hz, 1H), 7.05 (d, J = 7.0 Hz, 1H),

7.11-7.37 (m, 12H), 7.41 (d, J = 8.3 Hz, 1H). RT at the LC/MS system = 3.62 min. Exact mass calculated for $C_{34}H_{37}N_3O_5$ = 567.2733. Found at the LC/MS system = 568.4 [M + H]$^+$, 590.4 [M + Na]$^+$; fragments = 365.3 [M – hPhe-CHCHCOMe]. Exact mass determined for HRMS = 568.2804; found = 568.2806 [M+H]$^+$.

Benzyl ((S)-4-methyl-1-oxo-1-((S)-3-(((S,E)-6-oxo-1-phenylhept-4-en-3-yl)carbamoyl)-3,4-dihydroisoquinolin-2(1H)-yl)pentan-2-yl)carbamate (SPR75)
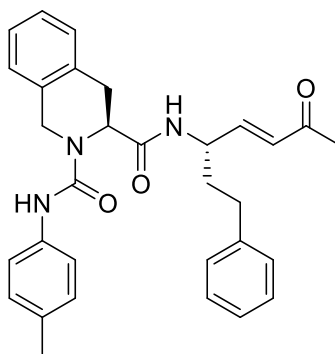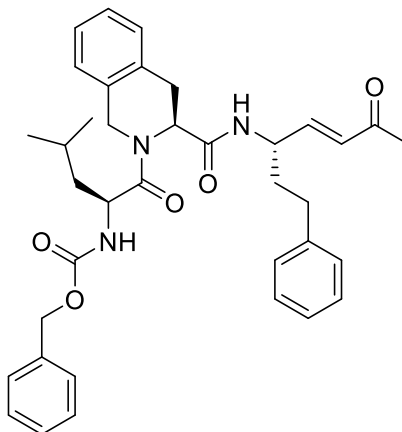

In this reaction **71j** was used as the starting material. R_f = 0.44 in light petroleum /EtOAc 1:1; Consistency = pale yellow powder; Yield = 38%. ^{1}H NMR (75 MHz, CDCl$_3$) δ = 0.91 (d, J = 6.7 Hz, 1H), 0.97 (d, J = 3.0 Hz, 2H), 0.99 (d, J = 3.1 Hz, 2H), 1.06 (d, J = 6.5 Hz, 1H), 1.41-1.47 (m, 0.5H), 1.49-1.56 (m, 0.5H), 1.65-1.72 (m, 1H), 1.73-1.83 (m, 2.5H), 1.83-1.89 (m, 0.5H), 2.15 (s, 1.7H), 2.19 (s, 1.3H), 2.22-2.31 (m, 0.5H), 2.32-2.41 (m, 0.5H), 2.41-2.51 (m, 1H), 2.95-3.09 (m, 1H), 3.32 (dd, J = 15.6, 5.6 Hz, 0.5H), 3.66 (dd, J = 15.5, 1.8 Hz, 0.5H), 4.31-4.40 (m, 0.5H), 4.45-4.59 (m, 2H), 4.76-4.84 (m, 1H), 4.89 (td, J = 9.6, 4.4 Hz, 0.5H), 4.95-5.04 (m, 1.5H), 5.05-5.12 (m, 1.5H), 5.31 (d, J = 7.0 Hz, 0.5H), 5.47 (d, J = 8.9 Hz, 0.5H), 6.03 (dd, J = 16.0, 1.5 Hz, 0.5H), 6.07 (d, J = 17.1 Hz, 0.5H), 6.20 (d, J = 8.2 Hz, 0.5H), 6.60 (ddd, J = 16.1, 11.7, 5.8 Hz, 1H), 6.91 (d, J = 7.0 Hz, 1H), 7.05 (d, J = 7.1 Hz, 1H), 7.09-7.37 (m, 12H), 7.50 (d, J = 8.2 Hz, 0.5H). RT at the LC/MS system = 4.03 min. Exact mass calculated for $C_{37}H_{43}N_3O_5$ = 609.3203. Found at the LC/MS system = 610.4 [M + H]$^+$, 632.4 [M + Na]$^+$; fragments = 407.3 [M – hPhe-CHCHCOMe]. Exact mass determined for HRMS = 610.3275; found = 610.3275 [M+H]$^+$.

Benzyl ((S)-3-cyclohexyl-1-oxo-1-((S)-3-(((S,E)-6-oxo-1-phenylhept-4-en-3-yl)carbamoyl)-3,4-dihydroisoquinolin-2(1H)-yl)propan-2-yl)carbamate (SPR76)
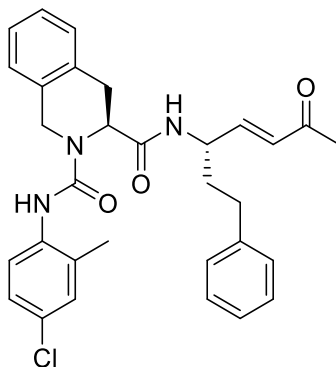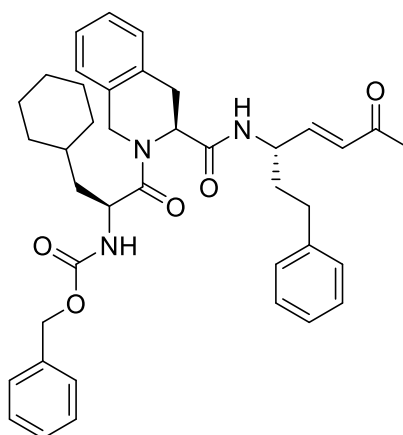
In this reaction **71k** was used as the starting material. R_f = 0.24 in light petroleum /EtOAc 7:3; Consistency = pale yellow powder; Yield = 34%. ^{1}H NMR (75 MHz, CDCl$_3$) δ = 0.85-1.02 (m, 2H), 1.11-1.28 (m, 4H), 1.40-1.52 (m, 2H), 1.64-1.85 (m, 7H), 2.15 (s, 1.8H), 2.19 (s, 1.2H), 2.22-2.31 (0.5H), 2.33-2.49 (m, 1.5H), 2.96-3.08 (m, 1H), 3.33 (dd, J = 15.5, 5.5 Hz, 0.5H), 3.66 (dd, J = 15.6, 2.2 Hz, 0.5H), 4.32-4.40 (m, 0.5H), 4.45-4.57 (m, 2H), 4.75-4.82 (m, 1H), 4.88-4.95 (m, 0.5H), 4.96-5.14 (m, 3H), 5.27 (d, J = 6.9 Hz, 0.5H), 5.43 (d, J = 9.0 Hz, 0.5H), 6.03 (dd, J = 16.0, 1.7 Hz, 0.5H), 6.07 (dd, J = 16.0, 1.1 Hz, 0.5H), 6.55-6.60 (m, 0.5H), 6.61 (dd, J = 16.0, 6.5 Hz, 0.5H), 6.91 (d, J = 7.0 Hz, 1H), 7.04 (d, J = 7.5 Hz, 1H), 7.11-7.28 (m, 8H), 7.28-7.37 (m, 4H), 7.53 (d, J = 8.3 Hz, 1H). RT at the LC/MS system = 4.34 min. Exact mass calculated for C$_{40}$H$_{47}$N$_3$O$_5$ = 649.3516. Found at the LC/MS system = 650.2[M + H]$^+$, 672.4[M + Na]$^+$; fragments = 447.3 [M − hPhe-CHCHCOMe]. Exact mass determined for HRMS = 650.3585; found = 650.3588 [M+H]$^+$.

Benzyl ((S)-1-oxo-1-((S)-3-(((S,E)-6-oxo-1-phenylhept-4-en-3-yl)carbamoyl)-3,4-dihydroisoquinolin-2(1H)-yl)-3-phenylpropan-2-yl)carbamate (SPR77)
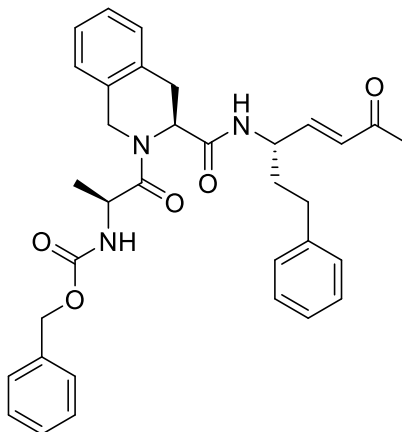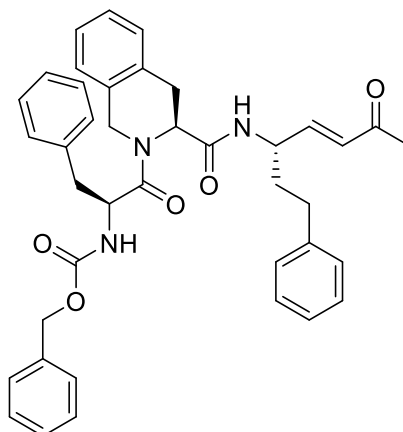

In this reaction **71l** was used as the starting material. R_f = 0.40 in light petroleum /EtOAc 1:1; Consistency = pale yellow powder; Yield = 15%. ^{1}H NMR (75 MHz, CDCl$_3$) δ = 1.66-1.82 (m, 2H), 2.19 (s, 2H), 2.17-2.24 (m, 1H), 2.22 (s, 1H), 2.28-2.37 (m, 1H), 2.95-3.14 (m, 3.2H), 3.33 (dd, J = 15.4, 4.6 Hz, 0.4H), 3.55-3.70 (m, 0.4H), 4.11-4.19 (m, 0.5H), 4.21-4.33 (m, 1.5H), 4.38-4.49 (m, 1H), 4.63-4.73 (m, 1H), 4.87-5.01 (m, 2H), 5.07-5.13 (m, 1.5H), 5.47 (d, J = 6.2 Hz, 0.5H), 6.02 (d, J = 16.0 Hz, 0.7H), 6.07 (d, J = 15.9 Hz, 0.3H), 6.55 (dd, J = 16.0, 6.6 Hz, 0.7H), 6.56-6.60 (m, 0.3H), 6.86 (d, J = 6.9 Hz, 1.5H), 6.98 (d, J = 7.7 Hz, 0.5H), 7.01-7.08 (m, 1.5H), 7.09-7.37 (m, 16H), 7.55 (d, J = 8.3 Hz, 0.5H). RT at the LC/MS system = 4.03 min.

Exact mass calculated for $C_{40}H_{41}N_3O_5 = 643.3046$. Found at the LC/MS system = 644.4 [M + H]$^+$, 666.3 [M + Na]$^+$; fragments = 441.3 [M – hPhe-CHCHCOMe]. Exact mass determined for HRMS = 644.3120; found = 644.3119 [M+H]$^+$.

Synthesis of Intermediates 73a-c

The intermediates **73a-c** were obtained following the procedure reported for compound **65.**

tert-butyl (2-(Methoxy(methyl)amino)-2-oxoethyl)carbamate (73a)
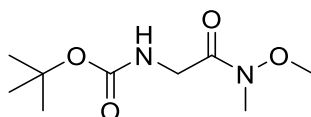
In this reaction Boc-Gly-OH **72a** is used as the acid. Yield: 88%. R_f = 0.42 in light petroleum /EtOAc 4:1; Consistency: pale yellow oil. ^{1}H NMR (75 MHz, CDCl$_3$): δ = 1.41 (s, 9H), 3.16 (s, 3H), 3.67 (s, 3H), 4.03 (d, J = 4.0 Hz, 2H), 5.26 (bs, 1H).

tert-butyl (S)-(1-(Methoxy(methyl)amino)-1-oxopropan-2-yl)carbamate (73b)
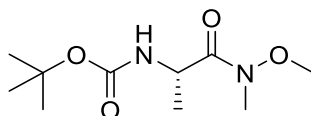
In this reaction Boc-Gly-OH **72b** is used as the acid. Yield: 81%. R_f = 0.31 in light petroleum /EtOAc 3:2; Consistency: pale yellow oil. ^{1}H NMR (75 MHz, CDCl$_3$): δ = 1.30 (d, J = 6.9 Hz, 3H), 1.42 (s, 9H), 3.19 (s, 3H), 3.75 (s, 3H), 4.60-4.73 (m, 1H), 5.24 (d, J = 7.0 Hz, 1H).

tert-butyl (S)-(1-(Methoxy(methyl)amino)-1-oxo-3-phenylpropan-2-yl)carbamate (73c)
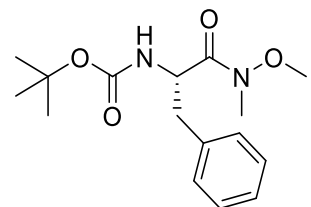
In this reaction Boc-Gly-OH **72c** is used as the acid. Yield: 86%. R_f = 0.48 in light petroleum /EtOAc 7:3; Consistency: pale yellow oil. ^{1}H NMR (75 MHz, CDCl$_3$): δ = 1.38 (s, 9H), 2.81-2.92 (m, 1H), 3.05 (dd, J = 13.4, 6.0 Hz, 1H), 3.16 (s, 3H), 3.65 (s, 3H), 4.90-4.99 (m, 1H), 5.16 (bs, 1H), 7.13-7.24 (m, 3H), 7.25-7.31 (m, 2H).

Synthesis of Intermediates 74a-c

The intermediates **74a-c** were obtained following the procedure reported for compound **66.**

2-(Methoxy(methyl)amino)-2-oxoethan-1-aminium 2,2,2-trifluoroacetate (74a)
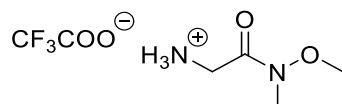
In this reaction the intermediate **73a** is used as starting material. Yield: 87%. Consistency: pale yellow powder. ^{1}H NMR (75 MHz, MeOD): δ = 3.24 (s, 3H), 3.77 (s, 3H), 3.97 (s, 2H).

(S)-1-(Methoxy(methyl)amino)-1-oxopropan-2-aminium 2,2,2-trifluoroacetate (74b)
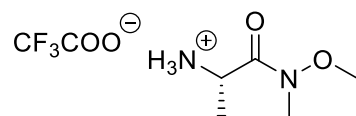
In this reaction the intermediate **73b** is used as starting material. Yield: 90%. Consistency: pale yellow powder. ^{1}H NMR (75 MHz, MeOD): δ = 1.48 (d, J = 7.0 Hz, 3H), 3.25 (s, 3H), 3.80 (s, 3H), 4.33 (q, J = 7.0 Hz, 1H).

(S)-1-Methoxy(methyl)amino)-1-oxo-3-phenylpropan-2-aminium   2,2,2-trifluoroacetate (74c)
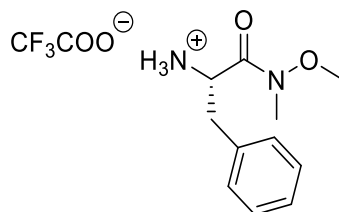
In this reaction the intermediate **73c** is used as starting material. Yield: 93%. Consistency: pale yellow powder. ^{1}H NMR (75 MHz, MeOD): δ = 3.04 (dd, J = 14.1, 8.0 Hz, 1H), 3.19-3.28 (m, 1H), 3.23 (s, 3H), 3.67 (s, 3H), 4.50-4.56 (m, 1H), 7.26 (d, J = 7.4 Hz, 1H), 7.29-7.35 (m, 1H), 7.35-7.41 (m, 2H).

Synthesis of Intermediates 75a-c

The intermediates **75a-c** were obtained following the procedure reported for compound **68.**

tert-butyl   (S)-3-((2-(Methoxy(methyl)amino)-2-oxoethyl)carbamoyl)-3,4-dihydroisoquinoline-2(1H)-carboxylate **(75a)**
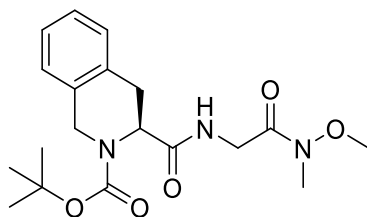
In this reaction the intermediate **74a** is used as amine. Yield: 84%. R_f = 0.36 in light petroleum /EtOAc 2:3. Consistency: pale yellow solid. ^{1}H NMR (75 MHz, CDCl$_3$): δ = 1.48 (s, 4.5H), 1.54 (s, 4.5H), 3.02-3.15 (m, 1H), 3.17 (s, 3H), 3.20-3.29 (m, 0.5H), 3.32-3.41 (m, 0.5H), 3.67 (s, 3H), 3.97-4.19 (m, 2H), 4.49 (d, J = 16.0 Hz, 1H), 4.62-4.80 (m, 1.5H), 4.95-5.04 (m, 0.5H), 6.65 (bs, 0.5H), 6.84 (bs, 0.5H), 7.05-7.25 (m, 4H). LC-MS = RT: 2.83 min. Exact mass: 377.195. Found mass: 378.3 [M + H]$^+$, 400.3 [M + Na]$^+$. Fragments: 322.3 [M – tBu], 278.3 [M – Boc].

tert-butyl *(S)-3-(((S)-1-(Methoxy(methyl)amino)-1-oxopropan-2-yl)carbamoyl)-3,4-dihydroisoquinoline-2(1H)-carboxylate* **(75b)**
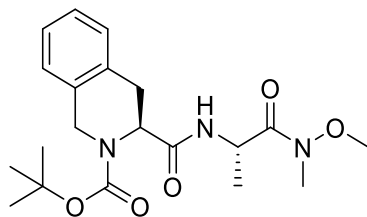
In this reaction the intermediate **74b** is used as amine. Yield: 88%. R_f = 0.36 in light petroleum /EtOAc 2:3. Consistency: pale yellow solid. ^{1}H NMR (75 MHz, CDCl$_3$): δ = 0.98 (d, J = 6.6 Hz, 3H), 1.46 (s, 4.5H), 1.53 (s, 4.5H), 3.00-3.11 (m, 1H), 3.15 (s, 3H), 3.19-3.37 (m, 1H), 3.70 (s, 3H), 4.45-4.58 (m, 1H), 4.58-4.66 (m, 1.5H), 4.73-4.90 (m, 1.5H), 6.47 (bs, 0.5H), 6.77 (bs, 0.5H), 7.09-7.24 (m, 4H). RT = 2.96 min. Exact mass: 391.210. Found mass: 392.4 [M + H]$^+$ e 414.4 [M + Na]$^+$. Fragments: 336.3 [M − tBu], 292.3 [M − Boc].

tert-butyl *(S)-3-(((S)-1-(Methoxy(methyl)amino)-1-oxo-3-phenylpropan-2-yl)carbamoyl)-3,4-dihydroisoquinoline-2(1H)-carboxylate* **(75c)**
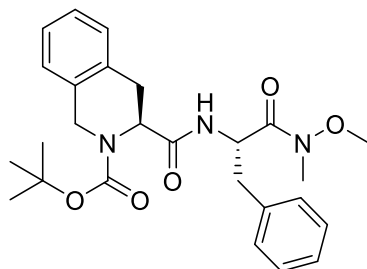
In this reaction the intermediate **74c** is used as amine. Yield: 41%. R_f = 0.46 in light petroleum /EtOAc 1:1. Consistency: pale yellow solid. ^{1}H NMR (75 MHz, CDCl$_3$): δ = 1.43 (s, 4.5H), 1.50 (s, 4.5H), 2.61-2.73 (m, 0.5H), 2.72-2.92 (m, 1.5H), 2.94-3.07 (m, 1.5H), 3.11 (s, 3H), 3.24-3.34 (m, 0.5H), 3.61 (s, 3H), 4.11-4.36 (m, 1H), 4.58 (d, J = 15.9 Hz, 1.5H), 4.85 (m, 0.5H), 5.03-5.19 (m, 1H), 6.45 (bs, 0.5H), 6.74 (bs, 0.5H), 6.87 (bs, 2H), 7.05-7.24 (m, 7H). RT = 3.65 min. Exact mass: 467.242. Massa trovata: 468.4 [M + H]$^+$ e 490.4[M + Na]$^+$. Frammenti: 412.3 [M − tBu], 368.3 [M − Boc].

Synthesis of Intermediates 76a-c

The intermediates **76a-c** were obtained following the procedure reported for compound **69**.

(S)-N-(2-(Methoxy(methyl)amino)-2-oxoethyl)-1,2,3,4-tetrahydroisoquinoline-3-carboxamide (76a)

In this reaction the intermediate **75a** is used as starting material. Yield: 95%. Consistency: pale yellow oil. ^{1}H NMR (75 MHz, CDCl$_3$): δ = 1.81 (bs, 1H), 2.83 (dd, J = 16.3, 10.7 Hz, 1H), 3.20

(dd, J = 16.4, 5.1 Hz, 1H), 3.20 (s, 3H), 3.58 (dd, J = 10.6, 5.1 Hz, 1H), 3.72 (s, 3H), 4.01 (s, 2H), 4.21 (d, J = 4.4 Hz, 2H), 7.00-7.05 (m, 1H), 7.10-7.17 (m, 3H), 7.82 (bs, 1H). ^{13}C NMR (125 MHz, CDCl$_3$): δ = 31.06, 32.39, 40.43, 47.60, 56.57, 61.59, 125.66, 126.21, 126.51, 129.23, 134.30, 136.14, 169.84, 173.50.

(S)-N-((S)-1-(Methoxy(methyl)amino)-1-oxopropan-2-yl)-1,2,3,4-tetrahydroisoquinoline-3-carboxamide (76b)
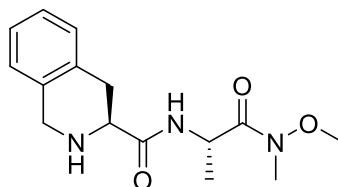
In this reaction the intermediate **75b** is used as starting material. Yield: 90%. Consistency: pale yellow oil. ^{1}H NMR (75 MHz, CDCl$_3$): δ = 1.33 (d, J = 6.9 Hz, 3H), 1.86 (bs, 1H), 2.82 (dd, J = 16.3, 10.6 Hz, 1H), 3.17 (dd, J = 16.3, 5.0 Hz, 1H), 3.20 (s, 3H), 3.54 (dd, J = 10.6, 5.0 Hz, 1H), 3.78 (s, 3H), 4.00 (d, J = 1.9 Hz, 2H), 4.89-5.05 (m, 1H), 7.00-7.06 (m, 1H), 7.10-7.17 (m, 3H), 7.73 (d, J = 7.8 Hz, 1H). ^{13}C NMR (125 MHz, CDCl$_3$): δ = 18.38, 31.22, 32.17, 45.12, 47.55, 56.59, 61.68, 125.71, 126.26, 126.56, 129.22, 134.28, 136.06, 172.86, 173.20.

(S)-N-((S)-1-(Methoxy(methyl)amino)-1-oxo-3-phenylpropan-2-yl)-1,2,3,4-tetrahydroisoquinoline-3-carboxamide (76c)
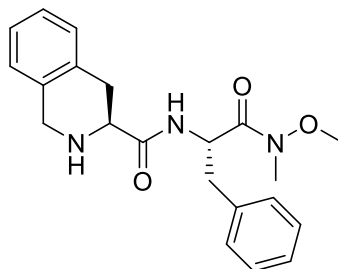
In this reaction the intermediate **75c** is used as starting material. Yield: 89%. Consistency: pale yellow oil. ^{1}H NMR (75 MHz, CDCl$_3$): δ = 1.64 (bs, 1H), 2.64 (dd, J = 16.2, 10.4 Hz, 1H), 2.92 (dd, J = 13.6, 7.9 Hz, 1H), 3.08-3.17 (m, 1H), 3.19 (s, 3H), 3.51 (dd, J = 10.4, 5.3 Hz, 1H), 3.73 (s, 3H), 3.86 (d, J = 16.2 Hz, 1H), 3.95 (d, J = 16.2 Hz, 1H), 5.22-5.33 (m, 1H), 6.98-7.07 (m, 1H), 7.10-7.18 (m, 5H), 7.17-7.23 (m, 1H), 7.23-7.28 (m, 2H), 7.75 (d, J = 8.3 Hz, 1H). ^{13}C NMR (125 MHz, CDCl$_3$): δ = 30.98, 32.16, 38.41, 47.35, 49.83, 56.37, 61.72, 125.67, 126.30, 126.64, 126.99, 128.48, 129.18, 129.51, 134.43, 136.37, 136.55, 171.95, 172.97.

Synthesis of Intermediates 77a-c

The intermediates **77a-c** were obtained following the procedure reported for compounds **71b-d, 71i-l**.

(S)-2-(2,4-Difluorobenzoyl)-N-(2-(methoxy(methyl)amino)-2-oxoethyl)-1,2,3,4-tetrahydroisoquinoline-3-carboxamide (77a)
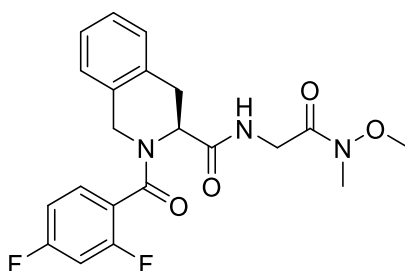
In this reaction the intermediate **70e** is used as the acid and **76a** as the amine. Yield: 56%. R_f = 0.36 in light petroleum /EtOAc 1:4. Consistency: white solid. ^{1}H NMR (75 MHz, CDCl$_3$): δ = 3.15-3.22 (m, 1H), 3.19 (s, 3H), 3.37 (dd, J = 15.9, 2.4 Hz, 0.2H), 3.45 (dd, J = 15.9, 2.4 Hz, 0.8H), 3.63 (s, 0.7H) 3.68 (s, 2.3H), 3.96-4.12 (m, 1.2H) 4.24 (dd, J = 18.4, 5.2 Hz, 0.8H), 4.44 (d, J = 15.8 Hz, 0.8H), 4.54 (dd, J = 5.9, 2.3 Hz, 0.2H), 4.66 (d, J = 17.4 Hz, 1H), 5.31 (d, J = 17.6 Hz, 0.2H), 5.43 (t, J = 5.6 Hz, 0.8H), 6.68 (bs, 0.2H), 6.84-7.02 (m, 3.8H), 7.11-7.16 (m, 1H), 7.17-7.24 (m, 2H), 7.49 (bs, 1H). RT = 2.66 min. Exact mass: 417.150. Found mass: 418.3 [M + H]$^+$, 440.2[M + Na]$^+$, 441.3 [M + H + Na]$^{+2}$. Fragments: 357.2 [M – N(CH$_3$)O(CH$_3$)], 300.0 [M – Gly-N(CH$_3$)O(CH$_3$)], 272.2 [M – -CO-Gly-N(CH$_3$)O(CH$_3$)].

(S)-2-(2,4-Difluorobenzoyl)-N-((S)-1-(methoxy(methyl)amino)-1-oxopropan-2-yl)-1,2,3,4-tetrahydroisoquinoline-3-carboxamide (77b)
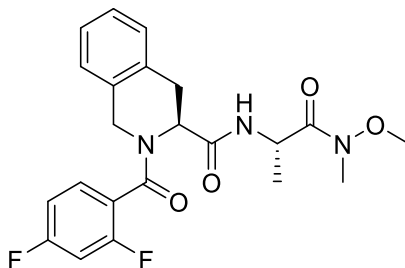
In this reaction the compound **70e** is used as the acid and **76b** as the amine. Yield: 60%. R_f = 0.40 in light petroleum /EtOAc 3:7. Consistency: white solid. ^{1}H NMR (75 MHz, CDCl$_3$): δ = 0.99 (d, J = 6.8 Hz, 1H), 1.18 (d, J = 7.0 Hz, 2H), 3.14-3.20 (m, 4H), 3.33 (dd, J = 15.6, 2.4 Hz, 0.3H), 3.38 (dd, J = 15.8, 5.1 Hz, 0.7H), 3.64 (s, 0.7H), 3.71 (s, 2.3H), 4.42 (d, J = 15.3 Hz, 0.8H), 4.45-4.49 (m, 0.2H), 4.55 (d, J = 15.4 Hz, 1H), 4.65-4.73 (m, 0.5H), 4.79-4.90 (m, 0.5H), 5.17 (d, J = 17.3 Hz, 0.3H), 5.21-5.27 (bs, 0.7H), 4.55 (d, J = 15.4 Hz, 0.3H), 6.83-7.01 (m, 3.7H), 7.11-7.24 (m, 3H), 7.41-7.50 (m, 1H). LC-MS = RT: 2.76 min. Exact mass: 431.17. Found mass: 432.2 [M + H]$^+$, 454.3 [M + Na]$^+$, 455.2 [M + H + Na]$^{+2}$. Fragments: 371.2 [M – N(CH$_3$)O(CH$_3$)], 300.0 [M – Ala-N(CH$_3$)O(CH$_3$)], 272.2 [M – -CO-Ala-N(CH$_3$)O(CH$_3$)].

(S)-2-(2,4-Difluorobenzoyl)-N-((S)-1-(methoxy(methyl)amino)-1-oxo-3-phenylpropan-2-yl)-1,2,3,4-tetrahydroisoquinoline-3-carboxamide (77c)
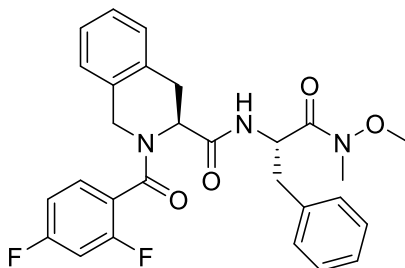
In this reaction the compound **70e** is used as the acid and **76c** as the amine. Yield: 69%. R_f = 0.33 in light petroleum /EtOAc 2:3. Consistency: pale yellow solid. ^{1}H NMR (75 MHz, CDCl$_3$): δ = 2.73 (dd, J = 13.9, 7.6 Hz, 0.3H), 2.88 (dd, J = 13.8, 7.0 Hz, 0.7H), 2.99-3.08 (m, 1H), 3.08-3.19 (m, 1H), 3.16 (s, 3H), 3.31 (dd, J = 15.8, 1.8 Hz, 0.3H), 3.37 (dd, J = 16.0, 4.5 Hz, 0.7H), 3.61 (s, 1H), 3.66 (s, 2H), 4.23 (d, J = 15.4 Hz, 0.7H), 4.30 (d, J = 15.6 Hz, 1H), 4.46 (d, J = 4.1 Hz, 0.3H), 4.97-5.05 (m, 0.3H), 5.17-5.24 (m, 1H), 5.33 (bs, 0.7H), 6.43 (d, J = 6.6 Hz, 0.2H), 6.80 (d, J = 7.9 Hz, 0.8H),
6.84-7.03 (m, 4H), 7.06-7.23 (m, 7H), 7.34-7.44 (m, 1H). RT = 3.41 min. Exact mass: 507.19. Found mass: 508.3 [M + H]$^+$, 530.3 [M + Na]$^+$, 531.3 [M + H + Na]$^+$. Fragments: 447.2 [M – N(CH$_3$)O(CH$_3$)], 300.2 [M – Phe-N(CH$_3$)O(CH$_3$)], 272.2 [M – -CO-Phe-N(CH$_3$)O(CH$_3$)].

Synthesis of Final Compounds SPR78-SPR80

The final compounds **SPR78-SPR80** were obtained following the procedure reported for compound **SPR66-SPR77.**

(S,E)-2-(2,4-Difluorobenzoyl)-N-(4-oxopent-2-en-1-yl)-1,2,3,4-tetrahydroisoquinoline-3-carboxamide (SPR78)
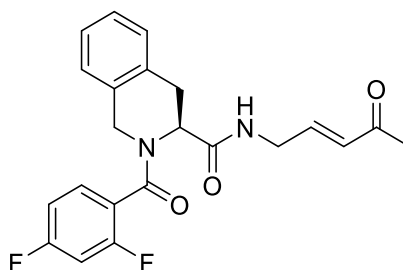
In this reaction the intermediate **77a** is used as starting material. Yield: 55%. R_f = 0.23 in light petroleum /EtOAc 3:7. Consistency: pale yellow solid. ^{1}H NMR (75 MHz, CDCl$_3$): δ = 2.12 (s, 0.5H), 2.22 (s, 2.5H), 3.16 (dd, J = 15.8, 6.6 Hz, 1H), 3.41 (d, J = 15.1 Hz, 0.2H), 3.50 (dd, J = 15.9, 5.8 Hz, 0.8H), 3.77-3.85 (m, 0.2H), 3.94-4.03 (m, 1H), 4.08-4.16 (m, 0.8H), 4.41 (d, J = 15.3 Hz, 0.8H), 4.48 (d, J = 15.2 Hz, 0.8H), 4.56-4.60 (m, 0.2H), 4.74 (d, J = 16.9 Hz, 0.2H), 5.15 (d, J = 17.8 Hz, 0.2H), 5.25-5.32 (m, 0.8H), 5.60 (d, J = 15.8 Hz, 0.2H), 6.02 (d, J = 16.1 Hz, 0.8H), 6.36-6.45 (m, 0.2H), 6.56-6.62 (m, 1H), 6.66 (dt, J = 16.0, 5.0 Hz, 0.8H), 6.94-7.04 (m, 2H), 7.17-7.21 (m, 1H), 7.24-7.26 (m, 2H), 7.36-7.44 (m, 1H), 7.44-7.49 (m, 0.5H), 7.63-7.71 (m, 0.5H). LC-MS = RT: 2.65 min. Exact mass: 398.14. Found mass: 399.3 [M + H]$^+$, 421.2 [M + Na]$^+$, 422.2 [M + H + Na]$^{2+}$. Fragments: 300.2 [M – Gly-CH=CH-COCH$_3$], 272.2 [M – -CO-Gly-N(CH$_3$)O(CH$_3$)]. HRMS: Calculated mass for C$_{22}$H$_{20}$F$_2$N$_2$O$_3$: 398.1442. Determined: 399.1518; Found mass: 399.1515 (adduct M + H).

(S)-2-(2,4-Difluorobenzoyl)-N-((S,E)-5-oxohex-3-en-2-yl)-1,2,3,4-tetrahydroisoquinoline-3-carboxamide (SPR79)
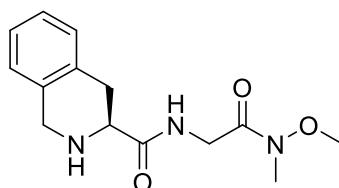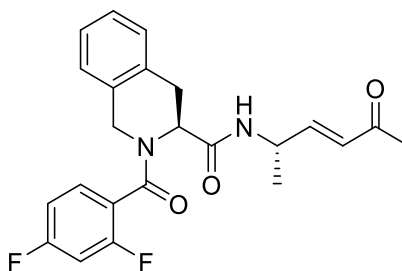
In this reaction the intermediate **77b** is used as starting material. Yield: 60%. $R_f = 0.58$ in light petroleum /EtOAc 1:4. Consistency: pale yellow solid. ^{1}H NMR (75 MHz, CDCl$_3$): $\delta = 1.01$ (d, $J = 7.0$ Hz, 0.5H), 1.22 (d, $J = 7.0$ Hz, 2.5H), 2.19 (s, 0.5H), 2.23 (s, 2.5H), 3.07-3.19 (m, 0.2H), 3.15 (dd, $J = 15.9$, 6.7 Hz, 0.8H), 3.37 (d, $J = 17.0$ Hz, 0.2H), 3.46 (dd, $J = 15.8$, 5.3 Hz, 0.8H), 4.39 (d, $J = 15.4$ Hz, 0.8H), 4.48 (d, $J = 15.3$ Hz, 1H), 4.52-4.56 (m, 0.2H), 4.60-4.71 (m, 1H), 5.16 (d, $J = 17.4$ Hz, 0.2H), 5.26-5.31 (m, 0.8H), 5.79 (d, $J = 6.9$ Hz, 0.2H), 5.88 (d, $J = 15.9$ Hz, 0.2H), 6.11 (dd, $J = 16.0$, 1.6 Hz, 0.8H), 6.38 (d, $J = 8.0$ Hz, 0.8H), 6.50 (dd, $J = 16.1$, 5.0 Hz, 0.2H), 6.66 (dd, $J = 16.0$, 4.9 Hz, 0.8H), 6.88-7.04 (m, 3H), 7.18-7.28 (m, 3H), 7.35-7.43 (m, 1H). LC-MS = RT: 2.81 min. Exact mass: 412.16. Found mass: 413.3 [M + H]$^+$, 435.3 [M + Na]$^+$, 436.3 [M + H + Na]$^{2+}$. Fragments: 300.2 [M – Ala-CH=CH-COCH$_3$], 272.2 [M – -CO-Ala-N(CH$_3$)O(CH$_3$)]. HRMS: Calculated mass for C$_{23}$H$_{22}$F$_2$N$_2$O$_3$: 412.1598. Determined: 413.1674; Found mass: 413.1671 (adduct M + H).

(S)-2-(2,4-Difluorobenzoyl)-N-((S,E)-5-oxo-1-phenylhex-3-en-2-yl)-1,2,3,4-tetrahydroisoquinoline-3-carboxamide (SPR80)
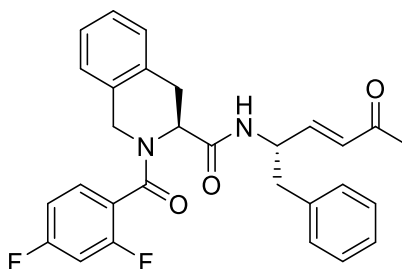
In this reaction the intermediate **77c** is used as starting material. Yield: 69%. $R_f = 0.33$ in light petroleum /EtOAc 2:3. Consistency: pale yellow solid. ^{1}H NMR (75 MHz, CDCl$_3$): $\delta = 2.16$ (s, 0.5H), and 2.20 (s, 2.5H), 2.68 (dd, $J = 13.9$, 8.1 Hz, 0.2), 2.82 (dd, $J = 14.1$, 8.1 Hz, 0.8H), 2.84-2.87 (m, 0.2H), 2.92 (dd, $J = 14.1$, 6.4 Hz, 0.8H), 2.98-3.05 (m, 0.2H), 3.10 (dd, $J = 16.0$, 6.6 Hz, 0.8H), 3.29-3.40 (m, 0.2H), 3.35 (dd, $J = 16.0$, 5.0 Hz, 0.8H), 4.02 (d, $J = 15.6$ Hz, 0.2H), 4.95-4.12 (m, 0.8H), 4.23 (d, $J = 15.6$ Hz, 0.8H), 4.47 (d, $J = 4.1$ Hz, 0.2H), 4.65-4.72 (m, 0.2H), 4.89-4.97 (m, 0.8H), 5.11 (d, $J = 17.6$ Hz, 0.2H), 5.24-5.31 (m, 0.8H), 5.82 (d, $J = 16.6$ Hz, 0.2H), 5.96 (d, $J = 7.0$ Hz, 0.2H), 6.13 (dd, $J = 16.0$, 1.6 Hz, 0.8H), 6.38 (d, $J = 8.4$ Hz, 0.8H), 6.57 (dd, $J = 16.1$, 5.5 Hz, 0.2H), 6.70 (dd, $J = 16.0$, 5.1 Hz, 0.8H), 6.82 (d, $J = 7.5$ Hz, 1H), 6.88-7.04 (m, 2H), 7.05-7.12 (m, 2H), 7.13-7.30 (m, 7H). RT = 3.41 min. Exact mass: 488.19. Found mass: 489.3 [M + H]$^+$, 511.3 [M + Na]$^+$, 5.12.3 [M + H + Na]$^{2+}$. Fragments: 300.2 [M – Phe-CH=CH-COCH$_3$], 272.2 [M – -CO-Phe-N(CH$_3$)O(CH$_3$)]. HRMS: Calculated mass for C$_{29}$H$_{26}$F$_2$N$_2$O$_3$: 488.1911. Determined: 489.1982; Found mass: 489.1984 (adduct M + H).

10.3.2. Biological Evaluations

Rhodesain Inhibition

Preliminary screening against rhodesain was performed at an inhibitor concentration of 20 µM, using an equivalent amount of DMSO as a negative control. The enzyme was expressed recombinantly as previously described.[204] The release of the substrate hydrolysis product (Cbz-Phe-Arg-AMC, 10 µM) was determined by reading fluorescence every 30 seconds over a period of 30 minutes. Compounds showing at least 50% inhibition at the screening concentration were subjected to further characterization. Second-order inhibition rate constants were calculated at 7 different inhibitor concentrations, ranging from those that minimally inhibited to those that completely inhibited the enzyme. The assay buffer was prepared with 50 mM sodium acetate at pH = 5.5, 5 mM EDTA, 200 mM NaCl, and 0.005% Brij 35. The enzyme buffer was prepared with the same components as the assay buffer but with 5 mM DTT instead of Brij 35. Product formation was monitored at room temperature continuously for 30 minutes. To calculate the first-order inactivation rate constants (k_{obs}) for irreversible inhibition, progress curves (fluorescence (F) vs. time) were analyzed using nonlinear regression with the equation $F = A(1-exp(-k_{obs}\,t)) + B$.[51] Fitting k_{obs} values as a function of inhibitor concentrations to the hyperbolic equation $k_{obs} = k_{inac}\,[I]/(K_{iapp} + [I])$ yielded individual values of K_{iapp} and k_{inac}.[205] The K_{iapp} values were corrected for substrate concentration by including the term $(1+[S]/K_m)$ in the equation $K_i = K_{iapp}/(1+[S]/K_m)$. The second-order rate constants $k_{2nd} = k_{inact}/K_i$ were calculated directly from the individual constants. The values of K_i and k_{inact} were calculated using nonlinear regression analysis with the software GraFit and Excel. The K_m value used to correct K_{iapp} values was determined to be 0.9 µM.[206] Inhibitor solutions were prepared from stock in DMSO. Each assay was performed in duplicate in 96-well plates with a total volume of 200 µL. The fluorescence of the AMC product resulting from substrate hydrolysis was measured with an Infinite 200 PRO microplate reader (Tecan, Männedorf, Switzerland) at room temperature with an excitation filter at 380 nm and an emission filter at 460 nm.

Antitripanosonic Activity

The *T. brucei brucei* parasites used in this study belonged to the 449 cell line, derived from the Lister 427 strain.[207] The cells were cultured in HMI-9 medium supplemented with 10% FCS, 50 U/ml penicillin, 50 µg/ml streptomycin, and 0.2 µg/ml phleomycin, at 37 °C and 5% CO2. The assessment of anti-trypanosomal activity was performed as described previously.[197]

Briefly, logarithmically growing *T. b. brucei* was distributed in 96-well plates at a concentration of 2.5 x 10^3 cells/mL. Stock solutions of compounds (10 mM in DMSO) were pre-diluted in HMI-9 medium and then further serially diluted in nine consecutive steps (1:2). The ten compound dilutions prepared were mixed with the cell suspensions in the wells of the 96-well plates, resulting in parasite incubation with compound concentrations ranging from 33.3 to 0.065 µM. Cells treated with 10% and 0.3% DMSO were used as positive and negative controls, respectively. After 24 hours of incubation, the cells and compound suspensions were mixed with ATPlite 1 step solution (PerkinElmer), and luminescence was recorded using a microplate reader (BMG Labtech).

Bibliography

(1)   *Situation Report-51 SITUATION IN NUMBERS Total and New Cases in Last 24 Hours*.

(2)   Jin, Z.; Du, X.; Xu, Y.; Deng, Y.; Liu, M.; Zhao, Y.; Zhang, B.; Li, X.; Zhang, L.; Peng, C.; Duan, Y.; Yu, J.; Wang, L.; Yang, K.; Liu, F.; Jiang, R.; Yang, X.; You, T.; Liu, X.; Yang, X.; Bai, F.; Liu, H.; Liu, X.; Guddat, L. W.; Xu, W.; Xiao, G.; Qin, C.; Shi, Z.; Jiang, H.; Rao, Z.; Yang, H. Structure of Mpro from SARS-CoV-2 and Discovery of Its Inhibitors. *Nature* **2020**, *582* (7811), 289–293. https://doi.org/10.1038/s41586-020-2223-y.

(3)   Akbulut, E. Investigation of Changes in Protein Stability and Substrate Affinity of 3CL-Protease of SARS-CoV-2 Caused by Mutations. *Genet Mol Biol* **2022**, *45* (2). https://doi.org/10.1590/1678-4685-gmb-2021-0404.

(4)   Shen, Z.; Ratia, K.; Cooper, L.; Kong, D.; Lee, H.; Kwon, Y.; Li, Y.; Alqarni, S.; Huang, F.; Dubrovskyi, O.; Rong, L.; Thatcher, G. R. J.; Xiong, R. Design of SARS-CoV-2 PLpro Inhibitors for COVID-19 Antiviral Therapy Leveraging Binding Cooperativity. *J Med Chem* **2022**, *65* (4), 2940–2955. https://doi.org/10.1021/acs.jmedchem.1c01307.

(5)   Sacco, M. D.; Ma, C.; Lagarias, P.; Gao, A.; Townsend, J. A.; Meng, X.; Dube, P.; Zhang, X.; Hu, Y.; Kitamura, N.; Hurst, B.; Tarbet, B.; Marty, M. T.; Kolocouris, A.; Xiang, Y.; Chen, Y.; Wang, J. Structure and Inhibition of the SARS-CoV-2 Main Protease Reveal Strategy for Developing Dual Inhibitors against M ^{pro} and Cathepsin L. *Sci Adv* **2020**, *6* (50). https://doi.org/10.1126/sciadv.abe0751.

(6)   Previti, S.; Ettari, R.; Calcaterra, E.; Maro, S. Di; Hammerschmidt, S. J.; Müller, C.; Ziebuhr, J.; Schirmeister, T.; Cosconati, S.; Zappalà, M. Structure-Based Lead Optimization of Peptide-Based Vinyl Methyl Ketones as SARS-CoV-2 Main Protease Inhibitors. *European Journal of Medicinal Chemistry* **2023**, *247*, 115021.

(7)   Vuong, W.; Khan, M. B.; Fischer, C.; Arutyunova, E.; Lamer, T.; Shields, J.; Saffran, H. A.; McKay, R. T.; van Belkum, M. J.; Joyce, M. A.; Young, H. S.; Tyrrell, D. L.; Vederas, J. C.; Lemieux, M. J. Feline Coronavirus Drug Inhibits the Main Protease of SARS-CoV-2 and Blocks Virus Replication. *Nat Commun* **2020**, *11* (1), 4282. https://doi.org/10.1038/s41467-020-18096-2.

(8)   Xia, Z.; Sacco, M.; Hu, Y.; Ma, C.; Meng, X.; Zhang, F.; Szeto, T.; Xiang, Y.; Chen, Y.; Wang, J. Rational Design of Hybrid SARS-CoV-2 Main Protease Inhibitors Guided by the Superimposed Cocrystal Structures with the Peptidomimetic Inhibitors GC-376, Telaprevir, and Boceprevir. *ACS Pharmacol Transl Sci* **2021**, *4* (4), 1408–1421. https://doi.org/10.1021/acsptsci.1c00099.

(9)   Previti, S.; Ettari, R.; Calcaterra, E.; Roggia, M.; Natale, B.; Weldert, A. C.; Müller-Ruttloff, C.; Salisch, F.; Irto, A.; Cigala, R. M.; Ziebuhr, J.; Schirmeister, T.; Cosconati, S.; Zappalà, M. Identification of Dual Inhibitors Targeting Main Protease (Mpro) and Cathepsin L as Potential Anti-SARS-CoV-2 Agents. *ACS Med Chem Lett* **2024**, *15* (5), 602–609. https://doi.org/10.1021/acsmedchemlett.3c00562.

(10) Giroud, M.; Harder, M.; Kuhn, B.; Haap, W.; Trapp, N.; Schweizer, W. B.; Schirmeister, T.; Diederich, F. Fluorine Scan of Inhibitors of the Cysteine Protease Human Cathepsin L: Dipolar and Quadrupolar Effects in the Π-Stacking of Fluorinated Phenyl Rings on Peptide Amide Bonds. *ChemMedChem* **2016**, *11* (10), 1042–1047. https://doi.org/10.1002/cmdc.201600132.

(11) Zhang, C. Fluorine in Medicinal Chemistry: In Perspective to COVID-19. *ACS Omega* **2022**, *7* (22), 18206–18212. https://doi.org/10.1021/acsomega.2c01121.

(12) Sacco, M. D.; Ma, C.; Lagarias, P.; Gao, A.; Townsend, J. A.; Meng, X.; Dube, P.; Zhang, X.; Hu, Y.; Kitamura, N.; Hurst, B.; Tarbet, B.; Marty, M. T.; Kolocouris, A.; Xiang, Y.; Chen, Y.; Wang, J. Structure and Inhibition of the SARS-CoV-2 Main Protease Reveal Strategy for Developing Dual Inhibitors against M [pro] and Cathepsin L. *Sci Adv* **2020**, *6* (50). https://doi.org/10.1126/sciadv.abe0751.

(13) Rut, W.; Lv, Z.; Zmudzinski, M.; Patchett, S.; Nayak, D.; Snipas, S. J.; El Oualid, F.; Huang, T. T.; Bekes, M.; Drag, M.; Olsen, S. K. Activity Profiling and Crystal Structures of Inhibitor-Bound SARS-CoV-2 Papain-like Protease: A Framework for Anti–COVID-19 Drug Design. *Sci Adv* **2020**, *6* (42). https://doi.org/10.1126/sciadv.abd4596.

(14) Zhou, P.; Yang, X.-L.; Wang, X.-G.; Hu, B.; Zhang, L.; Zhang, W.; Si, H.-R.; Zhu, Y.; Li, B.; Huang, C.-L.; Chen, H.-D.; Chen, J.; Luo, Y.; Guo, H.; Jiang, R.-D.; Liu, M.-Q.; Chen, Y.; Shen, X.-R.; Wang, X.; Zheng, X.-S.; Zhao, K.; Chen, Q.-J.; Deng, F.; Liu, L.-L.; Yan, B.; Zhan, F.-X.; Wang, Y.-Y.; Xiao, G.-F.; Shi, Z.-L. A Pneumonia Outbreak Associated with a New Coronavirus of Probable Bat Origin. *Nature* **2020**, *579* (7798), 270–273. https://doi.org/10.1038/s41586-020-2012-7.

(15) Zhu, N.; Zhang, D.; Wang, W.; Li, X.; Yang, B.; Song, J.; Zhao, X.; Huang, B.; Shi, W.; Lu, R.; Niu, P.; Zhan, F.; Ma, X.; Wang, D.; Xu, W.; Wu, G.; Gao, G. F.; Tan, W. A Novel Coronavirus from Patients with Pneumonia in China, 2019. *New England Journal of Medicine* **2020**, *382* (8), 727–733. https://doi.org/10.1056/NEJMoa2001017.

(16) Deng, S.-Q.; Peng, H.-J. Characteristics of and Public Health Responses to the Coronavirus Disease 2019 Outbreak in China. *J Clin Med* **2020**, *9* (2), 575. https://doi.org/10.3390/jcm9020575.

(17) Note from the Editors: World Health Organization Declares Novel Coronavirus (2019-NCoV) Sixth Public Health Emergency of International Concern. *Eurosurveillance* **2020**, *25* (5). https://doi.org/10.2807/1560-7917.ES.2020.25.5.200131e.

(18) Wu, Z.; McGoogan, J. M. Characteristics of and Important Lessons From the Coronavirus Disease 2019 (COVID-19) Outbreak in China. *JAMA* **2020**, *323* (13), 1239. https://doi.org/10.1001/jama.2020.2648.

(19) *Diagnosis and Treatment Protocol for Novel Coronavirus Pneumonia*.

(20) Gorbalenya, A. E.; Baker, S. C.; Baric, R. S.; de Groot, R. J.; Drosten, C.; Gulyaeva, A. A.; Haagmans, B. L.; Lauber, C.; Leontovich, A. M.; Neuman, B. W.; Penzar, D.; Perlman, S.; Poon,

L. L. M.; Samborskiy, D. V.; Sidorov, I. A.; Sola, I.; Ziebuhr, J. The Species Severe Acute Respiratory Syndrome-Related Coronavirus: Classifying 2019-NCoV and Naming It SARS-CoV-2. *Nat Microbiol* **2020**, *5* (4), 536–544. https://doi.org/10.1038/s41564-020-0695-z.

(21) *World Health Organization 2023 data.who.int, WHO Coronavirus (COVID-19) dashboard > Vaccines [Dashboard]. https://data.who.int/dashboards/covid19/vaccines.*

(22) Jin, Z.; Du, X.; Xu, Y.; Deng, Y.; Liu, M.; Zhao, Y.; Zhang, B.; Li, X.; Zhang, L.; Peng, C.; Duan, Y.; Yu, J.; Wang, L.; Yang, K.; Liu, F.; Jiang, R.; Yang, X.; You, T.; Liu, X.; Yang, X.; Bai, F.; Liu, H.; Liu, X.; Guddat, L. W.; Xu, W.; Xiao, G.; Qin, C.; Shi, Z.; Jiang, H.; Rao, Z.; Yang, H. Structure of Mpro from SARS-CoV-2 and Discovery of Its Inhibitors. *Nature* **2020**, *582* (7811), 289–293. https://doi.org/10.1038/s41586-020-2223-y.

(23) Huang, C.; Wang, Y.; Li, X.; Ren, L.; Zhao, J.; Hu, Y.; Zhang, L.; Fan, G.; Xu, J.; Gu, X.; Cheng, Z.; Yu, T.; Xia, J.; Wei, Y.; Wu, W.; Xie, X.; Yin, W.; Li, H.; Liu, M.; Xiao, Y.; Gao, H.; Guo, L.; Xie, J.; Wang, G.; Jiang, R.; Gao, Z.; Jin, Q.; Wang, J.; Cao, B. Clinical Features of Patients Infected with 2019 Novel Coronavirus in Wuhan, China. *The Lancet* **2020**, *395* (10223), 497–506. https://doi.org/10.1016/S0140-6736(20)30183-5.

(24) Guan, W.; Ni, Z.; Hu, Y.; Liang, W.; Ou, C.; He, J.; Liu, L.; Shan, H.; Lei, C.; Hui, D. S. C.; Du, B.; Li, L.; Zeng, G.; Yuen, K.-Y.; Chen, R.; Tang, C.; Wang, T.; Chen, P.; Xiang, J.; Li, S.; Wang, J.; Liang, Z.; Peng, Y.; Wei, L.; Liu, Y.; Hu, Y.; Peng, P.; Wang, J.; Liu, J.; Chen, Z.; Li, G.; Zheng, Z.; Qiu, S.; Luo, J.; Ye, C.; Zhu, S.; Zhong, N. Clinical Characteristics of Coronavirus Disease 2019 in China. *New England Journal of Medicine* **2020**, *382* (18), 1708–1720. https://doi.org/10.1056/NEJMoa2002032.

(25) Vivanti, A. J.; Vauloup-Fellous, C.; Prevot, S.; Zupan, V.; Suffee, C.; Do Cao, J.; Benachi, A.; De Luca, D. Transplacental Transmission of SARS-CoV-2 Infection. *Nat Commun* **2020**, *11* (1), 3572. https://doi.org/10.1038/s41467-020-17436-6.

(26) Chen, T.; Wu, D.; Chen, H.; Yan, W.; Yang, D.; Chen, G.; Ma, K.; Xu, D.; Yu, H.; Wang, H.; Wang, T.; Guo, W.; Chen, J.; Ding, C.; Zhang, X.; Huang, J.; Han, M.; Li, S.; Luo, X.; Zhao, J.; Ning, Q. Clinical Characteristics of 113 Deceased Patients with Coronavirus Disease 2019: Retrospective Study. *BMJ* **2020**, m1091. https://doi.org/10.1136/bmj.m1091.

(27) Jackson, L. A.; Anderson, E. J.; Rouphael, N. G.; Roberts, P. C.; Makhene, M.; Coler, R. N.; McCullough, M. P.; Chappell, J. D.; Denison, M. R.; Stevens, L. J.; Pruijssers, A. J.; McDermott, A.; Flach, B.; Doria-Rose, N. A.; Corbett, K. S.; Morabito, K. M.; O'Dell, S.; Schmidt, S. D.; Swanson, P. A.; Padilla, M.; Mascola, J. R.; Neuzil, K. M.; Bennett, H.; Sun, W.; Peters, E.; Makowski, M.; Albert, J.; Cross, K.; Buchanan, W.; Pikaart-Tautges, R.; Ledgerwood, J. E.; Graham, B. S.; Beigel, J. H. An MRNA Vaccine against SARS-CoV-2 — Preliminary Report. *New England Journal of Medicine* **2020**, *383* (20), 1920–1931. https://doi.org/10.1056/NEJMoa2022483.

(28)   Folegatti, P. M.; Ewer, K. J.; Aley, P. K.; Angus, B.; Becker, S.; Belij-Rammerstorfer, S.; Bellamy, D.; Bibi, S.; Bittaye, M.; Clutterbuck, E. A.; Dold, C.; Faust, S. N.; Finn, A.; Flaxman, A. L.; Hallis, B.; Heath, P.; Jenkin, D.; Lazarus, R.; Makinson, R.; Minassian, A. M.; Pollock, K. M.; Ramasamy, M.; Robinson, H.; Snape, M.; Tarrant, R.; Voysey, M.; Green, C.; Douglas, A. D.; Hill, A. V. S.; Lambe, T.; Gilbert, S. C.; Pollard, A. J.; Aboagye, J.; Adams, K.; Ali, A.; Allen, E.; Allison, J. L.; Anslow, R.; Arbe-Barnes, E. H.; Babbage, G.; Baillie, K.; Baker, M.; Baker, N.; Baker, P.; Baleanu, I.; Ballaminut, J.; Barnes, E.; Barrett, J.; Bates, L.; Batten, A.; Beadon, K.; Beckley, R.; Berrie, E.; Berry, L.; Beveridge, A.; Bewley, K. R.; Bijker, E. M.; Bingham, T.; Blackwell, L.; Blundell, C. L.; Bolam, E.; Boland, E.; Borthwick, N.; Bower, T.; Boyd, A.; Brenner, T.; Bright, P. D.; Brown-O'Sullivan, C.; Brunt, E.; Burbage, J.; Burge, S.; Buttigieg, K. R.; Byard, N.; Cabera Puig, I.; Calvert, A.; Camara, S.; Cao, M.; Cappuccini, F.; Carr, M.; Carroll, M. W.; Carter, V.; Cathie, K.; Challis, R. J.; Charlton, S.; Chelysheva, I.; Cho, J.-S.; Cicconi, P.; Cifuentes, L.; Clark, H.; Clark, E.; Cole, T.; Colin-Jones, R.; Conlon, C. P.; Cook, A.; Coombes, N. S.; Cooper, R.; Cosgrove, C. A.; Coy, K.; Crocker, W. E. M.; Cunningham, C. J.; Damratoski, B. E.; Dando, L.; Datoo, M. S.; Davies, H.; De Graaf, H.; Demissie, T.; Di Maso, C.; Dietrich, I.; Dong, T.; Donnellan, F. R.; Douglas, N.; Downing, C.; Drake, J.; Drake-Brockman, R.; Drury, R. E.; Dunachie, S. J.; Edwards, N. J.; Edwards, F. D. L.; Edwards, C. J.; Elias, S. C.; Elmore, M. J.; Emary, K. R. W.; English, M. R.; Fagerbrink, S.; Felle, S.; Feng, S.; Field, S.; Fixmer, C.; Fletcher, C.; Ford, K. J.; Fowler, J.; Fox, P.; Francis, E.; Frater, J.; Furze, J.; Fuskova, M.; Galiza, E.; Gbesemete, D.; Gilbride, C.; Godwin, K.; Gorini, G.; Goulston, L.; Grabau, C.; Gracie, L.; Gray, Z.; Guthrie, L. B.; Hackett, M.; Halwe, S.; Hamilton, E.; Hamlyn, J.; Hanumunthadu, B.; Harding, I.; Harris, S. A.; Harris, A.; Harrison, D.; Harrison, C.; Hart, T. C.; Haskell, L.; Hawkins, S.; Head, I.; Henry, J. A.; Hill, J.; Hodgson, S. H. C.; Hou, M. M.; Howe, E.; Howell, N.; Hutlin, C.; Ikram, S.; Isitt, C.; Iveson, P.; Jackson, S.; Jackson, F.; James, S. W.; Jenkins, M.; Jones, E.; Jones, K.; Jones, C. E.; Jones, B.; Kailath, R.; Karampatsas, K.; Keen, J.; Kelly, S.; Kelly, D.; Kerr, D.; Kerridge, S.; Khan, L.; Khan, U.; Killen, A.; Kinch, J.; King, T. B.; King, L.; King, J.; Kingham-Page, L.; Klenerman, P.; Knapper, F.; Knight, J. C.; Knott, D.; Koleva, S.; Kupke, A.; Larkworthy, C. W.; Larwood, J. P. J.; Laskey, A.; Lawrie, A. M.; Lee, A.; Ngan Lee, K. Y.; Lees, E. A.; Legge, H.; Lelliott, A.; Lemm, N.-M.; Lias, A. M.; Linder, A.; Lipworth, S.; Liu, X.; Liu, S.; Lopez Ramon, R.; Lwin, M.; Mabesa, F.; Madhavan, M.; Mallett, G.; Mansatta, K.; Marcal, I.; Marinou, S.; Marlow, E.; Marshall, J. L.; Martin, J.; McEwan, J.; McInroy, L.; Meddaugh, G.; Mentzer, A. J.; Mirtorabi, N.; Moore, M.; Moran, E.; Morey, E.; Morgan, V.; Morris, S. J.; Morrison, H.; Morshead, G.; Morter, R.; Mujadidi, Y. F.; Muller, J.; Munera-Huertas, T.; Munro, C.; Munro, A.; Murphy, S.; Munster, V. J.; Mweu, P.; Noé, A.; Nugent, F. L.; Nuthall, E.; O'Brien, K.; O'Connor, D.; Oguti, B.; Oliver, J. L.; Oliveira, C.; O'Reilly, P. J.; Osborn, M.; Osborne, P.; Owen, C.; Owens, D.; Owino, N.; Pacurar, M.; Parker, K.; Parracho, H.; Patrick-Smith, M.; Payne, V.; Pearce, J.; Peng, Y.; Peralta Alvarez, M.

P.; Perring, J.; Pfafferott, K.; Pipini, D.; Plested, E.; Pluess-Hall, H.; Pollock, K.; Poulton, I.; Presland, L.; Provstgaard-Morys, S.; Pulido, D.; Radia, K.; Ramos Lopez, F.; Rand, J.; Ratcliffe, H.; Rawlinson, T.; Rhead, S.; Riddell, A.; Ritchie, A. J.; Roberts, H.; Robson, J.; Roche, S.; Rohde, C.; Rollier, C. S.; Romani, R.; Rudiansyah, I.; Saich, S.; Sajjad, S.; Salvador, S.; Sanchez Riera, L.; Sanders, H.; Sanders, K.; Sapaun, S.; Sayce, C.; Schofield, E.; Screaton, G.; Selby, B.; Semple, C.; Sharpe, H. R.; Shaik, I.; Shea, A.; Shelton, H.; Silk, S.; Silva-Reyes, L.; Skelly, D. T.; Smee, H.; Smith, C. C.; Smith, D. J.; Song, R.; Spencer, A. J.; Stafford, E.; Steele, A.; Stefanova, E.; Stockdale, L.; Szigeti, A.; Tahiri-Alaoui, A.; Tait, M.; Talbot, H.; Tanner, R.; Taylor, I. J.; Taylor, V.; Te Water Naude, R.; Thakur, N.; Themistocleous, Y.; Themistocleous, A.; Thomas, M.; Thomas, T. M.; Thompson, A.; Thomson-Hill, S.; Tomlins, J.; Tonks, S.; Towner, J.; Tran, N.; Tree, J. A.; Truby, A.; Turkentine, K.; Turner, C.; Turner, N.; Turner, S.; Tuthill, T.; Ulaszewska, M.; Varughese, R.; Van Doremalen, N.; Veighey, K.; Verheul, M. K.; Vichos, I.; Vitale, E.; Walker, L.; Watson, M. E. E.; Welham, B.; Wheat, J.; White, C.; White, R.; Worth, A. T.; Wright, D.; Wright, S.; Yao, X. L.; Yau, Y. Safety and Immunogenicity of the ChAdOx1 NCoV-19 Vaccine against SARS-CoV-2: A Preliminary Report of a Phase 1/2, Single-Blind, Randomised Controlled Trial. *The Lancet* **2020**, *396* (10249), 467–478. https://doi.org/10.1016/S0140-6736(20)31604-4.

(29) Samad, A.; Ahammad, F.; Nain, Z.; Alam, R.; Imon, R. R.; Hasan, M.; Rahman, Md. S. Designing a Multi-Epitope Vaccine against SARS-CoV-2: An Immunoinformatics Approach. *J Biomol Struct Dyn* **2022**, *40* (1), 14–30. https://doi.org/10.1080/07391102.2020.1792347.

(30) Madhi, S. A.; Baillie, V.; Cutland, C. L.; Voysey, M.; Koen, A. L.; Fairlie, L.; Padayachee, S. D.; Dheda, K.; Barnabas, S. L.; Bhorat, Q. E.; Briner, C.; Kwatra, G.; Ahmed, K.; Aley, P.; Bhikha, S.; Bhiman, J. N.; Bhorat, A. E.; du Plessis, J.; Esmail, A.; Groenewald, M.; Horne, E.; Hwa, S.-H.; Jose, A.; Lambe, T.; Laubscher, M.; Malahleha, M.; Masenya, M.; Masilela, M.; McKenzie, S.; Molapo, K.; Moultrie, A.; Oelofse, S.; Patel, F.; Pillay, S.; Rhead, S.; Rodel, H.; Rossouw, L.; Taoushanis, C.; Tegally, H.; Thombrayil, A.; van Eck, S.; Wibmer, C. K.; Durham, N. M.; Kelly, E. J.; Villafana, T. L.; Gilbert, S.; Pollard, A. J.; de Oliveira, T.; Moore, P. L.; Sigal, A.; Izu, A. Efficacy of the ChAdOx1 NCoV-19 Covid-19 Vaccine against the B.1.351 Variant. *New England Journal of Medicine* **2021**, *384* (20), 1885–1898. https://doi.org/10.1056/NEJMoa2102214.

(31) *Vaccine Adverse Event Reporting System (VAERS). Available online: https://www.cdc.gov/vaccinesafety/ensuringsafety/ monitoring/vaers/index.html (accessed on 26 February 2022).*

(32) Dong, E.; Du, H.; Gardner, L. An Interactive Web-Based Dashboard to Track COVID-19 in Real Time. *Lancet Infect Dis* **2020**, *20* (5), 533–534. https://doi.org/10.1016/S1473-3099(20)30120-1.

(33)   Murakami, N.; Hayden, R.; Hills, T.; Al-Samkari, H.; Casey, J.; Del Sorbo, L.; Lawler, P. R.; Sise, M. E.; Leaf, D. E. Therapeutic Advances in COVID-19. *Nat Rev Nephrol* **2023**, *19* (1), 38–52. https://doi.org/10.1038/s41581-022-00642-4.

(34)   Wang, M.; Cao, R.; Zhang, L.; Yang, X.; Liu, J.; Xu, M.; Shi, Z.; Hu, Z.; Zhong, W.; Xiao, G. Remdesivir and Chloroquine Effectively Inhibit the Recently Emerged Novel Coronavirus (2019-NCoV) in Vitro. *Cell Res* **2020**, *30* (3), 269–271. https://doi.org/10.1038/s41422-020-0282-0.

(35)   RECOVERY Collaborative Group. Tocilizumab in Patients Admitted to Hospital with COVID-19 (RECOVERY): A Randomised, Controlled, Open-Label, Platform Trial. *Lancet* **2021**, *397* (10285), 1637–1645. https://doi.org/10.1016/S0140-6736(21)00676-0.

(36)   Wahl, A.; Gralinski, L. E.; Johnson, C. E.; Yao, W.; Kovarova, M.; Dinnon, K. H.; Liu, H.; Madden, V. J.; Krzystek, H. M.; De, C.; White, K. K.; Gully, K.; Schäfer, A.; Zaman, T.; Leist, S. R.; Grant, P. O.; Bluemling, G. R.; Kolykhalov, A. A.; Natchus, M. G.; Askin, F. B.; Painter, G.; Browne, E. P.; Jones, C. D.; Pickles, R. J.; Baric, R. S.; Garcia, J. V. SARS-CoV-2 Infection Is Effectively Treated and Prevented by EIDD-2801. *Nature* **2021**, *591* (7850), 451–457. https://doi.org/10.1038/s41586-021-03312-w.

(37)   Pinzi, L.; Tinivella, A.; Caporuscio, F.; Rastelli, G. Drug Repurposing and Polypharmacology to Fight SARS-CoV-2 Through Inhibition of the Main Protease. *Front Pharmacol* **2021**, *12*. https://doi.org/10.3389/fphar.2021.636989.

(38)   Lazniewski, M.; Dermawan, D.; Hidayat, S.; Muchtaridi, M.; Dawson, W. K.; Plewczynski, D. Drug Repurposing for Identification of Potential Spike Inhibitors for SARS-CoV-2 Using Molecular Docking and Molecular Dynamics Simulations. *Methods* **2022**, *203*, 498–510. https://doi.org/10.1016/j.ymeth.2022.02.004.

(39)   Li, D.; Sempowski, G. D.; Saunders, K. O.; Acharya, P.; Haynes, B. F. SARS-CoV-2 Neutralizing Antibodies for COVID-19 Prevention and Treatment. *Annu Rev Med* **2022**, *73* (1), 1–16. https://doi.org/10.1146/annurev-med-042420-113838.

(40)   Sharma, A.; Ahmad Farouk, I.; Lal, S. K. COVID-19: A Review on the Novel Coronavirus Disease Evolution, Transmission, Detection, Control and Prevention. *Viruses* **2021**, *13* (2), 202. https://doi.org/10.3390/v13020202.

(41)   Molecular Structure, Pathophysiology, and Diagnosis of COVID-19. *Biointerface Res Appl Chem* **2020**, *11* (3), 10215–10237. https://doi.org/10.33263/BRIAC113.1021510237.

(42)   Yadav, R.; Chaudhary, J. K.; Jain, N.; Chaudhary, P. K.; Khanra, S.; Dhamija, P.; Sharma, A.; Kumar, A.; Handu, S. Role of Structural and Non-Structural Proteins and Therapeutic Targets of SARS-CoV-2 for COVID-19. *Cells* **2021**, *10* (4), 821. https://doi.org/10.3390/cells10040821.

(43)   Andersen, K. G.; Rambaut, A.; Lipkin, W. I.; Holmes, E. C.; Garry, R. F. The Proximal Origin of SARS-CoV-2. *Nat Med* **2020**, *26* (4), 450–452. https://doi.org/10.1038/s41591-020-0820-9.

(44)   Biryukov, J.; Boydston, J. A.; Dunning, R. A.; Yeager, J. J.; Wood, S.; Ferris, A.; Miller, D.; Weaver, W.; Zeitouni, N. E.; Freeburger, D.; Dabisch, P.; Wahl, V.; Hevey, M. C.; Altamura, L. A. SARS-CoV-2 Is Rapidly Inactivated at High Temperature. *Environ Chem Lett* **2021**, *19* (2), 1773–1777. https://doi.org/10.1007/s10311-021-01187-x.

(45)   Zhang, T.; Wu, Q.; Zhang, Z. Probable Pangolin Origin of SARS-CoV-2 Associated with the COVID-19 Outbreak. *Current Biology* **2020**, *30* (7), 1346-1351.e2. https://doi.org/10.1016/j.cub.2020.03.022.

(46)   Jackson, C. B.; Farzan, M.; Chen, B.; Choe, H. Mechanisms of SARS-CoV-2 Entry into Cells. *Nat Rev Mol Cell Biol* **2022**, *23* (1), 3–20. https://doi.org/10.1038/s41580-021-00418-x.

(47)   Gao, Q.; Bao, L.; Mao, H.; Wang, L.; Xu, K.; Yang, M.; Li, Y.; Zhu, L.; Wang, N.; Lv, Z.; Gao, H.; Ge, X.; Kan, B.; Hu, Y.; Liu, J.; Cai, F.; Jiang, D.; Yin, Y.; Qin, C.; Li, J.; Gong, X.; Lou, X.; Shi, W.; Wu, D.; Zhang, H.; Zhu, L.; Deng, W.; Li, Y.; Lu, J.; Li, C.; Wang, X.; Yin, W.; Zhang, Y.; Qin, C. Development of an Inactivated Vaccine Candidate for SARS-CoV-2. *Science (1979)* **2020**, *369* (6499), 77–81. https://doi.org/10.1126/science.abc1932.

(48)   Wu, Z.; McGoogan, J. M. Characteristics of and Important Lessons From the Coronavirus Disease 2019 (COVID-19) Outbreak in China. *JAMA* **2020**, *323* (13), 1239. https://doi.org/10.1001/jama.2020.2648.

(49)   Zhong, L. L. D.; Lam, W. C.; Yang, W.; Chan, K. W.; Sze, S. C. W.; Miao, J.; Yung, K. K. L.; Bian, Z.; Wong, V. T. Potential Targets for Treatment of Coronavirus Disease 2019 (COVID-19): A Review of Qing-Fei-Pai-Du-Tang and Its Major Herbs. *Am J Chin Med (Gard City N Y)* **2020**, *48* (05), 1051–1071. https://doi.org/10.1142/S0192415X20500512.

(50)   Cesar-Silva, D.; Pereira-Dutra, F. S.; Moraes Giannini, A. L. M.; Jacques G. de Almeida, C. J. G. The Endolysosomal System: The Acid Test for SARS-CoV-2. *Int J Mol Sci* **2022**, *23* (9), 4576. https://doi.org/10.3390/ijms23094576.

(51)   Naqvi, A. A. T.; Fatima, K.; Mohammad, T.; Fatima, U.; Singh, I. K.; Singh, A.; Atif, S. M.; Hariprasad, G.; Hasan, G. M.; Hassan, Md. I. Insights into SARS-CoV-2 Genome, Structure, Evolution, Pathogenesis and Therapies: Structural Genomics Approach. *Biochimica et Biophysica Acta (BBA) - Molecular Basis of Disease* **2020**, *1866* (10), 165878. https://doi.org/10.1016/j.bbadis.2020.165878.

(52)   Pizzato, M.; Baraldi, C.; Boscato Sopetto, G.; Finozzi, D.; Gentile, C.; Gentile, M. D.; Marconi, R.; Paladino, D.; Raoss, A.; Riedmiller, I.; Ur Rehman, H.; Santini, A.; Succetti, V.; Volpini, L. SARS-CoV-2 and the Host Cell: A Tale of Interactions. *Frontiers in Virology* **2022**, *1*. https://doi.org/10.3389/fviro.2021.815388.

(53)   Galloway, S. E.; Paul, P.; MacCannell, D. R.; Johansson, M. A.; Brooks, J. T.; MacNeil, A.; Slayton, R. B.; Tong, S.; Silk, B. J.; Armstrong, G. L.; Biggerstaff, M.; Dugan, V. G. Emergence of SARS-CoV-2 B.1.1.7 Lineage — United States, December 29, 2020–January 12, 2021. *MMWR Morb Mortal Wkly Rep* **2021**, *70* (3), 95–99. https://doi.org/10.15585/mmwr.mm7003e2.

(54)   Davies, N. G.; Abbott, S.; Barnard, R. C.; Jarvis, C. I.; Kucharski, A. J.; Munday, J. D.; Pearson, C. A. B.; Russell, T. W.; Tully, D. C.; Washburne, A. D.; Wenseleers, T.; Gimma, A.; Waites, W.; Wong, K. L. M.; van Zandvoort, K.; Silverman, J. D.; Diaz-Ordaz, K.; Keogh, R.; Eggo, R. M.; Funk, S.; Jit, M.; Atkins, K. E.; Edmunds, W. J. Estimated Transmissibility and Impact of SARS-CoV-2 Lineage B.1.1.7 in England. *Science (1979)* **2021**, *372* (6538). https://doi.org/10.1126/science.abg3055.

(55)   Grint, D. J.; Wing, K.; Williamson, E.; McDonald, H. I.; Bhaskaran, K.; Evans, D.; Evans, S. J.; Walker, A. J.; Hickman, G.; Nightingale, E.; Schultze, A.; Rentsch, C. T.; Bates, C.; Cockburn, J.; Curtis, H. J.; Morton, C. E.; Bacon, S.; Davy, S.; Wong, A. Y.; Mehrkar, A.; Tomlinson, L.; Douglas, I. J.; Mathur, R.; Blomquist, P.; MacKenna, B.; Ingelsby, P.; Croker, R.; Parry, J.; Hester, F.; Harper, S.; DeVito, N. J.; Hulme, W.; Tazare, J.; Goldacre, B.; Smeeth, L.; Eggo, R. M. Case Fatality Risk of the SARS-CoV-2 Variant of Concern B.1.1.7 in England, 16 November to 5 February. *Eurosurveillance* **2021**, *26* (11). https://doi.org/10.2807/1560-7917.ES.2021.26.11.2100256.

(56)   Tegally, H.; Wilkinson, E.; Giovanetti, M.; Iranzadeh, A.; Fonseca, V.; Giandhari, J.; Doolabh, D.; Pillay, S.; San, E. J.; Msomi, N.; Mlisana, K.; von Gottberg, A.; Walaza, S.; Allam, M.; Ismail, A.; Mohale, T.; Glass, A. J.; Engelbrecht, S.; Van Zyl, G.; Preiser, W.; Petruccione, F.; Sigal, A.; Hardie, D.; Marais, G.; Hsiao, N.; Korsman, S.; Davies, M.-A.; Tyers, L.; Mudau, I.; York, D.; Maslo, C.; Goedhals, D.; Abrahams, S.; Laguda-Akingba, O.; Alisoltani-Dehkordi, A.; Godzik, A.; Wibmer, C. K.; Sewell, B. T.; Lourenço, J.; Alcantara, L. C. J.; Kosakovsky Pond, S. L.; Weaver, S.; Martin, D.; Lessells, R. J.; Bhiman, J. N.; Williamson, C.; de Oliveira, T. Detection of a SARS-CoV-2 Variant of Concern in South Africa. *Nature* **2021**, *592* (7854), 438–443. https://doi.org/10.1038/s41586-021-03402-9.

(57)   Wang, P.; Casner, R. G.; Nair, M. S.; Wang, M.; Yu, J.; Cerutti, G.; Liu, L.; Kwong, P. D.; Huang, Y.; Shapiro, L.; Ho, D. D. Increased Resistance of SARS-CoV-2 Variant P.1 to Antibody Neutralization. *Cell Host Microbe* **2021**, *29* (5), 747-751.e4. https://doi.org/10.1016/j.chom.2021.04.007.

(58)   Faria, N. R.; Mellan, T. A.; Whittaker, C.; Claro, I. M.; Candido, D. da S.; Mishra, S.; Crispim, M. A. E.; Sales, F. C.; Hawryluk, I.; McCrone, J. T.; Hulswit, R. J. G.; Franco, L. A. M.; Ramundo, M. S.; de Jesus, J. G.; Andrade, P. S.; Coletti, T. M.; Ferreira, G. M.; Silva, C. A. M.; Manuli, E. R.; Pereira, R. H. M.; Peixoto, P. S.; Kraemer, M. U.; Gaburo, N.; Camilo, C. da C.; Hoeltgebaum, H.; Souza, W. M.; Rocha, E. C.; de Souza, L. M.; de Pinho, M. C.; Araujo, L. J. T.; Malta, F. S. V; de Lima, A. B.; Silva, J. do P.; Zauli, D. A. G.; de S Ferreira, A. C.; Schnekenberg, R. P.; Laydon, D. J.; Walker, P. G. T.; Schlüter, H. M.; Dos Santos, A. L. P.; Vidal, M. S.; Del Caro, V. S.; Filho, R. M. F.; Dos Santos, H. M.; Aguiar, R. S.; Modena, J. L. P.; Nelson, B.; Hay, J. A.; Monod, M.; Miscouridou, X.; Coupland, H.; Sonabend, R.; Vollmer, M.; Gandy, A.; Suchard, M. A.; Bowden, T. A.; Pond, S. L. K.; Wu, C.-H.; Ratmann, O.; Ferguson, N. M.;

Dye, C.; Loman, N. J.; Lemey, P.; Rambaut, A.; Fraiji, N. A.; Carvalho, M. do P. S. S.; Pybus, O. G.; Flaxman, S.; Bhatt, S.; Sabino, E. C. Genomics and Epidemiology of a Novel SARS-CoV-2 Lineage in Manaus, Brazil. *medRxiv* **2021**. https://doi.org/10.1101/2021.02.26.21252554.

(59)   Raman, R.; Patel, K. J.; Ranjan, K. COVID-19: Unmasking Emerging SARS-CoV-2 Variants, Vaccines and Therapeutic Strategies. *Biomolecules* **2021**, *11* (7), 993. https://doi.org/10.3390/biom11070993.

(60)   Vaughan, A. Omicron Emerges. *New Sci (1956)* **2021**, *252* (3363), 7. https://doi.org/10.1016/S0262-4079(21)02140-0.

(61)   Callaway, E. Heavily Mutated Omicron Variant Puts Scientists on Alert. *Nature* **2021**, *600* (7887), 21–21. https://doi.org/10.1038/d41586-021-03552-w.

(62)   Abe, K.; Kabe, Y.; Uchiyama, S.; Iwasaki, Y. W.; Ishizu, H.; Uwamino, Y.; Takenouchi, T.; Uno, S.; Ishii, M.; Maruno, T.; Noda, M.; Murata, M.; Hasegawa, N.; Saya, H.; Kitagawa, Y.; Fukunaga, K.; Amagai, M.; Siomi, H.; Suematsu, M.; Kosaki, K. Pro108Ser Mutation of SARS-CoV-2 3CLpro Reduces the Enzyme Activity and Ameliorates the Clinical Severity of COVID-19. *Sci Rep* **2022**, *12* (1), 1299. https://doi.org/10.1038/s41598-022-05424-3.

(63)   Feng, J.; Li, D.; Zhang, J.; Yin, X.; Li, J. Crystal Structure of SARS-CoV 3C-like Protease with Baicalein. *Biochem Biophys Res Commun* **2022**, *611*, 190–194. https://doi.org/10.1016/j.bbrc.2022.04.086.

(64)   Barrila, J.; Gabelli, S. B.; Bacha, U.; Amzel, L. M.; Freire, E. Mutation of Asn28 Disrupts the Dimerization and Enzymatic Activity of SARS 3CL [pro] ,. *Biochemistry* **2010**, *49* (20), 4308–4317. https://doi.org/10.1021/bi1002585.

(65)   Akbulut, E. Investigation of Changes in Protein Stability and Substrate Affinity of 3CL-Protease of SARS-CoV-2 Caused by Mutations. *Genet Mol Biol* **2022**, *45* (2). https://doi.org/10.1590/1678-4685-gmb-2021-0404.

(66)   Dai, W.; Zhang, B.; Jiang, X.-M.; Su, H.; Li, J.; Zhao, Y.; Xie, X.; Jin, Z.; Peng, J.; Liu, F.; Li, C.; Li, Y.; Bai, F.; Wang, H.; Cheng, X.; Cen, X.; Hu, S.; Yang, X.; Wang, J.; Liu, X.; Xiao, G.; Jiang, H.; Rao, Z.; Zhang, L.-K.; Xu, Y.; Yang, H.; Liu, H. Structure-Based Design of Antiviral Drug Candidates Targeting the SARS-CoV-2 Main Protease. *Science (1979)* **2020**, *368* (6497), 1331–1335. https://doi.org/10.1126/science.abb4489.

(67)   Hu, Q.; Xiong, Y.; Zhu, G.; Zhang, Y.; Zhang, Y.; Huang, P.; Ge, G. The SARS-CoV-2 Main Protease (M [pro]): Structure, Function, and Emerging Therapies for COVID-19. *MedComm (Beijing)* **2022**, *3* (3). https://doi.org/10.1002/mco2.151.

(68)   Yin, J.; Niu, C.; Cherney, M. M.; Zhang, J.; Huitema, C.; Eltis, L. D.; Vederas, J. C.; James, M. N. G. A Mechanistic View of Enzyme Inhibition and Peptide Hydrolysis in the Active Site of the SARS-CoV 3C-like Peptidase. *J Mol Biol* **2007**, *371* (4), 1060–1074. https://doi.org/10.1016/j.jmb.2007.06.001.

(69) Achutha, A. S.; Pushpa, V. L.; Suchitra, S. Theoretical Insights into the Anti-SARS-CoV-2 Activity of Chloroquine and Its Analogs and In Silico Screening of Main Protease Inhibitors. *J Proteome Res* **2020**, *19* (11), 4706–4717. https://doi.org/10.1021/acs.jproteome.0c00683.

(70) Owen, D. R.; Allerton, C. M. N.; Anderson, A. S.; Aschenbrenner, L.; Avery, M.; Berritt, S.; Boras, B.; Cardin, R. D.; Carlo, A.; Coffman, K. J.; Dantonio, A.; Di, L.; Eng, H.; Ferre, R.; Gajiwala, K. S.; Gibson, S. A.; Greasley, S. E.; Hurst, B. L.; Kadar, E. P.; Kalgutkar, A. S.; Lee, J. C.; Lee, J.; Liu, W.; Mason, S. W.; Noell, S.; Novak, J. J.; Obach, R. S.; Ogilvie, K.; Patel, N. C.; Pettersson, M.; Rai, D. K.; Reese, M. R.; Sammons, M. F.; Sathish, J. G.; Singh, R. S. P.; Steppan, C. M.; Stewart, A. E.; Tuttle, J. B.; Updyke, L.; Verhoest, P. R.; Wei, L.; Yang, Q.; Zhu, Y. An Oral SARS-CoV-2 M ᵖʳᵒ Inhibitor Clinical Candidate for the Treatment of COVID-19. *Science (1979)* **2021**, *374* (6575), 1586–1593. https://doi.org/10.1126/science.abl4784.

(71) Ratia, K.; Kilianski, A.; Baez-Santos, Y. M.; Baker, S. C.; Mesecar, A. Structural Basis for the Ubiquitin-Linkage Specificity and DeISGylating Activity of SARS-CoV Papain-Like Protease. *PLoS Pathog* **2014**, *10* (5), e1004113. https://doi.org/10.1371/journal.ppat.1004113.

(72) Del Valle, D. M.; Kim-Schulze, S.; Huang, H.-H.; Beckmann, N. D.; Nirenberg, S.; Wang, B.; Lavin, Y.; Swartz, T. H.; Madduri, D.; Stock, A.; Marron, T. U.; Xie, H.; Patel, M.; Tuballes, K.; Van Oekelen, O.; Rahman, A.; Kovatch, P.; Aberg, J. A.; Schadt, E.; Jagannath, S.; Mazumdar, M.; Charney, A. W.; Firpo-Betancourt, A.; Mendu, D. R.; Jhang, J.; Reich, D.; Sigel, K.; Cordon-Cardo, C.; Feldmann, M.; Parekh, S.; Merad, M.; Gnjatic, S. An Inflammatory Cytokine Signature Predicts COVID-19 Severity and Survival. *Nat Med* **2020**, *26* (10), 1636–1643. https://doi.org/10.1038/s41591-020-1051-9.

(73) Wydorski, P. M.; Osipiuk, J.; Lanham, B. T.; Tesar, C.; Endres, M.; Engle, E.; Jedrzejczak, R.; Mullapudi, V.; Michalska, K.; Fidelis, K.; Fushman, D.; Joachimiak, A.; Joachimiak, L. A. Dual Domain Recognition Determines SARS-CoV-2 PLpro Selectivity for Human ISG15 and K48-Linked Di-Ubiquitin. *Nat Commun* **2023**, *14* (1), 2366. https://doi.org/10.1038/s41467-023-38031-5.

(74) Rut, W.; Lv, Z.; Zmudzinski, M.; Patchett, S.; Nayak, D.; Snipas, S. J.; El Oualid, F.; Huang, T. T.; Bekes, M.; Drag, M.; Olsen, S. K. Activity Profiling and Crystal Structures of Inhibitor-Bound SARS-CoV-2 Papain-like Protease: A Framework for Anti–COVID-19 Drug Design. *Sci Adv* **2020**, *6* (42). https://doi.org/10.1126/sciadv.abd4596.

(75) Osipiuk, J.; Azizi, S.-A.; Dvorkin, S.; Endres, M.; Jedrzejczak, R.; Jones, K. A.; Kang, S.; Kathayat, R. S.; Kim, Y.; Lisnyak, V. G.; Maki, S. L.; Nicolaescu, V.; Taylor, C. A.; Tesar, C.; Zhang, Y.-A.; Zhou, Z.; Randall, G.; Michalska, K.; Snyder, S. A.; Dickinson, B. C.; Joachimiak, A. Structure of Papain-like Protease from SARS-CoV-2 and Its Complexes with Non-Covalent Inhibitors. *Nat Commun* **2021**, *12* (1), 743. https://doi.org/10.1038/s41467-021-21060-3.

(76) Shin, D.; Mukherjee, R.; Grewe, D.; Bojkova, D.; Baek, K.; Bhattacharya, A.; Schulz, L.; Widera, M.; Mehdipour, A. R.; Tascher, G.; Geurink, P. P.; Wilhelm, A.; van der Heden van

Noort, G. J.; Ovaa, H.; Müller, S.; Knobeloch, K.-P.; Rajalingam, K.; Schulman, B. A.; Cinatl, J.; Hummer, G.; Ciesek, S.; Dikic, I. Papain-like Protease Regulates SARS-CoV-2 Viral Spread and Innate Immunity. *Nature* **2020**, *587* (7835), 657–662. https://doi.org/10.1038/s41586-020-2601-5.

(77)   Tripathi, D.; Sodani, M.; Gupta, P. K.; Kulkarni, S. Host Directed Therapies: COVID-19 and Beyond. *Current Research in Pharmacology and Drug Discovery* **2021**, *2*, 100058. https://doi.org/10.1016/j.crphar.2021.100058.

(78)   Conus, S.; Simon, H.-U. Cathepsins: Key Modulators of Cell Death and Inflammatory Responses. *Biochem Pharmacol* **2008**, *76* (11), 1374–1382. https://doi.org/10.1016/j.bcp.2008.07.041.

(79)   Maehr, R. Cathepsin L Is Essential for Onset of Autoimmune Diabetes in NOD Mice. *Journal of Clinical Investigation* **2005**, *115* (10), 2934–2943. https://doi.org/10.1172/JCI25485.

(80)   Turk, V.; Stoka, V.; Vasiljeva, O.; Renko, M.; Sun, T.; Turk, B.; Turk, D. Cysteine Cathepsins: From Structure, Function and Regulation to New Frontiers. *Biochimica et Biophysica Acta (BBA) - Proteins and Proteomics* **2012**, *1824* (1), 68–88. https://doi.org/10.1016/j.bbapap.2011.10.002.

(81)   Roth, W.; Deussing, J.; Botchkarev, V. A.; Pauly-Evers, M.; Saftig, P.; Hafner, A.; Schmidt, P.; Schmahl, W.; Scherer, J.; Anton-Lamprecht, I.; Von Figura, K.; Paus, R.; Peters, C. Cathepsin L Deficiency as Molecular Defect of *Furless:* Hyperproliferation of Keratinocytes and Pertubation of Hair Follicle Cycling. *The FASEB Journal* **2000**, *14* (13), 2075–2086. https://doi.org/10.1096/fj.99-0970com.

(82)   Garsen, M.; Rops, A. L. W. M. M.; Dijkman, H.; Willemsen, B.; van Kuppevelt, T. H.; Russel, F. G.; Rabelink, T. J.; Berden, J. H. M.; Reinheckel, T.; van der Vlag, J. Cathepsin L Is Crucial for the Development of Early Experimental Diabetic Nephropathy. *Kidney Int* **2016**, *90* (5), 1012–1022. https://doi.org/10.1016/j.kint.2016.06.035.

(83)   Koganti, R.; Suryawanshi, R.; Shukla, D. Heparanase, Cell Signaling, and Viral Infections. *Cellular and Molecular Life Sciences* **2020**, *77* (24), 5059–5077. https://doi.org/10.1007/s00018-020-03559-y.

(84)   Hopkins, J.; Yadavalli, T.; Agelidis, A. M.; Shukla, D. Host Enzymes Heparanase and Cathepsin L Promote Herpes Simplex Virus 2 Release from Cells. *J Virol* **2018**, *92* (23). https://doi.org/10.1128/JVI.01179-18.

(85)   Gomes, C. P.; Fernandes, D. E.; Casimiro, F.; da Mata, G. F.; Passos, M. T.; Varela, P.; Mastroianni-Kirsztajn, G.; Pesquero, J. B. Cathepsin L in COVID-19: From Pharmacological Evidences to Genetics. *Front Cell Infect Microbiol* **2020**, *10*. https://doi.org/10.3389/fcimb.2020.589505.

(86)   Chakraborty, C.; Sharma, A. R.; Bhattacharya, M.; Agoramoorthy, G.; Lee, S.-S. The Drug Repurposing for COVID-19 Clinical Trials Provide Very Effective Therapeutic Combinations:

Lessons Learned From Major Clinical Studies. *Front Pharmacol* **2021**, *12*. https://doi.org/10.3389/fphar.2021.704205.

(87) Keshavarzi Arshadi, A.; Webb, J.; Salem, M.; Cruz, E.; Calad-Thomson, S.; Ghadirian, N.; Collins, J.; Diez-Cecilia, E.; Kelly, B.; Goodarzi, H.; Yuan, J. S. Artificial Intelligence for COVID-19 Drug Discovery and Vaccine Development. *Front Artif Intell* **2020**, *3*. https://doi.org/10.3389/frai.2020.00065.

(88) Martinez, M. A. Efficacy of Repurposed Antiviral Drugs: Lessons from COVID-19. *Drug Discov Today* **2022**, *27* (7), 1954–1960. https://doi.org/10.1016/j.drudis.2022.02.012.

(89) GUO, N.; PENG, Z. MG132, a Proteasome Inhibitor, Induces Apoptosis in Tumor Cells. *Asia Pac J Clin Oncol* **2013**, *9* (1), 6–11. https://doi.org/10.1111/j.1743-7563.2012.01535.x.

(90) Longhitano, L.; Tibullo, D.; Giallongo, C.; Lazzarino, G.; Tartaglia, N.; Galimberti, S.; Li Volti, G.; Palumbo, G. A.; Liso, A. Proteasome Inhibitors as a Possible Therapy for SARS-CoV-2. *Int J Mol Sci* **2020**, *21* (10), 3622. https://doi.org/10.3390/ijms21103622.

(91) Schneider, M.; Ackermann, K.; Stuart, M.; Wex, C.; Protzer, U.; Schätzl, H. M.; Gilch, S. Severe Acute Respiratory Syndrome Coronavirus Replication Is Severely Impaired by MG132 Due to Proteasome-Independent Inhibition of M-Calpain. *J Virol* **2012**, *86* (18), 10112–10122. https://doi.org/10.1128/JVI.01001-12.

(92) Costanzi, E.; Kuzikov, M.; Esposito, F.; Albani, S.; Demitri, N.; Giabbai, B.; Camasta, M.; Tramontano, E.; Rossetti, G.; Zaliani, A.; Storici, P. Structural and Biochemical Analysis of the Dual Inhibition of MG-132 against SARS-CoV-2 Main Protease (Mpro/3CLpro) and Human Cathepsin-L. *Int J Mol Sci* **2021**, *22* (21), 11779. https://doi.org/10.3390/ijms222111779.

(93) Wang, Z.; Zhao, Y.; Wang, Q.; Xing, Y.; Feng, L.; Kong, J.; Peng, C.; Zhang, L.; Yang, H.; Lu, M. Identification of Proteasome and Caspase Inhibitors Targeting SARS-CoV-2 Mpro. *Signal Transduct Target Ther* **2021**, *6* (1), 214. https://doi.org/10.1038/s41392-021-00639-8.

(94) Hung, H.-C.; Ke, Y.-Y.; Huang, S. Y.; Huang, P.-N.; Kung, Y.-A.; Chang, T.-Y.; Yen, K.-J.; Peng, T.-T.; Chang, S.-E.; Huang, C.-T.; Tsai, Y.-R.; Wu, S.-H.; Lee, S.-J.; Lin, J.-H.; Liu, B.-S.; Sung, W.-C.; Shih, S.-R.; Chen, C.-T.; Hsu, J. T.-A. Discovery of M Protease Inhibitors Encoded by SARS-CoV-2. *Antimicrob Agents Chemother* **2020**, *64* (9). https://doi.org/10.1128/AAC.00872-20.

(95) Ito, H.; Watanabe, M.; Kim, Y.-T.; Takahashi, K. Inhibition of Rat Liver Cathepsins B and L by the Peptide Aldehyde Benzyloxycarbonyl-Leucyl-Leucyl-Leucinal and Its Analogues. *J Enzyme Inhib Med Chem* **2009**, *24* (1), 279–286. https://doi.org/10.1080/14756360802166921.

(96) Shenoy, R. T.; Sivaraman, J. Structural Basis for Reversible and Irreversible Inhibition of Human Cathepsin L by Their Respective Dipeptidyl Glyoxal and Diazomethylketone Inhibitors. *J Struct Biol* **2011**, *173* (1), 14–19. https://doi.org/10.1016/j.jsb.2010.09.007.

(97) Mondal, S.; Chen, Y.; Lockbaum, G. J.; Sen, S.; Chaudhuri, S.; Reyes, A. C.; Lee, J. M.; Kaur, A. N.; Sultana, N.; Cameron, M. D.; Shaffer, S. A.; Schiffer, C. A.; Fitzgerald, K. A.; Thompson,

P. R. Dual Inhibitors of Main Protease (M ^{Pro}) and Cathepsin L as Potent Antivirals against SARS-CoV2. *J Am Chem Soc* **2022**, *144* (46), 21035–21045. https://doi.org/10.1021/jacs.2c04626.

(98) Mondal, S.; Chen, Y.; Lockbaum, G. J.; Sen, S.; Chaudhuri, S.; Reyes, A. C.; Lee, J. M.; Kaur, A. N.; Sultana, N.; Cameron, M. D.; Shaffer, S. A.; Schiffer, C. A.; Fitzgerald, K. A.; Thompson, P. R. Dual Inhibitors of Main Protease (M ^{Pro}) and Cathepsin L as Potent Antivirals against SARS-CoV2. *J Am Chem Soc* **2022**, *144* (46), 21035–21045. https://doi.org/10.1021/jacs.2c04626.

(99) Ma, X. R.; Alugubelli, Y. R.; Ma, Y.; Vatansever, E. C.; Scott, D. A.; Qiao, Y.; Yu, G.; Xu, S.; Liu, W. R. MPI8 Is Potent against SARS-CoV-2 by Inhibiting Dually and Selectively the SARS-CoV-2 Main Protease and the Host Cathepsin L**. *ChemMedChem* **2022**, *17* (1). https://doi.org/10.1002/cmdc.202100456.

(100) Yang, K. S.; Ma, X. R.; Ma, Y.; Alugubelli, Y. R.; Scott, D. A.; Vatansever, E. C.; Drelich, A. K.; Sankaran, B.; Geng, Z. Z.; Blankenship, L. R.; Ward, H. E.; Sheng, Y. J.; Hsu, J. C.; Kratch, K. C.; Zhao, B.; Hayatshahi, H. S.; Liu, J.; Li, P.; Fierke, C. A.; Tseng, C. K.; Xu, S.; Liu, W. R. A Quick Route to Multiple Highly Potent SARS-CoV-2 Main Protease Inhibitors**. *ChemMedChem* **2021**, *16* (6), 942–948. https://doi.org/10.1002/cmdc.202000924.

(101) Ma, C.; Sacco, M. D.; Hurst, B.; Townsend, J. A.; Hu, Y.; Szeto, T.; Zhang, X.; Tarbet, B.; Marty, M. T.; Chen, Y.; Wang, J. Boceprevir, GC-376, and Calpain Inhibitors II, XII Inhibit SARS-CoV-2 Viral Replication by Targeting the Viral Main Protease. *Cell Res* **2020**, *30* (8), 678–692. https://doi.org/10.1038/s41422-020-0356-z.

(102) Zhang, L.; Lin, D.; Sun, X.; Curth, U.; Drosten, C.; Sauerhering, L.; Becker, S.; Rox, K.; Hilgenfeld, R. Crystal Structure of SARS-CoV-2 Main Protease Provides a Basis for Design of Improved α-Ketoamide Inhibitors. *Science (1979)* **2020**, *368* (6489), 409–412. https://doi.org/10.1126/science.abb3405.

(103) Chowdhury, S. R.; Kennedy, S.; Zhu, K.; Mishra, R.; Chuong, P.; Nguyen, A.; Kathman, S. G.; Statsyuk, A. V. Discovery of Covalent Enzyme Inhibitors Using Virtual Docking of Covalent Fragments. *Bioorg Med Chem Lett* **2019**, *29* (1), 36–39. https://doi.org/10.1016/j.bmcl.2018.11.019.

(104) Ciaglia, T.; Vestuto, V.; Di Sarno, V.; Musella, S.; Smaldone, G.; Di Matteo, F.; Napolitano, V.; Miranda, M. R.; Pepe, G.; Basilicata, M. G.; Novi, S.; Capolupo, I.; Bifulco, G.; Campiglia, P.; Gomez-Monterrey, I.; Snoeck, R.; Andrei, G.; Manfra, M.; Ostacolo, C.; Lauro, G.; Bertamino, A. Peptidomimetics as Potent Dual SARS-CoV-2 Cathepsin-L and Main Protease Inhibitors: In Silico Design, Synthesis and Pharmacological Characterization. *Eur J Med Chem* **2024**, *266*, 116128. https://doi.org/10.1016/j.ejmech.2024.116128.

(105) Fujishima, A.; Imai, Y.; Nomura, T.; Fujisawa, Y.; Yamamoto, Y.; Sugawara, T. The Crystal Structure of Human Cathepsin L Complexed with E-64. *FEBS Lett* **1997**, *407* (1), 47–50. https://doi.org/10.1016/S0014-5793(97)00216-0.

(106) Li, Y.; Wang, K.; Sun, H.; Wu, S.; Wang, H.; Shi, Y.; Li, X.; Yan, H.; Yang, G.; Wu, M.; Li, Y.; Ding, X.; Si, S.; Jiang, J.; Du, Y.; Li, Y.; Hong, B. Omicsynin B4 Potently Blocks Coronavirus Infection by Inhibiting Host Proteases Cathepsin L and TMPRSS2. *Antiviral Res* **2023**, *214*, 105606. https://doi.org/10.1016/j.antiviral.2023.105606.

(107) Ghosh, A. K.; Takayama, J.; Rao, K. V.; Ratia, K.; Chaudhuri, R.; Mulhearn, D. C.; Lee, H.; Nichols, D. B.; Baliji, S.; Baker, S. C.; Johnson, M. E.; Mesecar, A. D. Severe Acute Respiratory Syndrome Coronavirus Papain-like Novel Protease Inhibitors: Design, Synthesis, Protein−Ligand X-Ray Structure and Biological Evaluation. *J Med Chem* **2010**, *53* (13), 4968–4979. https://doi.org/10.1021/jm1004489.

(108) Ghosh, A. K.; Brindisi, M.; Shahabi, D.; Chapman, M. E.; Mesecar, A. D. Drug Development and Medicinal Chemistry Efforts toward SARS-Coronavirus and Covid-19 Therapeutics. *ChemMedChem* **2020**, *15* (11), 907–932. https://doi.org/10.1002/cmdc.202000223.

(109) Ratia, K.; Pegan, S.; Takayama, J.; Sleeman, K.; Coughlin, M.; Baliji, S.; Chaudhuri, R.; Fu, W.; Prabhakar, B. S.; Johnson, M. E.; Baker, S. C.; Ghosh, A. K.; Mesecar, A. D. A Noncovalent Class of Papain-like Protease/Deubiquitinase Inhibitors Blocks SARS Virus Replication. *Proceedings of the National Academy of Sciences* **2008**, *105* (42), 16119–16124. https://doi.org/10.1073/pnas.0805240105.

(110) Freitas, B. T.; Durie, I. A.; Murray, J.; Longo, J. E.; Miller, H. C.; Crich, D.; Hogan, R. J.; Tripp, R. A.; Pegan, S. D. Characterization and Noncovalent Inhibition of the Deubiquitinase and DeISGylase Activity of SARS-CoV-2 Papain-Like Protease. *ACS Infect Dis* **2020**, *6* (8), 2099–2109. https://doi.org/10.1021/acsinfecdis.0c00168.

(111) Ma, C.; Sacco, M. D.; Xia, Z.; Lambrinidis, G.; Townsend, J. A.; Hu, Y.; Meng, X.; Szeto, T.; Ba, M.; Zhang, X.; Gongora, M.; Zhang, F.; Marty, M. T.; Xiang, Y.; Kolocouris, A.; Chen, Y.; Wang, J. Discovery of SARS-CoV-2 Papain-like Protease Inhibitors through a Combination of High-Throughput Screening and a FlipGFP-Based Reporter Assay. *ACS Cent Sci* **2021**, *7* (7), 1245–1260. https://doi.org/10.1021/acscentsci.1c00519.

(112) Drag, M.; Mikolajczyk, J.; Bekes, M.; Reyes-Turcu, F. E.; Ellman, J. A.; Wilkinson, K. D.; Salvesen, G. S. Positional-Scanning Fluorigenic Substrate Libraries Reveal Unexpected Specificity Determinants of DUBs (Deubiquitinating Enzymes). *Biochemical Journal* **2008**, *415* (3), 367–375. https://doi.org/10.1042/BJ20080779.

(113) Rut, W.; Zmudzinski, M.; Snipas, S. J.; Bekes, M.; Huang, T. T.; Drag, M. Engineered Unnatural Ubiquitin for Optimal Detection of Deubiquitinating Enzymes. *Chem Sci* **2020**, *11* (23), 6058–6069. https://doi.org/10.1039/D0SC01347A.

(114) Rut, W.; Lv, Z.; Zmudzinski, M.; Patchett, S.; Nayak, D.; Snipas, S. J.; El Oualid, F.; Huang, T. T.; Bekes, M.; Drag, M.; Olsen, S. K. Activity Profiling and Crystal Structures of Inhibitor-Bound SARS-CoV-2 Papain-like Protease: A Framework for Anti–COVID-19 Drug Design. *Sci Adv* **2020**, *6* (42). https://doi.org/10.1126/sciadv.abd4596.

(115) Amendola, G.; Ettari, R.; Previti, S.; Di Chio, C.; Messere, A.; Di Maro, S.; Hammerschmidt, S. J.; Zimmer, C.; Zimmermann, R. A.; Schirmeister, T.; Zappalà, M.; Cosconati, S. Lead Discovery of SARS-CoV-2 Main Protease Inhibitors through Covalent Docking-Based Virtual Screening. *J Chem Inf Model* **2021**, *61* (4), 2062–2073. https://doi.org/10.1021/acs.jcim.1c00184.

(116) Previti, S.; Ettari, R.; Cosconati, S.; Amendola, G.; Chouchene, K.; Wagner, A.; Hellmich, U. A.; Ulrich, K.; Krauth-Siegel, R. L.; Wich, P. R.; Schmid, I.; Schirmeister, T.; Gut, J.; Rosenthal, P. J.; Grasso, S.; Zappalà, M. Development of Novel Peptide-Based Michael Acceptors Targeting Rhodesain and Falcipain-2 for the Treatment of Neglected Tropical Diseases (NTDs). *J Med Chem* **2017**, *60* (16), 6911–6923. https://doi.org/10.1021/acs.jmedchem.7b00405.

(117) Ettari, R.; Previti, S.; Maiorana, S.; Amendola, G.; Wagner, A.; Cosconati, S.; Schirmeister, T.; Hellmich, U. A.; Zappalà, M. Optimization Strategy of Novel Peptide-Based Michael Acceptors for the Treatment of Human African Trypanosomiasis. *J Med Chem* **2019**, *62* (23), 10617–10629. https://doi.org/10.1021/acs.jmedchem.9b00908.

(118) Maiorana, S.; Ettari, R.; Previti, S.; Amendola, G.; Wagner, A.; Cosconati, S.; Hellmich, U. A.; Schirmeister, T.; Zappalà, M. Peptidyl Vinyl Ketone Irreversible Inhibitors of Rhodesain: Modifications of the P2 Fragment. *ChemMedChem* **2020**, *15* (16), 1552–1561. https://doi.org/10.1002/cmdc.202000360.

(119) Ettari, R.; Previti, S.; Tamborini, L.; Cullia, G.; Grasso, S.; Zappalà, M. The Inhibition of Cysteine Proteases Rhodesain and TbCatB: A Valuable Approach to Treat Human African Trypanosomiasis. *Mini-Reviews in Medicinal Chemistry* **2016**, *16* (17), 1374–1391. https://doi.org/10.2174/1389557515666160509125243.

(120) Ettari, R.; Previti, S.; Cosconati, S.; Maiorana, S.; Schirmeister, T.; Grasso, S.; Zappalà, M. Development of Novel 1,4-Benzodiazepine-Based Michael Acceptors as Antitrypanosomal Agents. *Bioorg Med Chem Lett* **2016**, *26* (15), 3453–3456. https://doi.org/10.1016/j.bmcl.2016.06.047.

(121) Ettari, R.; Previti, S.; Cosconati, S.; Kesselring, J.; Schirmeister, T.; Grasso, S.; Zappalà, M. Synthesis and Biological Evaluation of Novel Peptidomimetics as Rhodesain Inhibitors. *J Enzyme Inhib Med Chem* **2016**, *31* (6), 1184–1191. https://doi.org/10.3109/14756366.2015.1108972.

(122) Di Chio, C.; Previti, S.; Amendola, G.; Cosconati, S.; Schirmeister, T.; Zappalà, M.; Ettari, R. Development of Novel Benzodiazepine-Based Peptidomimetics as Inhibitors of Rhodesain from *Trypanosoma Brucei Rhodesiense*. *ChemMedChem* **2020**, *15* (11), 995–1001. https://doi.org/10.1002/cmdc.202000158.

(123) Jin, Z.; Du, X.; Xu, Y.; Deng, Y.; Liu, M.; Zhao, Y.; Zhang, B.; Li, X.; Zhang, L.; Peng, C.; Duan, Y.; Yu, J.; Wang, L.; Yang, K.; Liu, F.; Jiang, R.; Yang, X.; You, T.; Liu, X.; Yang, X.; Bai, F.; Liu, H.; Liu, X.; Guddat, L. W.; Xu, W.; Xiao, G.; Qin, C.; Shi, Z.; Jiang, H.; Rao, Z.; Yang, H. Structure of Mpro from SARS-CoV-2 and Discovery of Its Inhibitors. *Nature* **2020**, *582* (7811), 289–293. https://doi.org/10.1038/s41586-020-2223-y.

(124) La Monica, G.; Bono, A.; Lauria, A.; Martorana, A. Targeting SARS-CoV-2 Main Protease for Treatment of COVID-19: Covalent Inhibitors Structure–Activity Relationship Insights and Evolution Perspectives. *J Med Chem* **2022**, *65* (19), 12500–12534. https://doi.org/10.1021/acs.jmedchem.2c01005.

(125) Gao, K.; Wang, R.; Chen, J.; Tepe, J. J.; Huang, F.; Wei, G.-W. Perspectives on SARS-CoV-2 Main Protease Inhibitors. *J Med Chem* **2021**, *64* (23), 16922–16955. https://doi.org/10.1021/acs.jmedchem.1c00409.

(126) Zhang, L.; Lin, D.; Sun, X.; Curth, U.; Drosten, C.; Sauerhering, L.; Becker, S.; Rox, K.; Hilgenfeld, R. Crystal Structure of SARS-CoV-2 Main Protease Provides a Basis for Design of Improved α-Ketoamide Inhibitors. *Science (1979)* **2020**, *368* (6489), 409–412. https://doi.org/10.1126/science.abb3405.

(127) Vuong, W.; Khan, M. B.; Fischer, C.; Arutyunova, E.; Lamer, T.; Shields, J.; Saffran, H. A.; McKay, R. T.; van Belkum, M. J.; Joyce, M. A.; Young, H. S.; Tyrrell, D. L.; Vederas, J. C.; Lemieux, M. J. Feline Coronavirus Drug Inhibits the Main Protease of SARS-CoV-2 and Blocks Virus Replication. *Nat Commun* **2020**, *11* (1), 4282. https://doi.org/10.1038/s41467-020-18096-2.

(128) Xia, Z.; Sacco, M.; Hu, Y.; Ma, C.; Meng, X.; Zhang, F.; Szeto, T.; Xiang, Y.; Chen, Y.; Wang, J. Rational Design of Hybrid SARS-CoV-2 Main Protease Inhibitors Guided by the Superimposed Cocrystal Structures with the Peptidomimetic Inhibitors GC-376, Telaprevir, and Boceprevir. *ACS Pharmacol Transl Sci* **2021**, *4* (4), 1408–1421. https://doi.org/10.1021/acsptsci.1c00099.

(129) Previti, S.; Ettari, R.; Calcaterra, E.; Di Chio, C.; Ravichandran, R.; Zimmer, C.; Hammerschmidt, S.; Wagner, A.; Bogacz, M.; Cosconati, S.; Schirmeister, T.; Zappalà, M. Development of Urea-Bond-Containing Michael Acceptors as Antitrypanosomal Agents Targeting Rhodesain. *ACS Med Chem Lett* **2022**, *13* (7), 1083–1090. https://doi.org/10.1021/acsmedchemlett.2c00084.

(130) Owen, D. R.; Allerton, C. M. N.; Anderson, A. S.; Aschenbrenner, L.; Avery, M.; Berritt, S.; Boras, B.; Cardin, R. D.; Carlo, A.; Coffman, K. J.; Dantonio, A.; Di, L.; Eng, H.; Ferre, R.; Gajiwala, K. S.; Gibson, S. A.; Greasley, S. E.; Hurst, B. L.; Kadar, E. P.; Kalgutkar, A. S.; Lee, J. C.; Lee, J.; Liu, W.; Mason, S. W.; Noell, S.; Novak, J. J.; Obach, R. S.; Ogilvie, K.; Patel, N. C.; Pettersson, M.; Rai, D. K.; Reese, M. R.; Sammons, M. F.; Sathish, J. G.; Singh, R. S. P.; Steppan, C. M.; Stewart, A. E.; Tuttle, J. B.; Updyke, L.; Verhoest, P. R.; Wei, L.; Yang, Q.; Zhu,

Y. An Oral SARS-CoV-2 M ^{pro} Inhibitor Clinical Candidate for the Treatment of COVID-19. *Science (1979)* **2021**, *374* (6575), 1586–1593. https://doi.org/10.1126/science.abl4784.

(131) Shin, D.; Mukherjee, R.; Grewe, D.; Bojkova, D.; Baek, K.; Bhattacharya, A.; Schulz, L.; Widera, M.; Mehdipour, A. R.; Tascher, G.; Geurink, P. P.; Wilhelm, A.; van der Heden van Noort, G. J.; Ovaa, H.; Müller, S.; Knobeloch, K.-P.; Rajalingam, K.; Schulman, B. A.; Cinatl, J.; Hummer, G.; Ciesek, S.; Dikic, I. Papain-like Protease Regulates SARS-CoV-2 Viral Spread and Innate Immunity. *Nature* **2020**, *587* (7835), 657–662. https://doi.org/10.1038/s41586-020-2601-5.

(132) Müller, P.; Maus, H.; Hammerschmidt, S. J.; Knaff, P. M.; Mailänder, V.; Schirmeister, T.; Kersten, C. Interfering with Host Proteases in SARS-CoV-2 Entry as a Promising Therapeutic Strategy. *Curr Med Chem* **2022**, *29* (4), 635–665. https://doi.org/10.2174/0929867328666210526111318.

(133) Zhao, M.-M.; Yang, W.-L.; Yang, F.-Y.; Zhang, L.; Huang, W.-J.; Hou, W.; Fan, C.-F.; Jin, R.-H.; Feng, Y.-M.; Wang, Y.-C.; Yang, J.-K. Cathepsin L Plays a Key Role in SARS-CoV-2 Infection in Humans and Humanized Mice and Is a Promising Target for New Drug Development. *Signal Transduct Target Ther* **2021**, *6* (1), 134. https://doi.org/10.1038/s41392-021-00558-8.

(134) Meewan, I.; Kattoula, J.; Kattoula, J. Y.; Skinner, D.; Fajtová, P.; Giardini, M. A.; Woodworth, B.; McKerrow, J. H.; Lage de Siqueira-Neto, J.; O'Donoghue, A. J.; Abagyan, R. Discovery of Triple Inhibitors of Both SARS-CoV-2 Proteases and Human Cathepsin L. *Pharmaceuticals* **2022**, *15* (6), 744. https://doi.org/10.3390/ph15060744.

(135) Previti, S.; Di Chio, C.; Ettari, R.; Zappalà, M. Dual Inhibition of Parasitic Targets: A Valuable Strategy to Treat Malaria and Neglected Tropical Diseases. *Curr Med Chem* **2022**, *29* (17), 2952–2978. https://doi.org/10.2174/0929867328666210810125309.

(136) Stanković, T.; Dinić, J.; Podolski-Renić, A.; Musso, L.; Burić, S. S.; Dallavalle, S.; Pešić, M. Dual Inhibitors as a New Challenge for Cancer Multidrug Resistance Treatment. *Curr Med Chem* **2019**, *26* (33), 6074–6106. https://doi.org/10.2174/0929867325666180607094856.

(137) Liu, C.; Boland, S.; Scholle, M. D.; Bardiot, D.; Marchand, A.; Chaltin, P.; Blatt, L. M.; Beigelman, L.; Symons, J. A.; Raboisson, P.; Gurard-Levin, Z. A.; Vandyck, K.; Deval, J. Dual Inhibition of SARS-CoV-2 and Human Rhinovirus with Protease Inhibitors in Clinical Development. *Antiviral Res* **2021**, *187*, 105020. https://doi.org/10.1016/j.antiviral.2021.105020.

(138) Ma, X. R.; Alugubelli, Y. R.; Ma, Y.; Vatansever, E. C.; Scott, D. A.; Qiao, Y.; Yu, G.; Xu, S.; Liu, W. R. MPI8 Is Potent against SARS-CoV-2 by Inhibiting Dually and Selectively the SARS-CoV-2 Main Protease and the Host Cathepsin L**. *ChemMedChem* **2022**, *17* (1). https://doi.org/10.1002/cmdc.202100456.

(139) Ludewig, S.; Kossner, M.; Schiller, M.; Baumann, K.; Schirmeister, T. Enzyme Kinetics and Hit Validation in Fluorimetric Protease Assays. *Curr Top Med Chem* **2010**, *10* (3), 368–382. https://doi.org/10.2174/156802610790725498.

(140) Klein, P.; Barthels, F.; Johe, P.; Wagner, A.; Tenzer, S.; Distler, U.; Le, T. A.; Schmid, P.; Engel, V.; Engels, B.; Hellmich, U. A.; Opatz, T.; Schirmeister, T. Naphthoquinones as Covalent Reversible Inhibitors of Cysteine Proteases—Studies on Inhibition Mechanism and Kinetics. *Molecules* **2020**, *25* (9), 2064. https://doi.org/10.3390/molecules25092064.

(141) Müller, C.; Schulte, F. W.; Lange-Grünweller, K.; Obermann, W.; Madhugiri, R.; Pleschka, S.; Ziebuhr, J.; Hartmann, R. K.; Grünweller, A. Broad-Spectrum Antiviral Activity of the EIF4A Inhibitor Silvestrol against Corona- and Picornaviruses. *Antiviral Res* **2018**, *150*, 123–129. https://doi.org/10.1016/j.antiviral.2017.12.010.

(142) Müller, C.; Obermann, W.; Schulte, F. W.; Lange-Grünweller, K.; Oestereich, L.; Elgner, F.; Glitscher, M.; Hildt, E.; Singh, K.; Wendel, H.-G.; Hartmann, R. K.; Ziebuhr, J.; Grünweller, A. Comparison of Broad-Spectrum Antiviral Activities of the Synthetic Rocaglate CR-31-B (−) and the EIF4A-Inhibitor Silvestrol. *Antiviral Res* **2020**, *175*, 104706. https://doi.org/10.1016/j.antiviral.2020.104706.

(143) Bianco, G.; Forli, S.; Goodsell, D. S.; Olson, A. J. Covalent Docking Using Autodock: Two-point Attractor and Flexible Side Chain Methods. *Protein Science* **2016**, *25* (1), 295–301. https://doi.org/10.1002/pro.2733.

(144) Jin, Z.; Du, X.; Xu, Y.; Deng, Y.; Liu, M.; Zhao, Y.; Zhang, B.; Li, X.; Zhang, L.; Peng, C.; Duan, Y.; Yu, J.; Wang, L.; Yang, K.; Liu, F.; Jiang, R.; Yang, X.; You, T.; Liu, X.; Yang, X.; Bai, F.; Liu, H.; Liu, X.; Guddat, L. W.; Xu, W.; Xiao, G.; Qin, C.; Shi, Z.; Jiang, H.; Rao, Z.; Yang, H. Structure of Mpro from SARS-CoV-2 and Discovery of Its Inhibitors. *Nature* **2020**, *582* (7811), 289–293. https://doi.org/10.1038/s41586-020-2223-y.

(145) Shenoy, R. T.; Sivaraman, J. Structural Basis for Reversible and Irreversible Inhibition of Human Cathepsin L by Their Respective Dipeptidyl Glyoxal and Diazomethylketone Inhibitors. *J Struct Biol* **2011**, *173* (1), 14–19. https://doi.org/10.1016/j.jsb.2010.09.007.

(146) Crea, F.; De Stefano, C.; Gigliuto, A.; Irto, A. Behavior of Antibacterial Ofloxacin; Hydronation Constants and Solubility in Aqueous Solutions of Sodium Chloride at Different Temperatures. *J Solution Chem* **2021**, *50* (9–10), 1236–1257. https://doi.org/10.1007/s10953-021-01114-2.

(147) Pereira, S. V.; Colombo, F. B.; de Freitas, L. A. P. Ultrasound Influence on the Solubility of Solid Dispersions Prepared for a Poorly Soluble Drug. *Ultrason Sonochem* **2016**, *29*, 461–469. https://doi.org/10.1016/j.ultsonch.2015.10.022.

(148) Castillo-Peinado, L. de los S.; Luque de Castro, M. D. The Role of Ultrasound in Pharmaceutical Production: Sonocrystallization. *Journal of Pharmacy and Pharmacology* **2016**, *68* (10), 1249–1267. https://doi.org/10.1111/jphp.12614.

(149) Sacco, M. D.; Ma, C.; Lagarias, P.; Gao, A.; Townsend, J. A.; Meng, X.; Dube, P.; Zhang, X.; Hu, Y.; Kitamura, N.; Hurst, B.; Tarbet, B.; Marty, M. T.; Kolocouris, A.; Xiang, Y.; Chen, Y.; Wang, J. Structure and Inhibition of the SARS-CoV-2 Main Protease Reveal Strategy for

Developing Dual Inhibitors against M ^{pro} and Cathepsin L. *Sci Adv* **2020**, *6* (50). https://doi.org/10.1126/sciadv.abe0751.

(150) Robello, M.; Barresi, E.; Baglini, E.; Salerno, S.; Taliani, S.; Settimo, F. Da. The Alpha Keto Amide Moiety as a Privileged Motif in Medicinal Chemistry: Current Insights and Emerging Opportunities. *J Med Chem* **2021**, *64* (7), 3508–3545. https://doi.org/10.1021/acs.jmedchem.0c01808.

(151) Rut, W.; Lv, Z.; Zmudzinski, M.; Patchett, S.; Nayak, D.; Snipas, S. J.; El Oualid, F.; Huang, T. T.; Bekes, M.; Drag, M.; Olsen, S. K. Activity Profiling and Crystal Structures of Inhibitor-Bound SARS-CoV-2 Papain-like Protease: A Framework for Anti–COVID-19 Drug Design. *Sci Adv* **2020**, *6* (42). https://doi.org/10.1126/sciadv.abd4596.

(152) Hoffman, R. L.; Kania, R. S.; Brothers, M. A.; Davies, J. F.; Ferre, R. A.; Gajiwala, K. S.; He, M.; Hogan, R. J.; Kozminski, K.; Li, L. Y.; Lockner, J. W.; Lou, J.; Marra, M. T.; Mitchell, L. J.; Murray, B. W.; Nieman, J. A.; Noell, S.; Planken, S. P.; Rowe, T.; Ryan, K.; Smith, G. J.; Solowiej, J. E.; Steppan, C. M.; Taggart, B. Discovery of Ketone-Based Covalent Inhibitors of Coronavirus 3CL Proteases for the Potential Therapeutic Treatment of COVID-19. *J Med Chem* **2020**, *63* (21), 12725–12747. https://doi.org/10.1021/acs.jmedchem.0c01063.

(153) Welker, A.; Kersten, C.; Müller, C.; Madhugiri, R.; Zimmer, C.; Müller, P.; Zimmermann, R.; Hammerschmidt, S.; Maus, H.; Ziebuhr, J.; Sotriffer, C.; Schirmeister, T. Structure-Activity Relationships of Benzamides and Isoindolines Designed as SARS-CoV Protease Inhibitors Effective against SARS-CoV-2. *ChemMedChem* **2021**, *16* (2), 340–354. https://doi.org/10.1002/cmdc.202000548.

(154) Maus, H.; Barthels, F.; Hammerschmidt, S. J.; Kopp, K.; Millies, B.; Gellert, A.; Ruggieri, A.; Schirmeister, T. SAR of Novel Benzothiazoles Targeting an Allosteric Pocket of DENV and ZIKV NS2B/NS3 Proteases. *Bioorg Med Chem* **2021**, *47*, 116392. https://doi.org/10.1016/j.bmc.2021.116392.

(155) Previti, S.; Ettari, R.; Di Chio, C.; Ravichandran, R.; Bogacz, M.; Hellmich, U. A.; Schirmeister, T.; Cosconati, S.; Zappalà, M. Development of Reduced Peptide Bond Pseudopeptide Michael Acceptors for the Treatment of Human African Trypanosomiasis. *Molecules* **2022**, *27* (12), 3765. https://doi.org/10.3390/molecules27123765.

(156) Ettari, R.; Pinto, A.; Previti, S.; Tamborini, L.; Angelo, I. C.; La Pietra, V.; Marinelli, L.; Novellino, E.; Schirmeister, T.; Zappalà, M.; Grasso, S.; De Micheli, C.; Conti, P. Development of Novel Dipeptide-like Rhodesain Inhibitors Containing the 3-Bromoisoxazoline Warhead in a Constrained Conformation. *Bioorg Med Chem* **2015**, *23* (21), 7053–7060. https://doi.org/10.1016/j.bmc.2015.09.029.

(157) Leatherbarrow RJ. GraFit 6. Erithacus Software Limited: East Grinstead, West Sussex, UK. 2007.

(158) Ludewig, S.; Kossner, M.; Schiller, M.; Baumann, K.; Schirmeister, T. Enzyme Kinetics and Hit Validation in Fluorimetric Protease Assays. *Curr Top Med Chem* **2010**, *10* (3), 368–382. https://doi.org/10.2174/156802610790725498.

(159) Klein, P.; Barthels, F.; Johe, P.; Wagner, A.; Tenzer, S.; Distler, U.; Le, T. A.; Schmid, P.; Engel, V.; Engels, B.; Hellmich, U. A.; Opatz, T.; Schirmeister, T. Naphthoquinones as Covalent Reversible Inhibitors of Cysteine Proteases—Studies on Inhibition Mechanism and Kinetics. *Molecules* **2020**, *25* (9), 2064. https://doi.org/10.3390/molecules25092064.

(160) Hoffmann, M.; Kleine-Weber, H.; Schroeder, S.; Krüger, N.; Herrler, T.; Erichsen, S.; Schiergens, T. S.; Herrler, G.; Wu, N.-H.; Nitsche, A.; Müller, M. A.; Drosten, C.; Pöhlmann, S. SARS-CoV-2 Cell Entry Depends on ACE2 and TMPRSS2 and Is Blocked by a Clinically Proven Protease Inhibitor. *Cell* **2020**, *181* (2), 271-280.e8. https://doi.org/10.1016/j.cell.2020.02.052.

(161) Müller, C.; Schulte, F. W.; Lange-Grünweller, K.; Obermann, W.; Madhugiri, R.; Pleschka, S.; Ziebuhr, J.; Hartmann, R. K.; Grünweller, A. Broad-Spectrum Antiviral Activity of the EIF4A Inhibitor Silvestrol against Corona- and Picornaviruses. *Antiviral Res* **2018**, *150*, 123–129. https://doi.org/10.1016/j.antiviral.2017.12.010.

(162) Morris, G. M.; Huey, R.; Lindstrom, W.; Sanner, M. F.; Belew, R. K.; Goodsell, D. S.; Olson, A. J. AutoDock4 and AutoDockTools4: Automated Docking with Selective Receptor Flexibility. *J Comput Chem* **2009**, *30* (16), 2785–2791. https://doi.org/10.1002/jcc.21256.

(163) Madhavi Sastry, G.; Adzhigirey, M.; Day, T.; Annabhimoju, R.; Sherman, W. Protein and Ligand Preparation: Parameters, Protocols, and Influence on Virtual Screening Enrichments. *J Comput Aided Mol Des* **2013**, *27* (3), 221–234. https://doi.org/10.1007/s10822-013-9644-8.

(164) Pettersen, E. F.; Goddard, T. D.; Huang, C. C.; Meng, E. C.; Couch, G. S.; Croll, T. I.; Morris, J. H.; Ferrin, T. E. <scp>UCSF ChimeraX</Scp> : Structure Visualization for Researchers, Educators, and Developers. *Protein Science* **2021**, *30* (1), 70–82. https://doi.org/10.1002/pro.3943.

(165) Jiang, W.; Phillips, J. C.; Huang, L.; Fajer, M.; Meng, Y.; Gumbart, J. C.; Luo, Y.; Schulten, K.; Roux, B. Generalized Scalable Multiple Copy Algorithms for Molecular Dynamics Simulations in NAMD. *Comput Phys Commun* **2014**, *185* (3), 908–916. https://doi.org/10.1016/j.cpc.2013.12.014.

(166) Harrach, M. F.; Drossel, B. Structure and Dynamics of TIP3P, TIP4P, and TIP5P Water near Smooth and Atomistic Walls of Different Hydroaffinity. *J Chem Phys* **2014**, *140* (17). https://doi.org/10.1063/1.4872239.

(167) P. Mark; L. Nilsson. Structure and Dynamics of the TIP3P, SPC, and SPC/E Water Models at 298 K. J. Phys. Chem. A 105 (2001) 9954-9960.

(168) G.J. Martyna; M.E. Tuckerman; D.J. Tobias; M.L. Klein. Explicit Reversible Integrators for Extended Systems Dynamics. Mol. Phys. 87 (1996) 1117-1157.

(169) W.G. Hoover. Canonical Dynamics: Equilibrium Phase-Space Distributions. Phys. Rev. A Gen. Phys. 31 (1985) 1695-1697.

(170) Roos, K.; Wu, C.; Damm, W.; Reboul, M.; Stevenson, J. M.; Lu, C.; Dahlgren, M. K.; Mondal, S.; Chen, W.; Wang, L.; Abel, R.; Friesner, R. A.; Harder, E. D. OPLS3e: Extending Force Field Coverage for Drug-Like Small Molecules. *J Chem Theory Comput* **2019**, *15* (3), 1863–1874. https://doi.org/10.1021/acs.jctc.8b01026.

(171) World Health Organization. Human African Trypanosomiasis (Sleeping Sickness). Available Online: Https://Www.Who.Int/Health-Topics/Human-African-Trypanosomiasis#tab=tab_1 (Accessed on January 29 2024).

(172) Kennedy, P. G. E.; Rodgers, J. Clinical and Neuropathogenetic Aspects of Human African Trypanosomiasis. *Front Immunol* **2019**, *10*. https://doi.org/10.3389/fimmu.2019.00039.

(173) Papagni, R.; Novara, R.; Minardi, M. L.; Frallonardo, L.; Panico, G. G.; Pallara, E.; Cotugno, S.; Ascoli Bartoli, T.; Guido, G.; De Vita, E.; Ricciardi, A.; Totaro, V.; Camporeale, M.; Segala, F. V.; Bavaro, D. F.; Patti, G.; Brindicci, G.; Pellegrino, C.; Mariani, M. F.; Putoto, G.; Sarmati, L.; Castellani, C.; Saracino, A.; Di Gennaro, F.; Nicastri, E. Human African Trypanosomiasis (Sleeping Sickness): Current Knowledge and Future Challenges. *Frontiers in Tropical Diseases* **2023**, *4*. https://doi.org/10.3389/fitd.2023.1087003.

(174) La Greca, F.; Magez, S. Vaccination against Trypanosomiasis. *Hum Vaccin* **2011**, *7* (11), 1225–1233. https://doi.org/10.4161/hv.7.11.18203.

(175) Jamabo, M.; Mahlalela, M.; Edkins, A. L.; Boshoff, A. Tackling Sleeping Sickness: Current and Promising Therapeutics and Treatment Strategies. *Int J Mol Sci* **2023**, *24* (15), 12529. https://doi.org/10.3390/ijms241512529.

(176) Ettari, R.; Tamborini, L.; Angelo, I. C.; Micale, N.; Pinto, A.; De Micheli, C.; Conti, P. Inhibition of Rhodesain as a Novel Therapeutic Modality for Human African Trypanosomiasis. *J Med Chem* **2013**, *56* (14), 5637–5658. https://doi.org/10.1021/jm301424d.

(177) Grab, D. J.; Garcia-Garcia, J. C.; Nikolskaia, O. V.; Kim, Y. V.; Brown, A.; Pardo, C. A.; Zhang, Y.; Becker, K. G.; Wilson, B. A.; de A. Lima, A. P. C.; Scharfstein, J.; Dumler, J. S. Protease Activated Receptor Signaling Is Required for African Trypanosome Traversal of Human Brain Microvascular Endothelial Cells. *PLoS Negl Trop Dis* **2009**, *3* (7), e479. https://doi.org/10.1371/journal.pntd.0000479.

(178) Santos, C. C.; Coombs, G. H.; Lima, A. P. C. A.; Mottram, J. C. Role of the *Trypanosoma Brucei* Natural Cysteine Peptidase Inhibitor ICP in Differentiation and Virulence. *Mol Microbiol* **2007**, *66* (4), 991–1002. https://doi.org/10.1111/j.1365-2958.2007.05970.x.

(179) Kerr, I. D.; Lee, J. H.; Farady, C. J.; Marion, R.; Rickert, M.; Sajid, M.; Pandey, K. C.; Caffrey, C. R.; Legac, J.; Hansell, E.; McKerrow, J. H.; Craik, C. S.; Rosenthal, P. J.; Brinen, L. S. Vinyl Sulfones as Antiparasitic Agents and a Structural Basis for Drug Design. *Journal of Biological Chemistry* **2009**, *284* (38), 25697–25703. https://doi.org/10.1074/jbc.M109.014340.

(180) Kerr, I. D.; Wu, P.; Marion-Tsukamaki, R.; Mackey, Z. B.; Brinen, L. S. Crystal Structures of TbCatB and Rhodesain, Potential Chemotherapeutic Targets and Major Cysteine Proteases of Trypanosoma Brucei. *PLoS Negl Trop Dis* **2010**, *4* (6), e701. https://doi.org/10.1371/journal.pntd.0000701.

(181) Giroud, M.; Dietzel, U.; Anselm, L.; Banner, D.; Kuglstatter, A.; Benz, J.; Blanc, J.-B.; Gaufreteau, D.; Liu, H.; Lin, X.; Stich, A.; Kuhn, B.; Schuler, F.; Kaiser, M.; Brun, R.; Schirmeister, T.; Kisker, C.; Diederich, F.; Haap, W. Repurposing a Library of Human Cathepsin L Ligands: Identification of Macrocyclic Lactams as Potent Rhodesain and *Trypanosoma Brucei* Inhibitors. *J Med Chem* **2018**, *61* (8), 3350–3369. https://doi.org/10.1021/acs.jmedchem.7b01869.

(182) Johé, P.; Jaenicke, E.; Neuweiler, H.; Schirmeister, T.; Kersten, C.; Hellmich, U. A. Structure, Interdomain Dynamics, and PH-Dependent Autoactivation of pro-Rhodesain, the Main Lysosomal Cysteine Protease from African Trypanosomes. *Journal of Biological Chemistry* **2021**, *296*, 100565. https://doi.org/10.1016/j.jbc.2021.100565.

(183) Ettari, R.; Previti, S.; Tamborini, L.; Cullia, G.; Grasso, S.; Zappalà, M. The Inhibition of Cysteine Proteases Rhodesain and TbCatB: A Valuable Approach to Treat Human African Trypanosomiasis. *Mini-Reviews in Medicinal Chemistry* **2016**, *16* (17), 1374–1391. https://doi.org/10.2174/1389557515666160509125243.

(184) dos Santos Nascimento, I. J.; de Aquino, T. M.; da Silva-Júnior, E. F. Cruzain and Rhodesain Inhibitors: Last Decade of Advances in Seeking for New Compounds Against American and African Trypanosomiases. *Curr Top Med Chem* **2021**, *21* (21), 1871–1899. https://doi.org/10.2174/1568026621666210331152702.

(185) Jornada, D.; Dos Santos Fernandes, G.; Chiba, D.; De Melo, T.; Dos Santos, J.; Chung, M. The Prodrug Approach: A Successful Tool for Improving Drug Solubility. *Molecules* **2015**, *21* (1), 42. https://doi.org/10.3390/molecules21010042.

(186) Previti, S.; Ettari, R.; Di Chio, C.; Legac, J.; Bogacz, M.; Zimmer, C.; Schirmeister, T.; Rosenthal, P. J.; Zappalà, M. Influence of Amino Acid Size at the P3 Position of N-Cbz-Tripeptide Michael Acceptors Targeting Falcipain-2 and Rhodesain for the Treatment of Malaria and Human African Trypanosomiasis. *Bioorg Chem* **2023**, *137*, 106587. https://doi.org/10.1016/j.bioorg.2023.106587.

(187) Previti, S.; Ettari, R.; Calcaterra, E.; Di Chio, C.; Ravichandran, R.; Zimmer, C.; Hammerschmidt, S.; Wagner, A.; Bogacz, M.; Cosconati, S.; Schirmeister, T.; Zappalà, M. Development of Urea-Bond-Containing Michael Acceptors as Antitrypanosomal Agents Targeting Rhodesain. *ACS Med Chem Lett* **2022**, *13* (7), 1083–1090. https://doi.org/10.1021/acsmedchemlett.2c00084.

(188) Maiorana, S.; Ettari, R.; Previti, S.; Amendola, G.; Wagner, A.; Cosconati, S.; Hellmich, U. A.; Schirmeister, T.; Zappalà, M. Peptidyl Vinyl Ketone Irreversible Inhibitors of Rhodesain:

Modifications of the P2 Fragment. *ChemMedChem* **2020**, *15* (16), 1552–1561. https://doi.org/10.1002/cmdc.202000360.

(189) Ettari, R.; Previti, S.; Maiorana, S.; Amendola, G.; Wagner, A.; Cosconati, S.; Schirmeister, T.; Hellmich, U. A.; Zappalà, M. Optimization Strategy of Novel Peptide-Based Michael Acceptors for the Treatment of Human African Trypanosomiasis. *J Med Chem* **2019**, *62* (23), 10617–10629. https://doi.org/10.1021/acs.jmedchem.9b00908.

(190) Previti, S.; Ettari, R.; Cosconati, S.; Amendola, G.; Chouchene, K.; Wagner, A.; Hellmich, U. A.; Ulrich, K.; Krauth-Siegel, R. L.; Wich, P. R.; Schmid, I.; Schirmeister, T.; Gut, J.; Rosenthal, P. J.; Grasso, S.; Zappalà, M. Development of Novel Peptide-Based Michael Acceptors Targeting Rhodesain and Falcipain-2 for the Treatment of Neglected Tropical Diseases (NTDs). *J Med Chem* **2017**, *60* (16), 6911–6923. https://doi.org/10.1021/acs.jmedchem.7b00405.

(191) Bozovičar, K.; Bratkovič, T. Small and Simple, yet Sturdy: Conformationally Constrained Peptides with Remarkable Properties. *Int J Mol Sci* **2021**, *22* (4), 1611. https://doi.org/10.3390/ijms22041611.

(192) Jung, S.; Fuchs, N.; Grathwol, C.; Hellmich, U. A.; Wagner, A.; Diehl, E.; Willmes, T.; Sotriffer, C.; Schirmeister, T. New Peptidomimetic Rhodesain Inhibitors with Improved Selectivity towards Human Cathepsins. *Eur J Med Chem* **2022**, *238*, 114460. https://doi.org/10.1016/j.ejmech.2022.114460.

(193) Ettari, R.; Previti, S.; Cosconati, S.; Maiorana, S.; Schirmeister, T.; Grasso, S.; Zappalà, M. Development of Novel 1,4-Benzodiazepine-Based Michael Acceptors as Antitrypanosomal Agents. *Bioorg Med Chem Lett* **2016**, *26* (15), 3453–3456. https://doi.org/10.1016/j.bmcl.2016.06.047.

(194) Cabrele, C.; Martinek, T. A.; Reiser, O.; Berlicki, Ł. Peptides Containing β-Amino Acid Patterns: Challenges and Successes in Medicinal Chemistry. *J Med Chem* **2014**, *57* (23), 9718–9739. https://doi.org/10.1021/jm5010896.

(195) Zhang, Y.; Fang, H.; Xu, W. Applications and Modifications of 1,2,3,4-Tetrahydroisoquinoline-3-Carboxylic Acid (Tic) in Peptides and Peptidomimetics Design and Discovery. *Curr Protein Pept Sci* **2010**, *11* (8), 752–758. https://doi.org/10.2174/138920310794557691.

(196) Di Chio, C.; Previti, S.; Amendola, G.; Ravichandran, R.; Wagner, A.; Cosconati, S.; Hellmich, U. A.; Schirmeister, T.; Zappalà, M.; Ettari, R. Development of Novel Dipeptide Nitriles as Inhibitors of Rhodesain of Trypanosoma Brucei Rhodesiense. *Eur J Med Chem* **2022**, *236*, 114328. https://doi.org/10.1016/j.ejmech.2022.114328.

(197) Previti, S.; Ettari, R.; Di Chio, C.; Ravichandran, R.; Bogacz, M.; Hellmich, U. A.; Schirmeister, T.; Cosconati, S.; Zappalà, M. Development of Reduced Peptide Bond Pseudopeptide Michael Acceptors for the Treatment of Human African Trypanosomiasis. *Molecules* **2022**, *27* (12), 3765. https://doi.org/10.3390/molecules27123765.

(198) Carter, N.; Li, X.; Reavey, L.; Meijer, A. J. H. M.; Coldham, I. Synthesis and Kinetic Resolution of Substituted Tetrahydroquinolines by Lithiation Then Electrophilic Quench. *Chem Sci* **2018**, *9* (5), 1352–1357. https://doi.org/10.1039/C7SC04435F.

(199) Al-Horani, R. A.; Desai, U. R. Electronically Rich N-Substituted Tetrahydroisoquinoline 3-Carboxylic Acid Esters: Concise Synthesis and Conformational Studies. *Tetrahedron* **2012**, *68* (8), 2027–2040. https://doi.org/10.1016/j.tet.2012.01.005.

(200) SAITOH, T.; ICHIKAWA, T.; HORIGUCHI, Y.; TODA, J.; SANO, T. A Synthesis of 3-Phenyl-1,2,3,4-Tetrahydroisoquinoline and 2-Phenyl-1,2,4,5-Tetrahydro-3H-3-Benzazepine via Pummerer-Type Cyclization: Enhancing Effect of Boron Trifluoride Diethyl Etherate on the Cyclization. *Chem Pharm Bull (Tokyo)* **2001**, *49* (8), 979–984. https://doi.org/10.1248/cpb.49.979.

(201) Mackey, Z. B.; O'Brien, T. C.; Greenbaum, D. C.; Blank, R. B.; McKerrow, J. H. A Cathepsin B-like Protease Is Required for Host Protein Degradation in Trypanosoma Brucei. *Journal of Biological Chemistry* **2004**, *279* (46), 48426–48433. https://doi.org/10.1074/jbc.M402470200.

(202) O'Brien, T. C.; Mackey, Z. B.; Fetter, R. D.; Choe, Y.; O'Donoghue, A. J.; Zhou, M.; Craik, C. S.; Caffrey, C. R.; McKerrow, J. H. A Parasite Cysteine Protease Is Key to Host Protein Degradation and Iron Acquisition. *Journal of Biological Chemistry* **2008**, *283* (43), 28934–28943. https://doi.org/10.1074/jbc.M805824200.

(203) Faheem; Karan Kumar, B.; Chandra Sekhar, K. V. G.; Chander, S.; Kunjiappan, S.; Murugesan, S. Medicinal Chemistry Perspectives of 1,2,3,4-Tetrahydroisoquinoline Analogs – Biological Activities and SAR Studies. *RSC Adv* **2021**, *11* (20), 12254–12287. https://doi.org/10.1039/D1RA01480C.

(204) Schirmeister, T.; Kesselring, J.; Jung, S.; Schneider, T. H.; Weickert, A.; Becker, J.; Lee, W.; Bamberger, D.; Wich, P. R.; Distler, U.; Tenzer, S.; Johé, P.; Hellmich, U. A.; Engels, B. Quantum Chemical-Based Protocol for the Rational Design of Covalent Inhibitors. *J Am Chem Soc* **2016**, *138* (27), 8332–8335. https://doi.org/10.1021/jacs.6b03052.

(205) Tian, W. X.; Tsou, C. L. Determination of the Rate Constant of Enzyme Modification by Measuring the Substrate Reaction in the Presence of the Modifier. *Biochemistry* **1982**, *21* (5), 1028–1032. https://doi.org/10.1021/bi00534a031.

(206) Vicik, R.; Hoerr, V.; Glaser, M.; Schultheis, M.; Hansell, E.; McKerrow, J. H.; Holzgrabe, U.; Caffrey, C. R.; Ponte-Sucre, A.; Moll, H.; Stich, A.; Schirmeister, T. Aziridine-2,3-Dicarboxylate Inhibitors Targeting the Major Cysteine Protease of Trypanosoma Brucei as Lead Trypanocidal Agents. *Bioorg Med Chem Lett* **2006**, *16* (10), 2753–2757. https://doi.org/10.1016/j.bmcl.2006.02.026.

(207) Biebinger, S.; Elizabeth Wirtz, L.; Lorenz, P.; Christine Clayton. Vectors for Inducible Expression of Toxic Gene Products in Bloodstream and Procyclic Trypanosoma Brucei. *Mol Biochem Parasitol* **1997**, *85* (1), 99–112. https://doi.org/10.1016/S0166-6851(96)02815-0.